MULTI WAVELENGTH STUDIES OF NARROW LINE SEYFERT 1 GALAXIES

A THESIS SUBMITTED TO THE UNIVERSITY OF LEICESTER
FOR THE DEGREE OF DOCTOR OF PHILOSOPHY
IN THE FACULTY OF SCIENCE AND ENGINEERING

August 2000

By
Paul Hirst
Department of Physics & Astronomy

Contents

List of Tables

List of Figures

Abstract

Narrow Line Seyfert 1 galaxies are an interesting subset of Seyfert 1 galaxies displaying intriguing optical and X-ray spectral properties that make them particularly difficult to unify with other types of Active Galactic Nuclei in terms of the standard orientation based unified scheme.

We review the literature on NLS1s and the theoretical models that have been hypothesised as an explanation of their properties, along with a brief overview of AGN unification schemes.

We present data from a near IR spectroscopic study of a sample of NLS1s carried out with CGS4 on UKIRT, an NLS1 radio imaging project utilising both archival and new data from MERLIN and the VLA, and a near IR imaging study on NLS1s carried out using UFTI on UKIRT. We also present Spectral Energy Distributions of NLS1s assembled from data mined from the literature, along with results from an ISO and SCUBA study of NLS1s examining the mid IR to sub-mm dust emission properties of the NLS1s.

Finally, in conclusion, we suggest a possible sub-division of the NLS1 class into two distinct sets of objects, one of which we believe fits in with the so called "pole-on" model, the other with models that suggest a high accretion rate onto a low mass black hole.

Preface

Acknowledgements

Many people have contributed in some way to this thesis, and I remain indebted to you all.

I should like to thank my supervisor, Martin Ward, for his guidance on academic and research matters, and for letting me get on with my research in my own way whilst providing insightful assistance when asked. I'd also like to thank Martin for enthusing about countless observing proposals, not minding me disappearing to climb mountains on every suitable observing trip, suggesting I go to a conference in an off-the-beaten-track mountain range, and of course, for introducing me to the world of airline frequent flier programmes.

I would like to thank Duncan Law-Green for his most useful input to my research, primarily for teaching me the practicalities of radio astronomy, and for his invaluable assistance in implementing the aforementioned enthusings.

Some mention of the rest of the X-ray astronomy group at Leicester is due here, both those who have enhanced my work with snippets of X-ray results and discussions, and those dedicated X-ray devotees (see Markl & Hauptmann 1983) who ended up being forced to tolerate me doing both radio and IR work, without so much as a ROSAT data set in sight.

Thanks also to the excellent team of scientists at UKIRT, who have provided excellent support through all my observing trips and data reduction battles; a team that from my first trip to Hawaii, I've aspired to be part of, and am now honoured to have been offered that opportunity.

Outside of research, many people have made my stay in Leicester a pleasure.

- Adrian and Steph for being comedy house mates, for getting me into this climbing lark, and for demonstrating that growing old ungracefully isn't really too hard.
- All the Tichborne St. people; past, present and honorary, especially the boy Linus for selflessly giving up his time to come and visit me in Hawaii, Johnny

for his medical insight, and for generally being Johnny, Barry, Ben and of course Will for generally being a great bloke, and the Sarahs, with their unique blend of randomness and liveliness.

- All those other people in the LUMC who got me in to climbing, provided great laughs during weekend escapes from dreary Leicester, and for trustingly following me up cliffs and snow clad mountains, down abseils and across rivers.

Huge thanks go to Yvonne for keeping me relatively sane whilst I struggled to write up my thesis and organise starting work in Hawaii, for being someone to laugh with, and for being there when I needed you most. Yv, words fail me... Thanks for so much more than you realise.

Finally, and most importantly, I'd like to express my heartfelt thanks and gratitude to my Mum and Dad, whose unconditional encouragement, support and love throughout my whole life have enabled me to freely follow my studies, interests and hobbies to where they have led me today.

The Author

I graduated from Lincoln College, Oxford, with a Half Blue in Gliding and a BA in Physics after taking finals in the summer of 1995, at which point I took a place on the MSc course at NRAL Jodrell Bank, and conducted research into the nature of Compact Steep Spectrum radio sources at high redshift (Hirst 1996). Upon completion of my MSc I moved to the X-ray Astronomy Group at the University of Leicester to carry out research leading to the production of this thesis, and to get engrossed in the sports of mountaineering and rock climbing.

After submitting this thesis, I plan to move to Hawaii to take up a job as a UKIRT support astronomer with the Joint Astronomy Centre.

Led by gaeten, they travel in search of a secret valley, marked simply "obscured by clouds" on the map, that is held in reverential esteem by the local people as the home of their gods...

– from "The valley", quoted by Pink Floyd in "Obscured by Clouds".

Publications

Apart from this Thesis, the following publications have resulted from this work:

- Hirst, P., Law-Green, J. D. B., Ward, M. J. Poster presentation and proceedings article, IAU symposium 194: Activity in Galaxies and Related Phenomena, August 1998. "Multiwavelength properties of the Narrow-line Seyfert 1's: Studying on extreme of the AGN primary eigenvector."

The following papers are in preparation for submission to MNRAS:

- Hirst, P. Law-Green, J. D. B., Ward, M. J. "The radio properties of Narrow Line Seyfert 1 galaxies".
- Hirst, P. Law-Green, J. D. B., Ward, M. J. "Near IR imaging studies of NLS1s".
- Hirst, P. Law-Green, J. D. B., Ward, M. J. "Near IR spectroscopy of NLS1s".
- Law-Green, J. D. B., Hirst, P., Boisson, C., O'Brien, P. T., Ward, M. "ISO and SCUBA photometry of Narrow-Line Seyfert 1's".
- Law-Green, J. D. B., Ueno, S., Miyata, T., Hirst, P. "Thermal infrared imaging and spectroscopy of Narrow-Line Seyfert 1's".

Chapter 1

Introduction - a Literature Review

1.1 AGN

Since their discovery, a vast array of different classes of Active Galactic Nuclei (AGN) have been found, each having its own set of observational properties. Various models have been proposed in which many of these classes are closely related. These models have, in general, been very successful in annexing most classes of AGN, generally by suggesting a single parameter which if changed, would give one class of AGN the observational properties of another type. An overview of these unification models will be given shortly.

This thesis documents my study of a certain type of AGN known as "Narrow Line Seyfert 1s" (NLS1s). NLS1s are unusual in that unification models have been so far unsuccessful in relating them to 'normal' AGN. Although it seems obvious that NLS1s are closely related to 'normal' Seyfert galaxies; indeed they are a subset of the Seyfert 1 class, they have unusual properties which have yet to be explained in terms of a convincing physical model.

It is not my intention to extensively review the general AGN literature here, though the aspects relevant to the discussions presented herein will be briefly reviewed.

1.1.1 Emission from AGN

AGN emit radiation in all wavebands from the long wavelength radio through to high energy γ-rays. The spectral energy distribution (SED) of this radiation can reveal aspects of the physics causing the emission, as can detailed study of individual smaller frequency ranges.

1.1.1.1 X-Rays

Seyfert galaxies are, in general, X-ray bright, with a substantial proportion (usually up to $\approx$ 30 %) of the total luminosity of the Seyfert nucleus being emitted in the X-ray band. The large and rapid amplitude variability shown by some Seyfert nuclei indicate that the X-ray flux is being emitted from a relatively small volume close to the central black hole. The majority of Seyfert 1s show a relatively flat 2 – 10 keV X-ray continuum, with a photon index, Γ, in the range 1.9 – 2.0. They often show an apparent soft X-ray excess below around 0.5 keV. Brandt (1996) identifies three X-ray emission components up to 50keV associated with the centres of Seyfert galaxies: (1) The hard power law continuum, (2) The soft excess and (3) a reflected continuum component.

As a first order approximation, the X-ray emission of Seyfert 1s can be described as a power law, modified at low energies by photoelectric absorption by neutral hydrogen:

$$f(E) = f(1\mathrm{keV})E^{-\Gamma}e^{-N_H\sigma_p}\mathrm{photons\ cm^{-2}\ s^{-1}\ keV^{-1}}$$

where E is energy in keV, $f(E)$ is the photon flux density at energy E, Γ is the photon index, N_H is the equivalent hydrogen column density of the absorbing material, and σ_p is the photoelectric cross-section per hydrogen atom.

Fitting such a model to many Seyfert 1 observations in the 2–10 keV band produces a photon index of 1.7 – 1.8 (e.g. Turner & Pounds 1989), though these values are thought to be influenced by X-ray reflection, and are thus not intrinsic. Fitted N_H values vary between sources, the main contribution being from the column through the Milky Way in the direction of the source, though some sources show evidence for intrinsic photoelectric absorption, which can vary strongly with time.

Second order additions to this model, required to achieve statistically good fits to observed data, include the iron Kα line and a flattening effect which is often observed with a $\Delta\Gamma \approx 0.5$ between the 2–10keV and 10–18keV bands. The iron Kα line is consistent with 6.4keV fluorescent emission from neutral iron, and is generally observed in all but the higher luminosity Seyfert 1 objects. Iron Kα features are easily observed due to the high abundance and fluorescent yield of iron and the relatively low photoelectric absorption cross-section at the iron Kα energy, along with the fact that this feature is well separated in energy from other possible confusing spectral features.

The iron Kα line and spectral flattening are believed to occur when the X-ray source illuminates optically thick obscuring material that subtends a large solid angle to the X-ray source (e.g. George & Fabian 1991, Matt et al. 1991, Pounds et al. 1990). The Compton scattered X-rays that emerge from the obscuring material are known as the reflection component. Above about 10keV, the reflection component becomes stronger, due to the falling photoelectric opacity, and thus the reflection component leads to the observed spectral flattening.

When spectral models are modified by iron Kα and reflection components, a typical intrinsic photon index for a Seyfert 1 becomes 1.9 – 2.0 (e.g. Pounds et al. 1990). Detailed analysis of iron Kα data (e.g. Mushotzky et al. 1995, Tanaka et al. 1995, Fabian et al. 1995) shows that the aforementioned obscuring material is moving at relativistic velocities and, to first order, has a disk like structure.

Power-law models with cold absorption can be improved further by the addition of some kind of soft X-ray excess. In some Seyfert 1s at least, the soft X-ray excess cannot be explained in terms of complex absorption, and is more consistent with a blackbody of temperature 10 - 100 eV. In some cases, Bremsstrahlung or multiple blackbody models provide statistically better fits. Rapid, large amplitude, variability has been observed in the soft X-ray excess of many sources (e.g. Turner & Pounds 1989, Brandt 1996).

There is some evidence to suggest that the soft X-ray excess is the high energy tail of the so called 'big blue bump' that is observed in optical and UV spectra (e.g. Shields 1978, Malkan & Sargent 1982); Walter & Fink (1993) find a correlation between the UV to X-ray flux ratio and the soft X-ray spectral slope in that objects with a high 1375Å to 2keV ratio tend to show large soft X-ray photon indices, suggesting that this correlation arises from changes in the flux of a singe UV to X-ray component relative to the underlying continuum. In addition, Puchnarewicz et al. (1996) have reported that the blue end of the optical spectra and the soft end of the X-ray spectra in active galaxies from the RIXOS survey appear to be correlated. This does not rule out the possibility of a contribution to the 'big blue bump' from blended line emission; this is consistent with the X-ray slope correlation in the X-rays might at least in part drive this line emission (Griffiths et al. 1998).

I shall henceforth assume that the big blue bump and soft X-ray excess result from the same emission component. The origin of this component is uncertain. It may originate via intrinsic thermal emission from some source such as the accretion disk, or through a non-thermal process such as reprocessing of X-rays from the power law continuum in Thomson thick matter. The matter which radiates the big blue bump may be the same matter responsible for the iron Kα line and the reflection component, though this has not been rigorously established.

Multi-wavelength observations of correlated flux variability from NGC 5548 (Clavel et al. 1991, Clavel et al. 1992) have suggested that a significant fraction of its big blue bump arises through hard X-ray re-processing, though there is sometimes evidence for intrinsic emission as well (Clavel et al. 1992, Done et al. 1995).

In addition to the soft X-ray excess, X-ray spectra are also modified by the presence of oxygen and iron absorption edges, often referred to as a 'warm absorber'. In the ROSAT band, the most prominent warm absorber is oxygen, due to its large abundance and photo-ionisation cross-section.

The X-ray spectrum of some sources may have non-nuclear components. Particularly in Starbursts and Seyfert 2s, with obscured nuclei, regions of hot diffuse gas, heated by nuclear radiation, supernovae or perhaps stellar winds, can produce significant emission and is sometimes spatially resolved. NGC 1068 is a good example, where such emission from diffuse gas dominates the spectrum below 2 – 3 keV (Ueno et al. 1994).

1.1.1.2 Optical and Near IR

The optical spectra of AGN is characterised by emission and absorption lines superimposed on an optical continuum. Most of the continuum emission in Seyfert 1s originates in the AGN core, whereas all the line features are generated at some relatively large distance from the central engine.

The optical continuum is usually power law in shape, though this is often modified by dust extinction in the host galaxy. In Seyfert 2s, the optical continuum is often dominated by starlight, though a contribution from a featureless continuum may be present, possibly due to the scattered component of the Seyfert 1 continuum, not visible directly. The orientation based unified scheme (OBUS) postulates the existence of an optically thick dust torus which is located in our line of sight to the nucleus of Seyfert 2s. The presence of obscuring material, rather than the absence of the intrinsic emission is supported in bright nearby objects, such as Cyg A, where a very weak optical continuum may be found in polarised light - this is consistent with some of the optical continuum being scattered into our line of sight by dust outside the putative obscuring torus.

The broad line emission from Seyfert 1 type objects is supposed, by the orientation based unified scheme, to originate from clouds deep within the putative obscuring dust torus, and are thus not visible in Seyfert 2 type objects. Again, weak, polarised broad lines have been observed in bright, nearby Seyfert 2 orientation objects such as Cyg A and NGC 1068, indicating that this light is being scattered into our line of sight by material outside the obscuring torus.

Only permitted atomic transitions lead to broad lines; the temperature and density of the radiating gas is such that any atoms excited into the higher level of a forbidden or semi-forbidden state will undergo collisional de-excitation on a time-scale that is much less than the radiative de-excitation lifetime of the excited state. The lines are broadened by the kinematic movement of the clouds of emitting gas, and typically have widths of order 10,000 – 50,000 km s^{-1}. It can be supposed that these clouds are the atmosphere of a central accretion disk, although disk-like line profiles are less common than expected, this could be explained by turbulence within or amongst the emitting clouds, or by the expected ‘dip’ in the peak of the line profile being filled in by Doppler boosting or a projected area effect.

The Broad line region is thought to be photo-ionised by radiation directly from the central engine, or from the accretion disk.

All AGN objects show narrow optical emission lines, and thus in the OBUS, the narrow line emitting region is supposed to be located sufficiently far away from the central engine that it is well clear of the obscuring torus. The temperature and density in the NLR are such that atoms in excited states may de-excite through radiative forbidden and semi-forbidden transitions before they get collisionally de-excited.

The narrow lines usually have widths about 300 km s^{-1}. Considerably larger widths than this can be taken to indicate turbulence or bulk motion within the narrow line region.

The narrow line region is probably photo-ionised by radiation from the nucleus of the AGN[1]. The fall-off of ionisation potential and critical density with distance from the nucleus determines the location at which certain species will radiate. For example, [O III] radiation is believed to be less isotropic than [O II] because it is radiated from regions closer to the nucleus, and is thus subject to more obscuration (Hes 1995).

1.1.1.3 Mid – Far IR

Most AGN show SEDs with rising flux density from the optical through the Near and Mid IR out to at least 100μm, beyond which the radio quiet majority of AGN show a falling flux level through the sub-mm to the radio. The two candidate emission processes in the Mid to Far IR are thermal emission from warm dust and self-absorbed synchrotron radiation. Current polarisation data, along with the lack of observed variability in this part of the AGN SED favour the thermal emission model for all radio quiet AGN.

1.1.1.4 Sub-mm

The Sub-millimetre part of the spectrum is particularly difficult to observe, though instruments exploiting recent advances in bolometer technology, such as SCUBA[2] on the JCMT[3] now give us reasonable sensitivity and resolution in this area. These observations, along with the far IR data from the ISO[4] satellite, support the hypothesis of thermal emission from dust in this region.

[1]In some objects, particularly radio loud AGN showing jets, shock ionisation appears to be a significant effect

[2]the Sub-mm Common User Bolometer Array has 2 arrays of diffraction limited detectors, 37 pixels at 750 and 850μm and 91 pixels at 350 and 450μm.

[3]The James Clerk Maxwell Telescope is a 15m sub-mm telescope located on Mauna Kea, Hawaii

[4]The Infrared Space Observatory is a helium cooled orbiting telescope providing photometry and spectroscopy in the 5 – 200μm range.

1.1.1.5 Radio

Although Seyferts are in general radio quiet objects, they are not radio silent, having radio fluxes easily detectable with current interferometry techniques. Results from a radio survey of the extended 12 micron survey show a 90% radio detection rate, and a mean radio power of 10^{21} Wm^{-2} at 8.5GHz (Thean et al. 1997).

The nuclear radio emission from Seyferts is non thermal in origin, and is produced from an unresolved compact region. A minority of Seyferts do show radio jets and somewhat more show lobes with multiple components up to 1kpc in size and reminiscent of the larger structures seen in radio loud AGN (Kukula et al. 1996, Pedlar et al. 1993).

All AGN reside in a host galaxy which may contribute to the total radio flux of the object in several ways. Neutral hydrogen in the host galaxy will radiate the 21cm line, which can be a useful diagnostic of the velocity field in the host galaxy. Additionally, any starburst or supernovae activity could be a significant contribution to the total flux. It is unlikely that many other stellar processes (eg pulsars, accreting binaries etc) will contribute significantly to the total radio flux.

Perhaps in contradiction to the unified scheme, recent studies of a large carefully selected sample of Seyfert galaxies show little or no significant difference between the radio morphologies of Seyfert 1 and Seyfert 2 objects (Thean et al. 2000).

1.1.2 Unification schemes of AGN

Unification is a keystone of current AGN research in that it allows us to unify several types of AGN with different observed parameters into a single prototypical object which will exhibit the observed parameters of one of several different classes, depending on the value of some physical parameter. This allows us to rationalise the vast array of observation properties observed in the array of AGN types.

1.1.2.1 Orientation Based Unified Schemes

A detailed review of the Orientation Based Unified Scheme (OBUS) would be out of place here; see Antonucci (1993) for a complete review. However, the OBUS is particularly relevant to some NLS1 models, and I will thus summarise the key points here.

Radio maps of radio galaxies show that their emission is highly anisotropic, often showing a linear structure consisting of a nucleus with a single or double jet and lobe structure (see figure 1.1). This prompts the question of what the object would look like if our sight line was closer to the jet axis. In addition, it is noted that all AGN show narrow, optical emission lines, though some also show a strong optical continuum along with broad permitted emission lines. A geometric model, based on the anisotropic

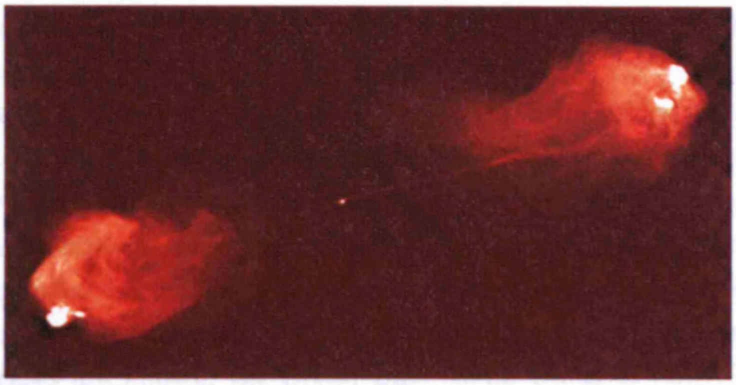

Figure 1.1: A 6cm Radio image of the relatively nearby radio galaxy Cygnus A, taken with the VLA by Conway (1984). The length of the double lobe structure is over 500,000 light years.

obscuration of the different emitting regions evolved, and is shown schematically in figure 1.2.

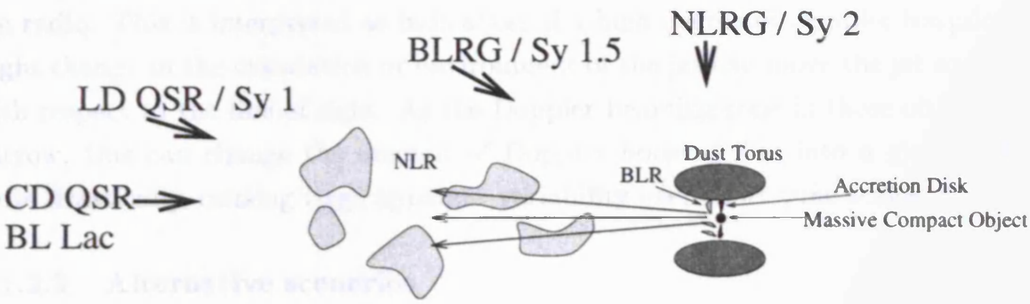

Figure 1.2: Schematic view of the OBUS population object. B/N LR = Broad / Narrow Line Region; B/N LRG = Broad / Narrow Line Radio Galaxy; C/L D QSR = Core / Lobe Dominated Quasar.

In this model, the central engine is supposed to be a disk of matter accreting onto a massive black hole. The atmosphere of the accretion disk, or at least gas clouds close to the central engine, is referred to as the broad line region (BLR) as it is believed to be responsible for the emission of optical permitted lines with velocity widths of order 20,000 km s^{-1}.

This central engine is surrounded by an optically thick dusty torus, axially aligned with the coincident spin axes of the black hole and accretion disk, and thus obscures the central engine to lines of sight which are not close to this axis, preventing the optical continuum and broad emission lines from being seen along these sight lines.

Further from the nucleus, and outside the putative obscuring torus, lie clouds of cooler optical line emitting gas referred to as the narrow line region (NLR), which emit optical spectral lines with velocity widths generally less than about 1000 km s^{-1}, and typically around 300 km s^{-1}.

Whilst the NLR radiates from both permitted and forbidden atomic transitions, the density in the BLR is such that ions will be collisionally de-excited before they can radiatively de-excite via a forbidden transition.

The transition from Quasar to Radio Galaxy, or correspondingly Seyfert 1 to Seyfert 2 in the radio quiet case, takes place when the edge of the torus begins to obscure the central engine. As the edge of the torus may not be well defined, a number of "borderline" cases are known; the Broad Line Radio Galaxies (BLRGs) in the radio loud case, and Seyfert types 1.2 through 1.9 are commonly discussed in the radio quiet domain.

A case that we shall meet in more detail later are the BL Lac objects. These can be considered to be extreme cases of Core dominated quasars, where the line of sight is aligned very closely with the Doppler beamed jet. This causes some interesting properties - obviously the central engine is unobscured, so we observe its continuum emission. BL Lac objects are characterised by being extremely variable, especially in the radio. This is interpreted as indication of a high degree of Doppler beaming - any slight change in the orientation or environment of the jet can move the jet axis slightly with respect to the line of sight. As the Doppler beaming cone in these objects is very narrow, this can change the amount of Doppler boosted flux into a given sight line quite drastically, causing large apparent variability over short time scales.

1.1.2.2 Alternative scenarios

The Orientation based unification is obviously not the complete answer. A variety of alternative hypotheses are available, and it is likely that some objects are best described by an OBUS like system, whereas others may require a different system. For example, Malkan et al. (1998) observe a large number of objects spectroscopically classified as Sy 1s, though which don't appear to have an unobscured bright nucleus in the HST WFPC images, and suggest a "Galactic Dust Model" in which the obscuration comes from dust clouds and lanes further out in the host galaxy, rather than a nuclear dust torus.

1.1.2.3 Radio Loud - Radio Quiet Unification

There is an obvious correspondence in the optical spectra of the Seyfert 1 / 2 pair and the Quasar / Radio Galaxy pair, and orientation based unified schemes have been successfully applied to both pairs. Assuming that orientation is the main difference between Sy 1 and 2 objects, and quasars and radio galaxies, we are led to ask how we can unify the two pairs. Observationally, most of the differences between the two can be attributed to the presence of relativistic jets and the radio lobes thus formed.

At the moment, there are few observational clues as to what might cause some objects to be "radio loud" and others (the vast majority) to be "radio quiet". In addition, there are a plethora of competing models of accretion disks and jet formation, acceleration and confinement, making it difficult to develop a theoretical model to explain radio loudness. However, Boroson & Green (1992) performed a principle components analysis of the emission line properties of low redshift QSOs and found that radio loud QSOs lie at one extreme of their primary eigenvector. They suggest that the parameter driving this eigenvector is black hole spin. Wilson & Colbert (1995) also conclude that black hole spin drives radio loudness, with radio loud QSOs postulated to have the most rapidly spinning black holes.

1.1.3 Notable Correlations

Correlations between observed parameters which are not obviously related can give us valuable information about unification and other AGN models. Some of the more relevant and prominent examples will be discussed here.

1.1.3.1 Quasar Hβ widths - Radio orientation

In discussions of radio loud objects, it has long been believed that the ratio of the radio flux from the core to that from the lobes, R, otherwise known as the *relative core strength*, is a good indicator of the orientation of the AGN jet with respect to the line of sight (e.g. Orr & Browne 1982). Early studies by Wills & Browne (1986) found a statistically significant anti-correlation between R and the Full Width at Half Maximum (FWHM) of the Hβ line. However, the statistical significance of this correlation was found to be considerably lower in Jackson & Browne's (1991) later study. A more recent study (Wills & Brotherton 1995, Brotherton 1996) suggests that the absolute visual magnitude of the quasar, M_v, provides a more reliable measure of the total quasar power output than the radio lobe flux, and thus that the ratio of the radio core flux to M_v provides a better indication of the orientation of the jet to the line of sight. Adopting this new indicator and using a larger sample, Srianand & Gopal-Krishna (1998) find a statistically significant anti-correlation between the orientation of the quasar, and the FWHM of its Hβ line, thus supporting the disk like BLR geometry suggested by Wills & Browne (1986).

1.1.3.2 Quasar Hβ widths - Radio size

Srianand & Gopal-Krishna (1998) also search for evidence of the evolution of the central engine in Quasars, postulating that the mass of the super massive black hole (SMBH) in the quasar nucleus should increase as matter accretes onto it over the lifetime of the quasar, and that as the large width of the broad lines is thought to be a result of their movement within the deep gravitational potential well of the SMBH, and increase in mass of the SMBH ought to be detectable in the resulting change in dynamics in the BLR clouds.

To this end, Srianand & Gopal-Krishna (1998) take the fact that most radio sources are thought to grow steadily with time (e.g. Fanti et al. 1995), to suggest the use of the size of the radio structure as an indicator of the age of the source (Best et al. 1996), and search for correlations between the size of the radio source and the FWHM of its broad lines. Srianand & Gopal-Krishna (1998) find such a correlation, although it seems we should regard this result with some care; no account has been taken of the fact that most of the radio structures will be foreshortened by projection, even if their sample has been selected so as not to include core dominated quasars, and the radio source size is known to be correlated or anti-correlated with many other parameters, including redshift and R. Although they answer some of the points raised by this, they neglect to model the possibility that higher power sources will have have radio structures with a faster growth rate, and thus the FWHM of the Hβ line may be more closely related to the AGN power, rather than it's age, though of course it could be argued that these two are related in that both the power and age of the AGN are related to the mass of its SMBH.

1.1.3.3 BLR size - AGN luminosity

Reverberation mapping techniques have revealed a relationship between the luminosity of nearby AGN, and the size of their BLRs; Netzer & Laor (1993) find $r \sim 0.06 L_{46}^{0.5} pc$, where L_{46} is the luminosity in units of 10^{46} erg s^{-1}.

1.1.3.4 Hβ width and X-ray spectral index

The recent increase in X-ray studies of Narrow Line Seyfert 1s has provided a lot of evidence for a correlation in which objects with a steep X-ray spectrum have narrower broad optical lines. (Laor et al. 1994, Boller et al. 1996). We note that NLS1s are somewhat arbitrarily defined, Seyfert line widths are continuously distributed, with the NLS1s simply being one extreme of the distribution. This correlation holds right across this line width distribution.

However, Grupe et al. (1999) show that this correlation only appears to hold for high luminosity AGN, but not for low luminosity objects, which is surprising in that the Fe Kα line is prominent in NLS1s, but usually preferentially found in low luminosity objects.

1.1.3.5 X-ray variability and spectra

Rapid X-ray variability has been observed in many AGN objects, and as we shall see later, is especially relevant to this thesis. However, not all AGN show such variability. Fiore et al. (1998) find that in their sample of 6 radio quiet quasars, the X-ray steep, narrow Hβ quasars show systematically larger amplitude variability than the X-ray flat, broad Hβ quasars. This can be explained with the hypothesis that the X-ray steep, narrow line objects are in a higher L/L_{Edd} state than the X-ray flat, broad line objects.

A strong correlation exists between the X-ray variability and Hβ FWHM. This strongly suggests that both are the result of the NLS1s having a lower mass black hole than the BLS1s (Leighly 2000, Turner et al. 1999).

1.2 Observations of NLS1s

1.2.1 Introduction

Narrow Line Seyfert 1s have recently become a fascination of X-ray astronomers. Given their extreme X-ray properties, this is hardly surprising. Much of the research of this thesis has involved studies of NLS1s in other wavebands, in order to determine if they appear unusual in the other wavebands, and to try to determine the validity of some of the theoretical models proposed for the NLS1 phenomenon. I now review the literature documenting NLS1 observations to date.

1.2.2 X-Rays

NLS1s have become a popular topic in the X-ray community due to their extreme X-ray spectra; ROSAT observations by Boller et al. (1996) have shown that NLS1s systematically show stronger, more variable, soft X-ray excesses in the 0.1 – 2 keV band than broad line Seyfert 1s (hereafter BLS1s).

We note that many BLS1s also show so called 'soft X-ray excesses'; this term is used loosely by X-ray astronomers to indicate that an extrapolated power law fit to the hard X-rays underestimates the soft X-ray flux. Boller et al. (1996) point out that this "soft X-ray excess" is significantly stronger in the NLS1 objects, and that there are two main explanations for this; firstly that the NLS1s genuinely have a stronger than usual soft X-ray component relative to their optical or IR flux, or secondly that the NLS1s have weaker than usual hard X-ray tail components.

Leighly et al. (1997) report on X-ray spectral features seen in a small sample of NLS1s, which they interpret as either Oxygen absorption features outflowing at 0.2–0.3c, or as broad absorption lines, with a velocity of 0.57c. However, interpretation of these features as blueshifted versions of the common O VII and O VIII absorption features from 0.74 and 0.87 keV lacks any supporting evidence. A better explanation is provided by Nicastro et al. (1999) who suggest that in NLS1 like AGN where the ionising continuum is steep below 2 keV ($\alpha \gtrsim 2$) and flattens above this energy to $\alpha \sim 0.7 - 1.5$, the resulting ionisation structure can differ from that of more usual warm absorbers in that C, O and Ne become almost fully ionised in the gas, quenching the O VII and O VIII absorbtion edges, yet Fe would still be distributed in low - medium ionisation states, producing spectra with no sharp absorption features below ~ 1 keV, and a broad absorption structure between 1 and 2 keV due to a complex mixture of L resonance absorption lines and edges from Fe X to Fe XX. These features are often neglected in simple X-ray spectral modeling.

1.2.2.1 Optical

NLS1s were originally noted as a class from their optical spectra. Osterbrock & Pogge (1985) describe a set of AGN with Sy 1 or Sy 1.5 optical spectral properties, but having unusually narrow optical permitted lines, though in most cases, the permitted lines are broader than the forbidden lines.

Figures 1.3 and 1.4 show example optical spectra of Sy 1 and Sy 2 objects, taken from Osterbrock (1989), illustrating the broad permitted lines and strong continuum in the Sy 1 as opposed to the narrow permitted lines and weak continuum in the Sy 2. Figure 1.5 shows an example NLS1 optical spectrum, from Osterbrock & Pogge (1985) showing the narrow permitted lines and yet the strong continuum and high ionisation species seen in the NLS1s.

Shuder & Osterbrock (1981) find that the criterion of [O III]λ5007Å / Hβ flux < 3 is a good discriminator between Sy 1s and 2s, and this, along with FWHM of Hβ $<$ 2000km s^{-1} are generally adopted as the defining properties of NLS1s.

Goodrich (1989) carried out optical spectra polarimetry observations of a sample of 18 NLS1s are report that 7 of these show polarisations higher than expected from polarisation by the galactic ISM. They find that that the NLS1 optical continuum polarisation generally rises towards the blue end of the spectrum, and that the emission lines profiles are not significantly broader in polarised light, indicating dust reflection as the primary source of polarisation, with the dust being located external to the BLR, but either inside, or mixed in with, the NLR.

Goodrich's (1989) spectral data also shows the presence of strong [Fe II] and high ionisation lines such as Fe VII λ6087Å and Fe X λ6375Å, indicating that NLS1s are more closely related to Sy 1s than to Sy 2s, which rarely show lines such as these.

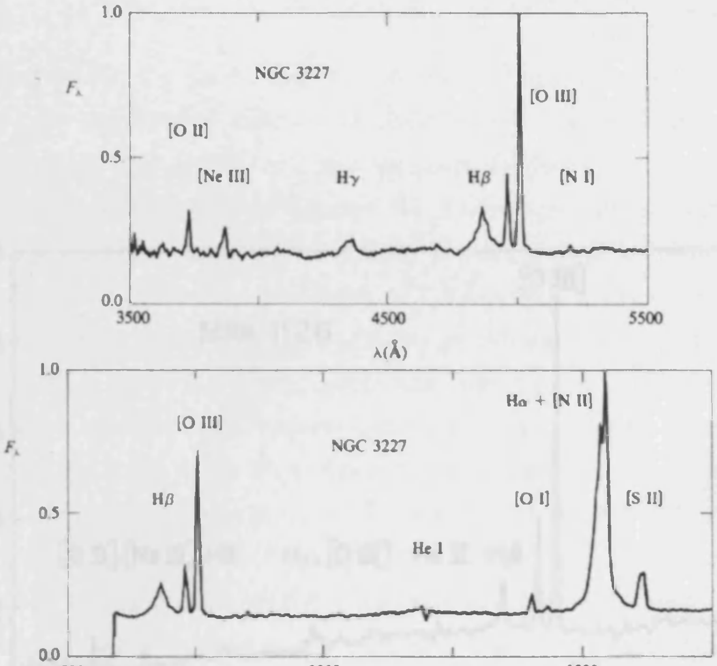

Figure 1.3: An example Sy 1 spectrum from Osterbrock & Pogge (1985)

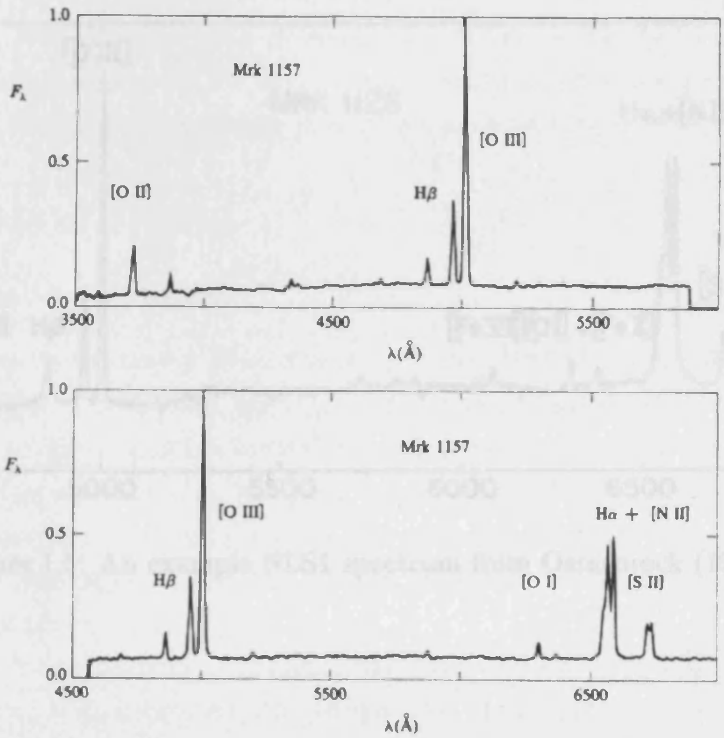

Figure 1.4: An example Sy 2 spectrum from Osterbrock & Pogge (1985)

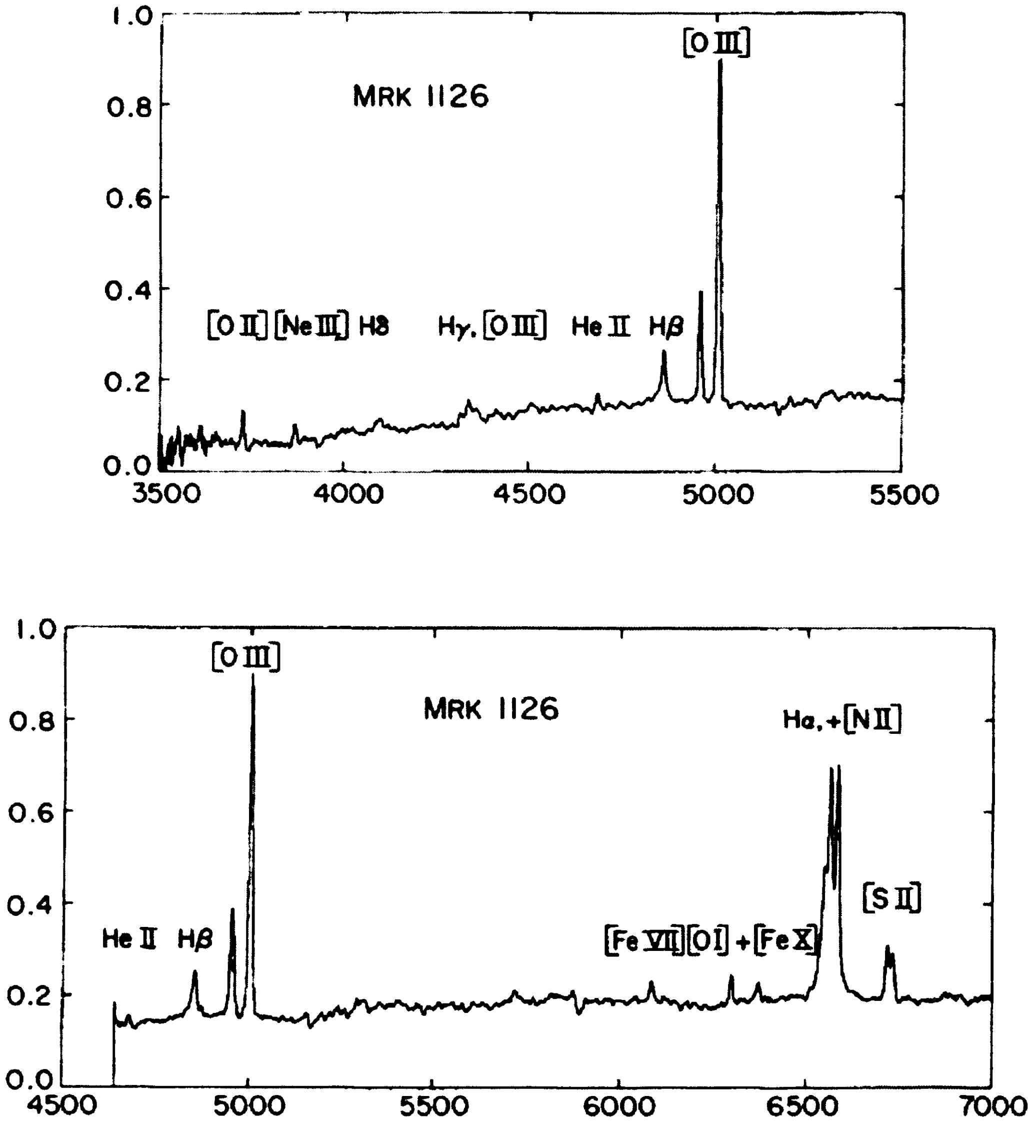

Figure 1.5: An example NLS1 spectrum from Osterbrock (1989)

1.2.3 Radio

Radio observations of NLS1s can be used to test the 'pole-on' model, which hypothesises that NLS1s are oriented preferentially with their rotation axis along our line of sight. In such an orientation, any collimated jet emission would strongly beam synchrotron radiation into our line of sight, as in Blazars, BL Lacs and core dominated quasars. In addition, relativistic material moving along the jet would appear superluminal.

Ulvestad et al. (1995) observed a sample of 7 NLS1s with the VLA and found that the NLS1s were broadly similar in the radio to published data on 'normal' Seyferts, with the median radio size of the VLA detected sample being no larger than 300pc. It is noted that two of the three objects which have significant optical polarisation and measurable radio axes, have their optical continuum polarisation angles almost perpendicular to their radio major axes, whilst the third has its polarisation axis nearly parallel to its inner radio axes. We should note that these VLA observations suffered a power failure in the northern arm of the VLA, rendering only 18 telescopes usable and resulting in a highly asymmetric beam shape and that the observations were carried out in poor weather conditions.

A recent high resolution radio study of BLS1s and Sy 2 objects has been carried out by Thean et al. (2000). Results suggest that in a complete, 12μm selected sample of Seyfert galaxies, it is impossible to distinguish the Sy 1 and Sy 2 objects given only the radio data, with the exception perhaps, that although the Sy 1s and Sy 2s show the same distribution of point-like and extended morphologies, the median size of the extended Sy 2s is slightly larger than that of the extended Sy 1s (730pc vs 493pc).

1.3 Models of NLS1s

1.3.1 The pole on model

The so called 'pole-on' model (Osterbrock & Pogge 1985, Puchnarewicz et al. 1992, Boller et al. 1996) was favored early in NLS1 research as a simple way to explain the narrowness of the permitted optical lines. It hypothesises that the BLR forms an atmosphere to the accretion disk, and that the accretion disk is oriented in the plane of the sky, such that the cloud velocities are all perpendicular to our line of sight. Having no velocity component along our line of sight, the lines from the BLR would not be Doppler broadened.

This model has problems in explaining the intense X-ray variability and soft X-ray excess in NLS1s. It is suggested that simply the higher projected area of a face on accretion disk would provide the X-ray spectrum observed, in that soft X-Ray emission is expected for face-on orientations of some geometrically thick accretion disk models (Madau 1988), and that Doppler beaming along a jet axis could explain the enhanced variability, though plausible models invoking all these effects are difficult to construct.

1.3.2 Dust in the BLR

It has been proposed that dust within the broad line region could preferentially suppress the broad line wings, though it is difficult to see how dust grains would survive in the high temperature and pressure environment of the BLR. It is also unclear how dust in the BLR could be viewed as a cause or perhaps consequence of the other intriguing NLS1 properties - for example X-ray spectrum and variability.

1.3.3 Principal Component Based Models

Though maybe not complete models in their own right, Boroson & Green (1992) and Wandel (1997) noted properties of NLS1s that feed useful information into the modeling process.

Boroson & Green (1992) performed a principal component analysis (PCA) of the emission line properties of AGN, and found that radio-loud QSOs lie to one end of their primary Eigenvector. They suggest that the parameter driving this vector is black hole spin. Black hole spin is also believed by Wilson & Colbert (1995) to drive radio loudness, with radio loud objects thought to have the most rapidly spinning black holes. Since radio loud AGN and NLS1s lie at opposite ends of the Boroson & Green (1992) Eigenvector, it can be suggested that NLS1s would be expected to have slowly spinning black holes, and thus to be very radio quiet.

Wandel (1997) proposes that objects with steep X-ray spectra such as NLS1s ionise large, slowly rotating BLRs, and hence give rise to narrow permitted line emission.

1.3.4 Low mass, high accretion rate

The most promising NLS1 model at the moment appears to be able to explain all the properties of NLS1s, and draws upon several independently presented ideas.

Similarity between NLS1s and Galactic Black Hole Candidates (GBHCs) in their 'high state' suggests that NLS1s might be accreting close to their Eddington limit, though they are not systematically brighter in bulk luminosity, so we must assume that the black hole is of a lower mass.

This produces the hot soft X-ray excess in the X-ray spectrum, and as the system is smaller, we can account for the fast variability.

Also, the smaller system means that the inner edge of the BLR is closer to the supermassive black hole, and thus sees a stronger ionising flux. The hydrogen gas in at least the inner BLR becomes fully ionised, though as in the BLS1s the outer BLR is partially ionised hydrogen. Fully ionised hydrogen is optically thin to the Lyman continuum and doesn't emit optical emission lines, though it does emit UV emission lines. As this is the high rotational velocity component of the BLR, the model suggests that we should see only broad permitted hydrogen line wings in the UV, consistent with Rodriguez-Pascual et al. (1997), but not in the optical. The fully ionised BLR clouds also provide the "warm absorber" features seen in the X-ray data. (Laor et al. 1997, Fiore et al. 1998)

Current accretion disk models are unable to generate an NLS1 like soft X-ray excess unless they are accreting almost at their Eddington limit (Hure et al. 1994, Pounds et al. 1995). However, this hypothesis is consistent with the observed fact that the NLS1 X-ray variability is correlated with the X-ray spectral slope (Fiore et al. 1998).

Rodriguez-Pascual et al. (1997) find broad components to the UV emission lines in NLS1s. It is unclear whether these exist in all NLS1s, and if so, whether they are consistent with the predictions of the model. In addition, Bischoff & Kollatschny (1999) report a broad (4900km s^{-1}), variable component to visible lines in Mkn 110, an NLS1. However it seems possible that these results could be attributed to emission from the extremities of the accretion disk, especially in that neither approach the 10,000s of km s^{-1} seen in powerful quasars. In addition, Rodriguez-Pascual et al. (1997) hypothesise that the soft X-ray continuum excess would fully ionise any hydrogen clouds that form too close to the black hole, and that fully ionised clouds will emit UV lines to some extent, but not optical lines. This could be used to explain the presence of weak, broader, components to the UV hydrogen lines.

1.4 Summary and Future work

We have briefly reviewed the orientation based, and other, unified schemes of Active Galactic Nuclei, and presented an overview of the emission mechanisms that are present in AGN.

Narrow Line Seyfert 1s show narrow permitted optical emission lines, though show many properties of Sy 1s, such as high H$\beta$to [O III] line flux ratio, strong optical continuum, high ionisation optical lines and low X-ray absorption column density. In addition X-ray observations reveal a remarkably strong and rapidly variable soft X-ray excess.

We have seen how it is not obvious how NLS1s can be explained in terms of an orientation based unification scheme, and discussed models which invoke orientation as well as other differences, as an explanation of NLS1s.

Detailed modeling of the emission line properties of the NLS1s requires an extensive project utilising some photo-ionisation modeling code such as CLOUDY (Ferland 1996) to model the line emission over a range of ionising continuum parameters, to determine the best solution consistent with the data.

Chapter 2

Near IR spectroscopy of NLS1s

2.1 Motivation and Aims

Many NLS1s show high excitation optical spectral lines. These can be used as a unique probe of the ultra-soft X-ray continuum, assuming that they are photo-ionised. This ultra-soft X-ray spectral region cannot be observed directly as it is heavily absorbed by galactic hydrogen. Near IR spectroscopy provides data on extra lines, thus allowing us to probe a wider range of ionisation potentials and thus sample the ultra-soft continuum at a wider range of energies.

In addition, near IR spectroscopy provides data on the Paschen and Bracket hydrogen line series, providing more data on the peculiar broad line regions of the NLS1s in our sample and providing more information on Balmer decrements and dust absorption along the line of sight to the BLS1 nucleus.

2.2 Observations

Observations were carried out using the current Cooled Grating Spectrometer (CGS4) on the United Kingdom Infrared Telescope (UKIRT) over the two partially clear nights 1997 May 9–10. The UKIRT is a 3.8m telescope sited at 4200m on Mauna Kea, Hawaii. It employs a tip-tilt secondary mirror for first order adaptive optics, which increases the sensitivity of narrow slit spectroscopy greatly, by reducing the spatial size of the telescope point spread function (PSF), which would otherwise be significantly larger than the spectrometer slit width. The CGS4 employs a 256$\times$256 pixel InSb detector array, which is sub-pixel position stepped between exposures. In this case, the grating was stepped over 6 positions in a 3$\times$2 pattern, with the positions separated by 1/3 of a pixel in the dispersion axis. This not only fully samples the spectral PSF, but also enables the application of a bad pixel mask for the array, without leaving gaps in the final image.

Object	Band	Exposure Time /s
RE 1034+396	J	2880

Table 2.1: Service observations on 1997-02-03

Object	Band	Exposure Time /s
Mkn 493	K	2400
Mkn 291	K	2400
Mkn 896	K	2400
Akn 564	K	1920

Table 2.2: Observations on 1997-05-09

The 751/mm grating was used in 1st order for both the J and K band observations. Spectra of a Copper-Argon arc lamp were used for accurate wavelength calibration, and standard stars from the UKIRT bright star catalogue were observed for flux calibration. All these data were taken with the 300mm focal length camera and the 1 pixel slit, giving a pixel scale and slit width of 0.6".

Tables 2.1, 2.2 and 2.3 summarise our service observations and two observing nights. The first half of 1997-05-09 was lost to poor weather, limiting the number of objects for which we have both J and K band data.

2.2.1 Sky line cancellation

The night sky atmosphere radiates strong H_2O and OH^- emission lines in the infrared which must be removed from the spectra. Rather than offsetting the spectrometer to blank sky to facilitate this, which would mean a significant loss in the flux collected from the target, the telescope is "nodded" such that the target is moved between two positions on the spectrometer slit inbetween exposures. The exposure times are kept short (30 seconds or so) because in some configurations, the skylines may saturate the

Object	Band	Exposure Time /s
Mkn 42	K	2400
Mkn 766	K	1200
RE 1034+396	K	2400
Mkn 766	J	1200
Mkn 291	J	1200
Mkn 493	J	1200
Mkn 896	J	1200
Akn 564	J	1200

Table 2.3: Observations on 1997-05-10

array with longer exposures, and also that in certain weather conditions, the sky lines may vary on timescales not much larger than this, making it harder to remove them from the final spectrum. Denoting the 2 positions of the object on the slit as 'A' and 'B', we make observations in the sequence 'ABBA', and subtract the sum of the A images from that of the B images. In this way, we shall see (in section 2.3.3) that the sky lines will cancel out, provided that they do not vary in a non-linear manner over time.

2.3 Data Reduction

2.3.1 Initial processing

The data were acquired in the UKIRT ND-STARE mode. In this mode, the array controller electronics non destructively read out the array every second throughout the exposure, and a straight line is fit through the multiple samples of each pixel to ascertain the flux incident on that pixel. This method leads to lower noise than single, destructive reads, and as an offset is allowed in the line fit, it also effectively de-biases the data.

The initial data processing was carried out by the online CGS4DR system. This involved flat fielding, using data acquired with the CGS4 internal flat field unit, along with bad pixel masking and interleaving of the sub-pixel stepped exposures.

2.3.2 Wavelength Calibration

The spectra are wavelength calibrated using observations of arc lamps built into CGS4. These observations are carried out after the CGS4 motors have driven the grating to the angle that will be used for observing. In this case, a Copper-Argon arc was used.

The IRAF task IDENTIFY was first used, along with published arc spectra giving the wavelength of each line to a suitable accuracy, to identify and specify the accurate wavelength of many lines in the arc lamp observation frames, extracting data from the central row of the exposed area of the detector array. The IRAF task REIDENTIFY was then used to automatically repeat this for the other rows of the array. This data was then read into the FITCOORDS task, where any obviously bad line identifications were deleted, and cubic spline curves fitted to the data to generate a transformation matrix which maps the observed arc frame onto one which has an accurate wavelength scale along the rows, and which has wavelength constant over the array columns. This step is necessary as the CGS4 optics distort the image of the slit on the array into a slight curve.

2.3.3 Frame Summing

This transformation matrix was then applied to each of the observed data frames. Individual 'object' and 'sky' frames were inspected and any faulty data frames[1] were rejected. The remaining object frames were then summed, as were the sky frames, and the "object-sky" composite frames constructed, using the IMARITH function in IRAF.

This produces a frame containing both a positive and negative image of the object, with the sky lines canceled out. The positive and negative images of the slit are extracted, and the spectrum obtained by taking the difference of these two.

Variance frames were also constructed, under the assumption that Poisson noise dominates in the final spectra. This is a reasonable assumption as the read noise in each frame is small, due to the ND-STARE non-destructive read mode used.

We note that the number of photons arriving at a given pixel of the detector array can be represented by a random variable following a Poisson distribution, with the distribution parameter being proportional to the flux of radiation arriving at that pixel. The distribution parameter will therefore vary depending upon whether or not the pixel in consideration forms part of the image of the object or is simply seeing light from the an area of sky near the object.

We let the photon count for a pixel be represented by a random variable having a distribution $\mathrm{Po}(\mu_o)$ for a pixel on the target, and $\mathrm{Po}(\mu_s)$ for a pixel on the sky[2].

We sum the Object (O) and sky (S) frames: $\sum_{i=1}^{n} O_i \sim \mathrm{Po}(n\mu)$ and $\sum_{i=1}^{n} S_i \sim \mathrm{Po}(n\mu)$

Now we can represent the Composite frame by $C = \sum_{i=1}^{n} O_i - \sum_{i=1}^{n} S_i$

We can also generate a frame D such that $D = \sum_{i=1}^{n} O_i + \sum_{i=1}^{n} S_i$

The distribution parameter for each pixel in the C and D frames depends on the position of the pixel on the chip (figure 2.1):

row O - the row on which the target falls in the "object" frames

$$\begin{aligned}
C_O &\sim \sum_{i=1}^{n} O_i - \sum_{i=1}^{n} S_i \sim \mathrm{Po}(n\mu_o) - \mathrm{Po}(n\mu_s) \\
&\sim \mathrm{N}(n\mu_o, n\mu_o) + \mathrm{N}(-n\mu_s, n\mu_s) \\
&\sim \mathrm{N}(n(\mu_o - \mu_s), n(\mu_o + \mu_s)) \\
D_O &\sim \sum_{i=1}^{n} O_i + \sum_{i=1}^{n} S_i \sim \mathrm{Po}(n\mu_o) + \mathrm{Po}(n\mu_s) \\
&\sim \mathrm{N}(n\mu_o, n\mu_o) + \mathrm{N}(n\mu_s, n\mu_s)
\end{aligned}$$

[1]for example, in a few frames, the telescope lost auto-guiding lock, and drifted off target.

[2]Notation: $\mathrm{Po}(\lambda)$ represents a Poisson distribution having mean and variance λ. $\mathrm{N}(\mu, \sigma^2)$ represents a Normal distribution having mean μ and variance σ^2. n represents the number of A and B frames.

$$\sim \mathrm{Po}(n(\mu_o + \mu_s))$$

row S - the row on which the target falls in the "sky" frames

$$\begin{aligned}
C_S &\sim \sum_{i=1}^{n} O_i - \sum_{i=1}^{n} S_i \sim \mathrm{Po}(n\mu_s) - \mathrm{Po}(n\mu_o) \\
&\sim \mathrm{N}(n\mu_s, n\mu_s) + \mathrm{N}(-n\mu_o, n\mu_o) \\
&\sim \mathrm{N}(n(\mu_s - \mu_o), n(\mu_s + \mu_o)) \\
D_S &\sim \sum_{i=1}^{n} O_i + \sum_{i=1}^{n} S_i \sim \mathrm{Po}(n\mu_s) + \mathrm{Po}(n\mu_o) \\
&\sim \mathrm{N}(n\mu_s, n\mu_s) + \mathrm{N}(n\mu_o, n\mu_o) \\
&\sim \mathrm{Po}(n(\mu_s + \mu_o))
\end{aligned}$$

elsewhere (on the sky)

$$\begin{aligned}
C_E &\sim \sum_{i=1}^{n} O_i - \sum_{i=1}^{n} S_i \sim \mathrm{Po}(n\mu_s) - \mathrm{Po}(n\mu_s) \\
&\sim \mathrm{N}(n\mu_s, n\mu_s) + \mathrm{N}(-n\mu_s, n\mu_s) \\
&\sim \mathrm{N}(0, 2n\mu_s) \\
D_E &\sim \sum_{i=1}^{n} O_i + \sum_{i=1}^{n} S_i \sim \mathrm{Po}(n\mu_s) + \mathrm{Po}(n\mu_s) \\
&\sim \mathrm{N}(n\mu_s, n\mu_s) + \mathrm{N}(n\mu_s, n\mu_s) \\
&\sim \mathrm{Po}(2n\mu_s)
\end{aligned}$$

We notice that in *all three cases*, the population variance of C is exactly equal to the population mean of D, thus we can consider D to be a frame containing the best estimate of the variance of frame C. Note that the approximation $\mathrm{Po}(\mu) \approx \mathrm{N}(\mu, \mu)$ is only valid for large μ, thus we are making the assumption that $n\mu_o$ and $n\mu_s$ are large ($\gtrsim 20$ say). This assumption is valid for the data used, except for a few points between sky-lines, where the read noise of the array dominates anyway.

We note that the output from the array recorded in the data files is actually a constant multiplied by the number of photons detected by the array. For all this data, this gain constant is 6. The sum of all the O and S frames was therefor divided by 6 to obtain the variance frame. It is not necessary to do this for the composite frames, provided that the source and calibration star frames are treated identically.

An observing sequence consisting of repeated sets of OSSO observations is preferable to the simple alternation of Object and Sky frames; supposing that the sky line emission

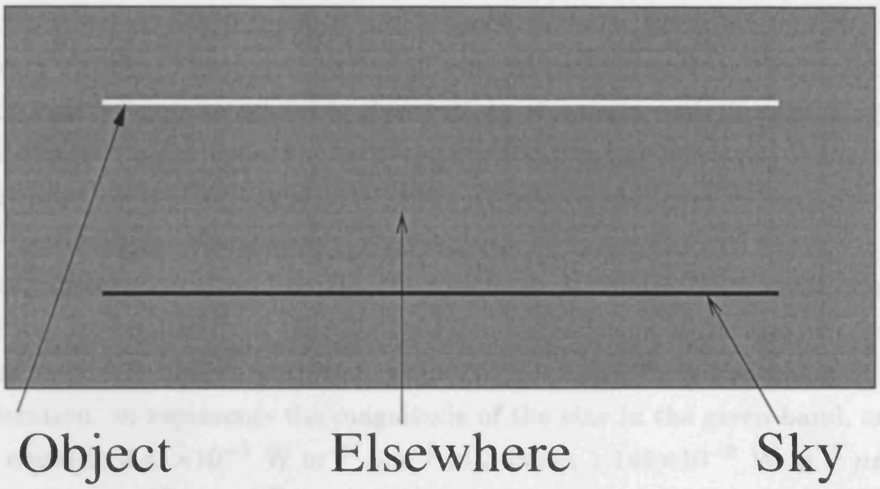

Figure 2.1: Schematic of a composite frame, showing the "Object" and "Sky" positions of the spectrum of the object on the chip.

is increasing or decreasing with time, over a long time-scale, as with deteriorating or improving weather - a simple O-S pair will leave a systematic residual sky component due to increase or decrease of sky emission in the second frame as compared to the first. If the O-S sequence is simply repeated (O-S)+(O-S)..., this systematic difference will simply accumulate. However, if, after the first OS sequence, we carry out an SO sequence, and then form the sum (O-S)+(-S+O), we find that the residual from the (O-S) pair will tend to cancel that of the (-S+O) pair, and thus the sky lines will still cancel out, provided that they vary reasonably linearly on a time-scale longer than our exposure time.

The error values thus generated do not, of course, reflect errors introduced in the flux calibration process by the variability of the sky transmission between the object and calibration star observations. However, this error is relatively spectrally flat compared to the Poisson errors which reflect the spectral complexity of the the source and sky emission. Thus, we plot the Poisson errors as error bars on the spectra, as they best reflect the uncertainty in the spectral morphology, whilst we present independently a representation of the flux calibration uncertainty determined both from the variance in successive Object-Sky-Sky-Object galaxy observation quads and the difference in atmospheric transmission between the flux calibration standard star observations taken before and after each object was observed.

2.3.4 Flux Calibration

The gain of the whole UKIRT-CGS4 system as a function of wavelength is highly non linear due to many effects including the complicated absorption and emission spectrum of the atmosphere in the Infra Red, and imperfections in the spectrometer, telescope and detector system. This complicates the flux calibration process significantly.

The process relies on interleaving observations of sources with those of 'bright stars', which have known magnitudes in the frequency band being observed. We assume that these stars have a black body spectrum in the IR, whose temperature can be determined from the spectral type of the star.

For each calibration star observed, the spectrum of a black body at the appropriate temperature, determined from the spectral type classification of the star, is constructed, and scaled so that it has an amplitude given by $A \times 2.518^{-m}$ at the centre of the band in consideration. m represents the magnitude of the star in the given band, and A is a constant equal to 3.41×10^{-9} W m^{-2} μm^{-1} in J band, 1.149×10^{-9} W m^{-2} μm^{-1} in H band, and 4.03×10^{-10} W m^{-2} μm^{-1} in K band. (Tokunga 1986)

This black body spectrum is then assumed to be the actual spectrum from the star, and is divided by the observed spectrum of the star from which any obvious spectral features have been removed by interpolation, to produce a function giving the actual flux per detector count as a function of wavelength. The observed spectra of the object is then multiplied by this function to obtain a flux calibrated spectrum of the object.

As mentioned in the previous section, the uncertainty in the flux calibration, determined from the difference in values of suitable calibration star observations, and from the measured changes in the transparency of the atmosphere during the observations of a given target, are represented on each spectra by an addition line labeled σ_{flux}.

2.4 Results

2.4.1 Calibration and data quality

The weather during the observing run was mixed, with about one half of a night lost due to high wind and (frozen) precipitation. However, the observations were carried out during relatively clear patches, and the flux calibration does not seem to have suffered too much. I present diagrams showing the calibration star model to observed flux ratio - effectively a plot how much flux is required to produce a detector count at each wavelength. As is evident from the plots (figures 2.2, 2.3, 2.4), the weather on the first night, during which only K band data was taken, was significantly worse than that on the second night, during which both J and K band data were taken. Figure 2.5 shows all the calibration stars over both nights and both bands.

2.4.2 Akn 564

Akn 564 is a well studied NLS1 and shows an interesting near IR spectrum. We detect strong He I λ10830Å, O I and neutral hydrogen emission lines from this object, along

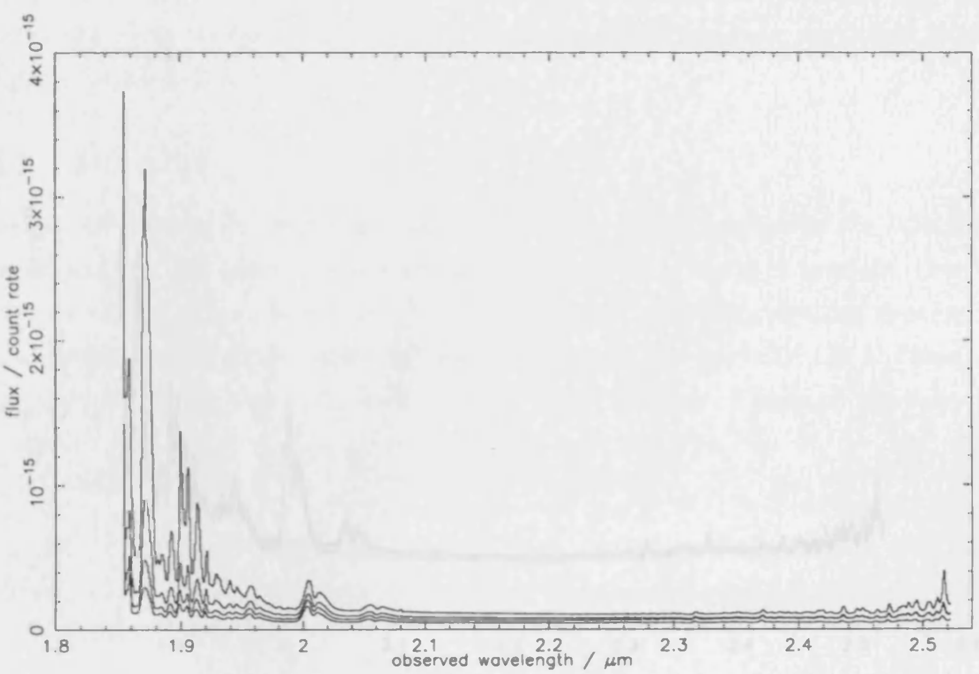

Figure 2.2: Calibration stars over the first night (19970509).

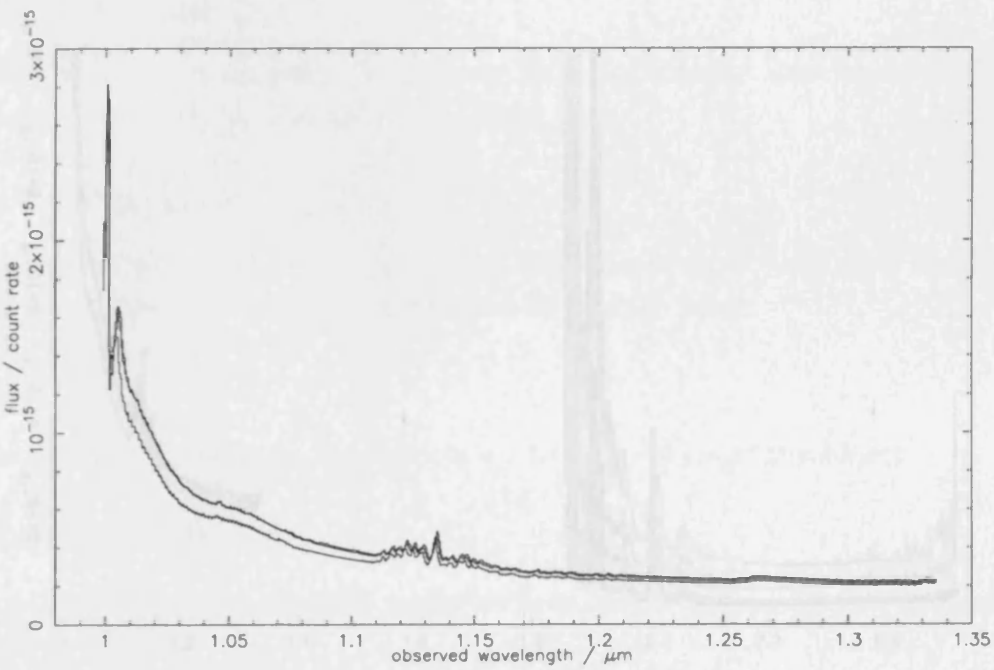

Figure 2.3: Calibration stars over the second night (19970510) in J bank.

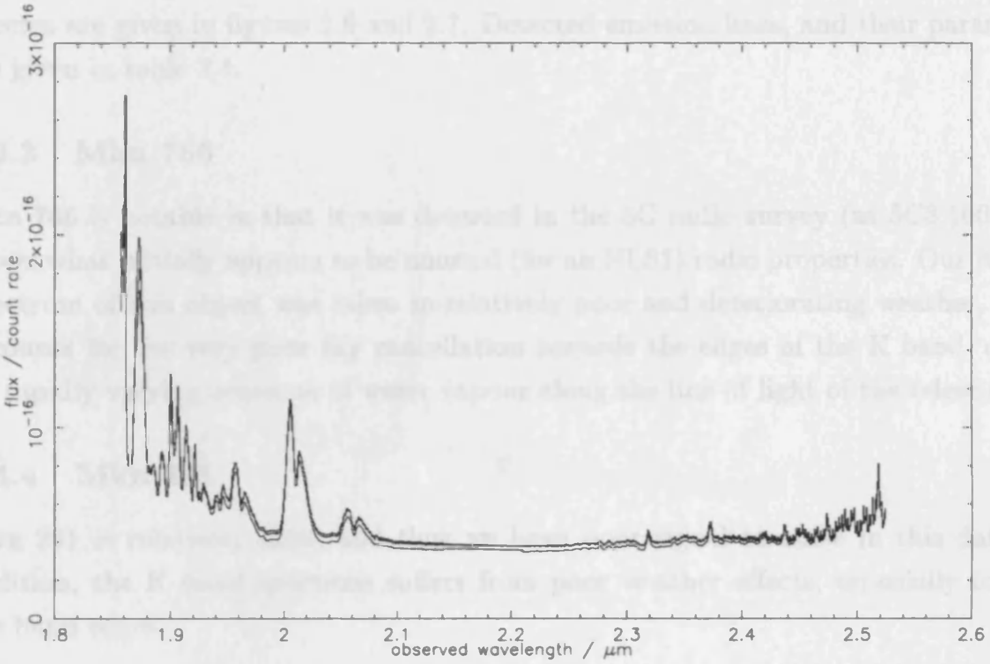

Figure 2.4: Calibration stars over the second night (19970510) in K band.

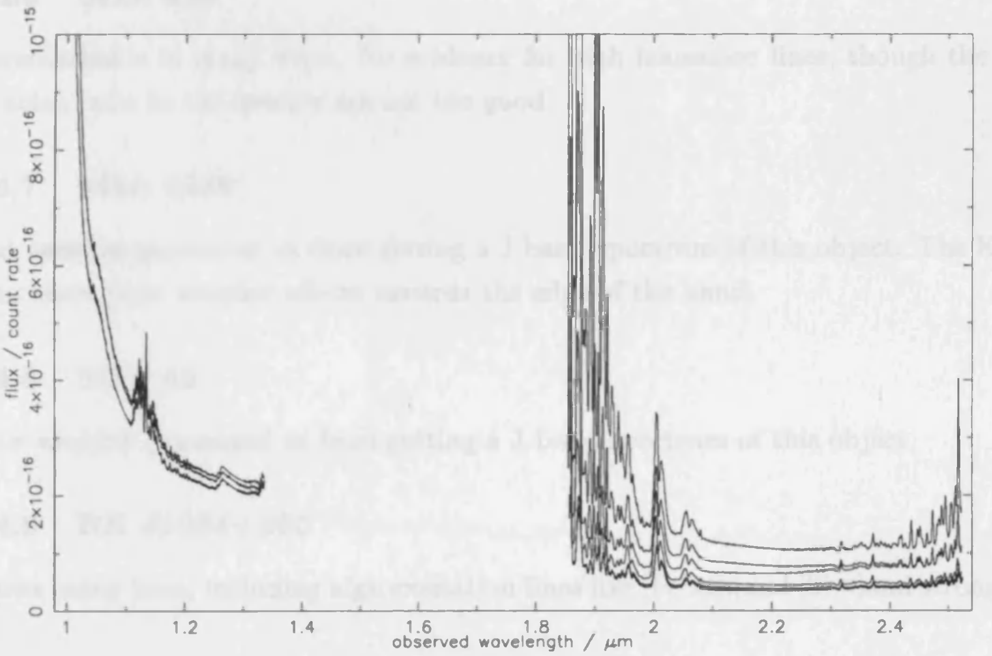

Figure 2.5: Calibration stars over both nights in both bands

with more marginal detections of a few high ionisation species such as [Ca VIII]. The spectra are given in figures 2.6 and 2.7. Detected emission lines, and their parameters are given in table 2.4.

2.4.3 Mkn 766

Mkn 766 is notable in that it was detected in the 5C radio survey (as 5C3.100), and shows what initially appears to be unusual (for an NLS1) radio properties. Our K band spectrum of this object was taken in relatively poor and deteriorating weather, which accounts for the very poor sky cancellation towards the edges of the K band, caused by rapidly varying amounts of water vapour along the line of light of the telescope.

2.4.4 Mkn 291

Mkn 291 is relatively faint, and thus we have poor signal to noise in this data. In addition, the K band spectrum suffers from poor weather effects, especially towards the band edges.

2.4.5 Mkn 493

Mkn 493 shows strong Fe II in J band, though has an otherwise unremarkable spectrum.

2.4.6 Mkn 896

Unremarkable in many ways. No evidence for high ionisation lines, though the signal to noise ratio in the spectra are not too good.

2.4.7 Mkn 1239

Bad weather prevented us from getting a J band spectrum of this object. The K band data show poor weather effects towards the edge of the band.

2.4.8 Mkn 42

Poor weather prevented us from getting a J band spectrum of this object.

2.4.9 RE J1034+396

Shows many lines, including high excitation lines like [Fe XIII]and [Si X]and strong Pa δ.

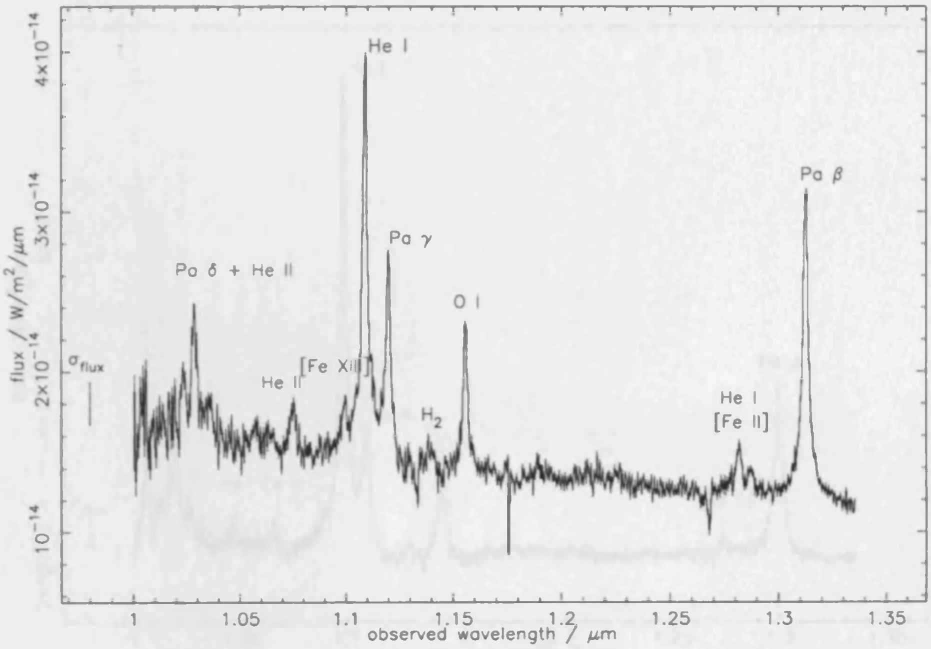

Figure 2.6: Akn 564 in J band. σ_{flux} indicates the flux calibration uncertanty. See text for details.

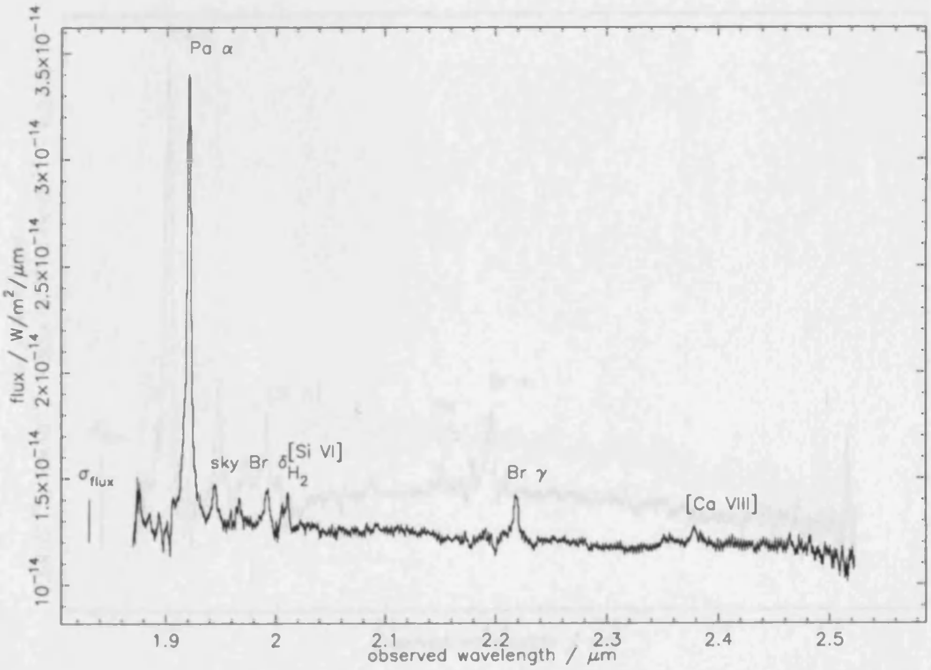

Figure 2.7: Akn 564 in K band

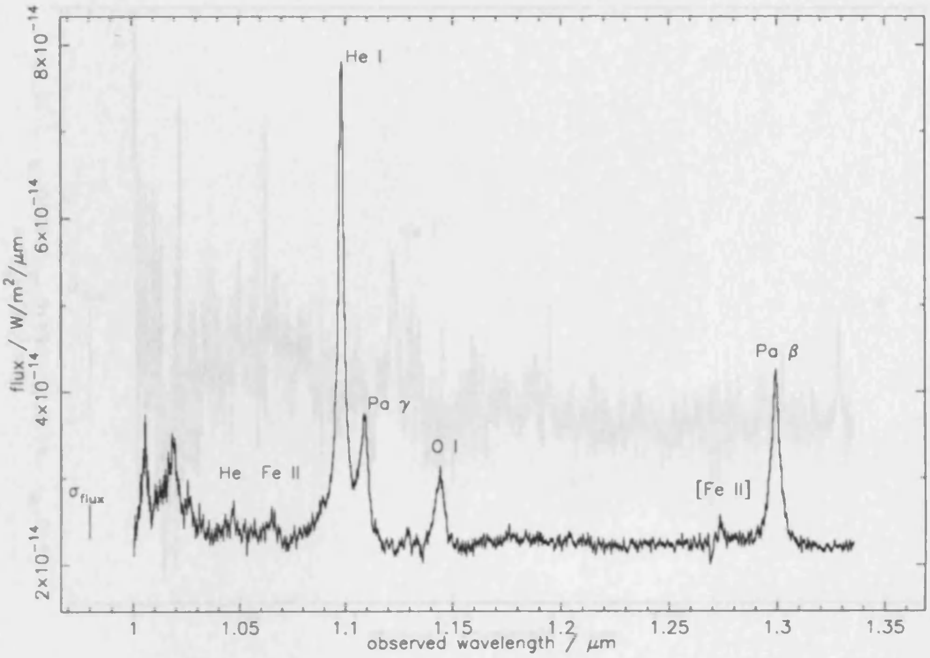

Figure 2.8: Mkn 766 in J band

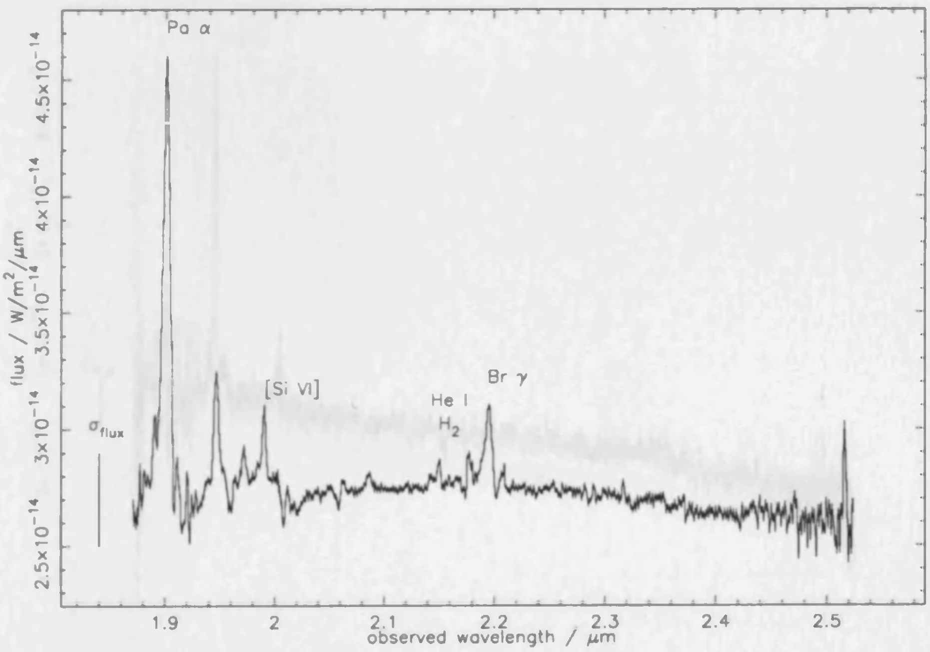

Figure 2.9: Mkn 766 in K band

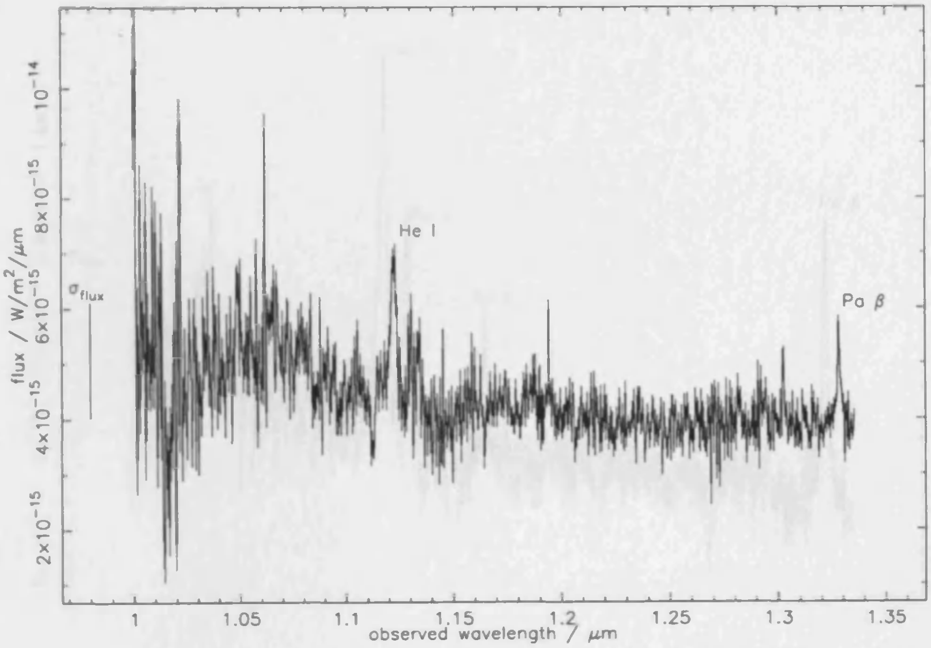

Figure 2.10: Mkn 291 in J band

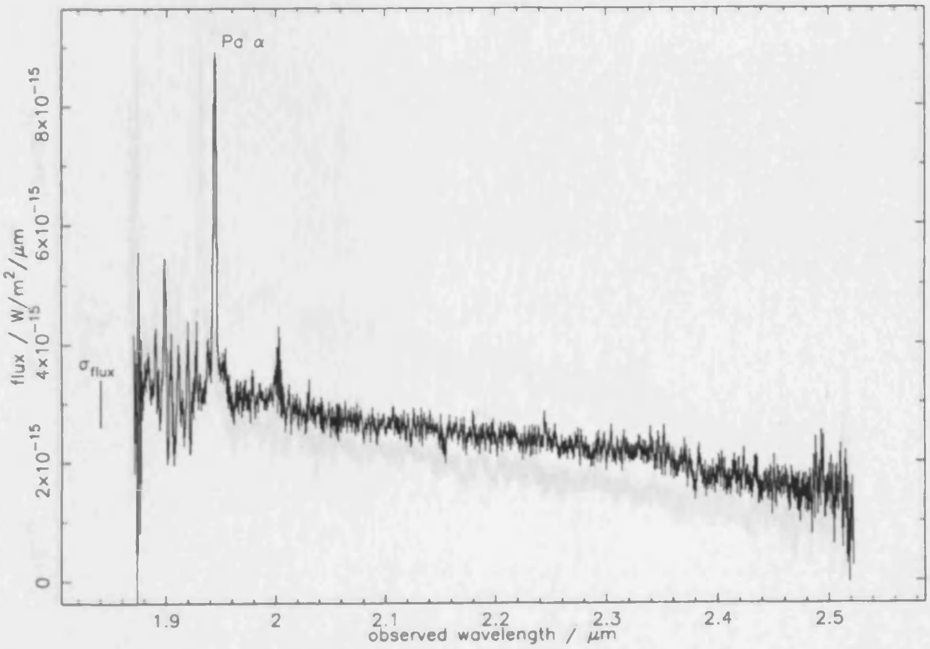

Figure 2.11: Mkn 291 in K band

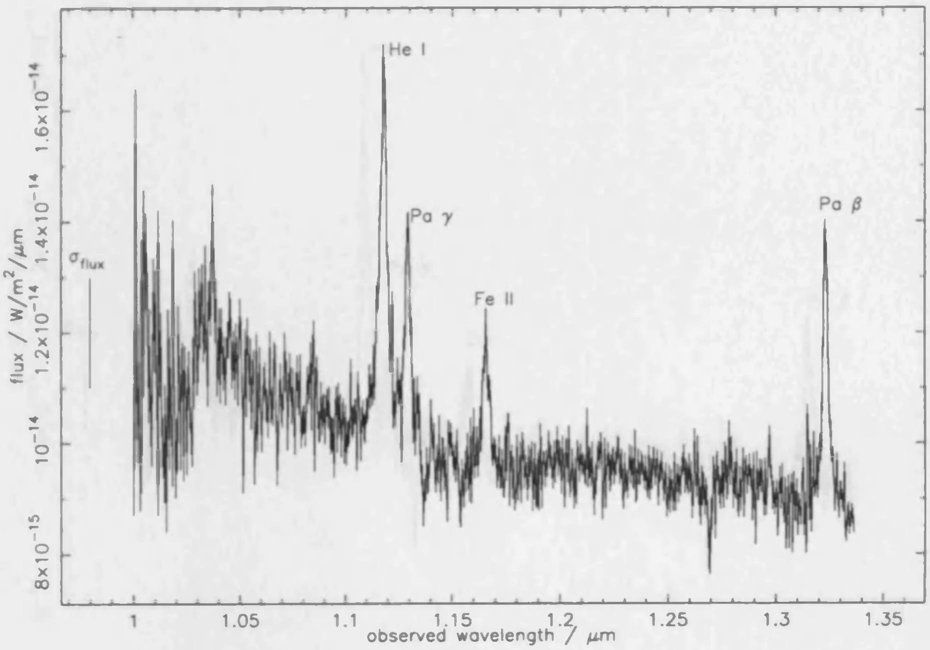

Figure 2.12: Mkn 493 in J band

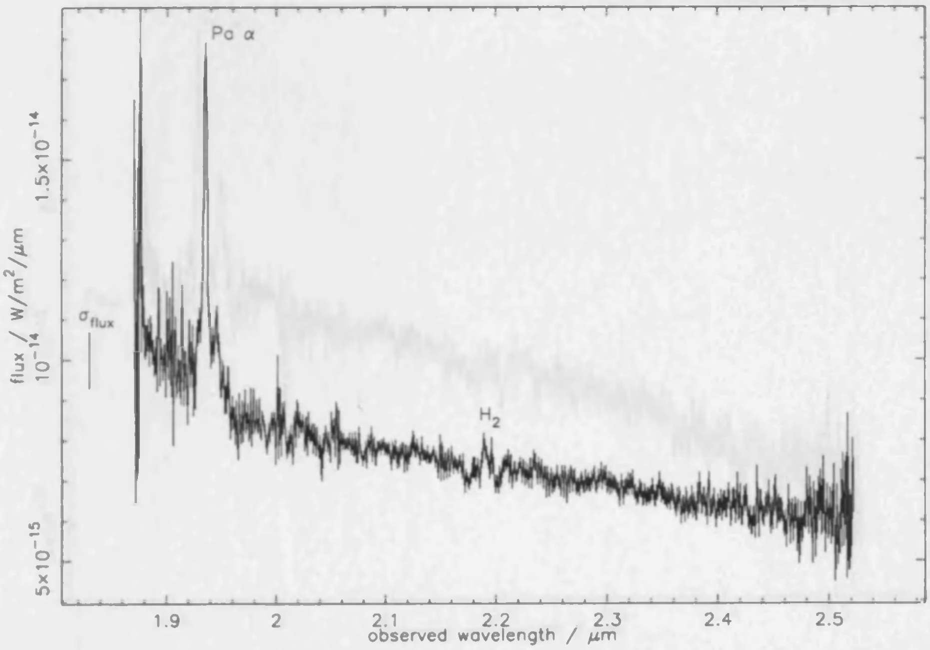

Figure 2.13: Mkn 493 in K band

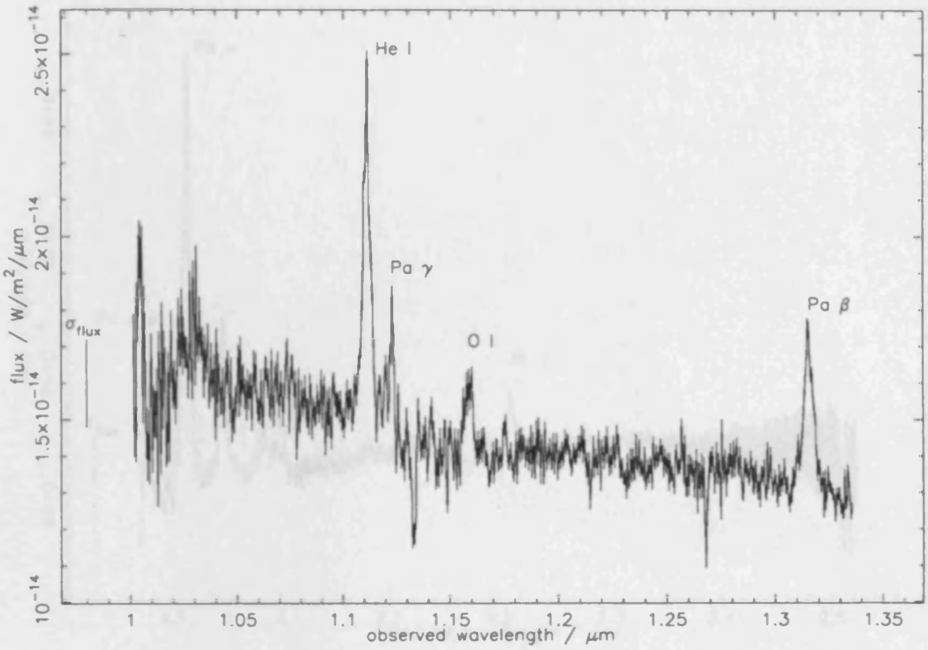

Figure 2.14: Mkn 896 in J band

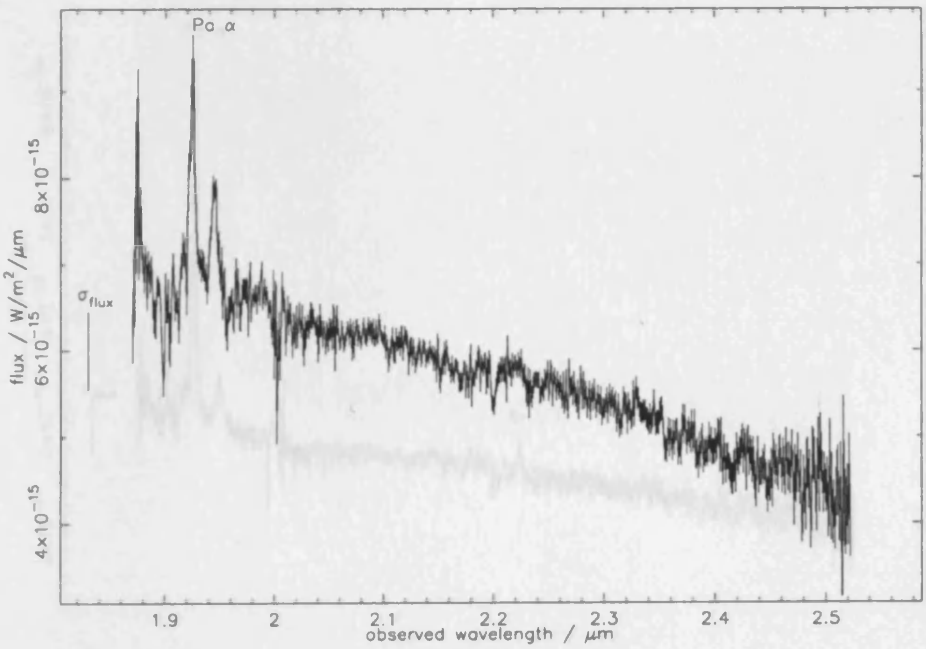

Figure 2.15: Mkn 896 in K band

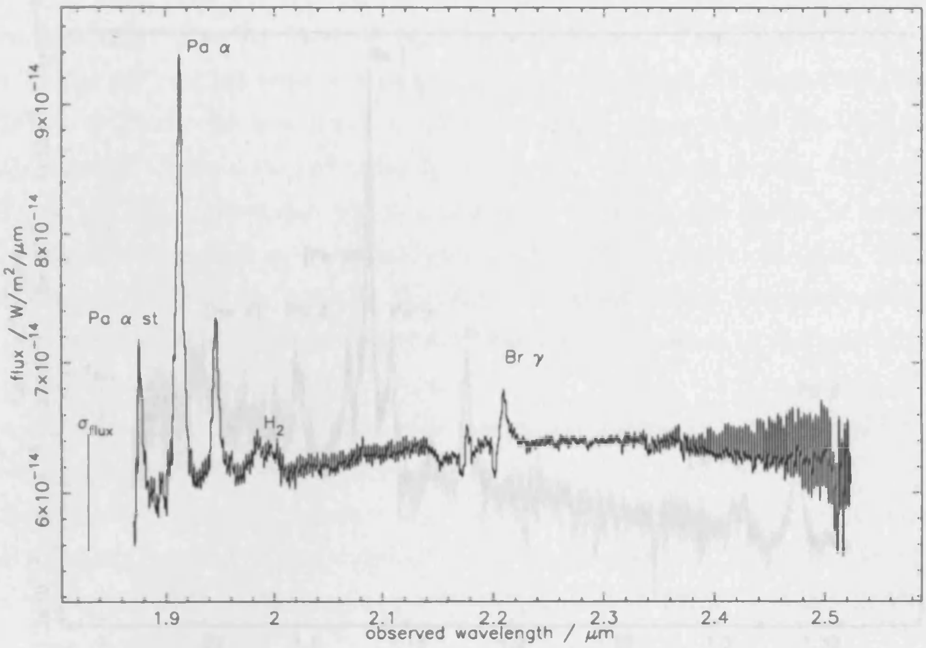

Figure 2.16: Mkn 1239 in K band

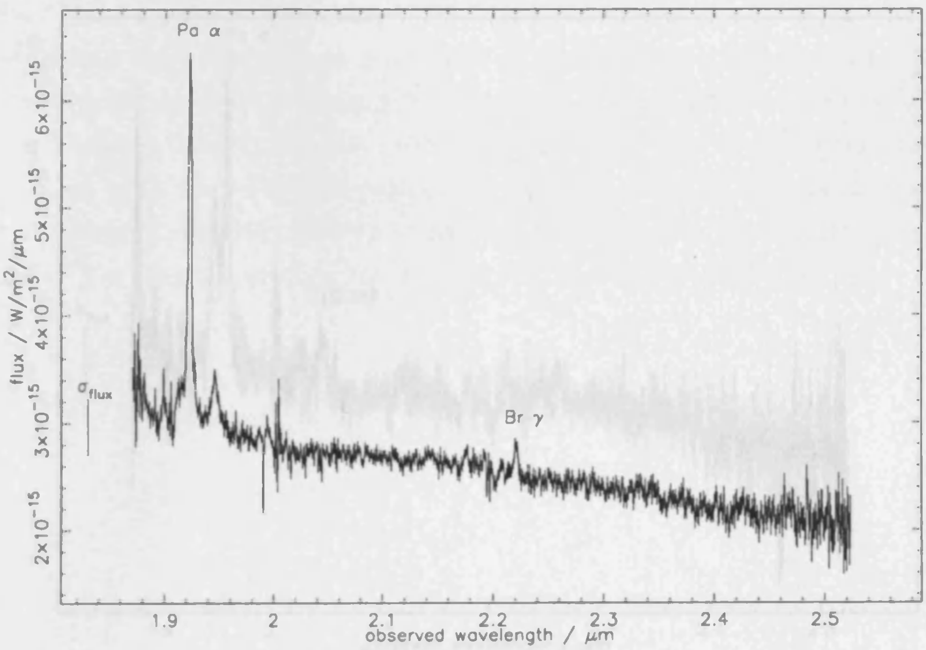

Figure 2.17: Mkn 42 in K band

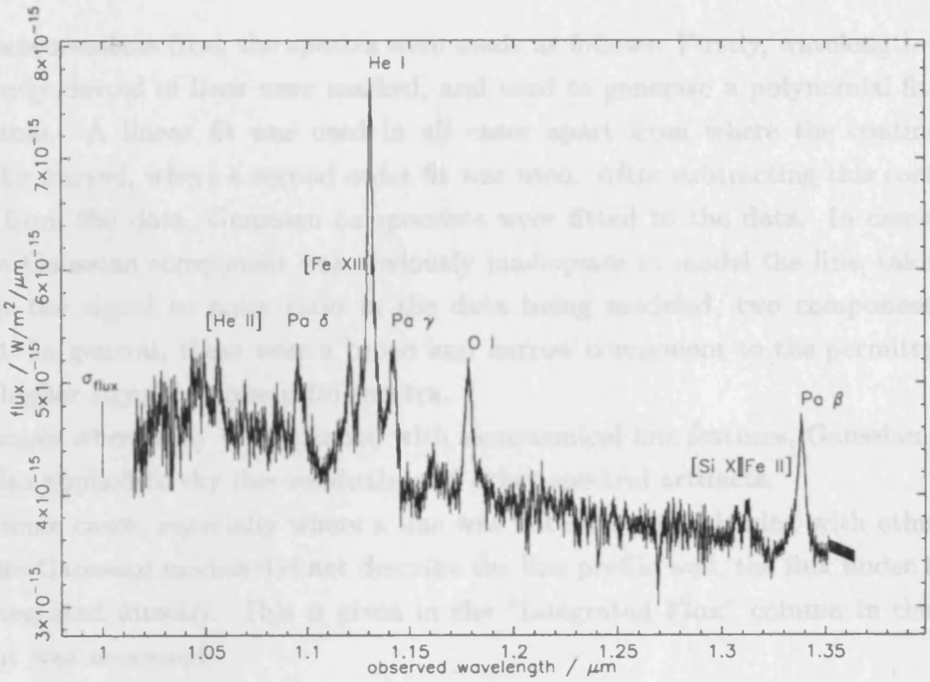

Figure 2.18: RE J1034+396 in J band

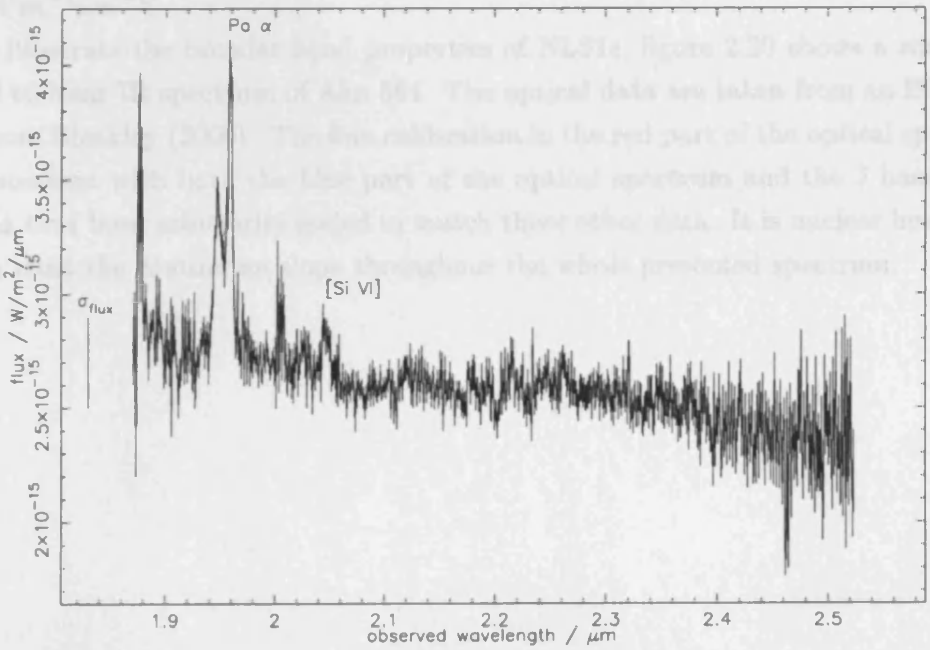

Figure 2.19: RE J1034+396 in K band

2.4.10 Line fitting

Line measurements from the spectra were made as follows. Firstly, wavelength regions apparently devoid of lines were marked, and used to generate a polynomial fit to the continuum. A linear fit was used in all cases apart from where the continuum is markedly curved, where a second order fit was used. After subtracting this continuum model from the data, Gaussian components were fitted to the data. In cases where a single Gaussian component was obviously inadequate to model the line, taking into account the signal to noise ratio in the data being modeled, two components were applied. In general, these were a broad and narrow component to the permitted lines in the higher signal to noise ratio spectra.

In cases where they were blended with astronomical line features, Gaussian models were also applied to sky line residuals, and other spectral artifacts.

In some cases, especially where a line was not obviously blended with other lines, or where Gaussian models did not describe the line profile well, the flux under the line was integrated directly. This is given in the "Integrated Flux" column in the tables where it was measured.

Suspect or uncertain line identifications are marked with a '?' in the tables. In the cases where model fitting failed to converge, some values were fixed (eg fixing line centres to the line peak in the data). These values do not have an uncertainty value in the tables. In the tables, wavelengths and FWHMs are given in nm, fluxes are in $10^{-17} W m^{-2} \mu m^{-1}$.

To illustrate the broader band properties of NLS1s, figure 2.20 shows a combined optical to Near IR spectrum of Akn 564. The optical data are taken from an ISIS INT data from Bleakley (2000). The flux calibration in the red part of the optical spectrum is inconsistent with both the blue part of the optical spectrum and the J band data, and has thus been arbitrarily scaled to match these other data. It is unclear how much we can trust the continuum slope throughout the whole presented spectrum.

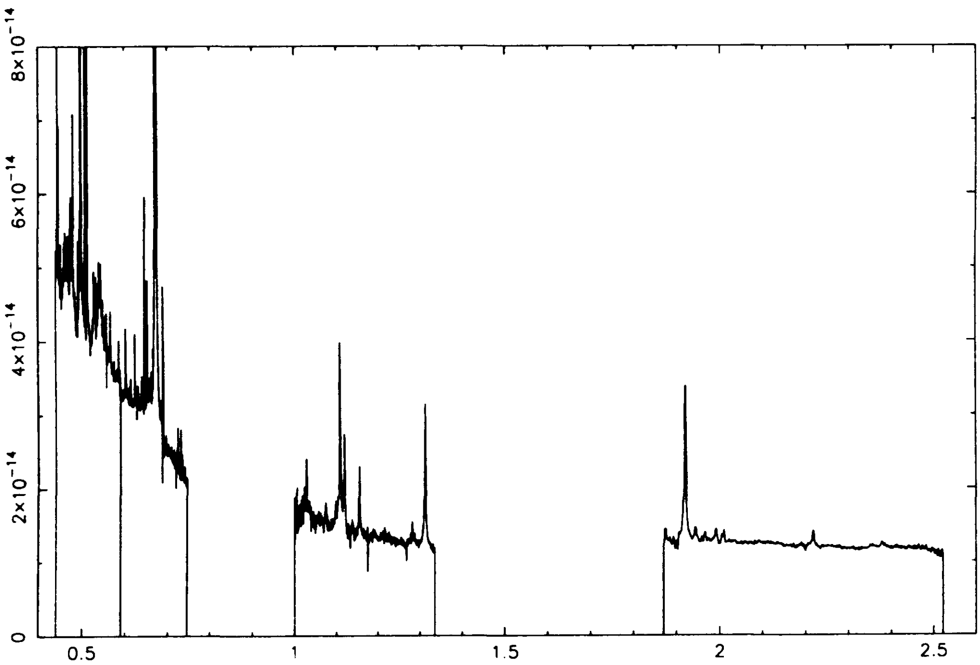

Figure 2.20: Combined optical and near IR spectrum of Akn 564

Identification	Observed Wavelength	Rest Frame Wavelength	Gaussian fit Flux	Gaussian fit FWHM	Velocity FWHM / km s^{-1}
?	1023.66±0.21	999.00±0.20	0.524±0.112	1.92± 0.48	563±141
[Si VIII] $\lambda 0.99\mu m$	1026.98±0.88	1002.24±0.86	5.64±0.38	23.43±1.98	6844±584
Pa δ	1028.84±0.11	1004.06±0.11	1.56±0.14	2.43±0.23	709±67
He II $\lambda 1.0129\mu m$?	1035.61±0.01	1010.66±0.01	0.0524±0.048	0.37±0.02	107±6
He + [S II] + O I	1056.98±0.42	1031.52±0.41	0.588±0.123	4.11±0.93	1167±264
He + [S II] + O I ?	1063.88±0.51	1038.25±0.50	0.538±0.118	4.49±1.16	1266±328
Fe II $\lambda 1.0501\mu m$?	1074.88±0.21	1048.99±0.20	1.02±0.12	3.53±0.48	985±134
[Fe XIII] $\lambda 1.0747\mu m$?	1098.97±0.21	1072.50±0.20	0.776±0.104	2.88±0.50	786±137
[He I]$\lambda 10830\mu m$ nar	1108.72±0.03	1082.01±0.03	4.06±0.11	2.14±0.06	579±16
[He I]$\lambda 10830\mu m$ brd	1108.7	1081.99	6.54±0.20	9.80±0.34	2652±92
Pa γ nar	1119.76±0.05	1092.79±0.05	3.04±0.11	2.79±0.11	747±30
Pa γ brd	1119.76	1092.79	1.18±0.20	10.00	2679
O I $\lambda 1.1287\mu m$	1155.69±0.06	1127.85±0.06	2.22±0.10	2.51±0.14	652±36
[Si X] $\lambda 1.2528\mu m$ + He I	1281.65±0.13	1250.78±0.13	0.924±0.076	3.06±0.31	716±73
[Fe II] $\lambda 1.2567\mu m$	1287.66±0.37	1256.64±0.36	0.937±0.103	6.17±0.81	1437±189
Pa β nar	1312.54±0.02	1280.92±0.02	4.15±0.07	2.63±0.05	601±11
Pa β brd	1312.16±0.14	1280.55±0.14	5.27±0.13	11.64±0.31	2661±71
Pa α nar	1920.64±0.04	1874.37±0.04	6.11±0.11	3.63±0.09	567±14
Pa α brd	1919.74±0.17	1873.49±0.17	7.56±2.05	13.87±0.35	2167±55
?	1944.20±0.25	1897.37±0.24	1.33±0.09	6.94±0.61	1071±94
?	1966.40±0.45	1919.03±0.44	0.669±0.108	5.00±5.00	763±763
?	1991.26±0.21	1943.29±0.20	1.33±0.08	7.32±0.49	1103±74
H_2(1-0)S3	2005.86±0.56	1957.54±0.55	0.503±0.123	4.50±1.29	673±193
[Si VI] $\lambda 1.9615\mu m$	2010.52±0.25	1962.09±0.24	0.555±0.089	3.15±0.54	470±81
absorption	2199.61±0.29	2146.62±0.28	-0.157±0.035	2.54±0.67	346±91
Br γ nar	2218.23±0.13	2164.79±0.13	0.637±0.044	3.72±0.29	503±39
Br γ brd	2218	2164.57	1.21±0.01	16.00	2164
?	2378	2320.71	0.506±0.051	7. 85±0.96	990±121

Table 2.4: Gaussian Line fit parameters for Akn 564. See section 2.4.10

Identification	Observed Wavelength	Rest Frame Wavelength	Gaussian fit Flux	Gaussian fit FWHM	Integrated Flux	Velocity Width / km s^{-1}
?	1005.28±0.14	992.49±0.14	3.71 ±0.29	3.63 ±0.31		1083±93
?	1013.69±0.28	1000.80±0.28	5.50 ±0.45	9.07 ±0.66		2684±196
?	1018.88±0.14	1005.92±0.14	2.74 ±0.22	3.68 ±0.31		1084±91
?	1025.15±0.45	1012.11±0.44	4.37 ±0.31	10.79±0.97		3158±285
He + [S II] + O I	1046.67±0.21	1033.36±0.21	1.01 ±0.14	3 ±3.51		860±1006
Fe II λ1.0501μm ?	1064.60±0.39	1051.06±0.39	1.30 ±0.16	6.00 ±0.90		1691±254
He I λ1.0830μm nar	1097.88±0.06	1083.92±0.06	13.50±0.66	2.99 ±0.14		817±38
He I λ1.0830μm brd	1098.42±0.58	1084.45±0.57	21.29±1.33	19.64±1.27		5364±350
Pa γ	1108.91±0.23	1094.81±0.23	3.95 ±0.52	3.61 ±0.49		977±133
O I	1143.89±0.40	1129.34±0.40	4.59 ±0.70	5.80 ±0.87		1521±229
[Si X] λ1.2528μm + He I	1269.56±5.57	1253.41±5.50	-0.16±0.25	0.70 ±12.00		165±2836
[Fe II] λ1.2567μm	1273.96±2.01	1257.76±1.98	1.17 ±0.87	5 ±5.85		1177±1379
?	1281.36±3.39	1265.06±3.35	0.65 ±0.88	5 ±5.85		1171±1373
Pa β brd	1298.08±1.26	1281.57±1.24	6.16 ±1.29	13.16±2.76		3041±641
Pa β nar	1299.22±0.23	1282.70±0.23	6.38 ±0.73	4.20 ±0.54		970±125
Pa α	1900.76±0.32	1876.59±0.32	18.15±1.23	9.82 ±0.72	21.572±0.080	1550±114
?	1946.55±0.06	1921.79±0.06	2.54 ±0.06	5.05 ±0.14	5.457 ±0.060	778±22
?	1971.82±1.22	1946.74±1.20	0.80 ±0.39	5.22 ±2.76	0.782 ±0.035	794±420
[Si VI] λ1.9615μm ?	1990.09±0.22	1964.78±0.22	1.54 ±0.14	4.76 ±0.49	1.768 ±0.030	718±74
He I ?	2143.80±1.55	2116.53±1.53	0.37 ±0.19	6.08 ±3.50		851±490
H_2 (1-0)S(1) ?	2150.57±0.68	2123.22±0.67	0.48 ±0.18	3.72 ±1.51		519±211
?	2178.09±0.29	2150.39±0.29	0.75 ±0.08	4.80 ±0.67		661±92
Br γ	2194.51±0.18	2166.60±0.18	2.80 ±0.12	8.17 ±0.39		1117±53
?	2208.09±0.46	2180.01±0.45	0.36 ±0.08	4.01 ±1.03		545±140

Table 2.5: Gaussian line fit parameters for Mkn 766. See section 2.4.10

Identification	Observed Wavelength	Rest Frame Wavelength	Gaussian fit Flux	Gaussian fit FWHM	Integrated Flux	Velocity Width / km s^{-1}
He I $\lambda 1.0830 \mu m$	1122.08±0.13	1083.89±0.13	0.87±0.07	3.29 ±0.29	0.837±0.037	880±78
Pa β nar	1328.25±0.06	1283.05±0.06	0.14±0.02	1.02 ±0.13		230±29
Pa β brd	1328.07±0.28	1282.87±0.27	0.32±0.03	4.82 ±0.69	0.391±0.023	1089±156
Pa α nar	1943.99±0.03	1877.83±0.03	1.59±0.03	2.93 ±0.07		452±11
Pa α brd	1944.15±0.63	1877.99±0.61	1.47±0.08	18.53±1.58	2.959±0.086	2859±245
?	1999.63±0.30	1931.58±0.29	0.36±0.03	8 ±9.36	0.456±0.165	1200±1404

Table 2.6: Gaussian Line fit parameters for Mkn 291. See section 2.4.10

Identification	Observed Wavelength	Rest Frame Wavelength	Gaussian fit Flux	Gaussian fit FWHM	Velocity Width / km s^{-1}
He I $\lambda 1.0830 \mu m$ brd	1117.52±0.17	1083.60±0.16	2.03±0.10	6.95 ±0.36	1866±97
He I $\lambda 1.0830 \mu m$ nar	1117.82±0.08	1083.89±0.08	0.91±0.06	2.45 ±0.19	658±51
Pa γ	1129.02±0.09	1094.75±0.09	0.97±0.07	2.70 ±0.20	717±53
Fe II $\lambda 1.1126 \mu m$?	1165.53±0.23	1130.15±0.22	1.27±0.11	5.38 ±0.51	1385±132
Pa β nar	1323	1282.84±5	0.62±0.07	1.91 ±0.24	433±54
Pa β brd	1323	1282.84±5	1.35±0.11	6 ±7	1361±1587
Pa α nar	1935.31±0.11	1876.57±0.11	2.52±0.19	3.36 ±0.23	521±36
Pa α brd	1937.14±1.22	1878.34±1.18	4.40±0.39	25.53±3.07	3954±478
?	1945.99±0.47	1886.93±0.46	0.34±0.11	3.09 ±1.02	476±157
?	2175.35±0.68	2109.32±0.66	-0.24±0.04	6.02 ±1.70	830±235
H_2 (1-0)S(1)	2190.11±0.29	2123.64±0.28	0.27±0.04	4.40 ±0.69	603±95
?	2201.26±0.53	2134.45±0.51	-0.18±0.04	4.25 ±1.29	579±176

Table 2.7: Gaussian Line fit parameters for Mkn 493. See section 2.4.10

Identification	Observed Wavelength	Rest Frame Wavelength	Gaussian fit Flux	Gaussian fit FWHM	Integrated Flux	Velocity Width / km s^{-1}
He I $\lambda 1.0830 \mu m$	1111.04±0.06	1082.67±0.06	3.48±0.11	4.09±0.15		1104±41
Pa γ	1122.85±0.11	1094.18±0.11	0.55±0.07	1.66±0.23		444±61
absorption	1133.07±0.15	1104.14±0.15	-0.85±0.09	2.53±0.34		670±90
O I $\lambda 1.1287 \mu m$	1158.76±0.29	1129.17±0.28	0.57±0.12	3.27±0.60		847±156
Pa β	1315.37±0.09	1281.79±0.09	2.21±0.08	5.51±0.20		1257±46
abs	1268.03±0.13	1235.65±0.13	-0.27±0.06	1.11±0.28		263±66
Pa α	1924.14±0.11	1875.01±0.11	2.01±0.08	6.75±0.23	1.913±0.057	1052±36
?	1944.28±0.19	1894.64±0.19	1.76±0.05	10.34±0.48	1.678±0.052	1595±74

Table 2.8: Gaussian Line fit parameters for Mkn 896. See section 2.4.10

Identification	Observed Wavelength / nm	Rest Frame Wavelength /nm	Gaussian fit Flux $\times 10^{-17}$	Gaussian fit FWHM	Integrated Flux	Velocity Width
Pa α star	1877.28±0.19	1840.60±0.19	5.04±0.45	5.08±0.40		812±64
Pa α brd	1913.30±0.10	1875.92±0.10	20.84±0.38	10.47±0.22		1642±35
Pa α nar	1913.68±0.07	1876.29±0.07	5.33±0.24	3.38±0.16		530±25
?	1946.29±0.11	1908.26±0.11	4.37±0.21	4.68±0.25		721±39
?	1947.18±0.50	1909.14±0.49	6.07±0.38	15 ±17.5		2311±2697
?	1983.99±0.68	1945.23±0.67	3.95±0.32	15.69±1.56		2372±237
H_2 (1-0)S(3)	1998.15±0.88	1959.11±0.86	1.48±0.27	8.75±2.01		1314±302
?	2156.12±0.74	2113.99±0.73	-2.31±0.21	16.80±1.61		2338±225
?	2175.98±0.25	2133.47±0.25	-3.85±0.16	11.05±0.55		1523±76
?	2177.45±0.12	2134.91±0.12	2.18±0.11	4.80±0.29		661±40
?	2201.41±0.17	2158.40±0.17	-1.15±0.09	3.91±0.39		533±53
Br γ	2209.89±0.21	2166.71±0.21	2.52±0.14	7.10±0.46	1.891±0.099	964±63

Table 2.9: Gaussian line fit parameters for Mkn 1239. See section 2.4.10

Identification	Observed Wavelength	Rest Frame Wavelength	Gaussian fit	Gaussian fit FWHM	Velocity Width / km s^{-1}
?	1912.26±0.56	1867.41±0.55	0.123±0.026	4.92±1.36	772±214
Pa α nar	1923.09±0.05	1877.99±0.05	1.084±0.024	3.41±0.11	532±17
Pa α brd	1923.09	1877.99	1.146±0.061	17.87±0.97	2788±151
?	1946.89±0.45	1901.23±0.44	0.722±0.049	13.17±0.98	2029±151
Br γ	2220.68±0.24	2168.60±0.23	0.115±0.015	3.66±0.56	494±76

Table 2.10: Gaussian line fit parameters for Mkn 42. See section 2.4.10

Identification	Observed Wavelength	Rest Frame Wavelength	Gaussian fit Flux	Gaussian fit FWHM	Velocity Width / km s^{-1}
He II $\lambda 1.0129\mu m$	1056.31±0.50	1012.76±0.48	0.184±0.054	3.23±1.13	917±321
Pa δ	1095.92±0.50	1050.74±0.48	0.341±0.068	5.00±1.03	1369±283
[Fe XIII] $\lambda 1.0747\mu m$	1120.18±0.25	1074.00±0.24	0.309±0.040	3.88±0.58	1039±156
He I $\lambda 1.0830\mu m$ nar	1130.67±0.08	1084.06±0.08	0.567±0.038	2.42±0.19	642±50
He I $\lambda 1.0830\mu m$ brd	1130.70±0.33	1084.08±0.32	1.242±0.078	10.41±0.71	2762±189
Pa γ	1141.80±0.25	1094.73±0.24	0.433±0.049	4.04±0.60	1061±158
O I $\lambda 1.1287\mu m$	1178.44±0.18	1129.86±0.17	0.466±0.037	4.19±0.42	1067±107
[Si X] $\lambda 1.2528\mu m$	1306.89±1.11	1253.01±1.06	0.080±0.051	3.04±2.64	698±607
[Fe II] $\lambda 1.279\mu m$	1312.10±0.79	1258.01±0.76	0.115±0.056	3.18±1.82	727±417
Pa β brd	1337.12±0.74	1281.99±0.71	0.385±0.063	8.15±1.66	1829±373
Pa β nar	1338.40±0.26	1283.22±0.25	0.232±0.037	3.11±0.59	697±132
?	1877.34±0.32	1799.94±0.31	0.290±0.059	3.55±0.61	567±98
?	1946.51	1866.26	0.020	2.15	331
?	1946.69±0.30	1866.43±0.29	0.412±0.025	6.98±0.70	1076±108
Pa α brd	1956.52±1.12	1875.86±1.07	0.527±0.024	13.48±2.53	2067±389
Pa α nar	1958.52±0.10	1877.78±0.10	0.418±0.025	4.25±0.21	651±32
[Si VI] $\lambda 1.9615\mu m$	2046.16±0.69	1961.80±0.66	0.183±0.023	9.12±1.53	1337±225

Table 2.11: Gaussian line fit parameters for RE J1034+396. See section 2.4.10

Object	RA (J2000)	Dec (J2000)	mag	Redshift
RE J1034+396	10 34 38.608	+39 38 28.20	V = 16.6	0.042
Mkn 42	11 53 41.772	+46 12 42.85	B = 15.2	0.0240
Mkn 766	12 18 26.516	+29 48 46.51	V = 13.6	0.0129
Mkn 291	15 55 07.926	+19 11 32.82	V = 15.5	0.0352
Mkn 493	15 59 09.622	+35 01 47.62	B = 14.5	0.0313
Mkn 896	20 46 20.869	-02 48 45.28	V = 16.0	0.0264
Akn 564	22 42 39.345	+29 43 31.31	V = 14.2	0.0247

Table 2.12: Summary of the CGS4 observed sample

2.5 Analysis

2.5.1 The Objects

Table 2.12 summarises the general properties of the objects in this sample.

2.5.2 Hydrogen Lines

We have obtained data on several of the IR Paschen lines in most of our targets. Ratios of these lines are here analysed for consistency with case B recombination (Osterbrock 1989). Plots 2.21 - 2.26 show the ratio to Pa α of the Paschen lines for which we have data. The broad and narrow components of the lines have been plotted separately where available. A line representing the ratios that would be expected from case B recombination at 20,000K has also been plotted. Whilst this choice of temperature is somewhat arbitrary, it should be noted that under case B, the line ratio variation with temperature is small at such a high temperature. Our results show that the data are broadly consistent with case B recombination. There is no evidence that the class as a whole shows Paschen lines significantly redder or bluer than case B recombination. The two objects which show significant reddening (Mkn 291 and Mkn 493), show Pa α to Pa β ratios equivalent to case B recombination reddened by an A_V of $\sim$ 5, as compared to a typical value of 1 in the optical, though we do not consider this result as particularly significant in the light of the large scatter in hydrogen line ratios shown in the data, especially considering the number of objects which show line ratios *bluer* than case B.

However, it is interesting to comment briefly on the plots. Mkn 896 shows a strange plot; from fig 2.25 we might suggest that the spectrum is poor, or that the Pa β line is contaminated or otherwise poorly fit. However the spectrum shows no signs of this. Ignoring this peculiar case, we note that the remaining 3 objects which show Paschen line spectra bluer than case B are: Akn 564, Mkn 766 and RE J1034+396. These objects are the ones with more interesting spectra, tending to show high ionisation lines, though we also note that they are the brighter objects; this could itself be an interesting and potentially important result in the light of beaming hypotheses, or it could simply be the trigger of a selection effect whereby we do not see the weaker high ionisation lines in the poor signal to noise ratio spectra. It is not clear how a good signal to noise ratio spectrum would appear to apparently enhance the bluer Paschen lines.

2.5.3 Other lines

Figure 2.28 shows diagrammatically the contents of tables 2.4 – 2.11, with the previously described Hydrogen lines omitted. The points plotted represent the line flux (relative to Pa α) vs observed wavelength for each line.

None of the objects appear to be particularly outstanding in this plot, though there is a suggestion that RE J1034+396 appears to show strong lines relative to Pa α. Not all the lines in this diagram have been identified.

In figure 2.29 we display the same information, but plotting flux relative to Pa α against ionisation potential for each line.

Ferguson, Korista & Ferland (1997) carried out CLOUDY modeling of the coronal line emission in Seyfert galaxies, and present plots showing equivalent width contours over a range of physical conditions for a number of high excitation (coronal) lines that are likely to be observed in ISO spectrometry observations. Some of these lines are within the wavelength regions of our CGS4 spectra, although our signal to noise is often insufficient to detect them. A rough comparison of the data from Ferguson, Korista & Ferland (1997) with our results shows the two to be broadly consistent, without any particular lines standing out as being radically different from the models. More specific model data from CLOUDY runs over grids of different continuum parameters should help us to constrain the ionising continuum in the NLS1s.

Figure 2.30 shows a plot of the line Equivalent widths (relative to Pa β) predicted by the "dusty" model of Ferguson, Korista, Baldwin & Ferland (1997) against the corresponding values from our data. Detailed comparison of a single object is difficult due to the low number of lines included in the model that are detected in our spectra, thus we plot points from all our detected lines in all our spectra which are included in the model. We note that the model as published covers a very broad range of wavelengths, and is better suited to comparison with very broad band data for example from the ISO satellite. It is noted that a good correlation appears to exist between the model and our data, with no particular bias for any given lines to be stronger or weaker in our data than in the model, within the scatter, which is entirely consistent with the errors quoted on our observed data.

Hints of the detection of stellar absorption lines in our data are difficult to verify. In many cases, the weak absorption features are co-incident, or very close to sky line

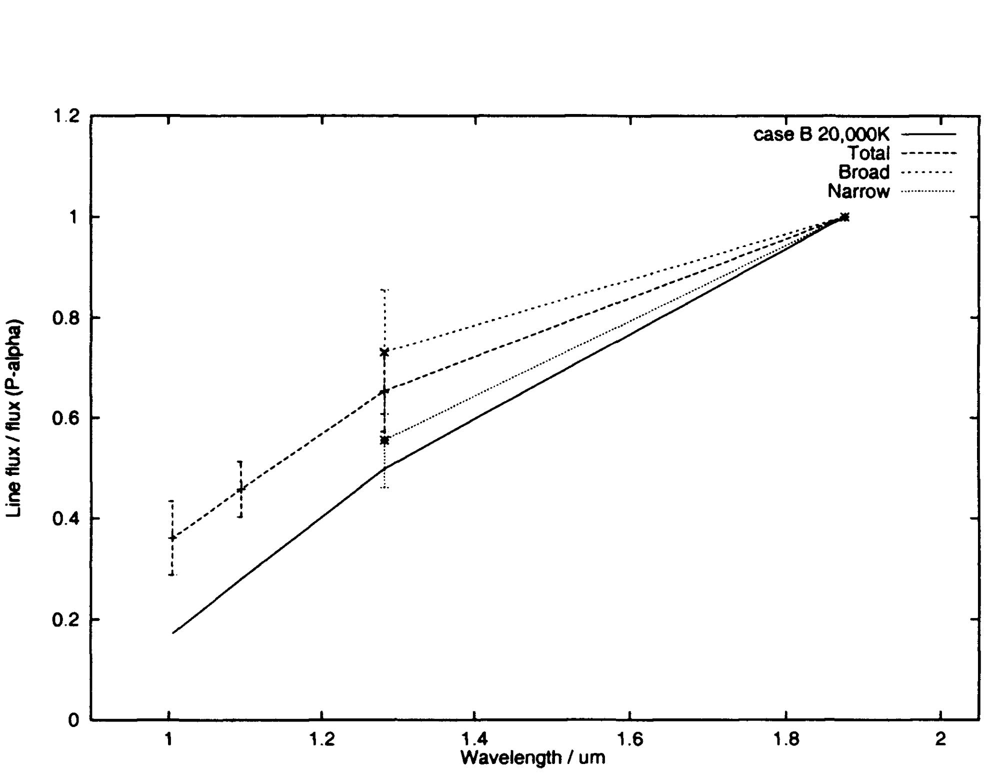

Figure 2.21: Paschen line ratio plot for RE 1034+396

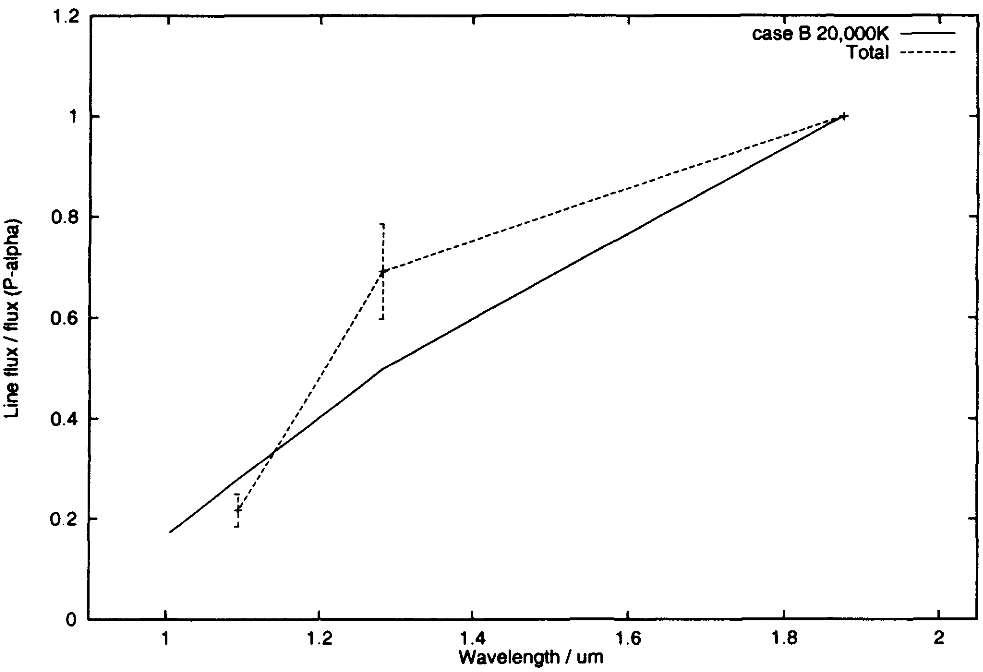

Figure 2.22: Paschen line ratio plot for Mkn 766

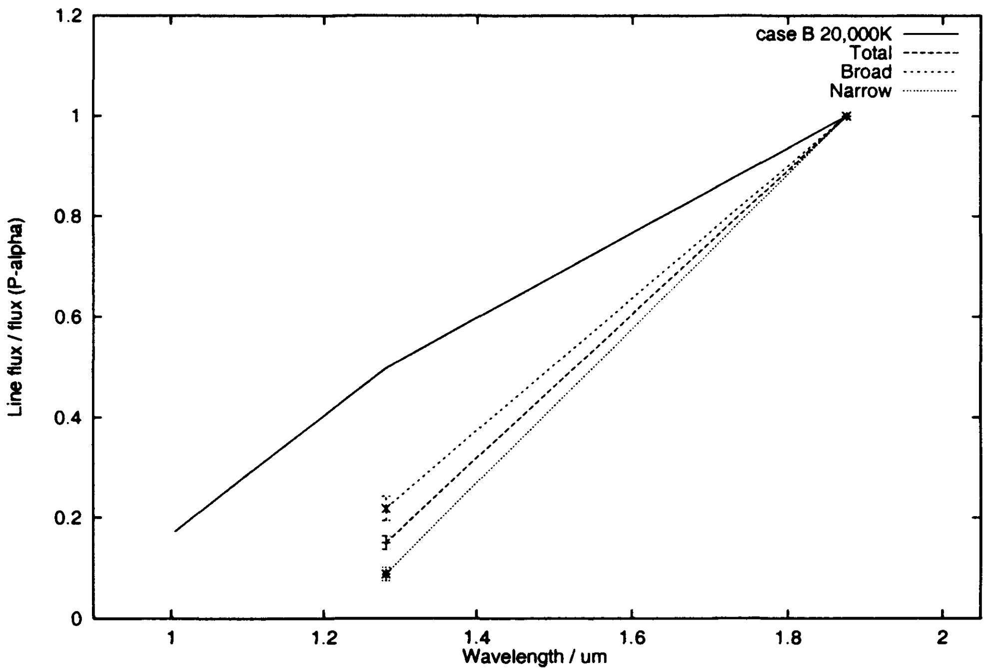

Figure 2.23: Paschen line ratio plot for Mkn 291

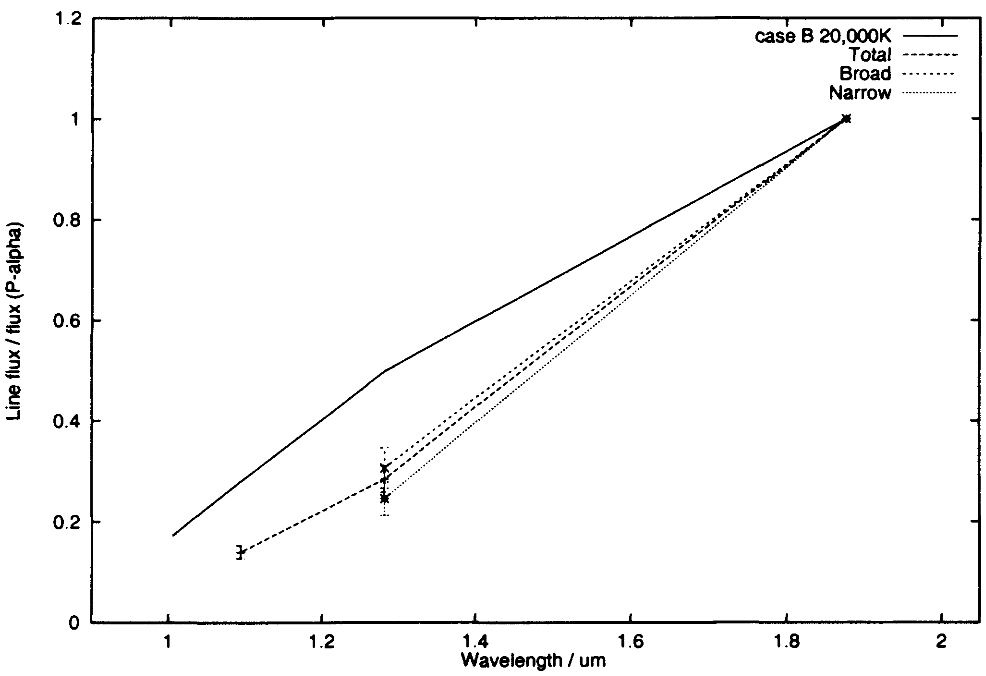

Figure 2.24: Paschen line ratio plot for Mkn 493

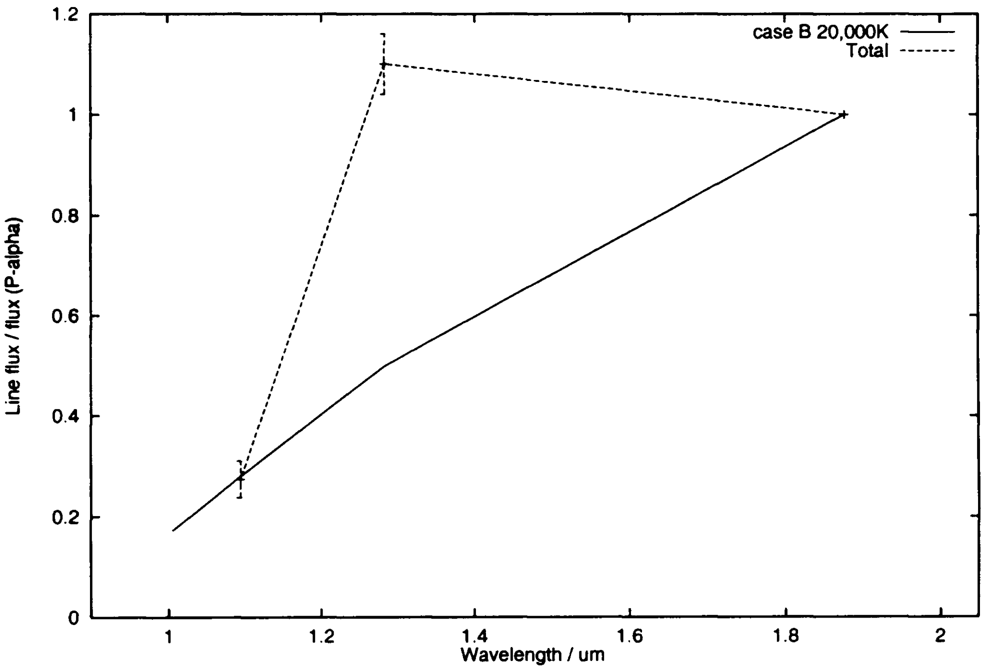

Figure 2.25: Paschen line ratio plot for Mkn 896

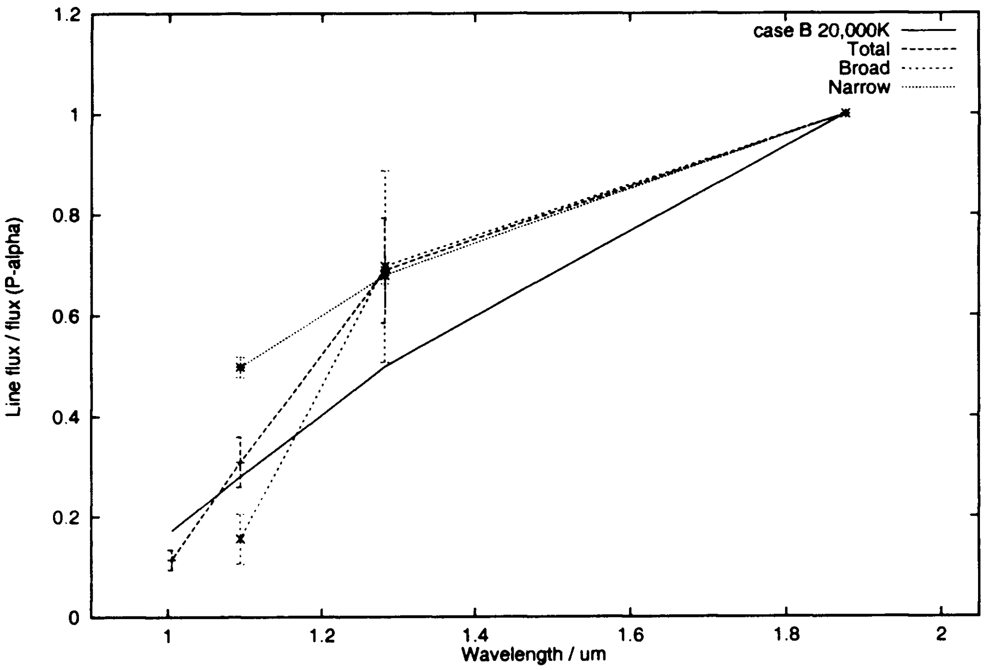

Figure 2.26: Paschen line ratio plot for Akn 564

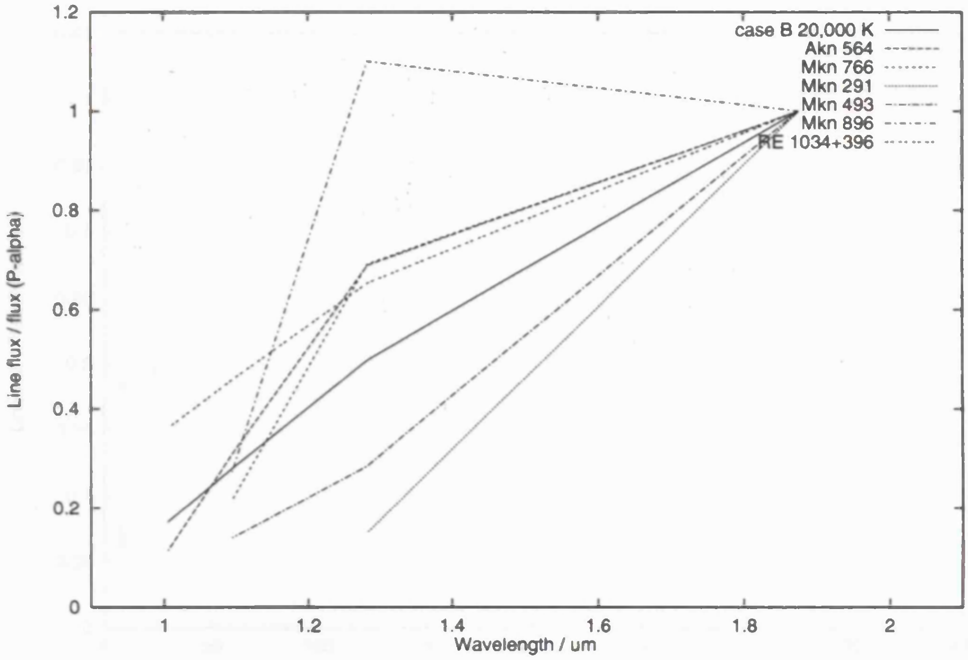

Figure 2.27: Combined Paschen line ratio plot for all the objects. Error bars have been omitted for clarity

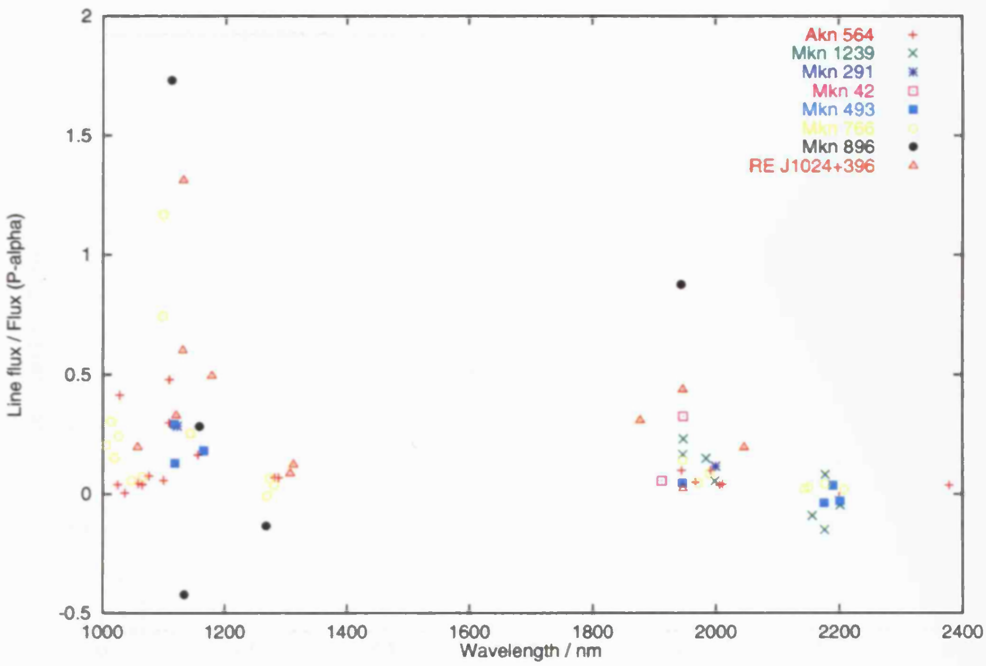

Figure 2.28: Diagram showing the non-Hydrogen lines detected in all the observed NLS1s

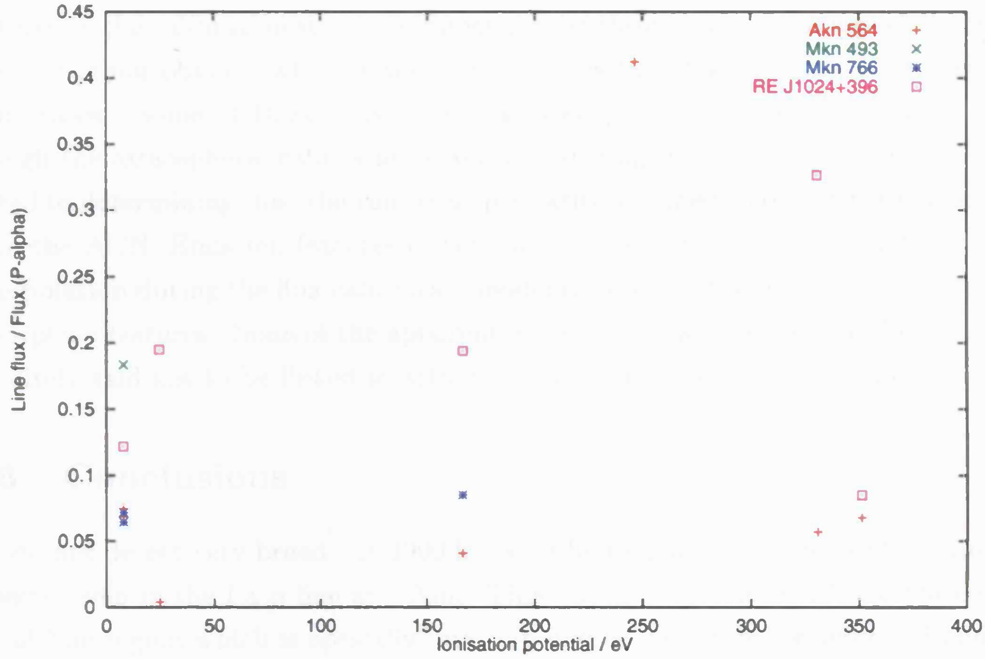

Figure 2.29: Non-hydrogen lines vs ionisation potential.

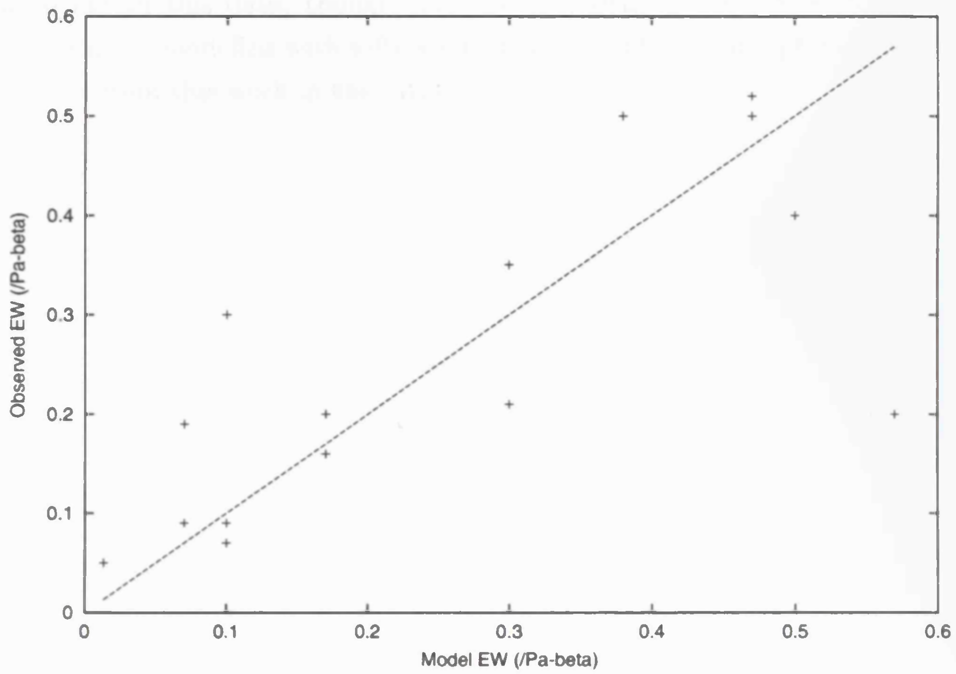

Figure 2.30: Model vs observed Equivalent widths

features in the original data which have not subtracted well. In addition, weak emission features in the calibration stars sometimes persist through the data, especially in places where it is not obvious whether the feature arises from the star or the atmosphere in some cases. Some of these may be stellar absorption features in the AGN objects, though the atmospheric calibration stars used during this run were not especially well suited to determining this, the run being primarily designed to detect the emission lines from the AGN. Emission features in the calibration stars which were not removed by interpolation during the flux calibration model show up in the AGN spectra as spurious absorption features. None of the apparent absorption features seem in the data can be definitely said not to be linked to artifacts in the data resulting from this.

2.6 Conclusions

We do not detect very broad (> 3000 km s^{-1}) hydrogen line components in any of our objects, even in the Pa α line at 1.9μm. This implies that the NLS1s do not contain a broad line region which is optically invisibly due to moderate reddening. In addition, we do not find any evidence for significant reddening in either the Broad or Narrow line regions.

Only some of the objects show the high excitation coronal lines which are apparent in optical spectra of most NLS1s. We do not detect any significant trends with ionisation potential etc in this data, though combination with optical emission line data and photo-ionisation modeling with software such as "Cloudy" should provide more tangible conclusions from this work in the future.

Chapter 3

Radio Observations of NLS1s

3.1 Motivation and Aims

Multi frequency radio studies of NLS1s provide a good way to test the "pole on" hypothesis, (section 1.3.1) which was popular before the rise of the X-ray driven models suggesting a high accretion rate onto a low mass black hole. We investigate whether the pole-on model might apply to some NLS1s.

3.2 Method

These images were obtained using aperture synthesis interferometry techniques with radio telescope arrays. Although a detailed review of this technique would be out of place here, a brief overview will be presented.

3.2.1 Basic Interferometry Principles

Radio telescopes usually consist of a circular, parabolic reflector, of order 20–70 metres diameter, and function at wavelengths around 20–2cm. This gives each telescope a diffraction limited spatial resolution of order 0.5–0.02 degrees, which is too low to resolve structure within an extragalactic radio source, and invites source confusion problems.

However, if we have two telescopes, A and B, separated by some distance D, and looking at an astronomical point source (see figure 3.1), telescope A generates a voltage $V_A = A\cos(\omega t + \phi_A)$, B generates a voltage $V_B = B\cos(\omega t + \phi_A + \omega\tau)$, where τ is the light travel time between the two telescopes, projected along the line of sight to the source.

We multiply these two signals to get $V_A V_B = AB\cos(\omega t + \phi_A)\cos(\omega t + \phi_A + \omega\tau) = \frac{AB}{2}(\cos(2\omega t + 2\phi_A + \omega t) + cos(\omega\tau))$. The term in $\cos(2\omega t)$ goes to zero on integration over

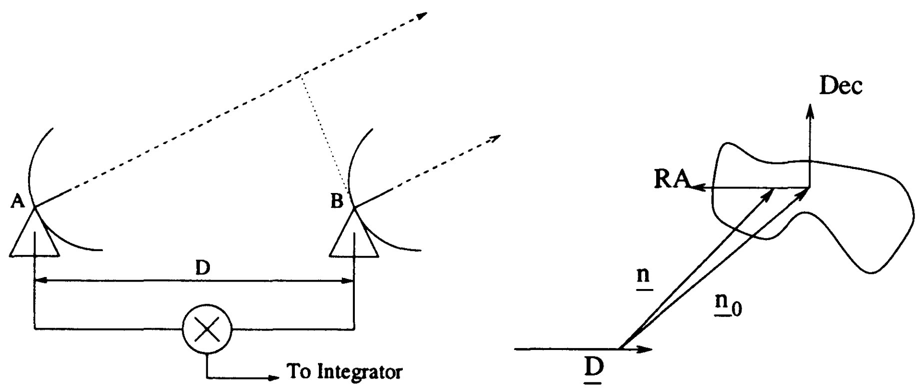

Figure 3.1: Basic Interferometry diagrams

time, leaving us with[1] $< V_A V_B >= \frac{1}{2} AB \cos(\omega\tau)$. We can define a complex equivalent, $< V_A * V_B >= \frac{1}{2} AB e^{i\omega\tau}$. By simple geometry, $\omega\tau = \frac{2\pi D}{\lambda} \sin\theta$.

We can extend this model to extended sources, by considering the extended source to be composed of point source elements;

$$\begin{aligned} < V_A * V_B > &= \int AB e^{i\omega\tau} d\Omega \\ &= e^{i\omega\tau_0} \int AB e^{i\omega(\tau-\tau_0)} d\Omega \end{aligned}$$

where $A \propto \sqrt{P_A(x,y)T(x,y)dxdy}$, $B \propto \sqrt{P_B(x,y)T(x,y)dxdy}$, $P_{A,B}(x,y)$ are the beam profiles the antennas, and $T(x,y)$ is the brightness Temperature of the source as a function of position on the sky.

Projecting D into sky co-ordinates (x, y in the plane of the sky, z along the telescopes line of sight), and defining $u = \frac{D_x}{\lambda}$, $v = \frac{D_y}{\lambda}$, $w = \frac{D_z}{\lambda}$, we note that $\tau_0 = \frac{\vec{D}.\hat{n_0}}{c}$, and $\tau = \frac{\vec{D}.\hat{n}}{c}$, and thus $\omega(\tau - \tau_0) = \frac{\vec{D}}{\lambda}.(\hat{n} - \hat{n_0}) = ux + vy + wz$. We can neglect the term in wz, as we are considering a small field of view, over which the "field curvature" is negligible. We thus write

$$\begin{aligned} < V_A * V_B > &= e^{i\omega\tau_0} \iint \sqrt{P_A T P_B T} e^{2\pi i(ux+vy)} dxdy \\ &= e^{i\omega\tau_0} \iint \sqrt{P_A P_B} T e^{2\pi i(ux+vy)} dxdy \end{aligned}$$

Note that the field of view of the interferometer is limited by the fact that we made a flat field assumption, amongst other things, this means that the terms in $P_A(x,y)$

[1]Notation: $< X >$ denotes an average of X over time

and $P_B(x, y)$ are essentially constant over the imaged area of sky.

$$\begin{aligned} < V_A * V_B > (u, v) &= e^{i\omega\tau_0} \int\int_{FOV} T e^{2\pi i(ux+vy)} dxdy \\ &\equiv \text{2D fourier transform of } T(x, y) \end{aligned}$$

Note also that $e^{i\omega\tau_0}$ is the point source response of the interferometer. We denote the rest of the response expression as $V(u, v)$, known as the "complex visibility function". It is this function, integrated over periods of a few seconds, that the correlator electronics record for each baseline. In a real interferometer system, we sample partial ellipses of the (u, v) plane, formed by the changing orientation and projection of the baseline along the line of sight to the target, and limited by the rise and set times of the source at each telescope, as the earth rotates during the observation. Incomplete sampling of the (u, v) plane means that we only sample a limited range of spatial frequencies in the source, and that the point spread function of the interferometer will be complex and very extended.

The Fourier transform necessary to transform the visibility function measurements back into an image is carried out computationally after the visibility measurements have been calibrated, as part of the mapping process.

3.2.2 Practical limitations on interferometry

The main practical limitation of interferometry is due to the incomplete sampling of the (u, v) plane inherent in the observations. The maximum projected baseline length determines the highest resolution component to the image, though the lack of short baselines will degrade the sensitivity to extended structure. The field of view of an interferometer is determined by several factors, including the bandwidth of the integrator. Our derivation above assumed a monochromatic source, which is obviously not valid. As greater bandwidth leads to greater sensitivity, the trade off is often handled by splitting the band pass of the receiver into several low bandwidth (eg 1 MHz) channels, which are correlated separately when wide fields of view are required. Obviously, this method requires more computation time to image. An additional factor is the integration time of the correlator. Long integration times produce a lower volume of data for a given observation, though lead again to a restricted imagable field.

3.3 Observations

We have obtained a significant amount of broad band[2], aperture synthesis, imaging data from the VLA archive, and have supplemented this with successful observing proposals on both the VLA and MERLIN. The VLA consists of 27 25m antennae, arranged in a Y shape, and spaced in one of four configurations, from A array (with 36km diameter), to D array (1km diameter). The VLA is located in on the Plains de St. Augustine, near Socorro in New Mexico, USA. MERLIN is a microwave linked interferometer, consisting of 7 antennae, most of which are 25m diameter, arranged randomly throughout England. It is run by Jodrell Bank and has a maximum baseline length of 250km.

This results in a diverse data set covering a range of frequencies, resolutions and UV spacings. Most of the VLA data has been taken in "snapshot" mode, with observations lasting around 10 minutes. This relies on the geometry of the array to provide the UV coverage - the projection and orientation of the baselines do not change significantly during the observation due to the rotation of the earth. The MERLIN data, however, is long track observations, where the observations last for around 8 hours. The rotation of the earth changes the orientation and projection of the baselines to better fill the UV plane. This is more necessary with MERLIN than the VLA due to the random layout and smaller number of MERLIN antennae, compared to the Y shaped VLA layout.

In the case where an object has been observed more than once, we check for variability, though different instrument configurations or observing frequencies can lead to uncertainties here.

3.4 Data Reduction

Standard mapping techniques for VLA broad band data were applied. These are well documented (e.g. Bridle & Greisen 1998), and will not be described in detail here. However, an overview for those not familiar with the process will be presented.

The data output from the correlator are raw visibility function measurements for each baseline in the array. The first stage in the data reduction sequence is an approximate calibration of these values, based on an observation of a primary flux standard source such as 3C186 or 3C273. The AIPS[3] software (versions 15OCT98 and 15APR99) was used to carry out all the calibration and reduction of this data. AIPS contains a model of these two primary flux calibrators to estimate the flux accepted by a given VLA baseline at a given frequency from the source. Following this initial calibration,

[2]Terminology - the radio bands we have used are referred to by letters as follows: L band = 1.4GHz = 20cm, C band = 5GHz = 6cm, X band = 8.4GHz = 3.6cm

[3]The National Radio Astronomy Observatory's "Astronomical Image Processing System"

Dataset	Date	Instrument	Cfg	Freq	Target	Notes
AL454	1998-09-02	VLA	B	C	Mkn 896	ND
					Ark 564	PS
					IRAS F22453-1744	PS ART
					UCM 2257+2438	PS
					Mkn 1126	PS ART
					IRAS F23410+0228	PS ART
					Mkn 957	PS ART
					I Zw 1	PS ART
					Mkn 359	PS ART
					PKS 0129-066	ND
					PHL 1092	ND
					IRAS F04416+1215	ND
					IRAS F04576+0912	PS ART
					IRAS F05262+4432	MD
					IRAS F06269+0542	PS ART
		MERLIN		C	IRAS F05262+4432	See
					IRAS F04576+0912	Text
					Mkn 359	
					Mkn 493	
					Mkn 957	
					Mkn 1239	
AM 492	1995-07-12	VLA	A	X	Z1702+45	PS ART
					Z1631+47	PS
					Z2018-22	PS
					Z2052-23	PS MD
					Z2245-17	PS
					Z2341+02	PS
				L	Z1631+47	PS ?
					Z1702+45	PS
					Z2018-22	PS ART
					Z2052-23	PS
					Z2245-17	PS
					Z2341+02	PS
	1995-07-10			L	Z0441+12	PS ART
					Z0457+09	PS ART
					Z0626-05	PS
					Z0526+44	ND
				X	Z0441+12	PS ART
					Z0457+09	PS ART
					Z0626-05	PS
					Z0526+44	ND

Table 3.1: Radio Observations Summary. Notes: ND = Not Detected. PS = Point Source. ART = Any apparent structure is an imaging artifact. MD = Marginal Detection

the data are examined for spurious values, such as those caused by high levels of Radio Frequency Interference (RFI) or other causes of obviously bad data, which generally show up as anomalously high data values. Any obviously bad data is marked and deleted in all 4 Stokes channels.

The cleaned up data is then used to regenerate the initial calibration solution, and from this, a table of the complex gains of each antenna is built up. This table is then used to calibrate the observations of the secondary flux density calibrators, observations of which are interleaved between the target observations.

Calibration solutions from a given secondary flux density calibrator are then applied to the data from the actual target observations, usually selecting the calibrator which is closest to the target both in sky position and in observing sequence.

The calibrated observations of the targets were then mapped using the IMAGR task in AIPS. Initially, a "dirty" map was generated, simply based upon the Fourier transform of the visibility function. This reveals the location of any radio sources within the image, around which areas of the image are marked for CLEANing. If any confusing sources are present, either inside or just outside the mapped area, these are also apparent, either directly, or from the side-lobes of the interferometer Point Spread Function (PSF) if the source is outside the imaged field. Confusing sources must be mapped separately, after which their visibility values can be subtracted out of the data set to simplify mapping of the intended target.

Where a significant amount of signal exists in the map, the area of the image around the source was processed using the CLEAN de-convolution algorithm built into IMAGR. CLEAN (Clarke 1980, Högbom 1974) is an image de-convolution algorithm especially suited to de-convolving the PSF of an interferometer from an image field containing point sources. In principle, CLEAN works by finding the highest value pixel in an image, scaling a copy of the PSF to some fraction of that pixel value, shifting the PSF to be centred at that pixel location, then subtracting the scaled, shifted PSF image from the "dirty map". The scale factor and offset of the PSF image are noted as a "CLEAN component". This is repeated until all the bright sources have been removed from the dirty map, leaving a residual image containing only sky background and noise. A "reconstruction beam" is then synthesised - usually an elliptical Gaussian beam representing the diffraction limited resolution of the interferometer. This beam is then convolved with the list of clean components and the resulting image added back into the residual image to give the final "Clean image".

In some cases, PSF like features persist in the image, generally taking the form of a PSF which switches sign across the phase centre. This is due to phase errors in the data, and where the target contains a strong point source, can be removed by the technique of "self-calibration". This technique relies on using CLEAN to identify

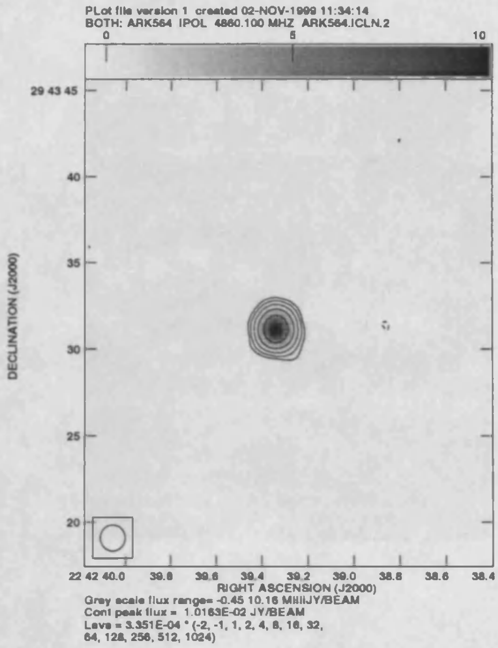

Figure 3.2: Akn 564 - 5GHz from AL454

a few clean components associated with a strong point source. The self calibration algorithm then adjusts the phase of the complex gain calibration in the data in such a way that the data corresponding to these clean components genuinely does correspond to a point source. Assuming that this point source is real, the gain solution is now better than before, and artifacts in the image due to phase errors in this calibration are correspondingly reduced.

As these images were taken in "snapshot" mode, the phase calibrator observations that would normally be interleaved throughout a long track observation were not made, and thus targets which do not contain a strong enough point source are unable to be phase calibrated.

3.5 Results

3.5.1 VLA archival Images

The UV datasets were extracted from the VLA archive, and recalibrated and mapped. The contours in these plots are at factors of 2 in flux, starting at 3σ, taking σ as the RMS flux / beam in the off-source parts of the image. We show a grey-scale image overlayed with contours, with a grey-scale wedge along the top, and the CLEAN algorithm reconstruction beam FWHM ellipse in the lower left.

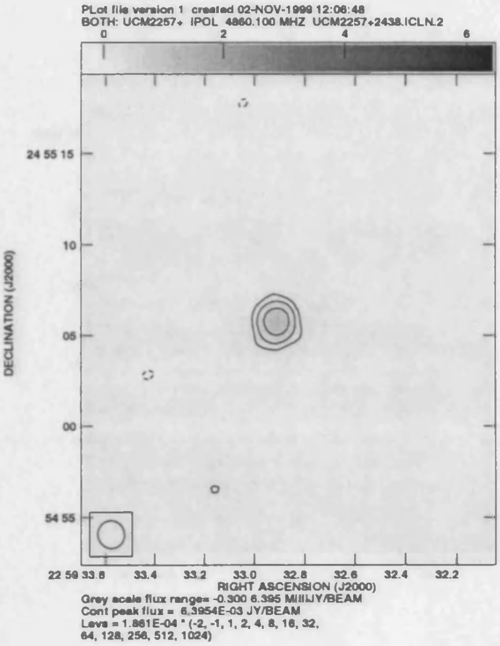

Figure 3.3: UCM 2257+2438 - 5GHz from AL454

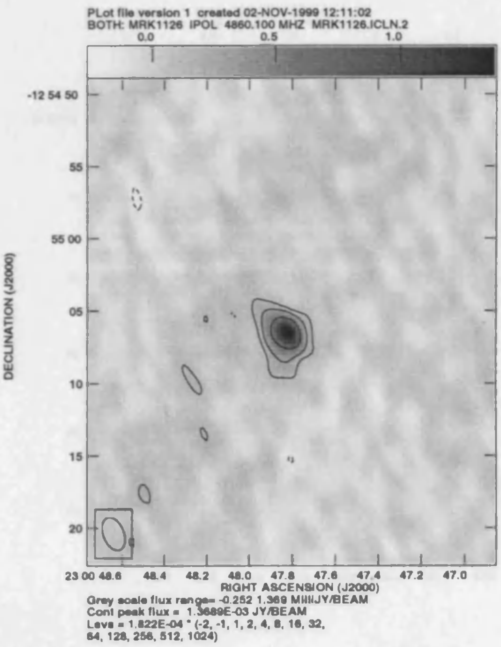

Figure 3.4: Mkn 1126 - 5GHz from AL454

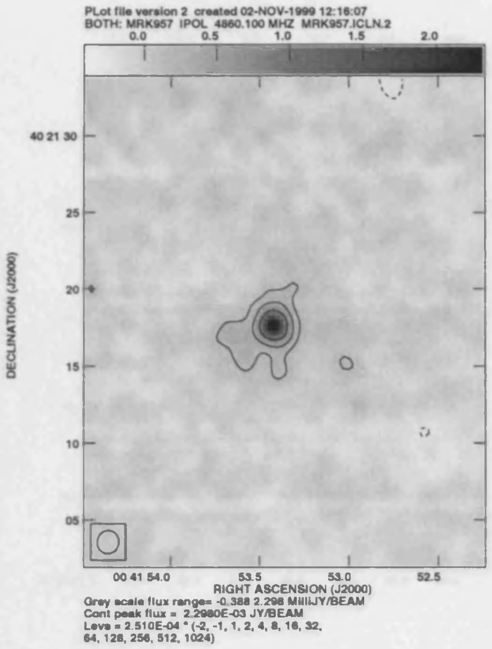

Figure 3.5: Mkn 957 - 5GHz from AL454

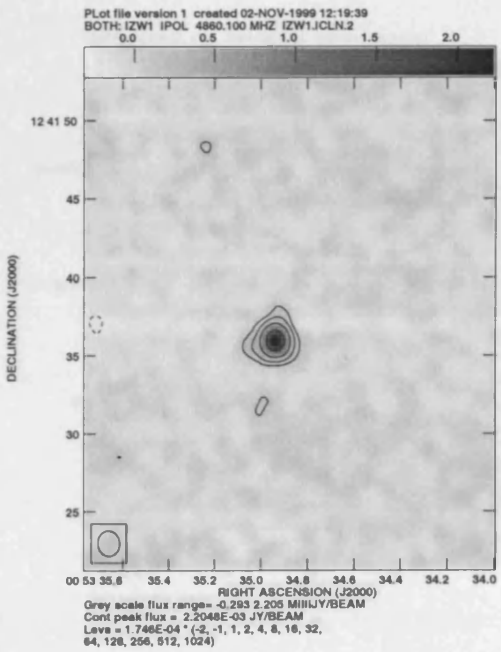

Figure 3.6: I Zw 1 - 5GHz from AL454

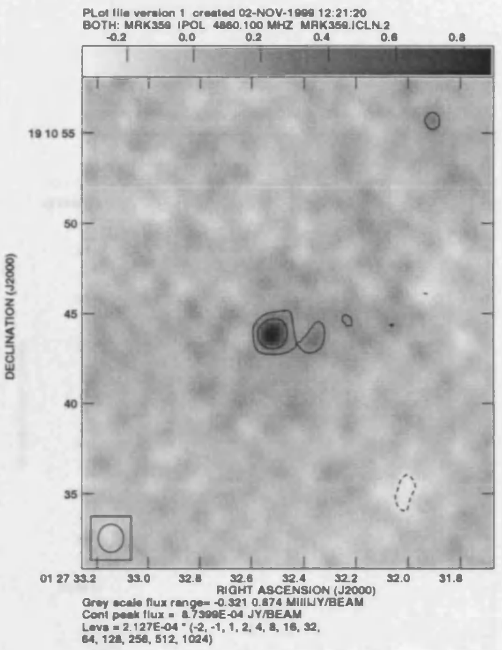

Figure 3.7: Mkn 359 - 5GHz from AL454

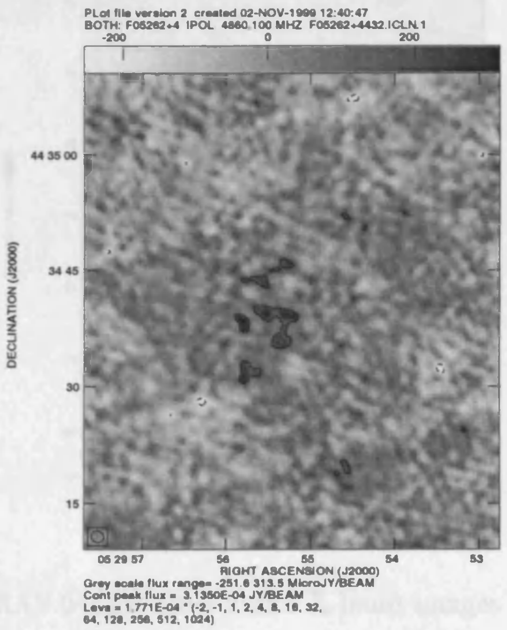

Figure 3.8: IRAS 05262+4432 - 5GHz from AL454

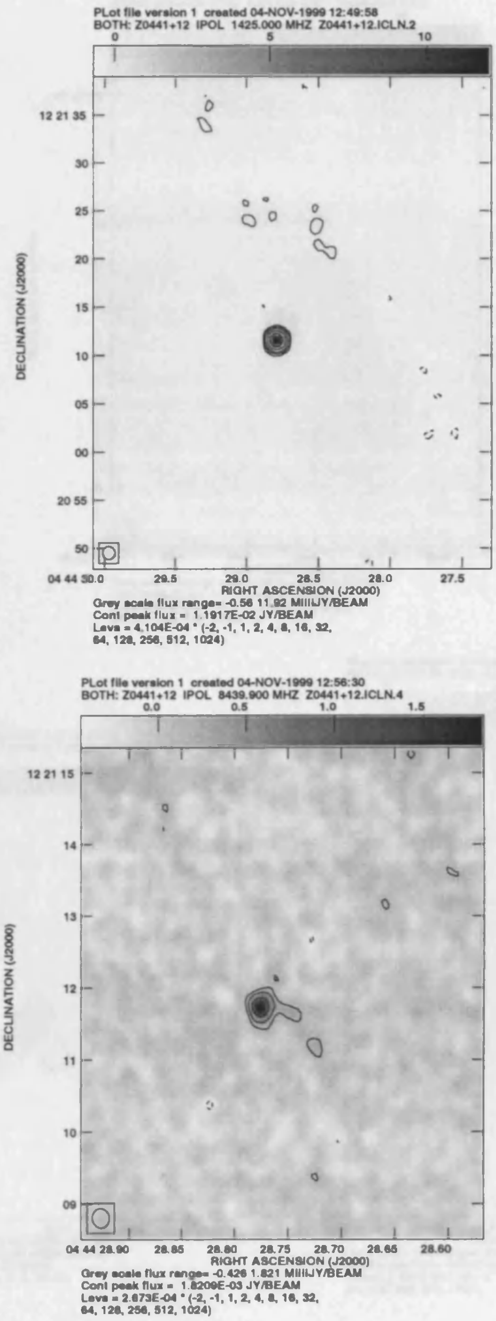

Figure 3.9: IRAS 04416+1215 L and X band images from AM 492

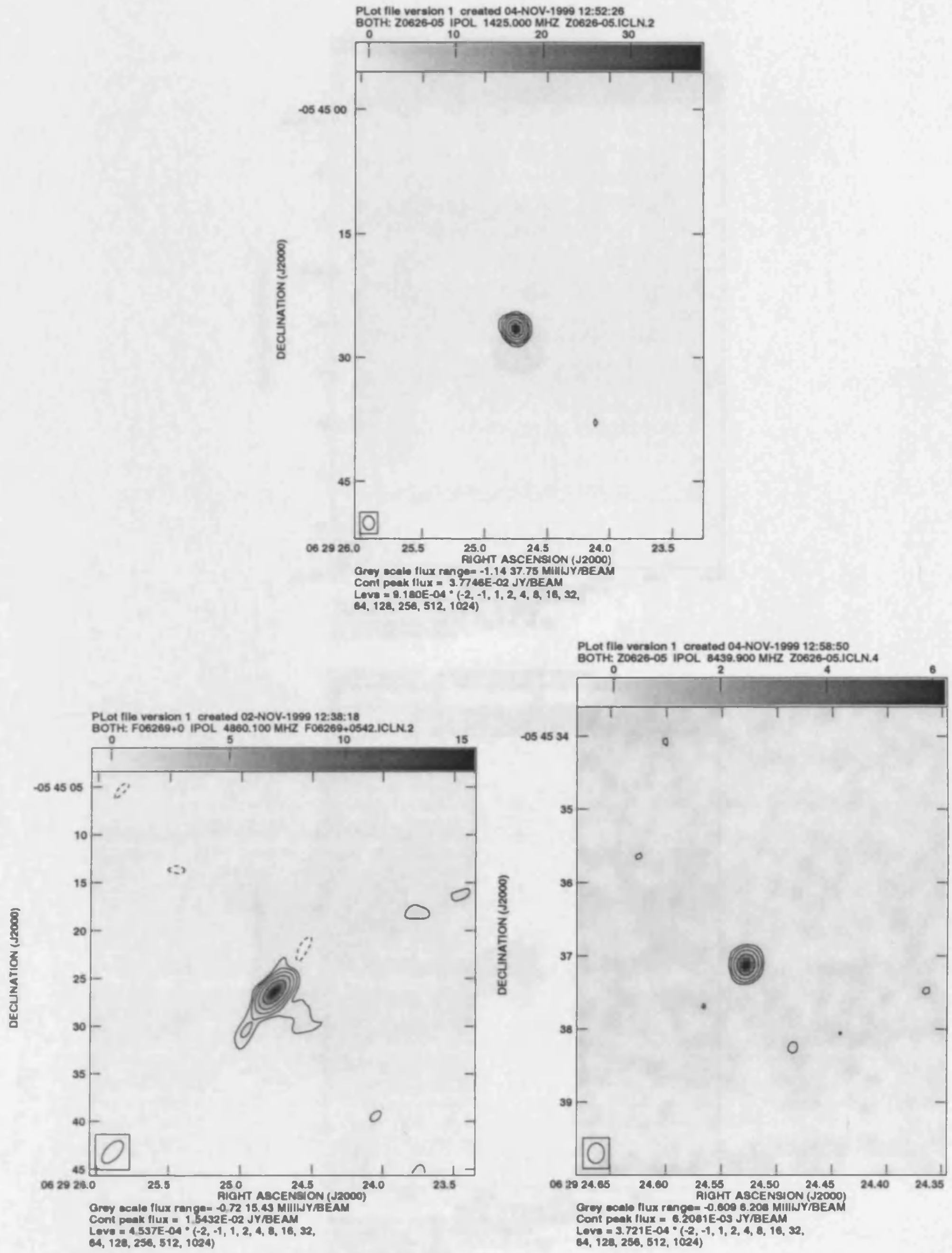

Figure 3.10: IRAS 06269-0543 L, C and X band images, from AM492 (L,X) and AL454 (C)

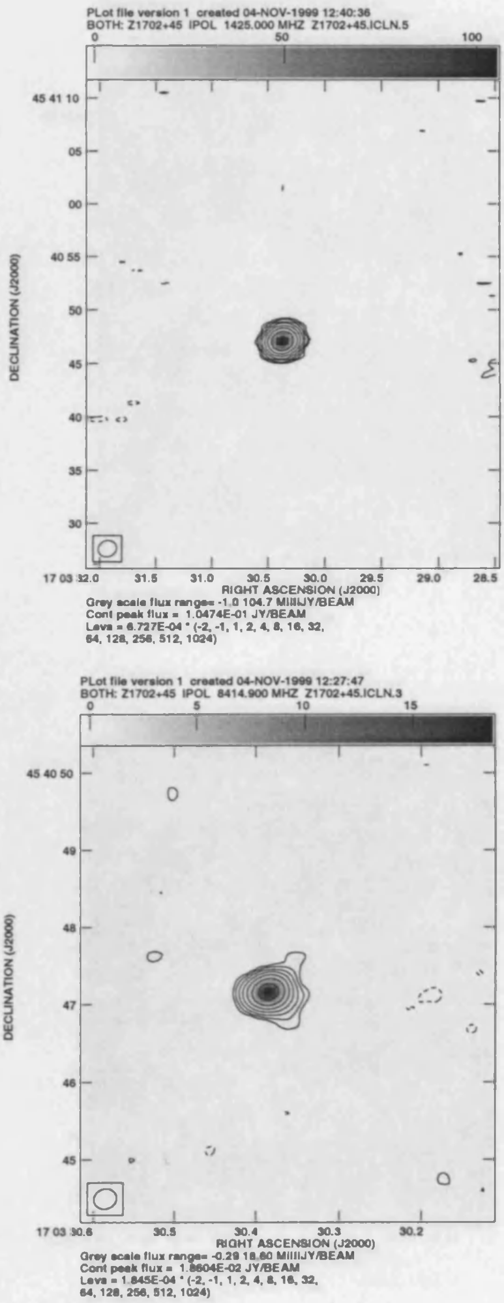

Figure 3.11: IRAS 17020+4544 L and X band images from AM492

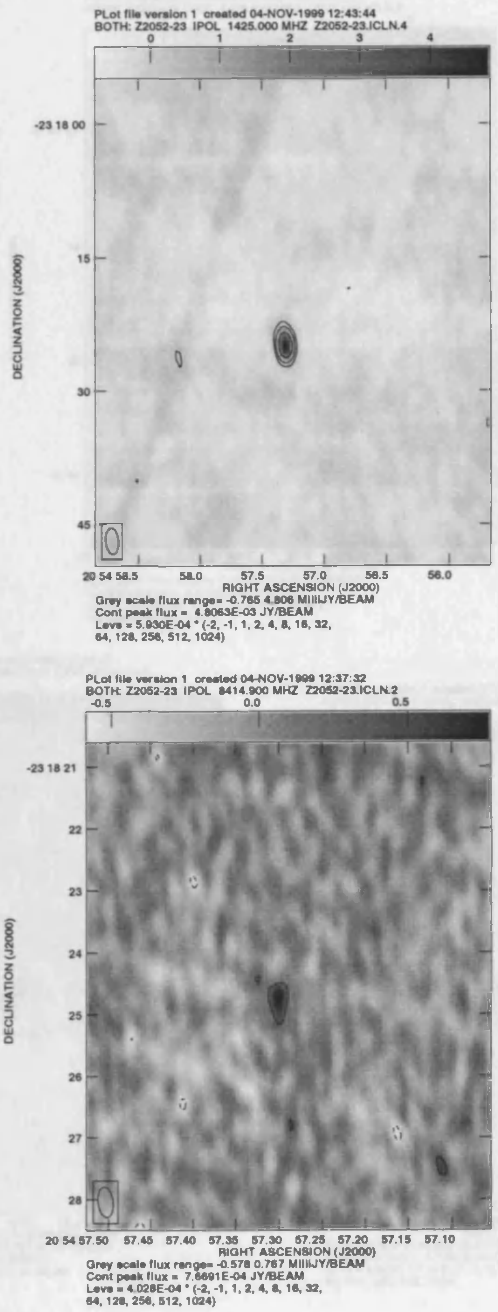

Figure 3.12: IRAS 20520-2329 L and X band images from AM492

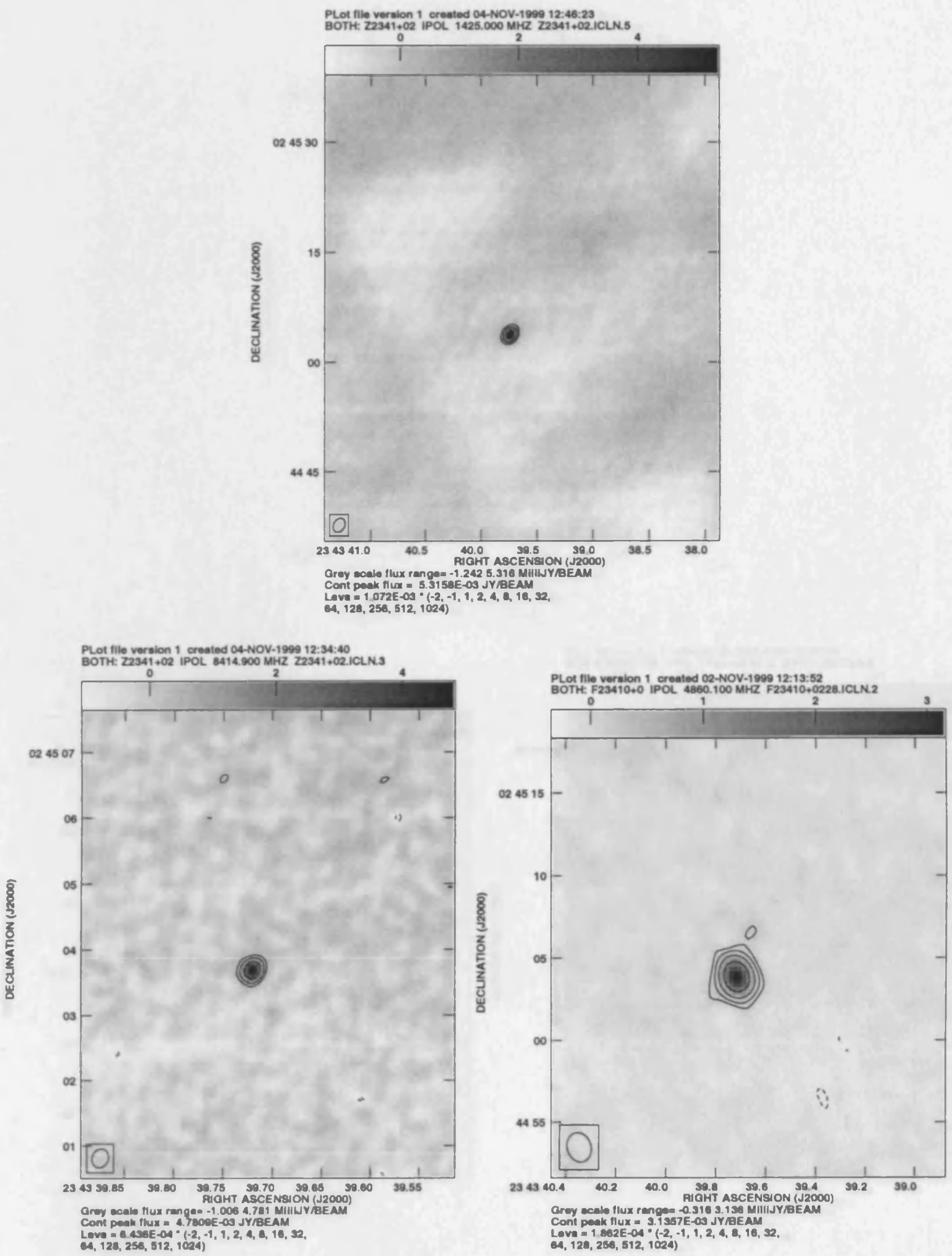

Figure 3.13: IRAS 23410+0228 L, C and X band images from AM492 (L,X) and AL454 (C)

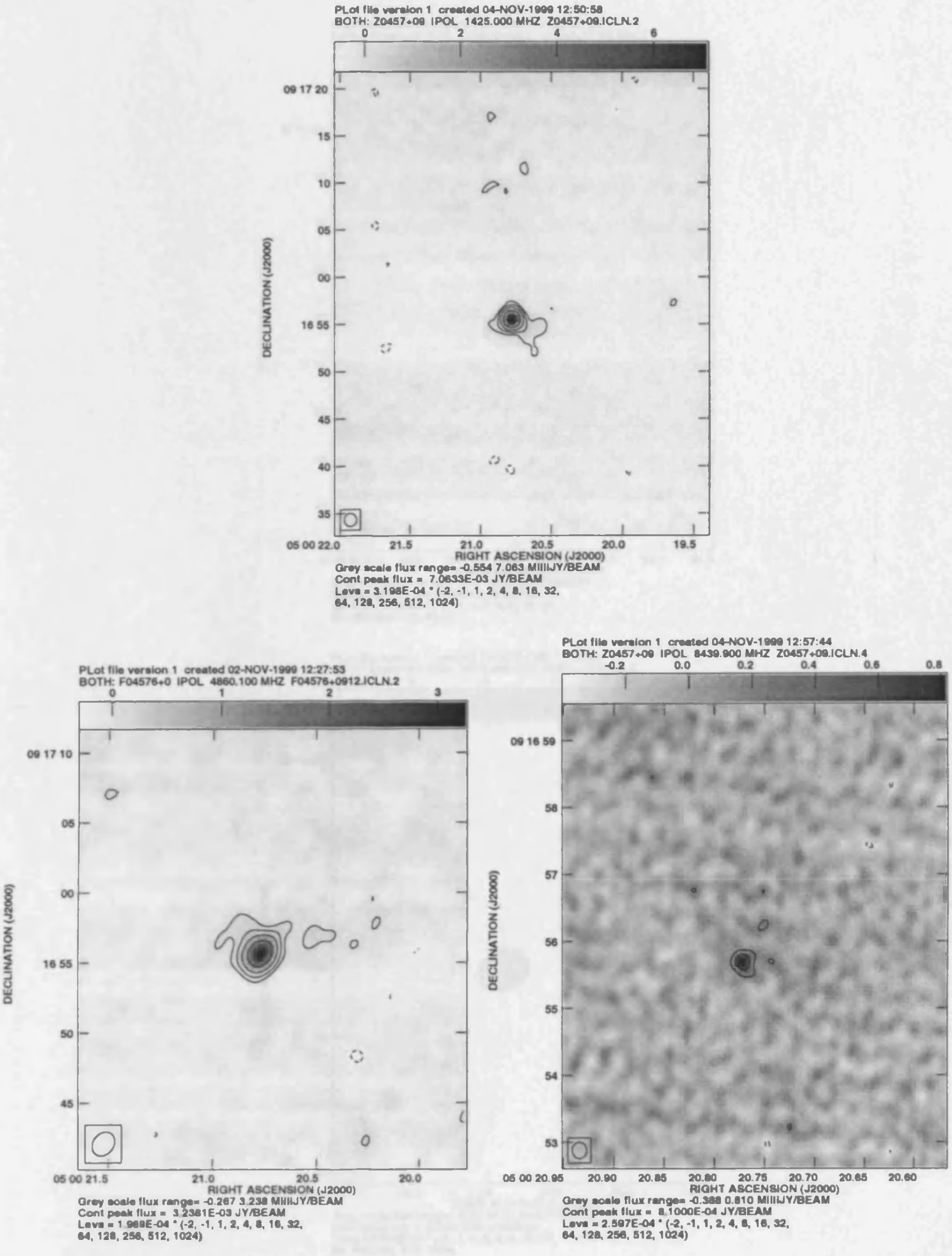

Figure 3.14: IRAS 04576+0912 L, C and X band images from AM492 (L,X) and AL454 (C)

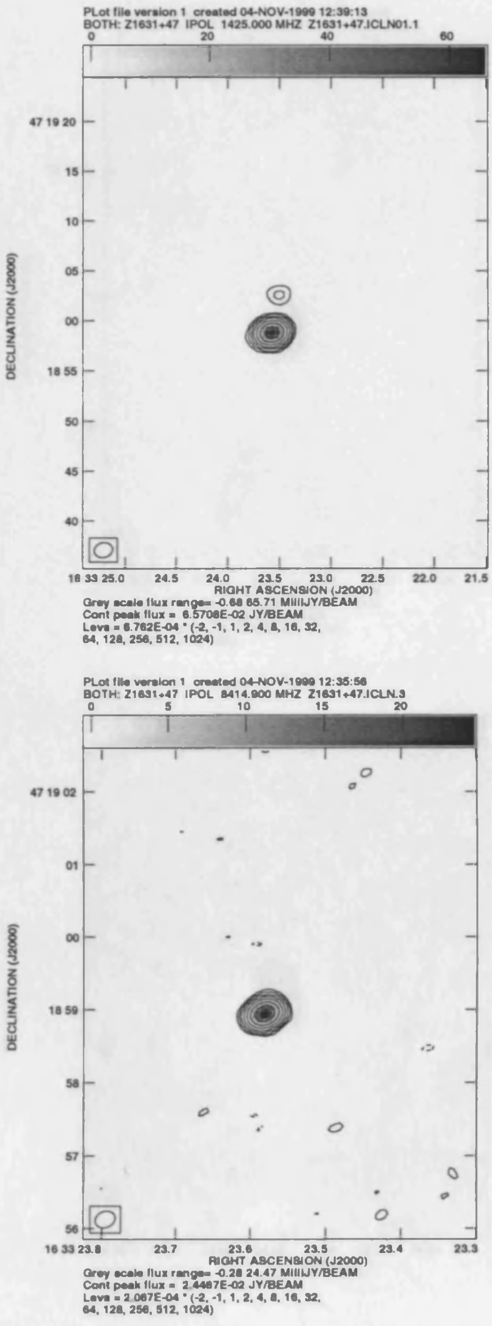

Figure 3.15: IRAS 16319+4725 L and X band images from AM492

Figure 3.16: IRAS 20181-2244 L and X band images from AM492

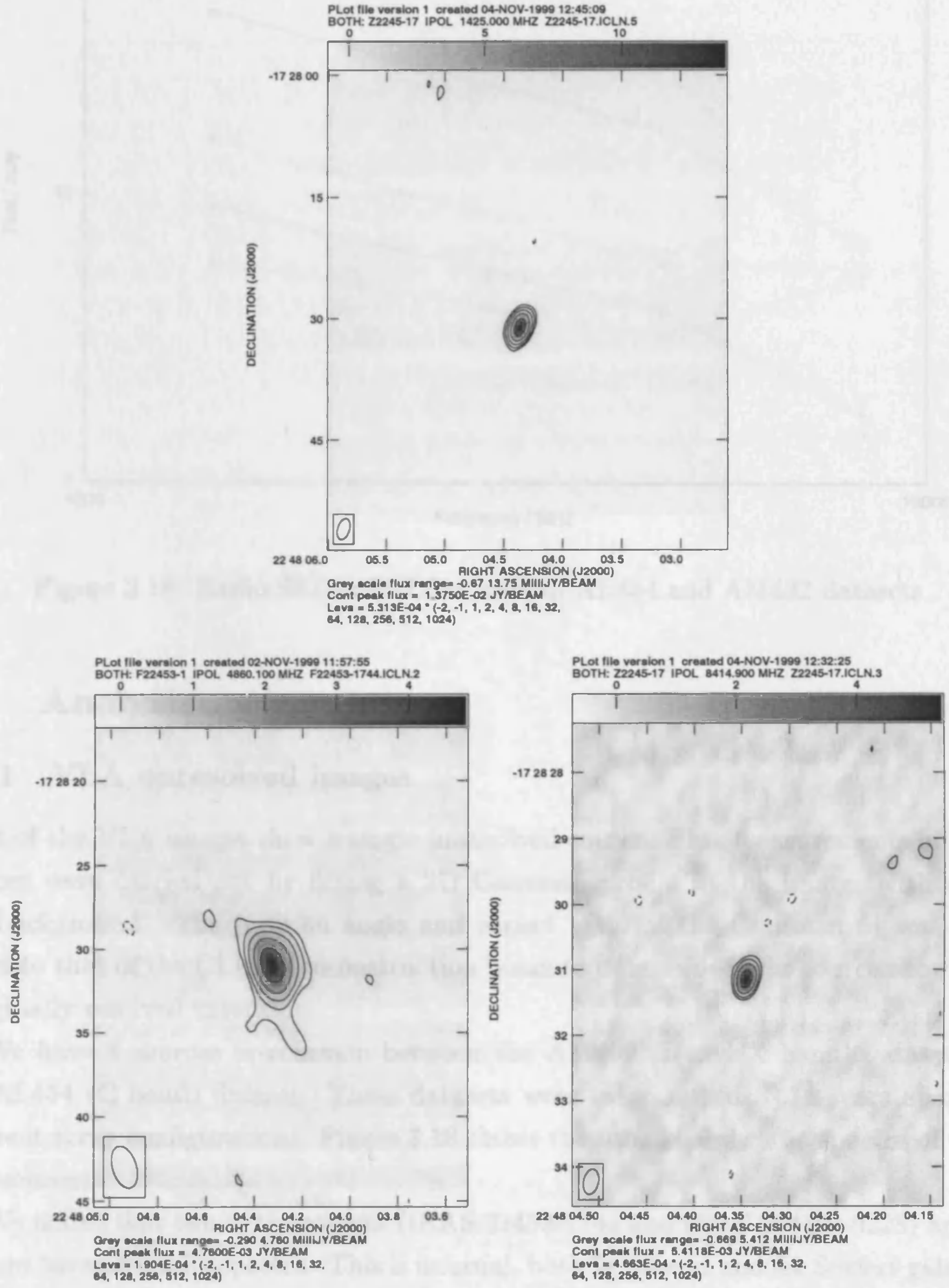

Figure 3.17: IRAS 22453-1744 L, C and X band images from AM492 (L,X) amd AL454(C)

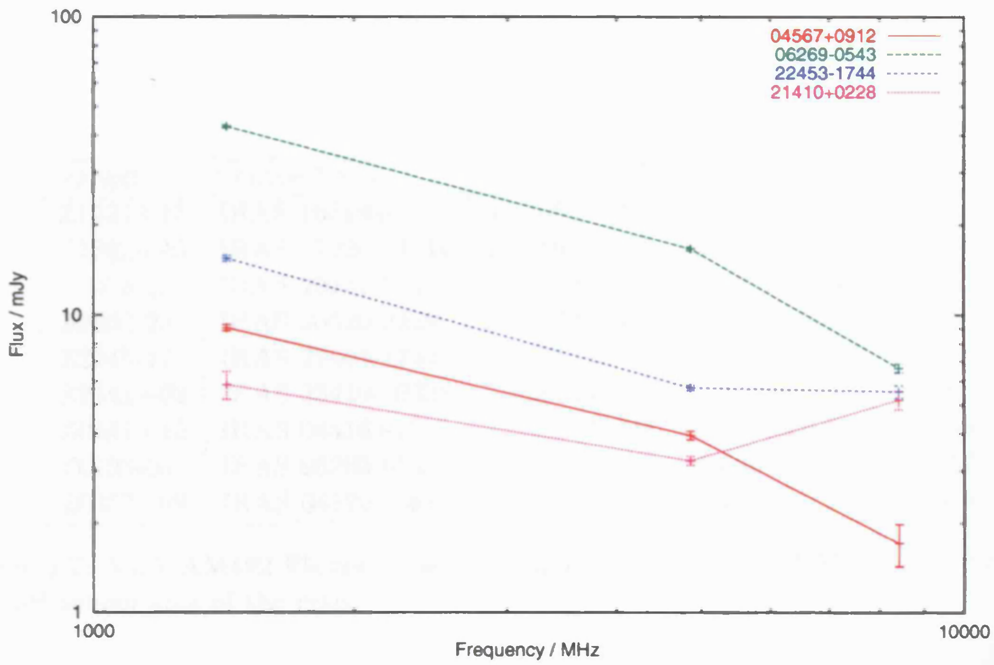

Figure 3.18: Radio SEDs of NLS1s in both AL454 and AM492 datasets

3.6 Analysis

3.6.1 VLA unresolved images

Most of the VLA images show a single unresolved source. Flux measurements of these sources were carried out by fitting a 2D Gaussian profile to the image, with a flat sky background. The position angle and aspect ratio of the Gaussian fit was compared to that of the CLEAN reconstruction beam to determine if the source shows any marginally resolved extension.

We have 4 sources in common between the AM492 (L and X band) dataset and the AL454 (C band) dataset. These datasets were taken approx 3.14 years apart, in different array configurations. Figure 3.18 shows the broad band radio spectra of these four sources.

We notice that two of the sources (IRAS 22453-1744 and IRAS 21410+0228) appear to show inverted radio spectra. This is unusual, both in general and for Seyfert galaxies. As mentioned earlier, we cannot be sure whether the spectra really are inverted, or whether the source has varied inbetween the observations, though we also note that radio variability of this magnitude is unusual in Seyfert galaxies.

Target	Source Name	L Flux / mJy	X Flux / mJy	α_X^L
Z1631+47	IRAS 16319+4725	66.165±0.312	25.138±0.118	0.544
Z1702+45	IRAS 17020+4544	110.86±0.375	21.364±0.118	0.926
Z2018-22	IRAS 20181-2244	29.879±0.459	3.4377±0.105	1.216
Z2052-23	IRAS 20520-2329	5.1726±0.341	2.0885±0.529	0.510
Z2245-17	IRAS 22453-1744	15.521±0.333	5.5518±0.270	0.578
Z2341+02	IRAS 23410+0228	5.8381±0.624	5.1936±0.375	0.066
Z0441+12	IRAS 04416+1215	13.385±0.248	2.4330±0.182	0.959
Z0626-05	IRAS 06269-0543	43.060±0.532	6.6569±0.223	1.057
Z0457+09	IRAS 04576+0912	9.0627±0.213	1.7136±0.281	0.936

Table 3.2: VLA AM492 Fluxes. The error figures are from the RMS noise / beam in the off source area of the map.

Target	Source Name	C Flux / mJy
ARK564		11.316±0.205
F22453	IRAS 22453-1744	5.7156±0.125
UCM2257	UCM 2257+2438	1.6031±0.133
MRK1126		2.1970±0.152
F23410	IRAS 23410+0228	3.2515±0.115
MRK957		3.8308±0.224
I Zw 1		2.5111±0.117
MRK359		4.2594±0.081
F04576	IRAS 04576+0912	3.9512±0.132
F06269	IRAS 06269-0543	16.728±0.260

Table 3.3: VLA AL454 Fluxes. The error figures are from the RMS noise / beam in the off source area of the map.

3.6.2 MERLIN images - Mkn 766

Hirst et al. (1998) note that the NLS1 Mkn 766 had been observed with MERLIN by Thean et al as part of a MERLIN study of the Extended 12μm sample (Thean et al. 2000). The map from this data (reduced data kindly provided by Thean et al, figure 3.19) shows a curved feature, reminiscent of a bent jet. As an initial result, this suggests that Mkn 766 *is* oriented face on to our line of sight, and supports the NLS1 "pole-on" hypothesis. A VLA X band (8.4GHz) image (figure 3.20) shows an extended feature at the same position angle as the outer segment of the MERLIN jet.

3.6.3 New MERLIN data

We have successfully obtained MERLIN observing time to observe NLS1s, the observations have been carried out, though we have come across several problems during the data reduction. The problems arise from the fact that in broad band mode (15 channels, each 1 MHz wide), with all the channels averaged together before mapping, as is common practice for radio continuum observations, the mappable field of view is often smaller than the positional accuracy to which the source positions are known. The observations were planned using the best available co-ordinates from the literature, though these do not appear to have been accurate enough.

However, we have recently obtained VLA observations of some of the MERLIN targets. These observations have a sufficiently wide field of view to find the target, and sufficient resolution to get sufficiently accurate co-ordinates, though insufficient resolution to show any structure. Once we have obtained accurate (VLA) co-ordinates for our MERLIN observed objects, we will attempt to re-map the existing MERLIN data, carrying out the mapping process for each channel individually, then averaging together the final maps. The narrower bandwidth of the separate channels should allow us to map sufficiently far from the phase centre of the observations to map our targets, and hopefully resolve structure in them. At the time of writing our VLA proposals have been allocated time, though are yet to be carried out. It is not practical to map the entire MERLIN field in each separate channel, simply due to the amount of compute time required to do this on the available computing facilities.

We have successfully mapped Mkn 1239 from this data - figure 3.21 shows the map. We note the double, and tentative triple, structure resolved in this source, again indicative of jet activity in the radio source.

3.6.4 Structure and polarisation angles

Hirst, Law-Green & Ward (1998) present a diagram (figure 3.22) showing a plot of radio power vs optical continuum polarisation for a sample of NLS1s. Though the statistics

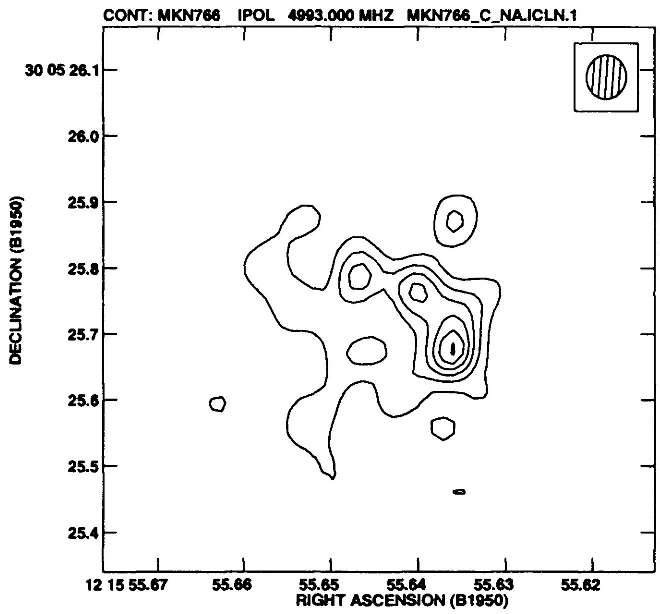

Figure 3.19: MERLIN Mkn 766 C band map from Thean et al

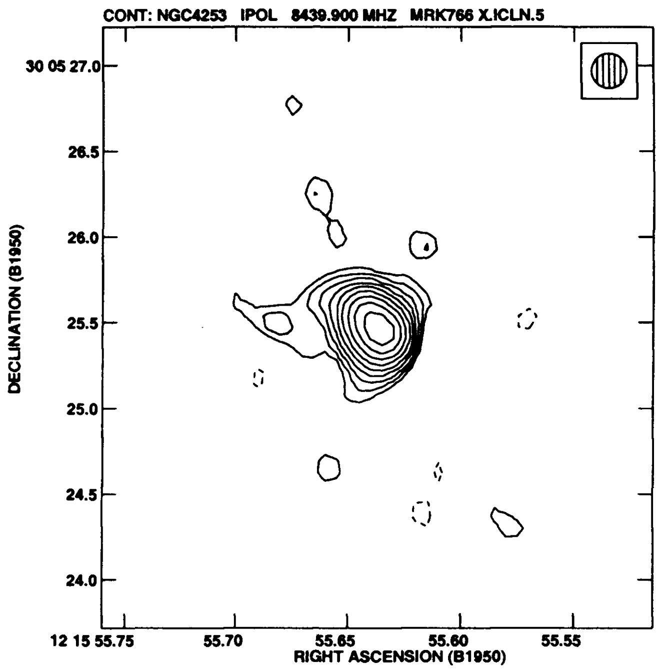

Figure 3.20: VLA Mkn 766 X band map

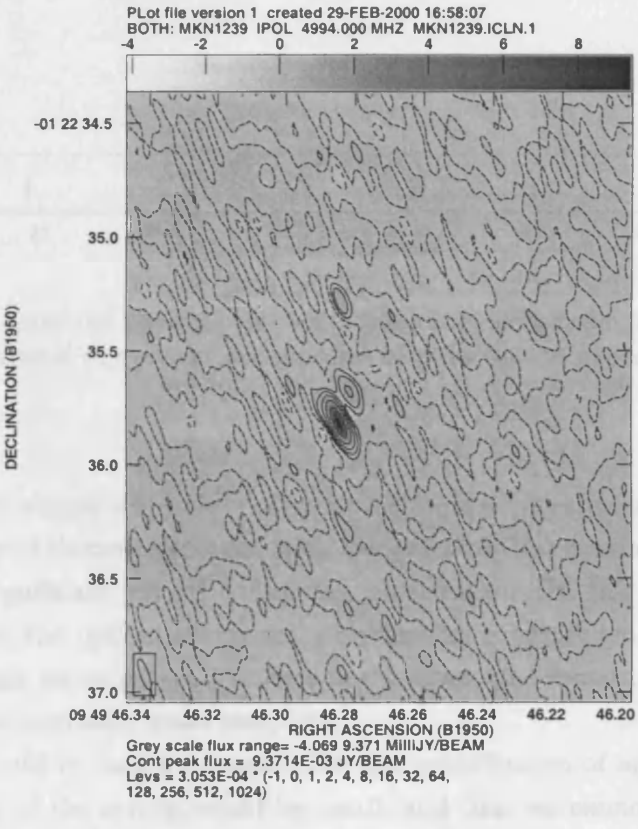

Figure 3.21: MERLIN Mkn 1239 C band map

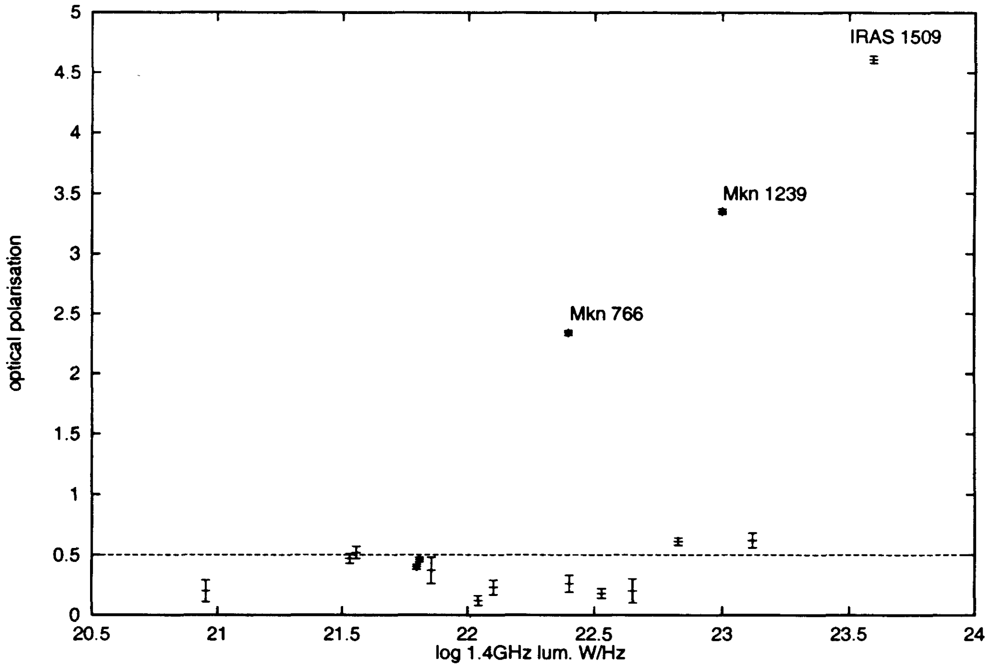

Figure 3.22: Line corrected optical continuum polarisation vs radio power for an NLS1 sample. The horizontal line marks the amount of polarisation expected from galactic dust.

are obviously poor, simply due to a small sample size, it would appear that we can split the NLS1s into two sub samples, those with low or no optical continuum polarisation, and those with significant optical continuum polarisation. In this latter group, our data suggests that the optical continuum polarisation is correlated with the 1.4GHz radio power, though we only have 3 sources in this class, and remain very suspicious of conclusions drawn from such small samples.

This result is odd in that we assume that the contribution of any jet to the total optical continuum of the source would be small, and thus we cannot invoke beaming to explain the polarisation. This would imply that scattering would be the dominant polarising factor for the optical continuum, and thus that the radio stronger objects are those with more scattering in their optical line of sights. This does not appear to be consistent with orientation based schemes invoking scattering by the edge of the obscuring torus and radio Doppler boosting.

We note that Mkn 766, whose bent jet feature has been previously noted (section 3.6.2), is one of the high polarisation sources, suggesting that the jet may have some role in, or share some common cause with, the optical polarising mechanism.

Also, Mkn 1239, another of the high polarisation objects, reveals a multi-component structure (figure 3.21) in the MERLIN image.

3.6.5 Variability

We have a suggestion of radio variability in two of our sources. The 1.4GHz flux of IRAS 13349+2438 reported by Beichman et al. (1986) is 2.8±0.5 mJy, compared to later values of 20.1 mJy in NVSS (Condon et al. 1998) and 19.02 mJy in FIRST (Becker et al. 1995). We treat this result with a certain amount of scepticism in that the data points come from different array configurations, and so sample emission over different spatial frequencies in the object, should it be partially resolved by one of the configurations. Though we suspect that this is not an issue, and the NVSS (D array) and FIRST (B array) values, taken at similar epochs, are similar, suggesting that the source is not resolved out in B array as compared to D array. We are in the process of re-analysing the archival data of these observations to check, in particular, the flux calibration of the Beichman et al. (1986) point, and to search for other possible anomalies with the data.

In addition, IRAS 17020+4544 is reported in 87GB (Gregory & Condon 1991) to be 26 mJy at 1.4GHz, yet is detected by NVSS (Condon et al. 1998) as 121.8 mJy. This could be a case of a confusing source being present in the NVSS D array beam.

Siebert et al. (1999) also note apparent radio variability in an NLS1, RGB J0044+193. This source was detected with a flux of 24 mJy in the 87GB survey (Gregory & Condon 1991), though higher resolution followup observations with the VLA, also at 4.85GHz show a flux of only 7 mJy (Laurent-Muehleisen et al. 1997). Though this could be due to the longer VLA baselines resolving out some extended flux, this seems unlikely as the VLA map shows an unresolved point source, indicating that the source is most likely variable. In addition, the source was not detected in the NRAO VLA Sky Survey (NVSS) (Condon et al. 1998), sensitive to 2.5 mJy at 1.4GHz. A 'normal' steep spectrum would mean that the 1.4GHz flux should have been greater than 7 mJy, and thus easily detectable in the NVSS. This implies either that the source is strongly variable, and / or that it has an inverted spectrum between 1.4GHz and 4.85GHz, possibly due to synchrotron self absorption. Alternatively, if this source is very compact, interstellar scintillation could be responsible for this apparent variability.

Radio variability of this scale in Seyfert galaxies is very unusual, and thus if confirmed, this result would bring out another waveband in which the NLS1s have unusual, and so far yet to be explained, properties.

3.7 Discussion and future work

From the analysis so far, we cannot say that our radio data supports the pole-on model as a general explanation of NLS1s. It does, however appear, that some pole-on oriented Sy type AGN may take on some or all of the properties that have come to define the

NLS1 class.

Our future work in mapping our high resolution MERLIN data of NLS1s will hopefully shed more light on the orientation issue, especially when compared with the results of Thean et al. (2000) whose comparable data on the CfA sample should provide an excellent comparison sample for this work. We also hope to significantly expand the statistics in the study of the alignment between the radio position angle and the optical polarisation angle found by Ulvestad et al. (1995). If the finding that the NLS1s show these two axes to be perpendicular holds, then we can make significant deductions about the orientation based unified scheme and / or the origin of the optical polarisation.

We also aim to combine the MERLIN and VLA UV datasets where we have raw data for the same targets, this will allow us to trace small scale (MERLIN resolution) structure into any extended (VLA resolution) regions of the source.

As is often the case, this initial work has been plagued by poor statistics due to small sample sizes. We hope to improve this situation when we receive and analyse the next batch of VLA data, thus enabling us to make use of our MERLIN observations.

It would also appear to be useful to fully investigate the radio variability of the NLS1s. It would be reasonably simple to propose VLA re-observations of a sample of NLS1s, and perhaps also BLS1s to act as a comparison sample, selecting previously detected objects, and observing in the same frequency bands and array configurations, so as to eliminate spectral and spatial resolution uncertainties. Care would have to be taken in this study that a viable BLS1 comparison sample really is available in the literature, or observations proposed; this is another field where surprisingly little has been published.

Chapter 4

Near IR imaging of NLS1s

4.1 Motivation and Aims

A currently popular model of NLS1s, initiated mainly from X-Ray observations, suggests that the NLS1 phenomenon arises in objects which are accreting on to a relatively low mass black hole, with an accretion rate close to the Eddington rate. If the accretion rate is actually higher than in most "normal" BLS1s, then we might expect to see morphological signatures of matter transport in the host galaxy, for example, a higher prominence of bars.

In addition, NIR imaging of the NLS1 hosts allows us to compare NLS1 and BLS1 host galaxies for systematic differences in for example dust distributions or starburst activity, which might shed light on the NLS1 phenomenon.

4.2 Instrumentation

This project centred around the new UKIRT Fast Track Imager (UFTI). As UFTI is a recent addition to the UKIRT instrumentation suite, it will be briefly reviewed here.

UFTI is a cooled 1–2.5μm imaging camera utilising a HAWAII 1 type 1024$\times$1024 HgCdTe detector array. It has a plate scale is 0.091 arc-sec per pixel, giving a detector field of view of 92 arc-sec, although the observing modes used with UFTI often use a jitter pattern to carry out sky subtraction and bad pixel elimination, thus in practice a larger field will be observed, though the actual exposure time, and thus the signal to noise ratio of the image, is lower towards the edge of the observed field.

The small pixel scale of UFTI was designed to utilise the excellent imaging available following the UKIRT upgrade program. Our observations were carried out commencing 1999 June 5, shortly *before* the installation of the latest UKIRT secondary mirror, and hence suffered from image degradation due to the known flaws in that mirror[1]. Another

[1]Primarily, print through from the light weighting holes milled into the back of the mirror, 5th order

potential source of image degradation that applies to the setup used for our observations is the mechanism by which the telescope is focussed. This involved taking a series of images of a star at different focus positions[2], then plotting the FWHM and peak count rate of the images against focus position to select the optimum setting. As pointed out by Hawarden (1999), this method of focusing is fundamentally flawed in that attempting to select the best position from a set of seeing degraded images means attempting to maximise a function whose value at maximum is independent of the parameter you can adjust. In effect, this method almost always results in mis focusing being the dominant optical misalignment within the telescope system. UKIRT has now been equipped with a near-real-time autofocussing system.

However, the UKIRT fast guider, and tip-tilt system were in use throughout these observations, along with primary mirror shape corrections being calculated from a lookup model based on telescope pointing.

4.3 Observations

The observations were carried out over 2 clear nights commencing 1996-June-05. Standard UFTI observing sequences were used. These involve generating sky flat field frames by moving the telescope in a jitter pattern inbetween exposures. The large field of view (90") of the UFTI array allows these movements to be sufficiently large that the object occupies a completely different area of the array detector in each frame. A sky flat is then generated by masking out the object from each frame, then averaging the resulting areas of blank sky with median filtering. Jitter patterns used involved 10 and 20 arc-sec 5 position mosaics, and moving the object between the four quadrants of the array. The standard star observations were made on a 512 pixel square sub array of the detector, using a 5 arc-second, 5 position jitter pattern.

4.4 Data Reduction

The Observatory Reduction And Control (ORAC) Data Reduction pipeline software was used to reduce the data, using the standard UFTI data reduction recipes, modified slightly to increase the sizes of the masks used to mask off the targets to generate flat fields, as it was found that the extended components of some the galaxies fell outside the default masked areas. The software also generates mosaics from the data. As the area surrounding the target in the centre of the mosaic appears in all the data frames,

trefoil, and some uncorrected 3rd order trefoil and 4th order spherical aberration, along with the fact that the mirror was manufactured with a turned down edge.

[2]On UKIRT, the focus is set by moving the secondary mirror along its z-axis. The secondary is supported on a hexapod.

but the areas at the edge of the mosaic only appear in a few of the data frames, the signal to noise ratio in the sky in the mosaics decreases towards the edge of the mosaic. None of our targets are extended over such a scale that this becomes an issue, though the effect is cosmetically noticeable in the images.

4.5 Results

Images and profiling results of the images are given here. The UFTI J, H and K images are presented with North upwards and East leftwards, and are 657 $\times$ 456 arcsec. Image profiling was carried out using the Starlink Extended Surface Photometry (ESP) software. Isophotal ellipses were fit to the galaxy images, at decreasing flux values and thus increasing semi-major ellipse radius, until the signal to noise ratio fell below a preset value. The semi-major axis radius, flux density, position angle and ellipticity of each isophotal ellipse are recorded, and are plotted in the results figures.

4.5.1 Mkn 766

J, H and K band images are given in figures 4.2 - 4.4. Profiling results are shown in figures 4.5 - 4.7.

Mkn 766 appears as an elliptical galaxy, with a characteristic, bright, point source at its centre. Profiling results show that the ellipticity is approx 0.45 (1=circle) in the galaxy at a position angle of around 75 degrees.

We also have An HST WFPC image of Mkn 766 retrieved from the HST public archive. The filter used equates roughly to V band, and the image is centred in the Planetary camera chip.

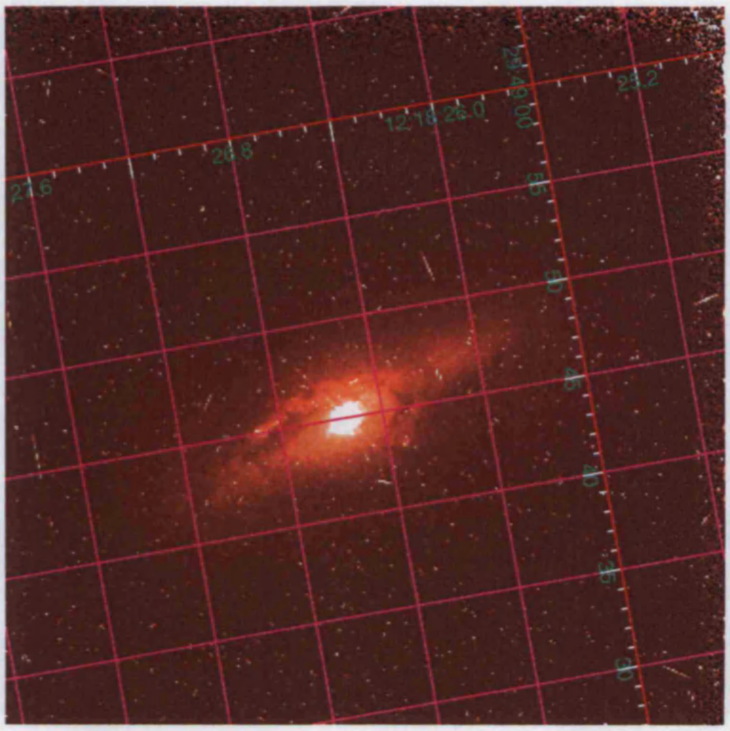

Figure 4.1: Mkn 766 from the HST Planetary Camera

Figure 4.2: Mkn 766 in J band

Figure 4.3: Mkn 766 in H band

Figure 4.4: Mkn 766 in K band

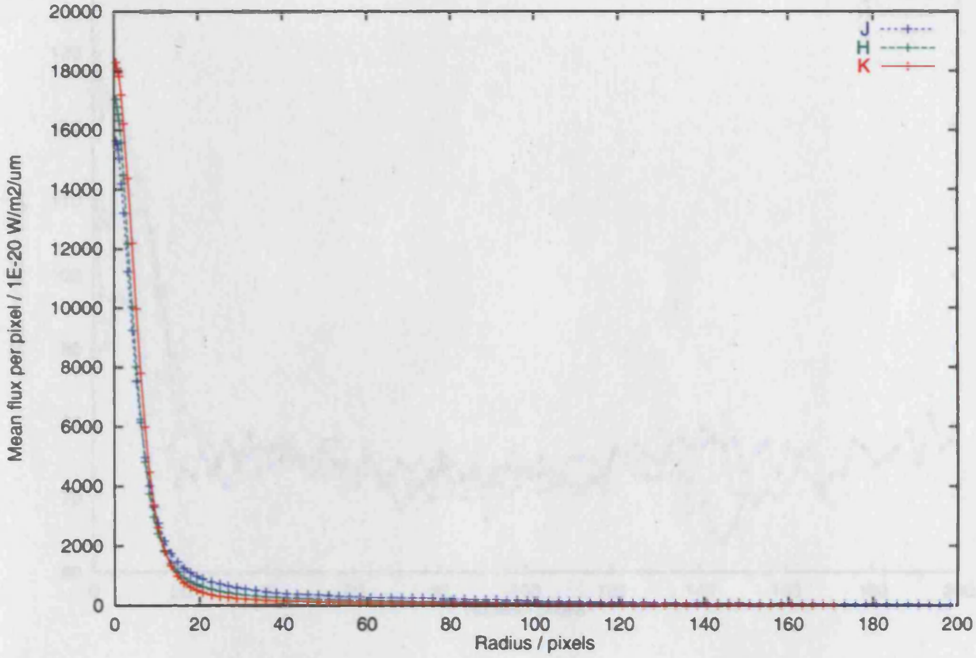

Figure 4.5: Mkn 766 profile results - flux

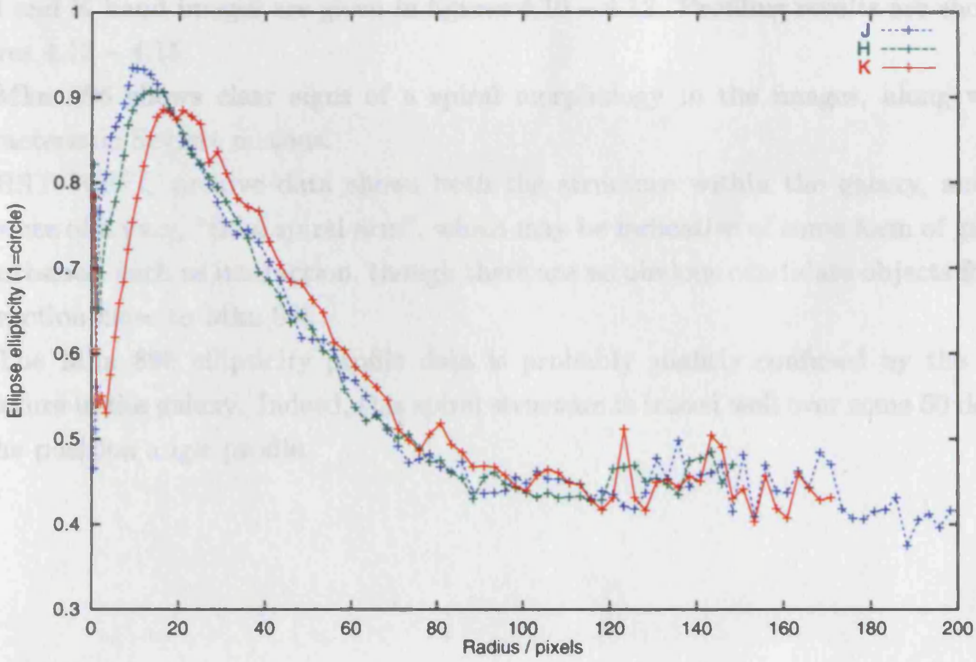

Figure 4.6: Mkn 766 profile results - ellipticity

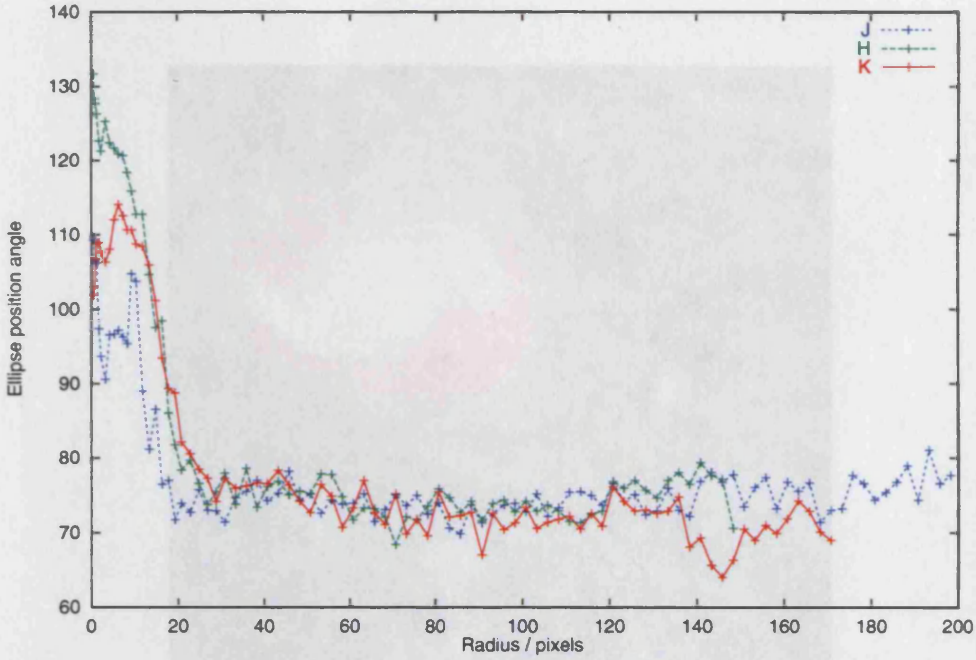

Figure 4.7: Mkn 766 profile results - position angle

4.5.2 Mkn 896

J, H and K band images are given in figures 4.10 – 4.12. Profiling results are shown in figures 4.13 – 4.15.

Mkn 896 shows clear signs of a spiral morphology in the images, along with a characteristic Seyfert nucleus.

HST WFPC archive data shows both the structure within the galaxy, and also evidence of a long, "tidal spiral arm", which may be indicative of some form of galactic disturbance, such as interaction, though there are no obvious candidate objects for this interaction close to Mkn 896.

The Mkn 896 ellipticity profile data is probably slightly confused by the spiral structure in the galaxy. Indeed, this spiral structure is traced well over some 50 degrees in the position angle profile.

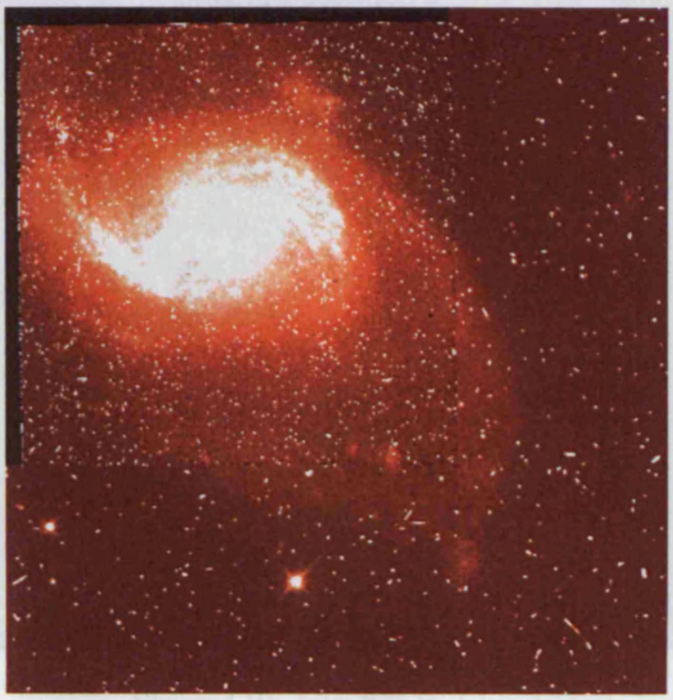

Figure 4.8: Mkn 896 in HST WFPC

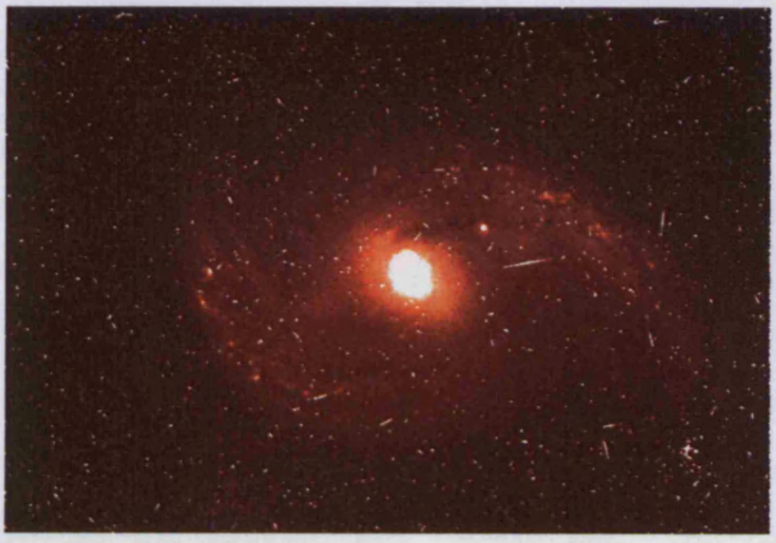

Figure 4.9: Mkn 896 in HST PC

Figure 4.10: Mkn 896 in J band

Figure 4.11: Mkn 896 in H band

Figure 4.12: Mkn 896 in K band

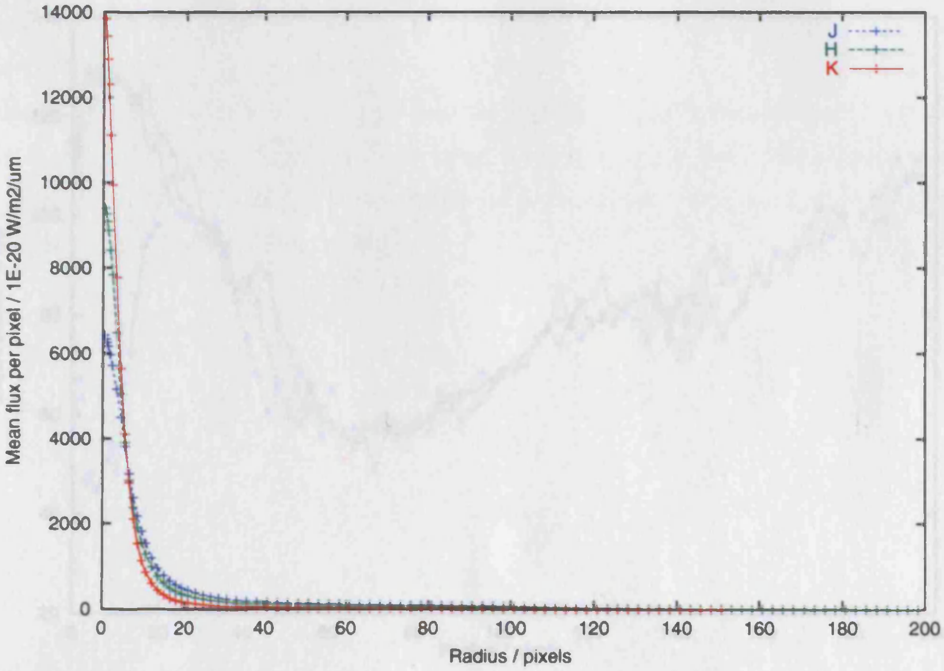

Figure 4.13: Mkn 896 profile results - flux

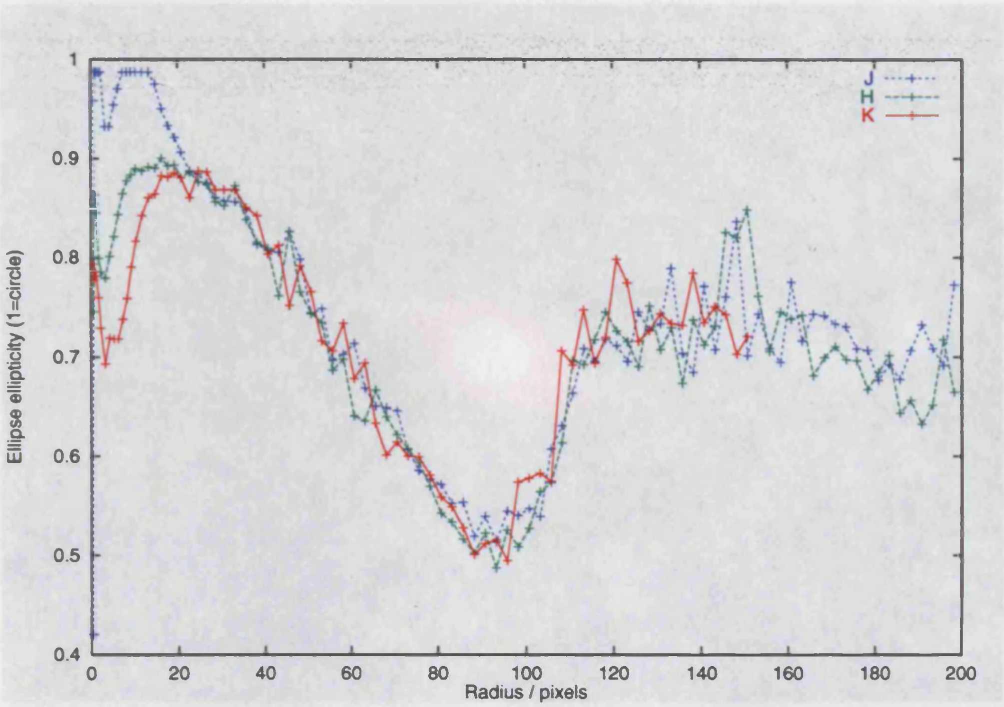

Figure 4.14: Mkn 896 profile results - ellipticity

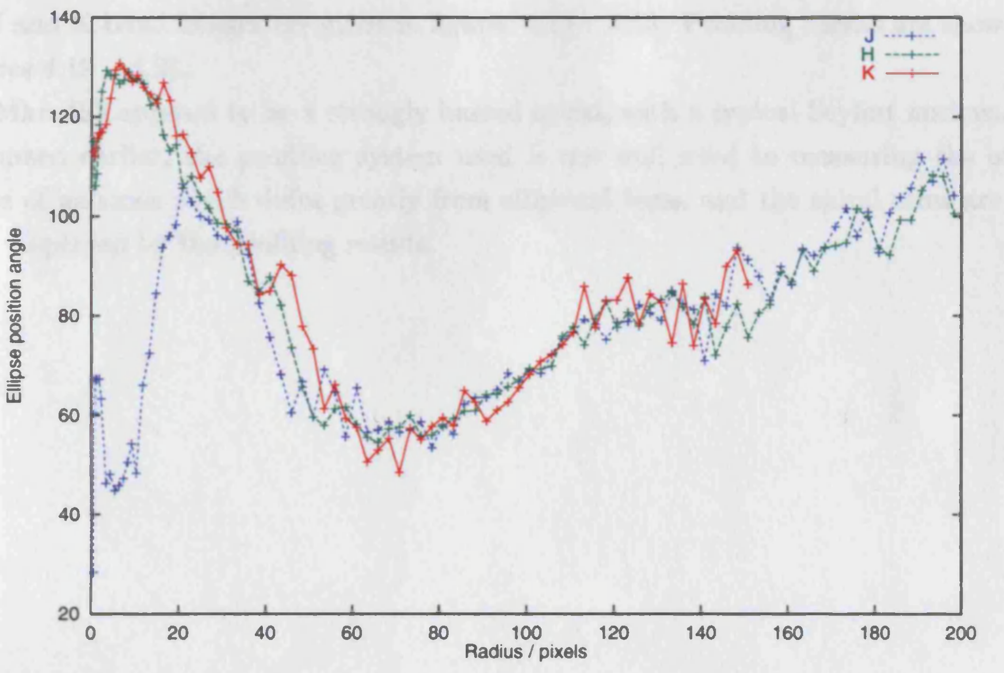

Figure 4.15: Mkn 896 profile results - position angle

Figure 4.16: Mkn 493 in J band

4.5.3 Mkn 493

J, H and K band images are given in figures 4.16 - 4.18. Profiling results are shown in figures 4.19 - 4.21.

Mkn 493 appears to be a strongly barred spiral, with a typical Seyfert nucleus. As discussed earlier, the profiling system used is not well sited to measuring the outer parts of galaxies which differ greatly from elliptical form, and the spiral arms are not well displayed by the profiling results.

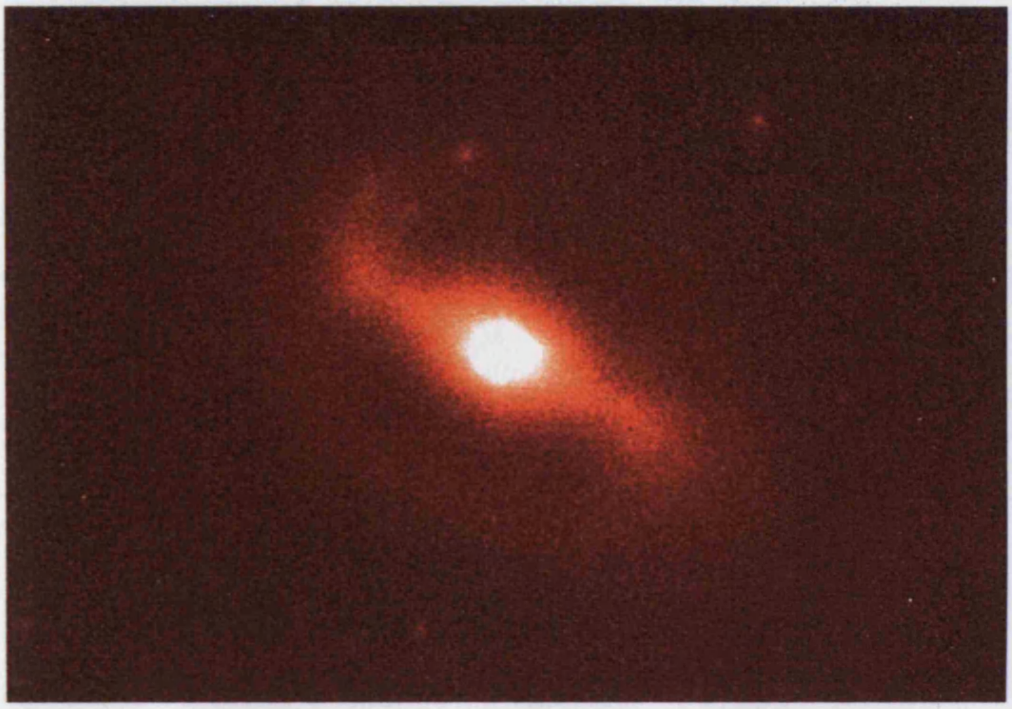

Figure 4.17: Mkn 493 in H band

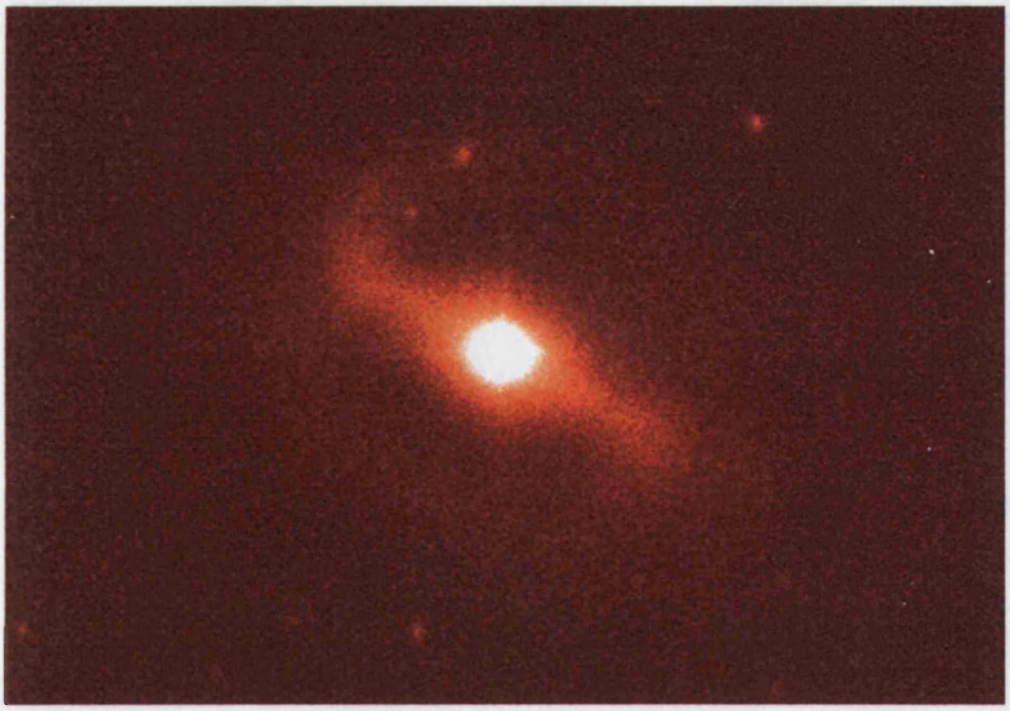

Figure 4.18: Mkn 493 in K band

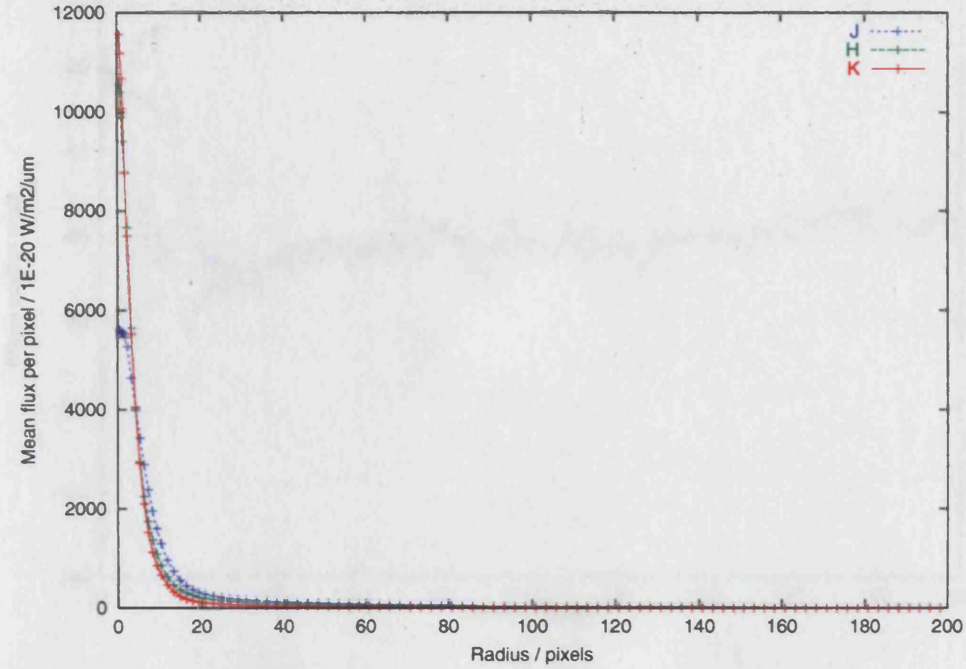

Figure 4.19: Mkn 493 profile results - flux

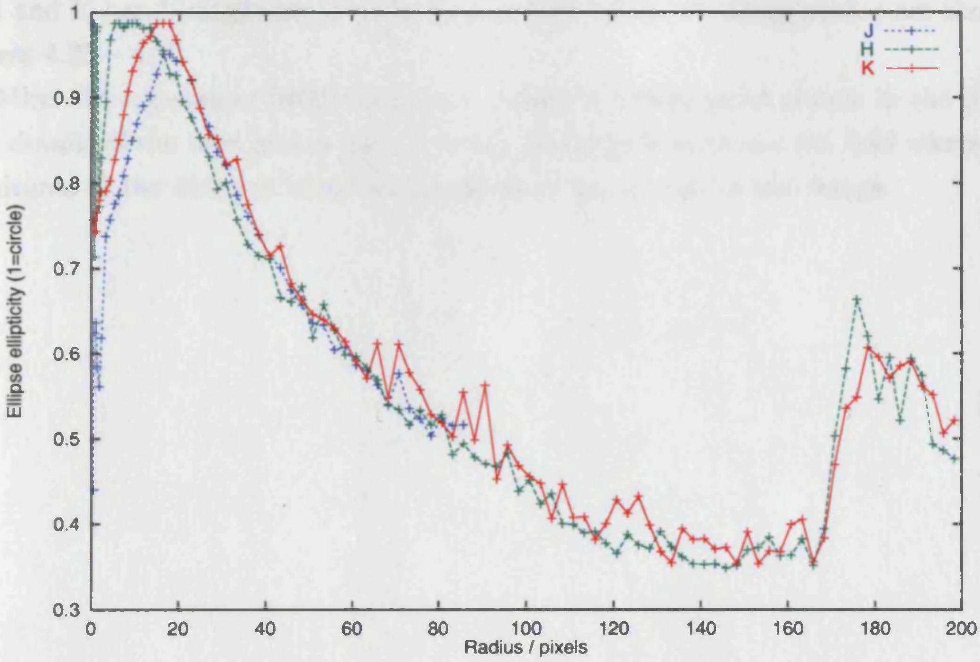

Figure 4.20: Mkn 493 profile results - ellipticity

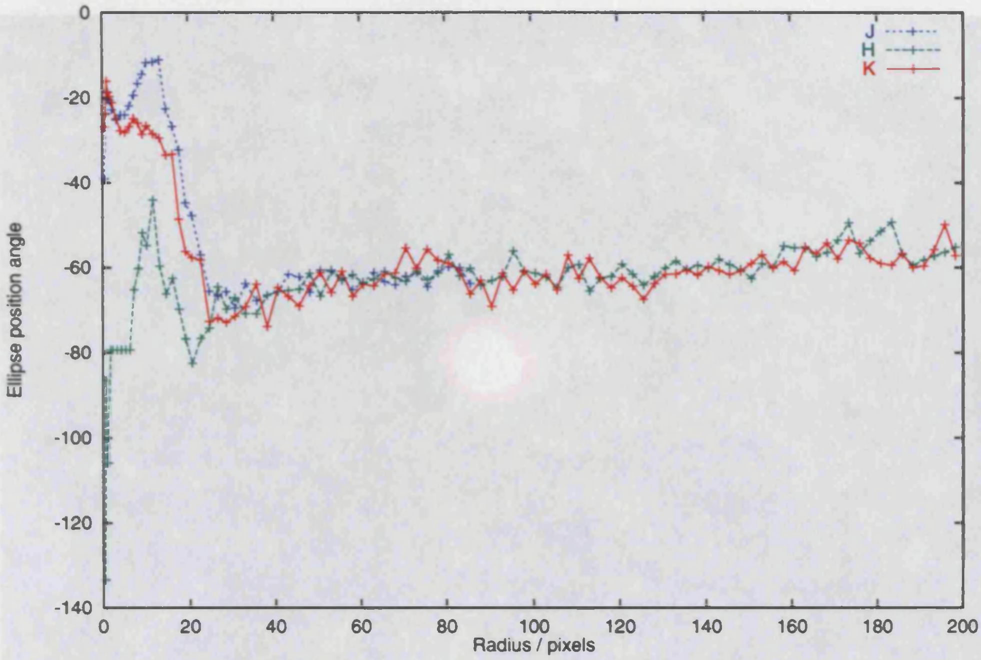

Figure 4.21: Mkn 493 profile results - position angle

4.5.4 Mkn 478

J, H and K band images are given in figures 4.22 – 4.24. Profiling results are shown in figures 4.25 – 4.27.

Mkn 478 appears as little more than a slightly diffuse point source in the images. Few details of the host galaxy are apparent. Slight defects in the flat field where the 4 quadrants of the detector array are joined show up slightly in this image.

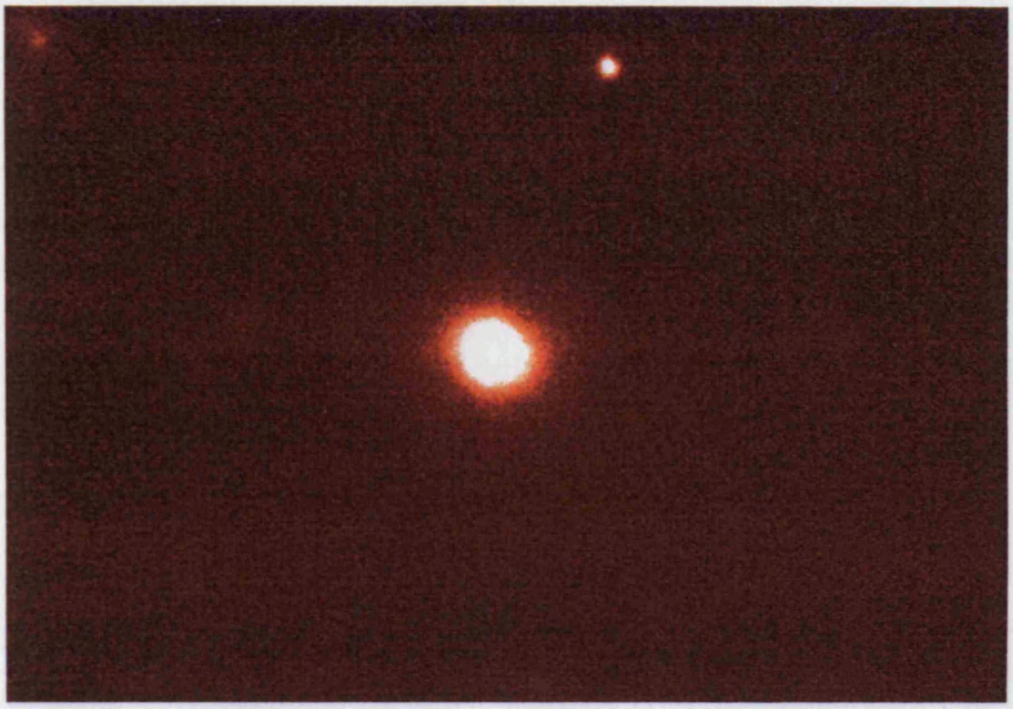

Figure 4.22: Mkn 478 in J band

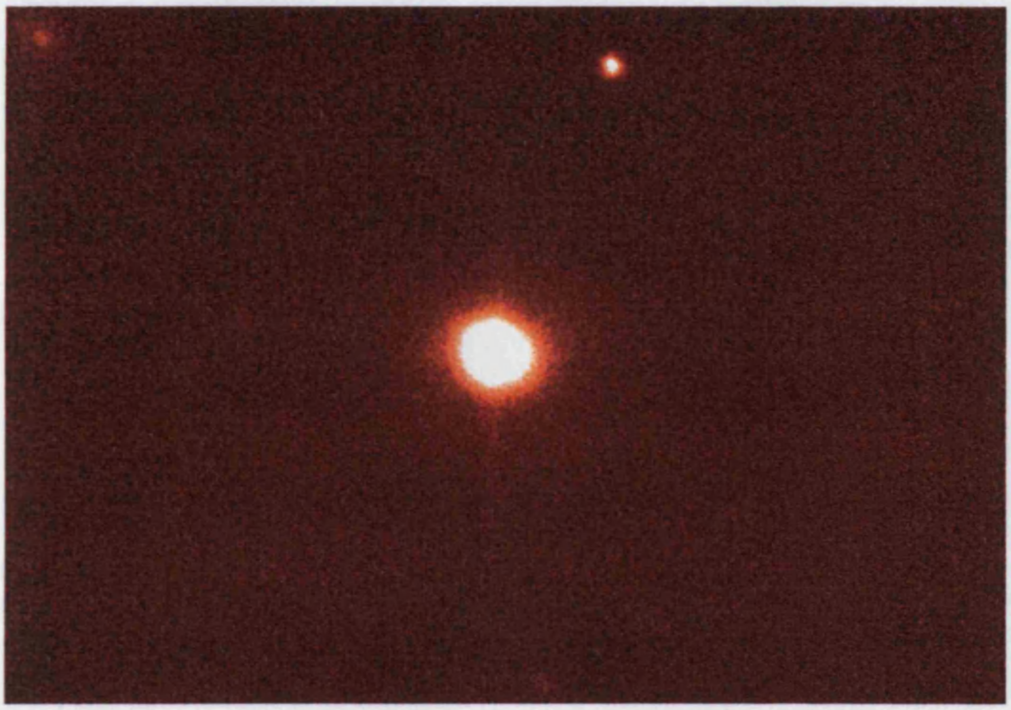

Figure 4.23: Mkn 478 in H band

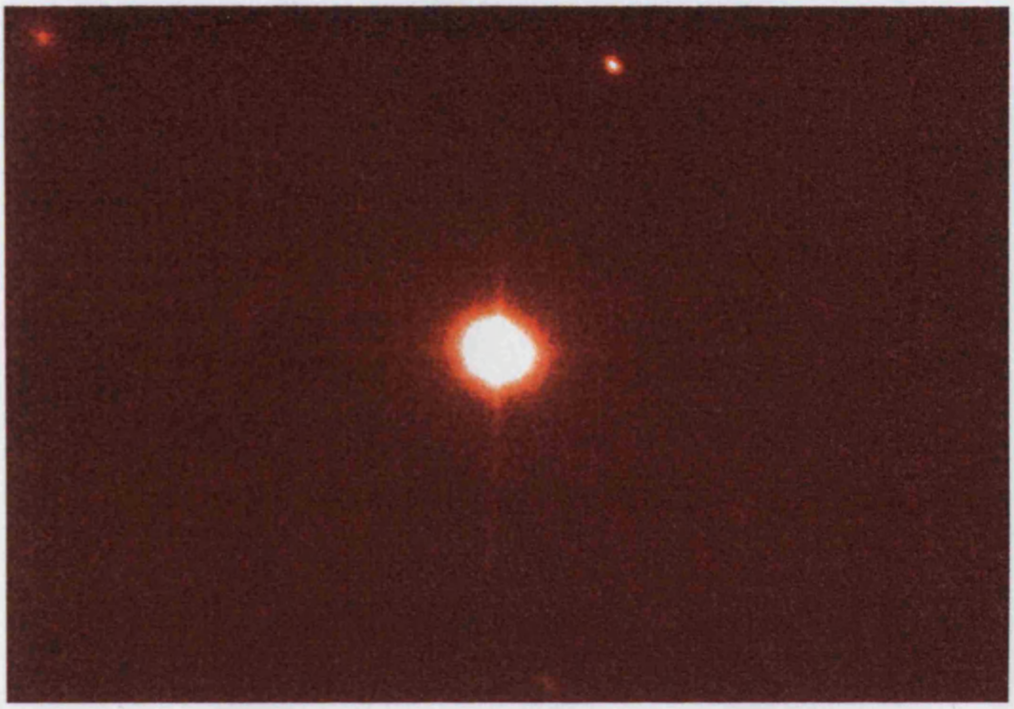

Figure 4.24: Mkn 478 in K band

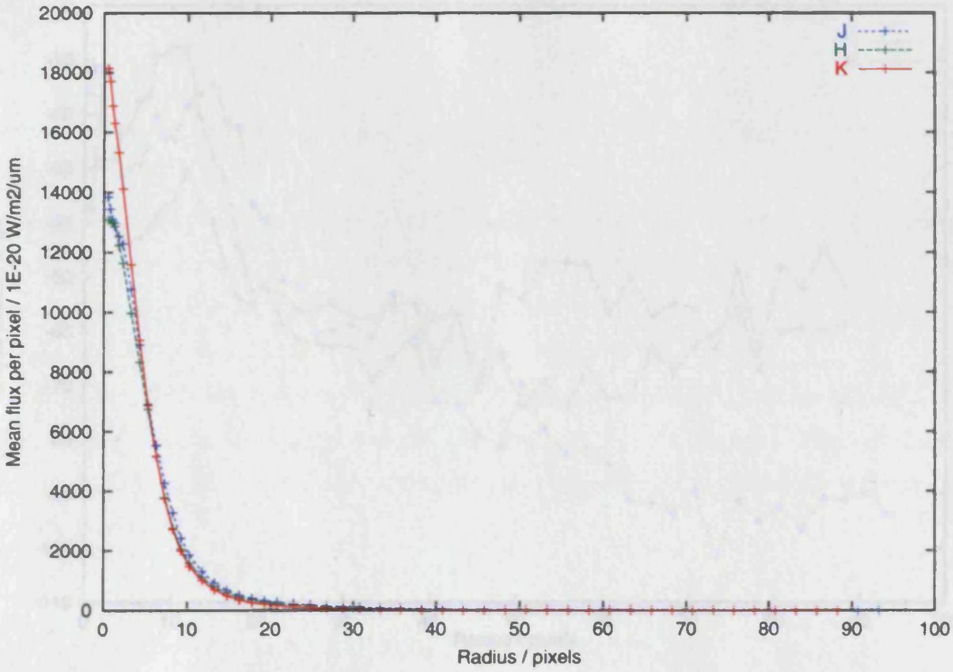

Figure 4.25: Mkn 478 profile results - flux

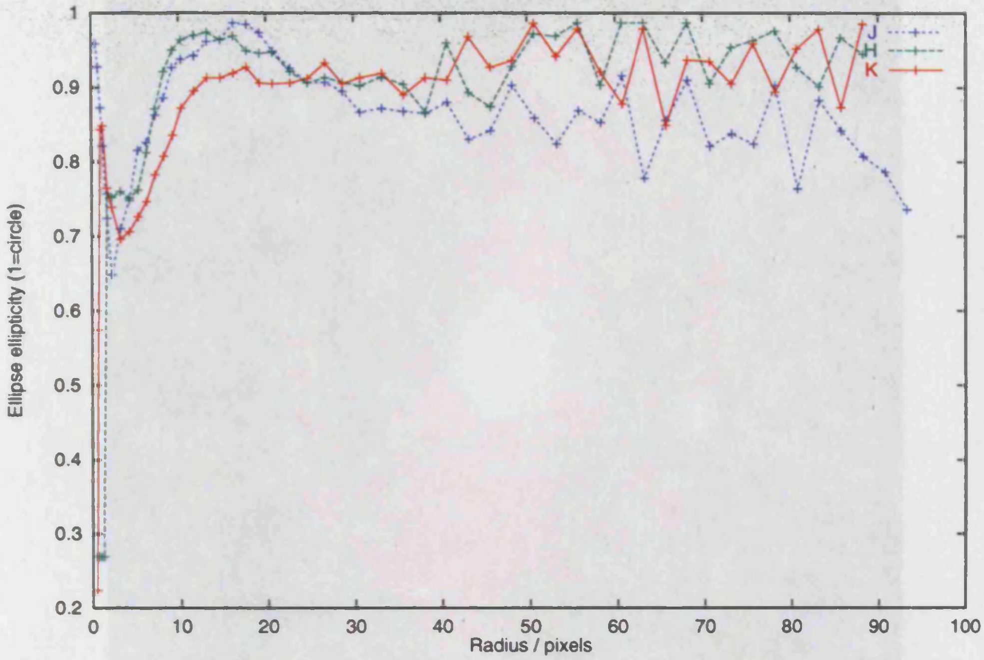

Figure 4.26: Mkn 478 profile results - ellipticity

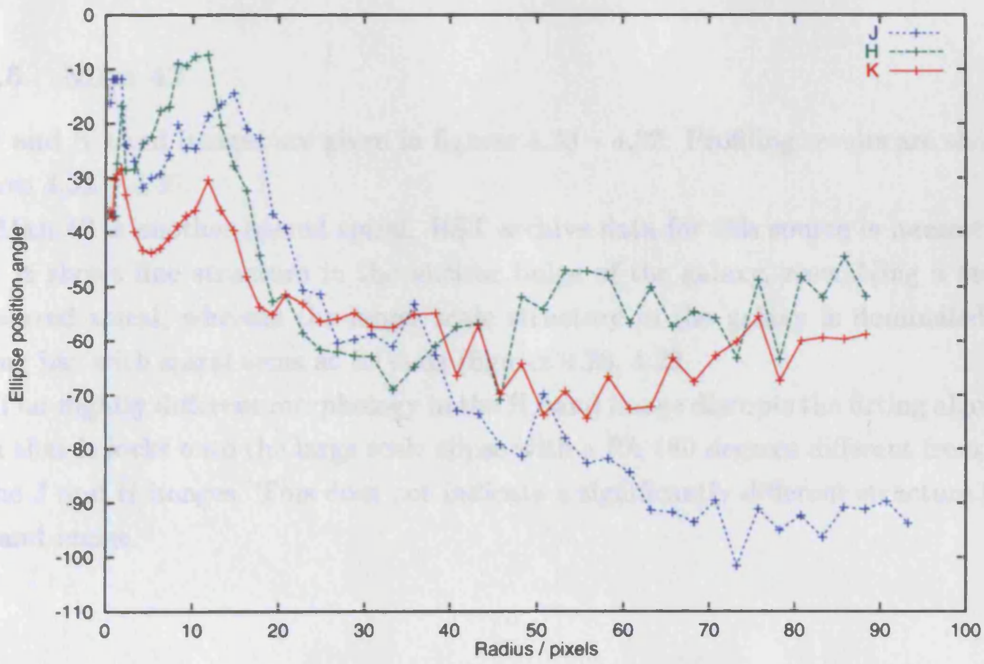

Figure 4.27: Mkn 478 profile results - position angle

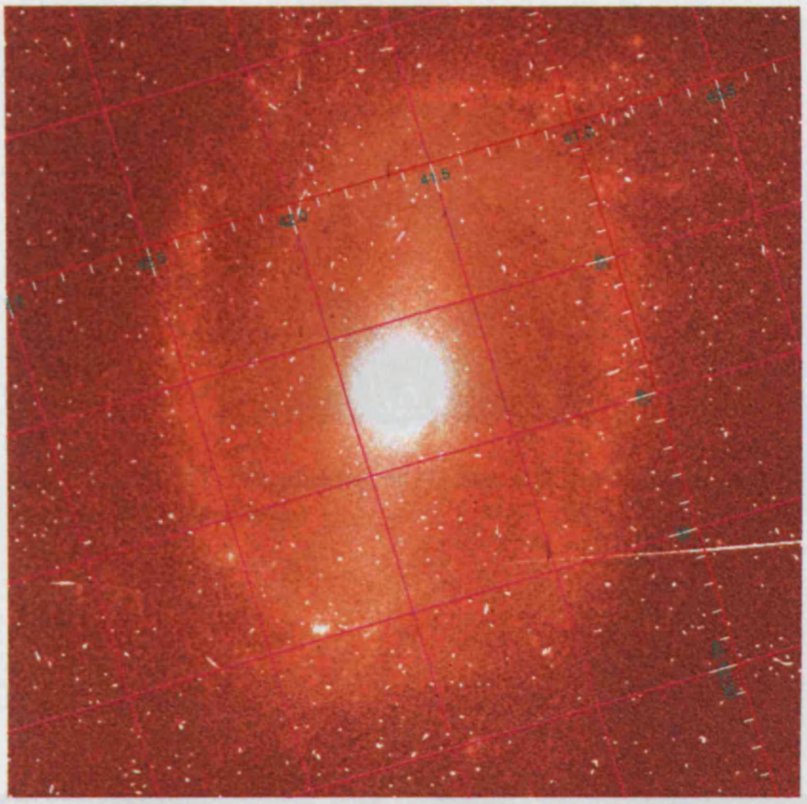

Figure 4.28: Mkn 42 in HST PC

4.5.5 Mkn 42

J, H and K band images are given in figures 4.30 - 4.32. Profiling results are shown in figures 4.33 - 4.35.

Mkn 42 is another barred spiral. HST archive data for this source is interesting in that it shows fine structure in the nuclear bulge of the galaxy, resembling a face on, un-barred spiral, whereas the larger scale structure in the galaxy is dominated by a strong bar with spiral arms at its ends (figures 4.28, 4.29.

The slightly different morphology in the K band image disrupts the fitting algorithm such that it locks onto the large scale elipse with a PA 180 degrees different from those of the J and H images. This does not indicate a significantly different structure in the K band image.

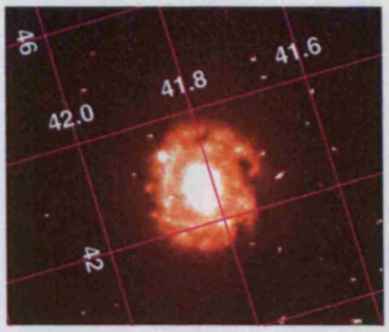

Figure 4.29: Mkn 42 in HST PC, closeup of circum nuclear structure. The numbers on the grid are in units of arc seconds.

Figure 4.30: Mkn 42 in J band

Figure 4.31: Mkn 42 in H band

Figure 4.32: Mkn 42 in K band

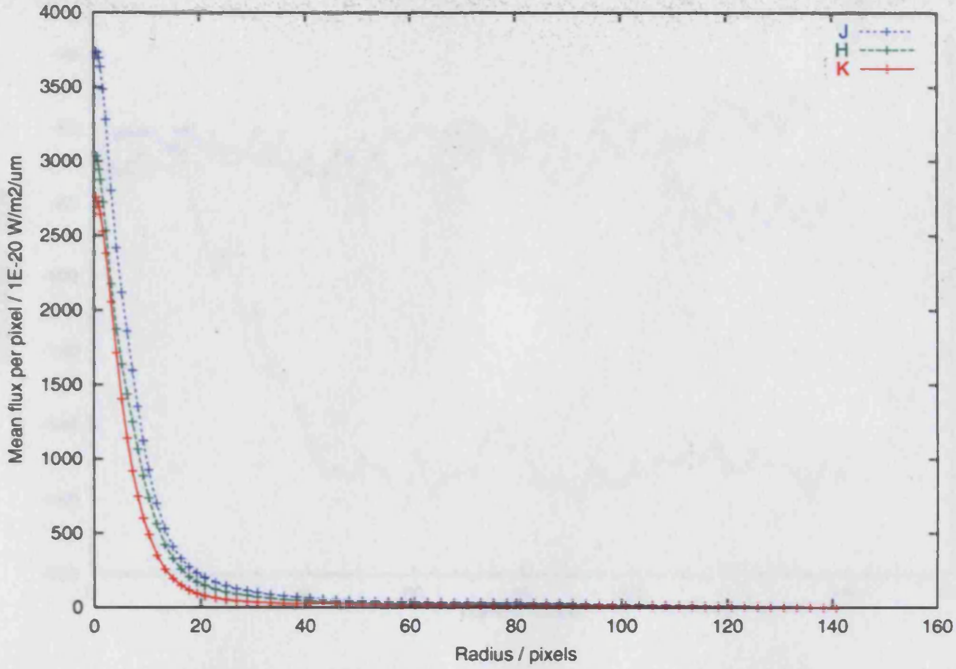

Figure 4.33: Mkn 42 profile results - flux

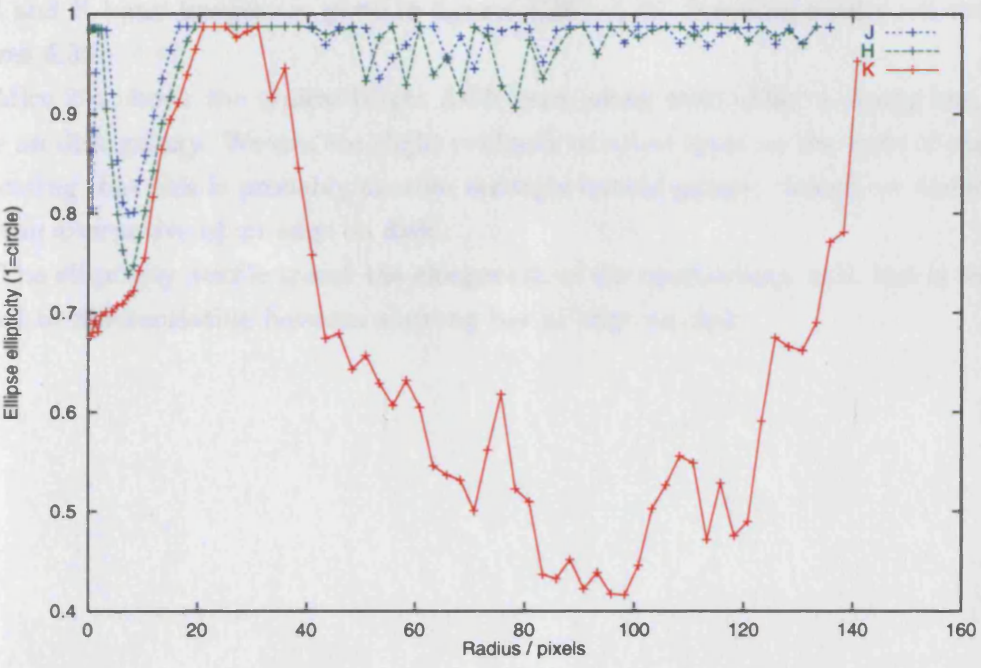

Figure 4.34: Mkn 42 profile results - ellipticity

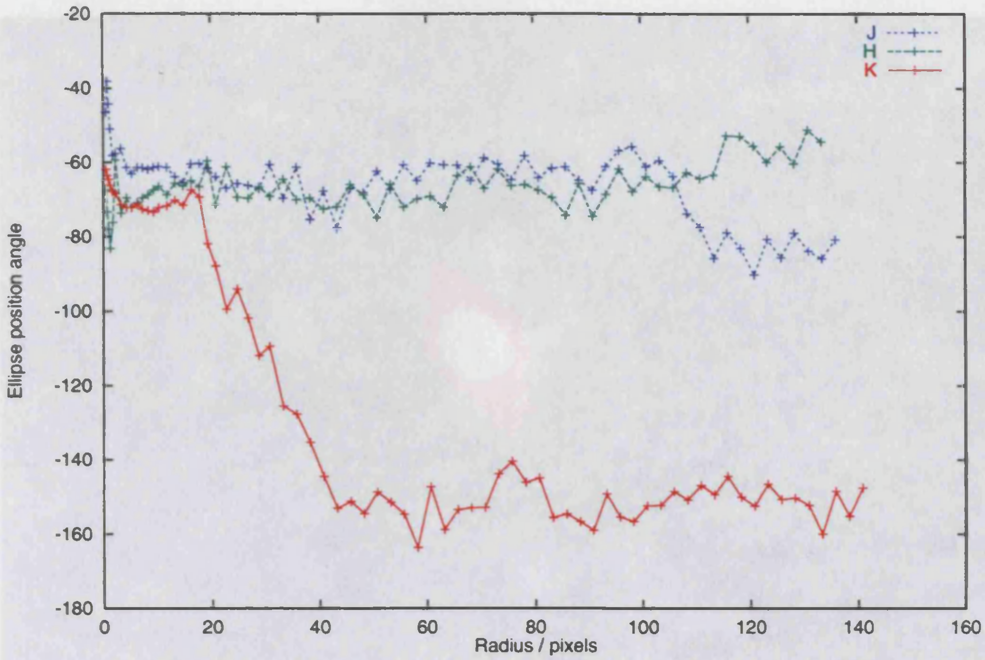

Figure 4.35: Mkn 42 profile results - position angle

4.5.6 Mkn 291

J, H and K band images are given in figures 4.36 – 4.38. Profiling results are shown in figures 4.39 – 4.41.

Mkn 291 shows the typical bright AGN core, along with either a strong bar, or an edge on disk galaxy. We can see slight evidence of spiral arms on the ends of the bars, indicating that this is probably another strongly barred galaxy, though we cannot rule out the alternative of an edge on disk..

The ellipticity profile traces the elongation of the morphology well, but is not well suited to differentiating between a strong bar or edge on disk.

Figure 4.36: Mkn 291 in J band

Figure 4.37: Mkn 291 in H band

Figure 4.38: Mkn 291 in K band

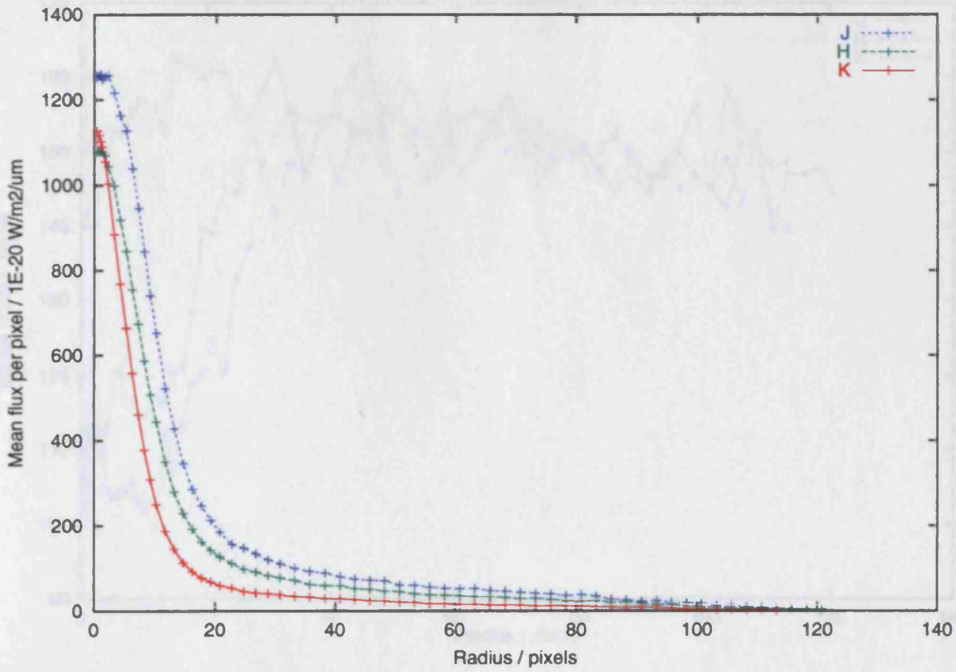

Figure 4.39: Mkn 291 profile results - flux

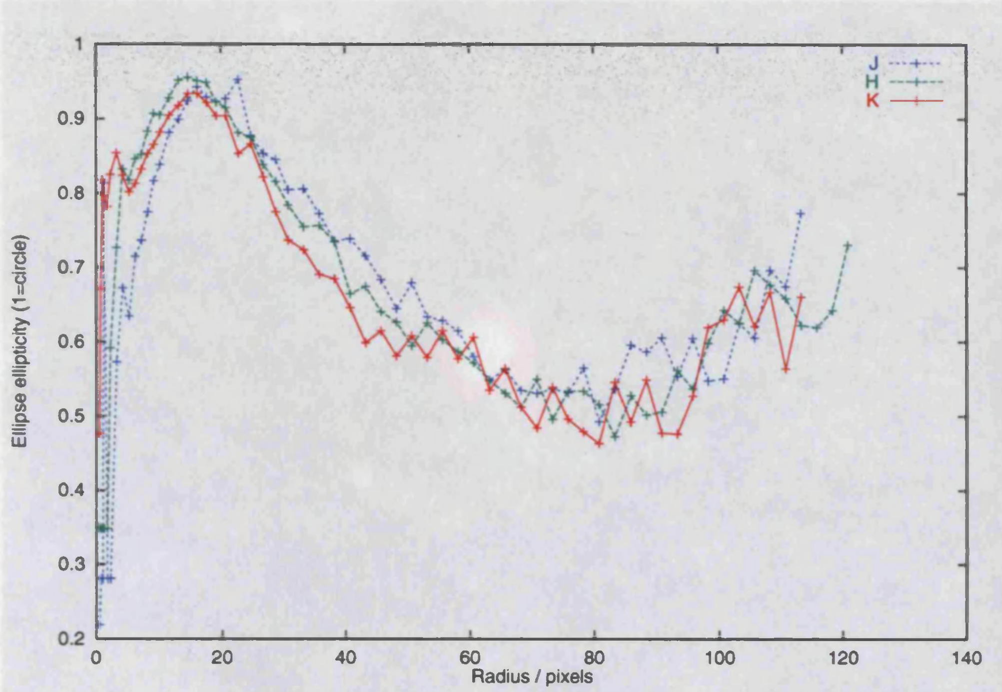

Figure 4.40: Mkn 291 profile results - ellipticity

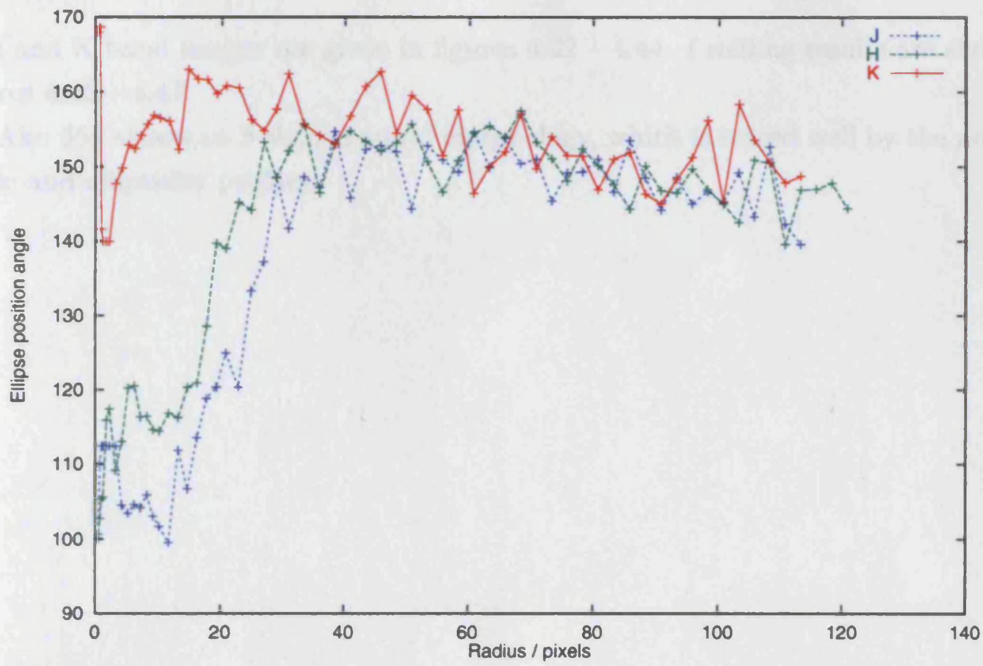

Figure 4.41: Mkn 291 profile results - position angle

Figure 4.42: Akn 564 in J band

4.5.7 Akn 564

J, H and K band images are given in figures 4.42 – 4.44. Profiling results are shown in figures 4.45 – 4.47.

Akn 564 shows an S shaped spiral morphology, which is traced well by the position angle and ellipticity profiles.

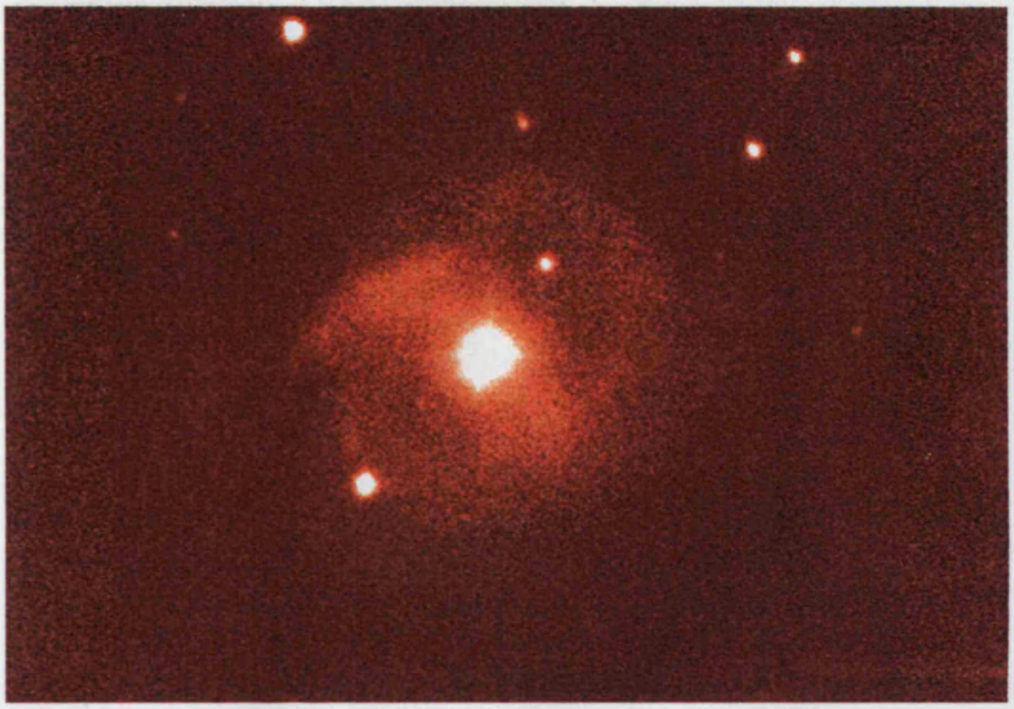

Figure 4.43: Akn 564 in H band

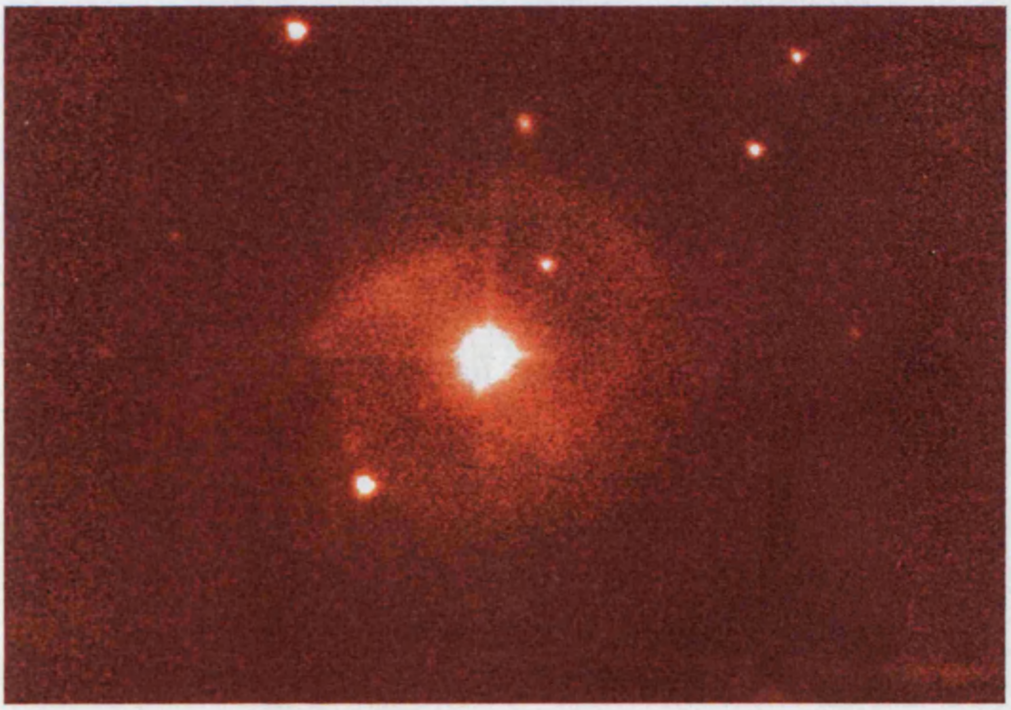

Figure 4.44: Akn 564 in K band

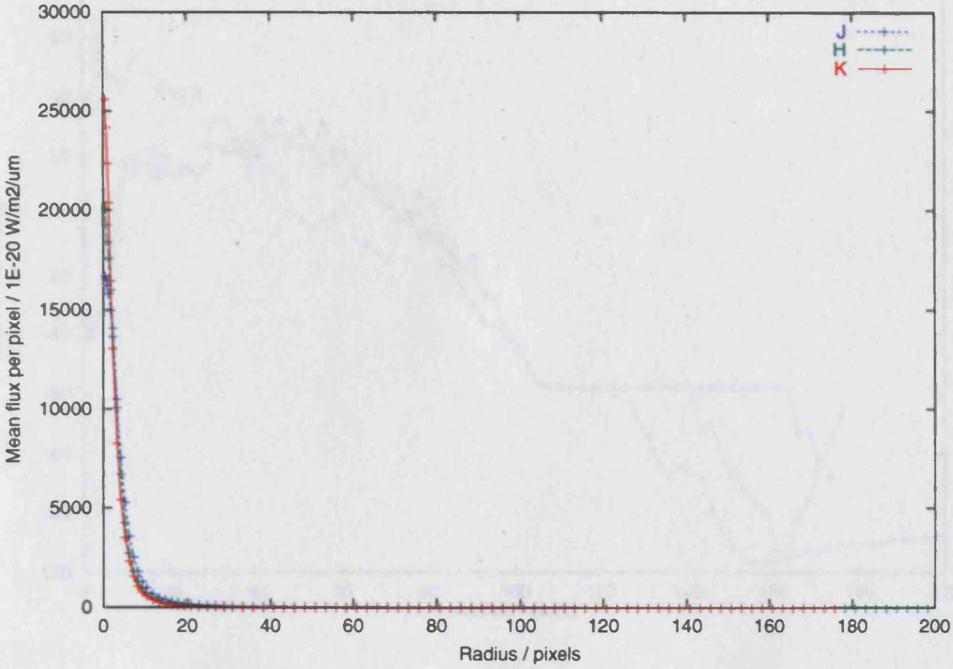

Figure 4.45: Akn 564 profile results - flux

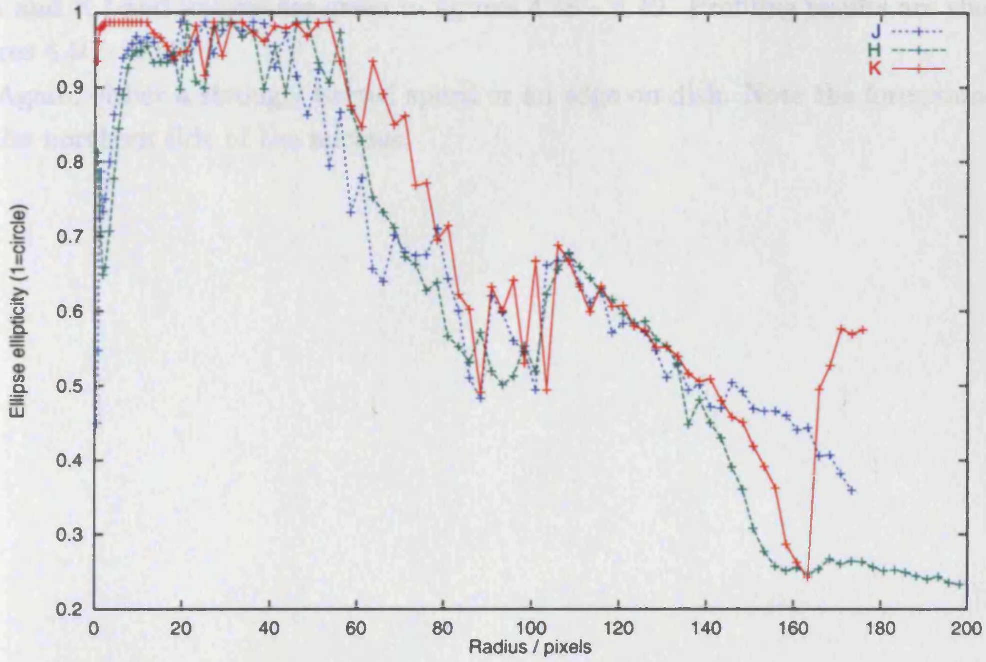

Figure 4.46: Akn 564 profile results - ellipticity

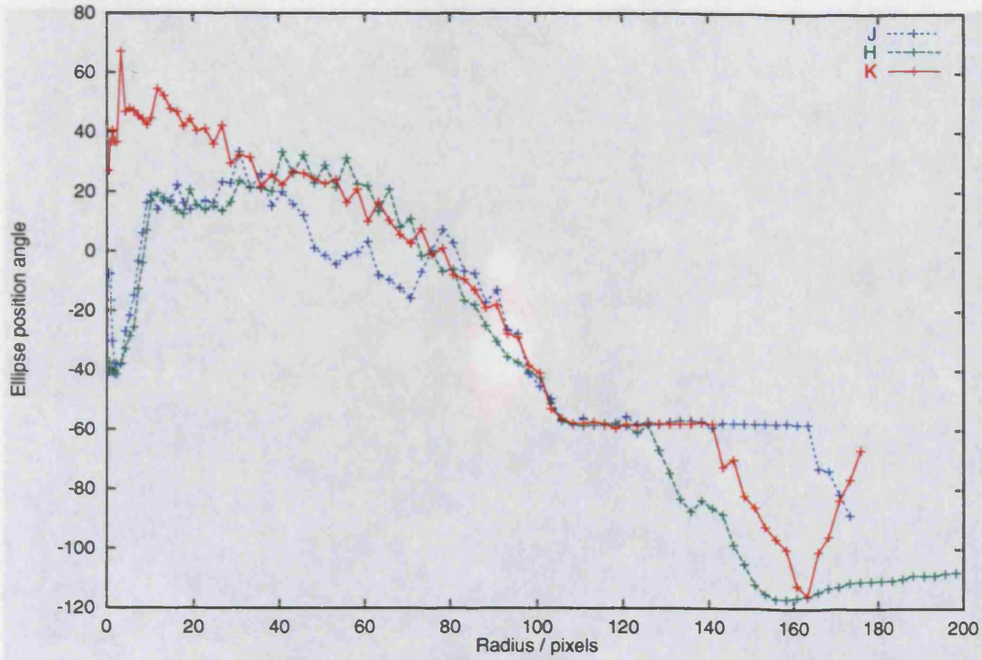

Figure 4.47: Akn 564 profile results - position angle

4.5.8 IRAS 17020

J, H and K band images are given in figures 4.48 – 4.49. Profiling results are shown in figures 4.50 – 4.52.

Again, either a strongly barred spiral or an edge on disk. Note the foreground star on the northern side of the nucleus.

Figure 4.48: IRAS 17020 in J band

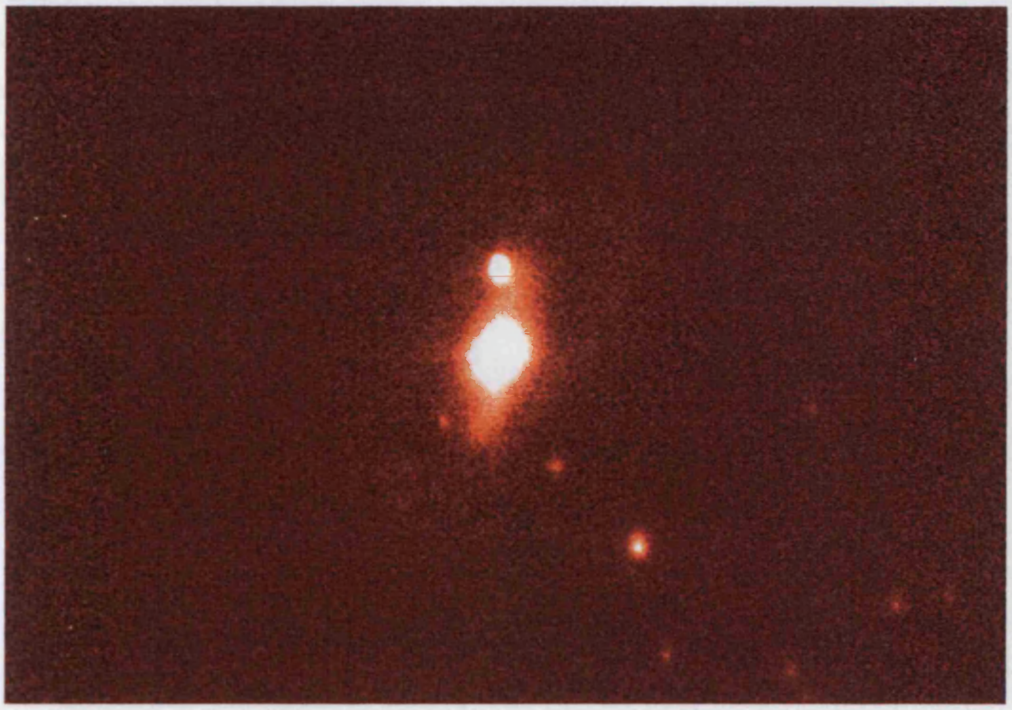

Figure 4.49: IRAS 17020 in K band

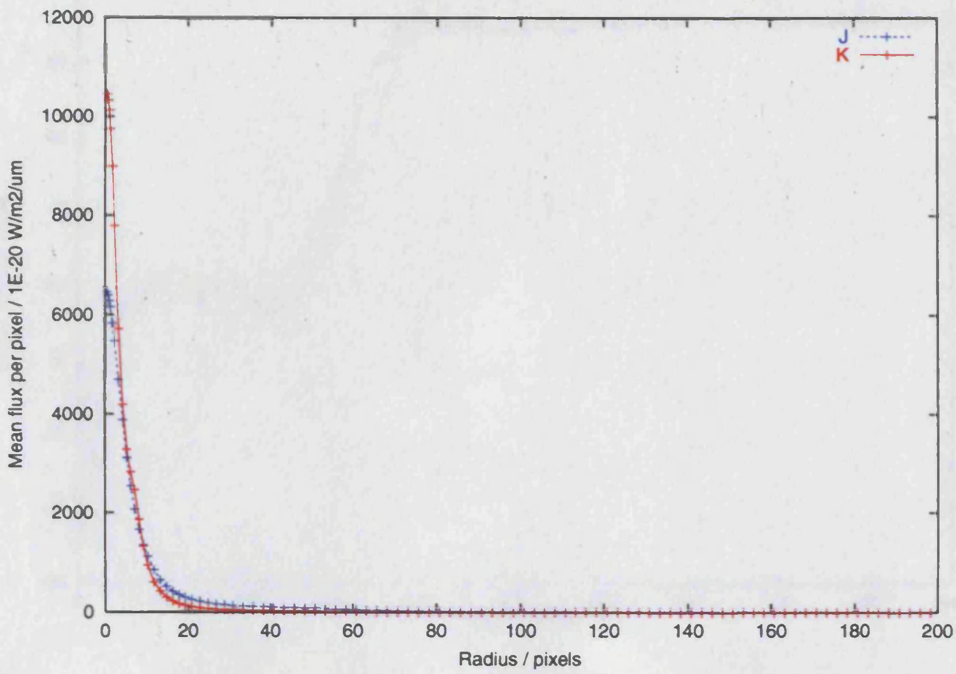

Figure 4.50: IRAS 17020 profile results - flux

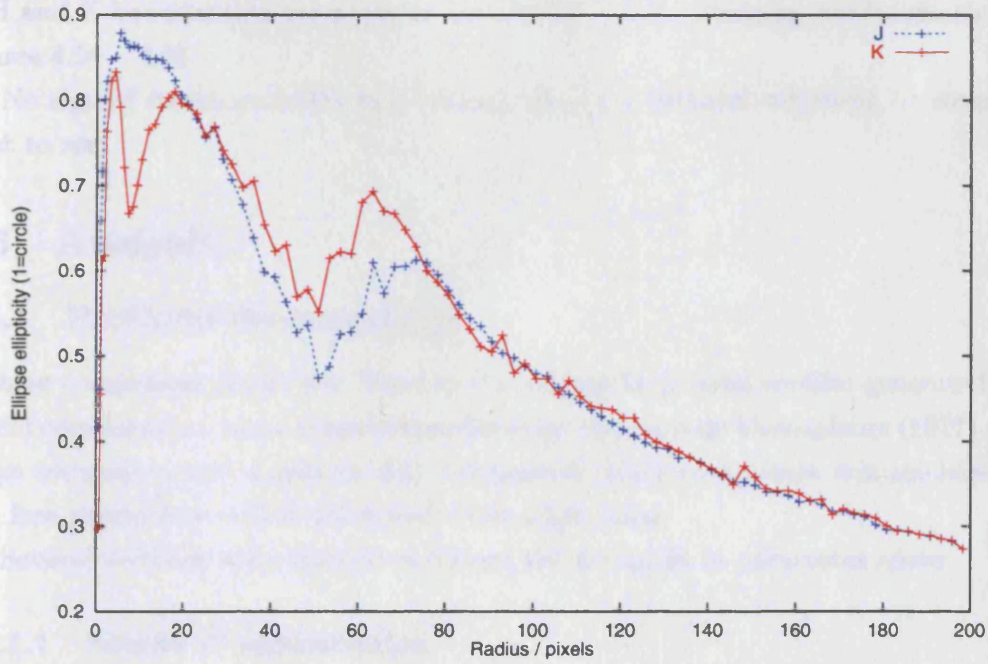

Figure 4.51: IRAS 17020 profile results - ellipticity

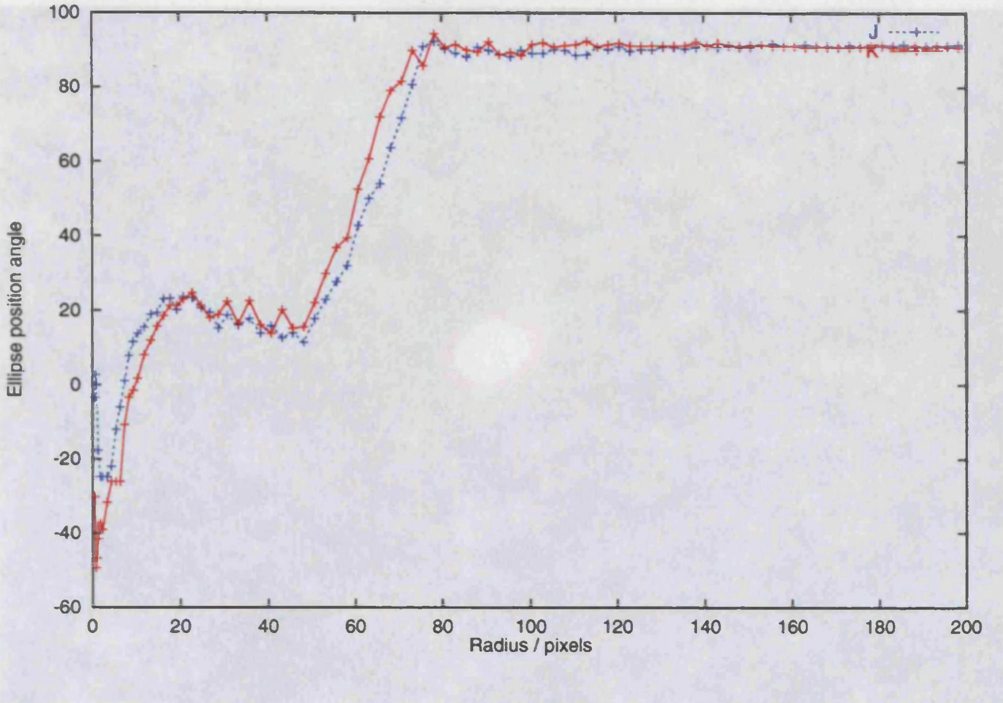

Figure 4.52: IRAS 17020 profile results - position angle

4.5.9 IRAS 13349

J, H and K band images are given in figures 4.53 - 4.55. Profiling results are shown in figures 4.56 - 4.58.

No sign of structure in the host galaxy. Maybe a compact elliptical, or simply too faint to see.

4.6 Analysis

4.6.1 Profile fit decomposition

A three component model was fitted to the surface brightness profiles generated. This model consists of a central Gaussian profile point source, a de Vaucouleurs (1977) profile bulge component and a galactic disk component. Each component was modeled with two free parameters, a flux value and a size scale value.

Several methods were tried to carry out the actual fit in parameter space.

4.6.1.1 Simple χ^2 minimisation

Fit optimisation was carried out using a simple χ^2 minimisation algorithm. Similar, two component models, lacking the nuclear Gaussian component, have been successfully applied to normal galaxies (Kent 1985, Kodaira et al. 1986).

Figure 4.53: IRAS 13349 in J band

Figure 4.54: IRAS 13349 in H band

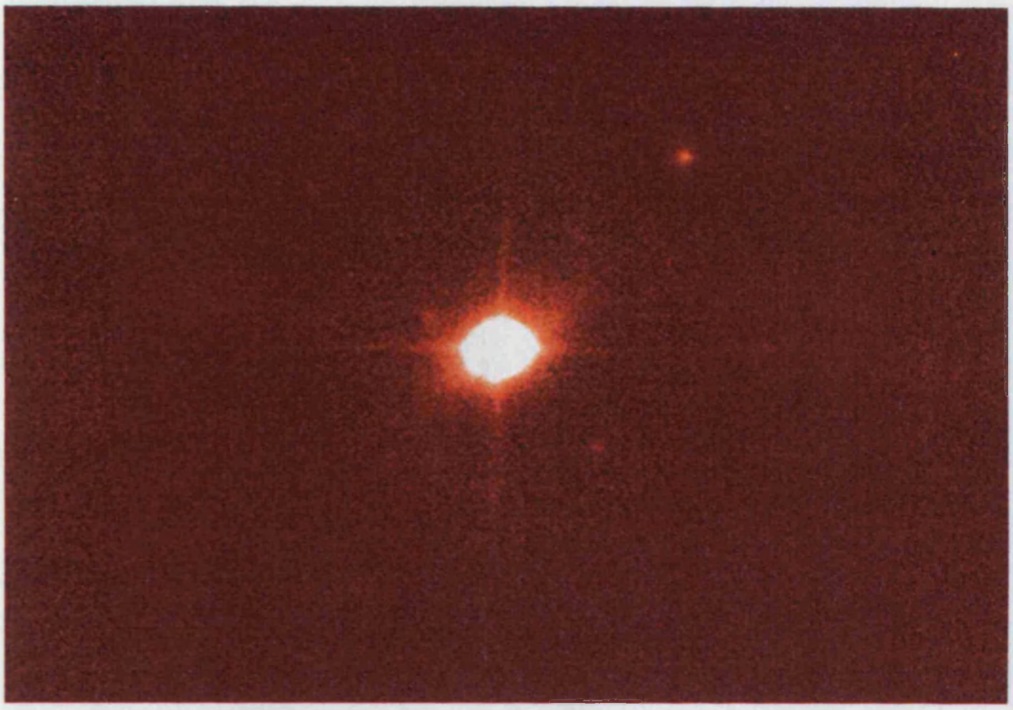

Figure 4.55: IRAS 13349 in K band

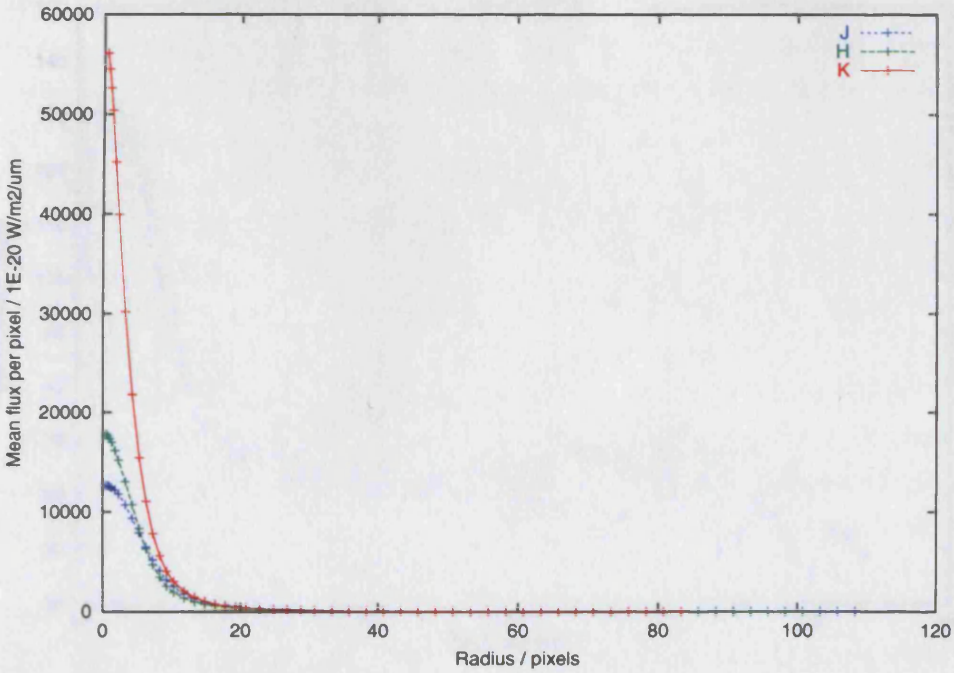

Figure 4.56: IRAS 13349 profile results - flux

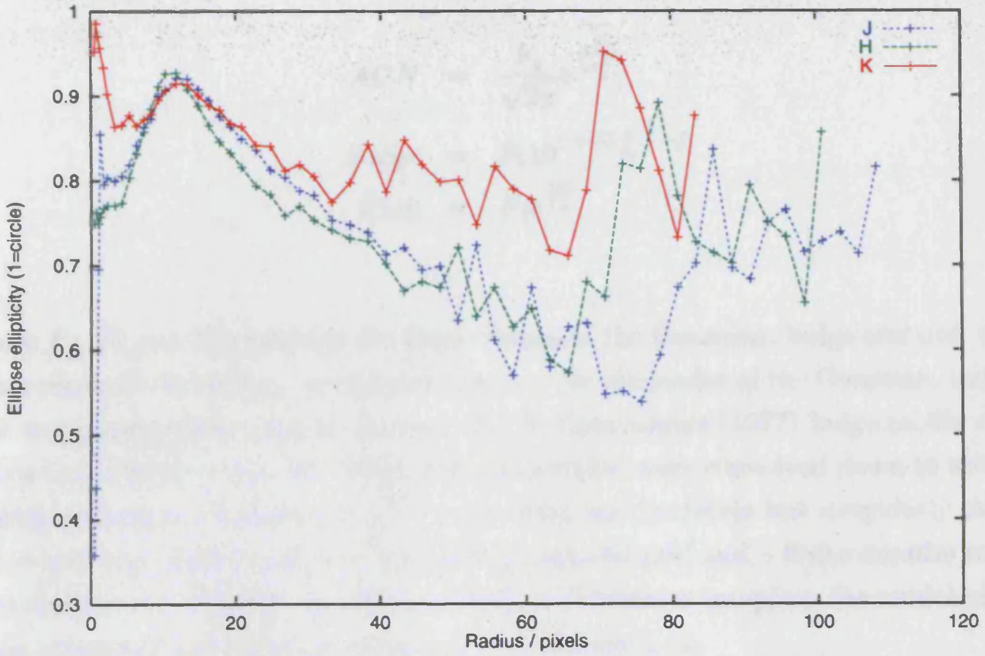

Figure 4.57: IRAS 13349 profile results - ellipticity

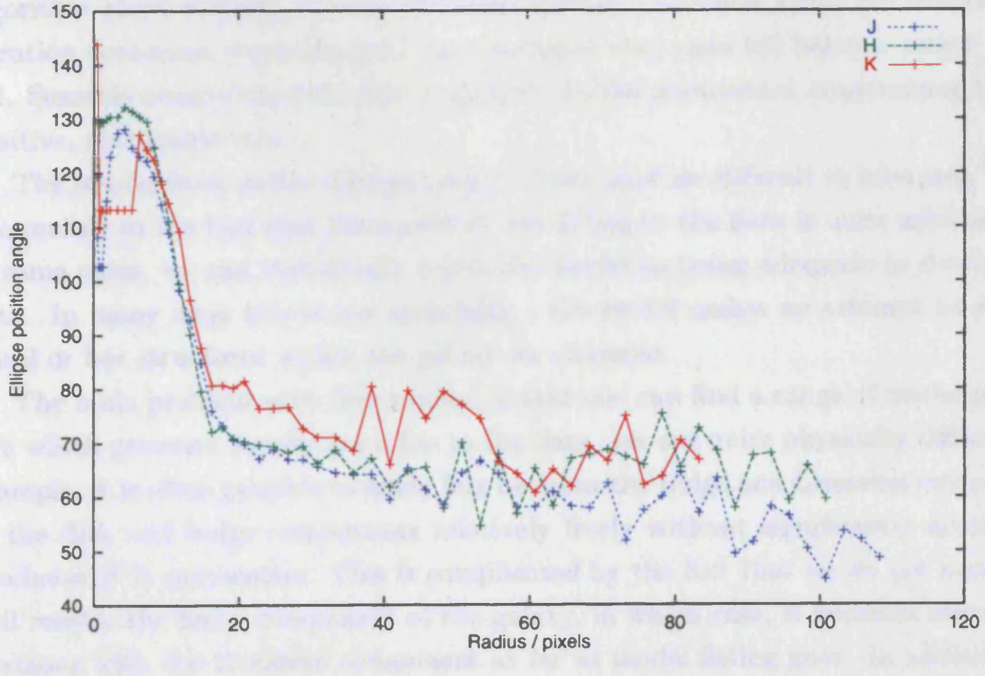

Figure 4.58: IRAS 13349 profile results - position angle

The model used the sum of the following three components,

$$\begin{aligned} AGN &= \frac{F_g}{\sqrt{2\pi}} e^{\frac{-r^2}{2r_g^2}} \\ Bulge &= F_b 10^{-3.33\frac{r}{r_b}^{\frac{1}{4}}-1} \\ Disk &= F_d e^{\frac{-r}{r_d}} \end{aligned}$$

where F_g, F_b and F_d represent the brightnesses of the Gaussian, bulge and disk components respectively, and r_g, r_b and r_d represent the size scales of the Gaussian, bulge and disk components respectively. Because the de Vaucouleurs (1977) bulge profile shows a sharp rise towards $r = 0$, the bulge and disk profiles were convolved down to the image resolution before calculation of χ^2. As the data are discretely but irregularly sampled, the model was constructed over a regularly sampled grid and a finite impulse response convolution (e.g. Press et al. 1992) carried out before re sampling the model onto the same (irregular) grid that the data had been sampled on.

Fit optimisation through the 6 dimensional parameter space was carried out by an iterative algorithm, implemented by custom software in C, that approximates $\frac{d(\chi^2)}{dA_{1-6}}$ by calculating finite difference differentials with respect to each of the 6 parameters, then adjusting the parameter which leads to the largest reduction in χ^2. When the algorithm stops making progress, the step sizes in parameter space are reduced, and iteration continues, repeating until the parameter step sizes fall below a preset threshold. Sensible constraints were places upon the model parameters, constraining them to positive, reasonable values.

The results from profile decomposition of this kind are difficult to interpret. This is due mainly to the fact that the model we are fitting to the data is quite arbitrary, and in some cases, we can statistically reject the model as being adequate to describe the data. In many ways this is not surprising - the model makes no attempt to describe spiral or bar structures within the galaxy for example.

The main problem with this method is that one can find a range of model parameters which generate equally good fits to the data, yet are quite physically different; for example, it is often possible to trade flux between the bulge and Gaussian components, or the disk and bulge components relatively freely without significantly altering the goodness of fit parameters. This is complicated by the fact that we do not necessarily well resolve the bulge component of the galaxy, in which case, it becomes almost synonymous with the Gaussian component as far as model fitting goes. In addition, this resolution effect changes significance as we move between bands, the K band images are generally higher resolution than the J and H band images. This possibly has a very serious consequence in attempting to plot say colour-colour diagrams of one particular component of the model - say the Gaussian representation of the AGN nucleus.

4.6.1.2 Fitting individual regions

In an attempt to force the mathematical model of the data into a more physically plausible state, a fitting algorithm was implemented thus:

Firstly, the profile is inspected by eye, and the smallest radius at which the disk component appears to dominate is estimated by eye. Data at radii greater than this are then fed to software which carries out a two parameter χ^2 reduction fit (along the same principles as the 6 parameter fit described above) of an exponential disk component (as described above) to this data, determining a disk size scale and characteristic brightness.

These disk parameters are then used to construct a disk model over the entire radius range, and this model is subtracted from the data.

The disk subtracted data are then inspected by eye, and the largest radius at which the Gaussian component appears to dominate is estimated. Data at radii lower than this are then fed to a Gaussian fitting routine, to determine a size scale and brightness for the Gaussian component. A Gaussian model over the entire radius range is then constructed and subtracted from the disk-subtracted data. These residuals are then examined to determine if the data warrants the fitting of a bulge component.

If it is decided to fit a bulge, the radius range in which the bulge falls outside the Gaussian, yet still dominates above the disk, is estimated by eye, and this data range is taken from the disk subtracted data and fed to a bulge fitting algorithm. The bulge fit parameters are then used to construct a bulge model over the entire data range, which is subtracted from the disk-subtracted data, the low-radius part of this data is then used to construct a Gaussian component as before, which is again subtracted to determine the final residuals.

This method was found to give models which are physically much more acceptable than simple 6 dimensional parameter fitting.

Plots are presented showing the data, all the model components along with the total model, and the residuals, for each image.

4.6.1.3 IRAS 13349

IRAS 13349 is fit reasonably well by a simple disk + nucleus model. The fit parameters are given in table 4.1. It is clear from the residuals that fitting an additional bulge component to the data would not be simple and would give difficult to interpret results.

From analysis of the residuals, we can suggest that if a bulge component does exist, it should have a half width size scale of order 10 pixels (1 arc-sec), and appears to be more prominent at K band, though it should be stressed that especially in these

Object		J flux	J Wid	H Flux	H Wid	K flux	K wid
IRAS 13349	Disk	798.6	19.92	743.6	17.64	1496.7	13.36
	Nucleus	30048	5.38	40306	4.51	112053	3.58
IRAS 17020	Disk	61.78	98.24			22.275	110.6
	Nucleus	15681	4.51			22229	4.10
Ark 564	Disk	101.96	97.29	43.71	173.4	27.83	89.77
	Nucleus	41850	3.42	45441	3.09	42566	2.94
Mkn 291	Disk	324.28	32.2	257.93	30.9	117.68	32.1
	Nucleus	2434.9	8.07	2136.2	6.64	2385.2	5.32
Mkn 42	Disk	161.54	47.59	119.18	44.76	80.24	45.84
	Bulge	1732.8	11.02	1552.0	10.63	3799.5	6.70
	Nucleus	7320.8	3.93	5688.3	3.73	3022.5	2.82
Mkn 478	Disk	817.57	17.27	725.93	15.68	790.4	12.74
	Nucleus	23121	4.56	31667	4.43	40723	3.87
Mkn 493	Disk	308.55	50.93	148.7	81.88	75.54	77.78
	Bulge	3191.4	8.99	3001.7	9.04	3248.8	7.87
	Nucleus	104064	4.56	21864	2.90	21585	2.96
Mkn 766	Disk	833.3	56.98	786.6	39.39	329.06	47.88
	Bulge	7259.4	9.95	9610.7	7.89	14875	7.39
	Nucleus	28764	3.75	30395	3.63	30995	3.86
Mkn 896	Disk	449.93	51.06	269.0	56.82	166.95	49.09
	Bulge	4138	9.44	4090.8	8.94	4638.3	7.26
	Nucleus	10722	4.27	17615	3.55	24922	3.23

Table 4.1: Profile decomposition parameters

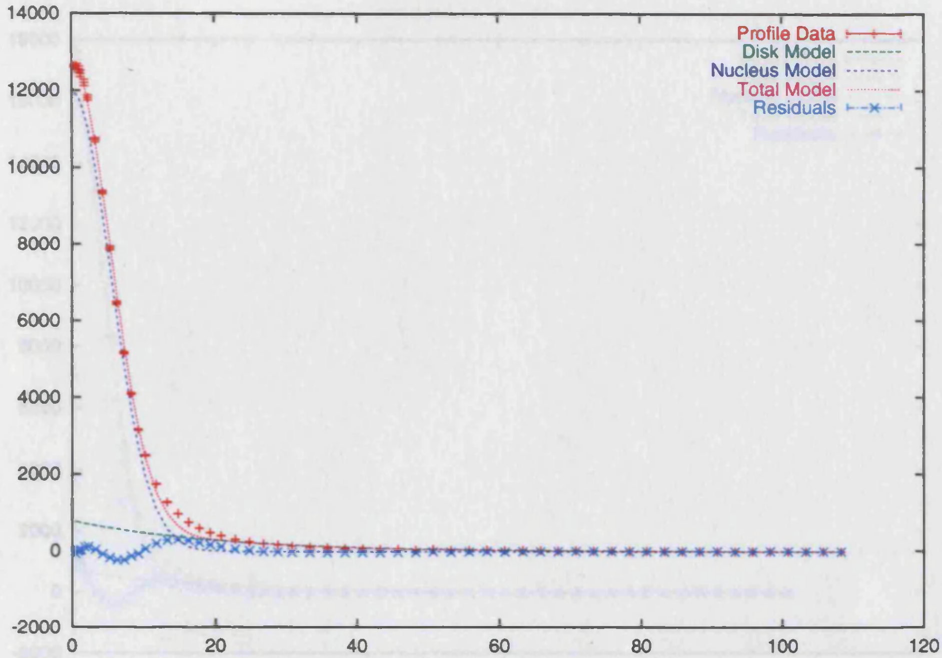

Figure 4.59: IRAS 13349 J band profile decomposition

images, it is very difficult to say that this is not simply an effect of the PSF being non Gaussian. The residuals show that the PSF is more peaked at K band, as would be expected for UKIRT, especially with the tip-tilt system active. We conclude that any bulge component in this galaxy is spatially unresolved, even at its periphery, and thus cannot be separated from the nuclear AGN component.

4.6.1.4 IRAS 17020

At first sight, we suspect a viable bulge component in the residuals from disk + Gaussian fitting to the IRAS 17020 profiles, though on further investigation, we are unable to generate a viable fit to the data. We can suggest from visual inspection of the data that any bulge component should have a half width size scale of around 20 pixels (2 arc sec), though it does not appear to follow a de Vaucouleurs profile. Due to time constraints during the observing run, we do not have an H band image of this object.

The fit parameters for a disk + nucleus model of IRAS 17020 are given in table 4.1.

IRAS 17020 shows a barred morphology, with a bright spot in the northern arm. It is not clear whether this is a foreground star or intrinsic to the galaxy. As the profile data is azimuthally averaged, albeit determined from elliptical isophotes, both the bar and this bright spot will be modelled in the disk component of our models. Since the main purpose of the model is to separate the starlight from the emission from the

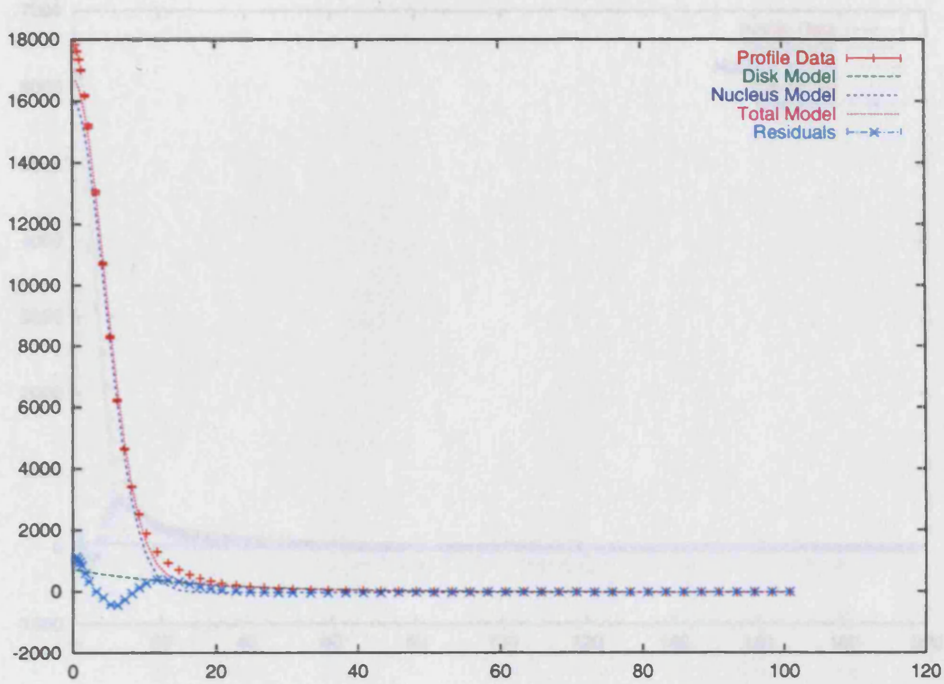

Figure 4.60: IRAS 13349 H band profile decomposition

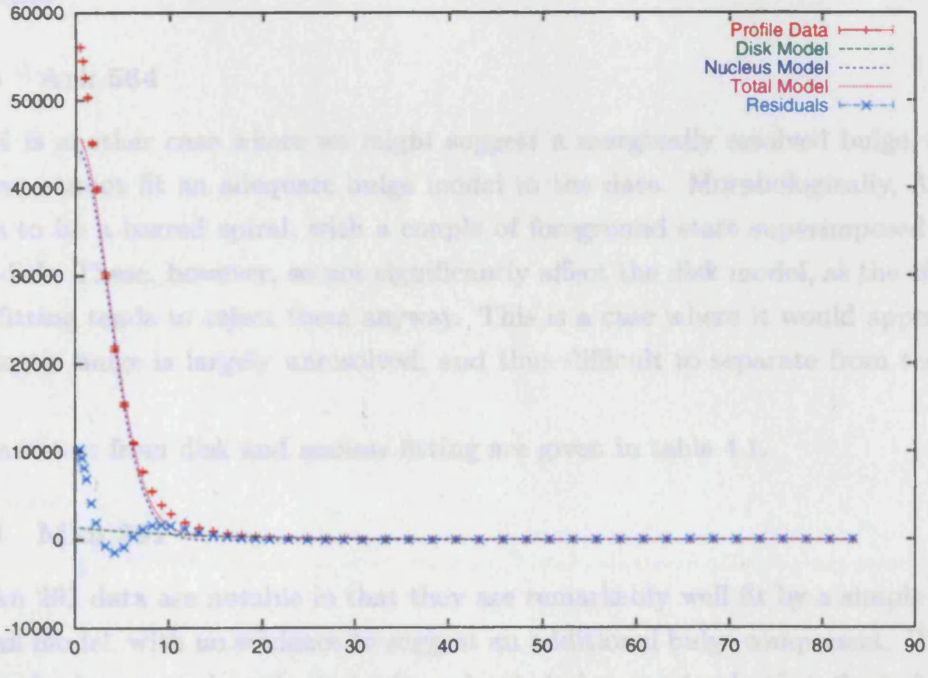

Figure 4.61: IRAS 13349 K band profile decomposition

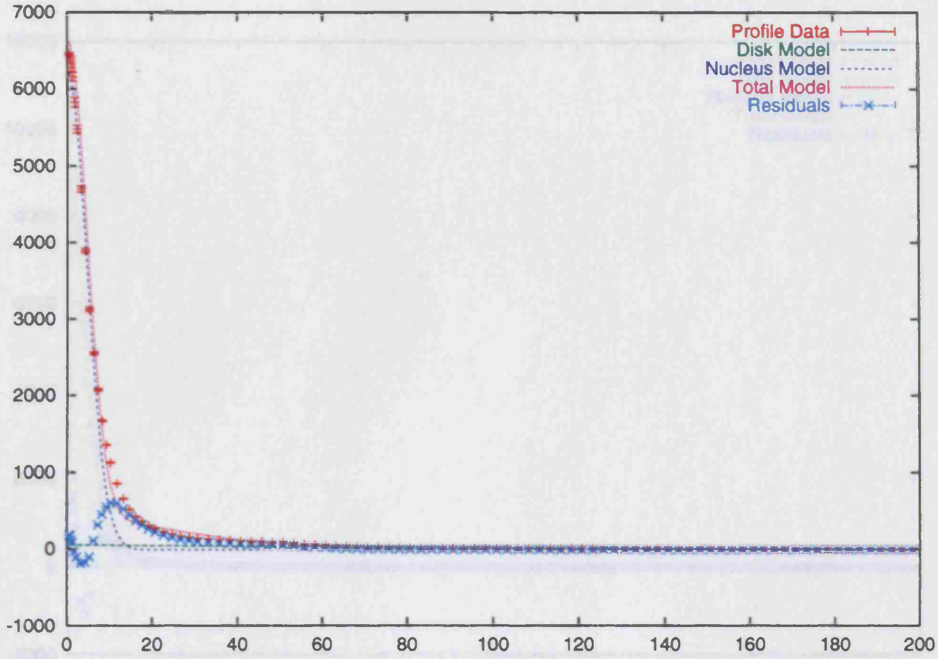

Figure 4.62: IRAS 17020 J band profile decomposition

AGN nucleus, this is not a problem, as both the bar and bright spot are obviously non-nuclear.

4.6.1.5 Ark 564

Ark 564 is another case where we might suggest a marginally resolved bulge, though where we cannot fit an adequate bulge model to the data. Morphologically, Akn 564 appears to be a barred spiral, with a couple of foreground stars superimposed on the galaxy disk. These, however, so not significantly affect the disk model, as the elliptical profile fitting tends to reject them anyway. This is a case where it would appear that any galactic bulge is largely unresolved, and thus difficult to separate from the AGN light.

Parameters from disk and nuclear fitting are given in table 4.1.

4.6.1.6 Mkn 291

The Mkn 291 data are notable in that they are remarkably well fit by a simple disk + Gaussian model, with no evidence to suggest an additional bulge component. Whether this is to be interpreted as the lack of a galactic bulge, or simply that the bulge is so unresolved as to be completely contained within the Gaussian component is unclear. To further confuse the situation we note that the Gaussian component in these images,

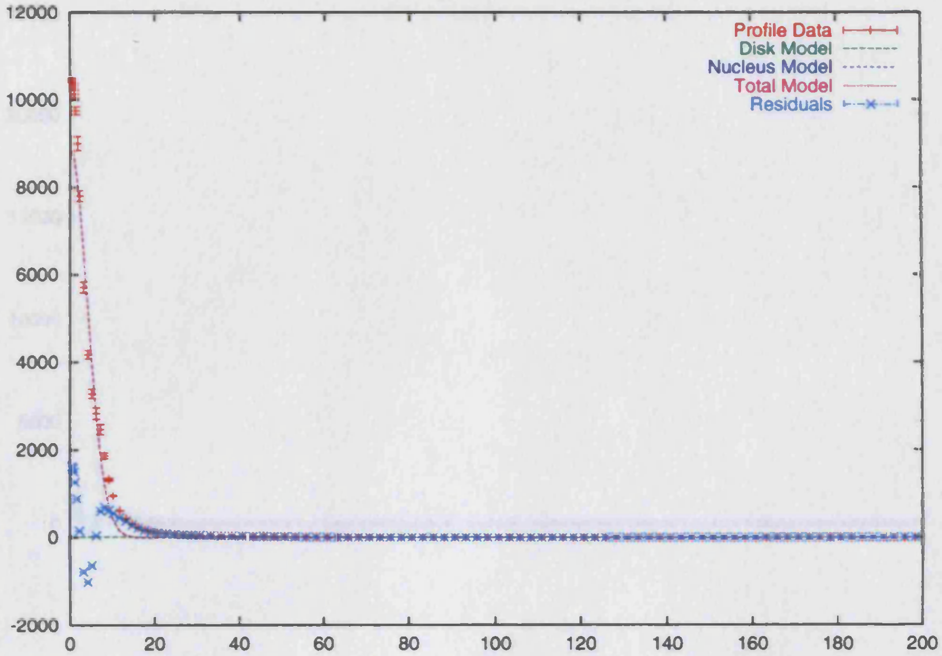

Figure 4.63: IRAS 17020 K band profile decomposition

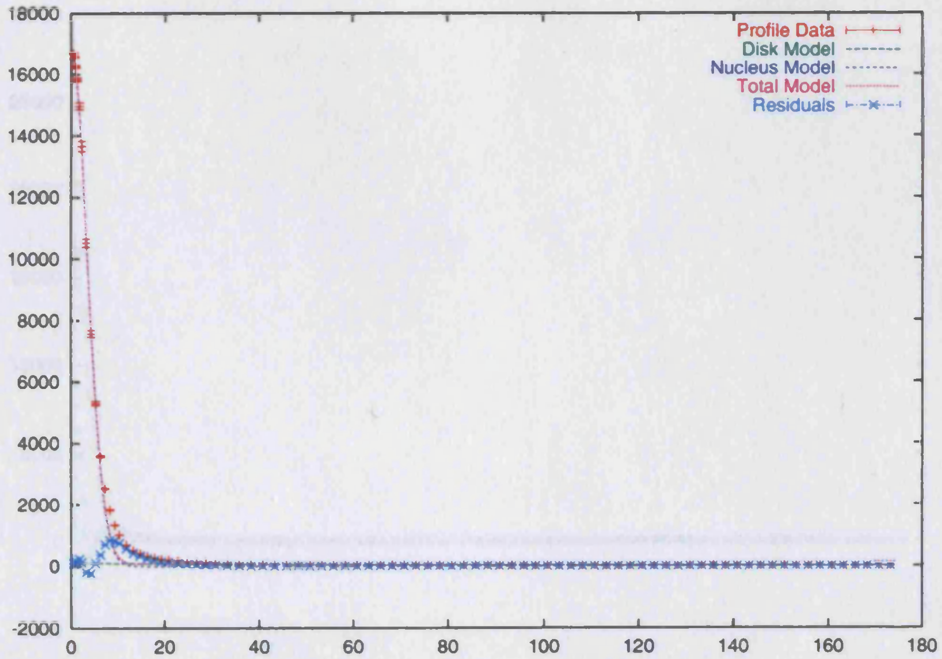

Figure 4.64: Akn 564 J band profile decomposition

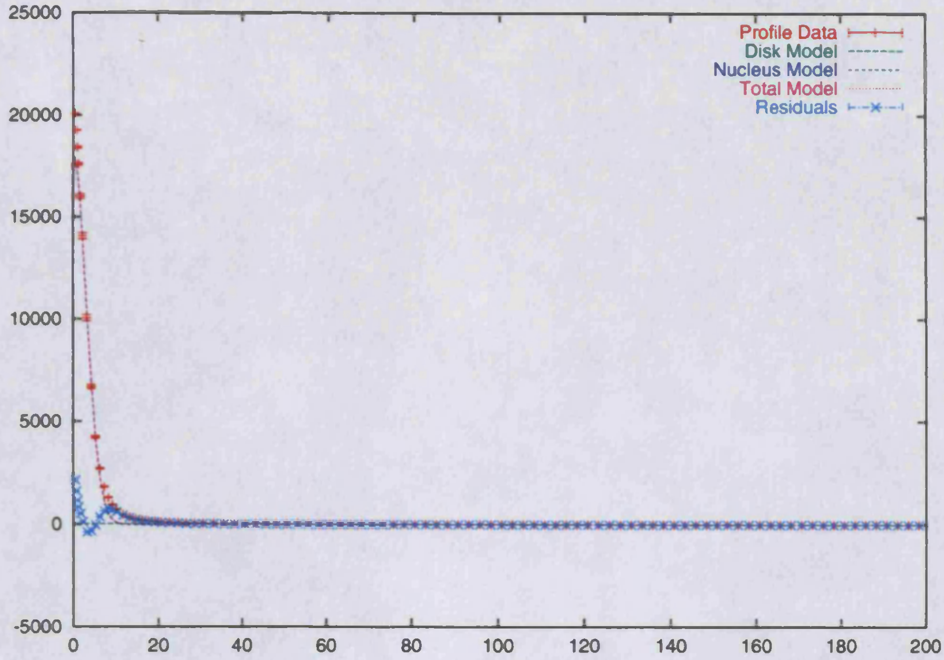

Figure 4.65: Akn 564 H band profile decomposition

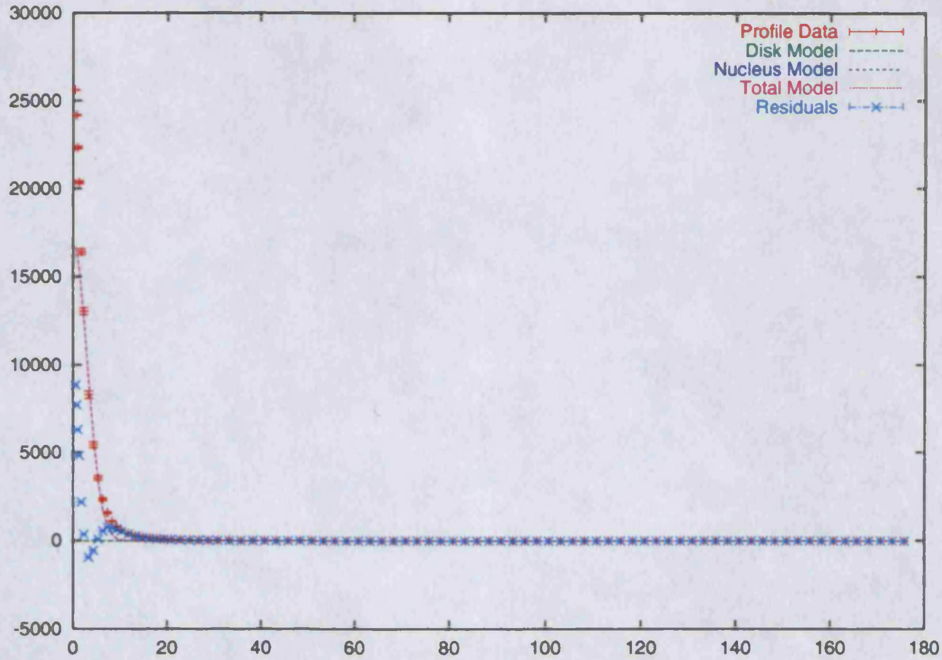

Figure 4.66: Akn 564 K band profile decomposition

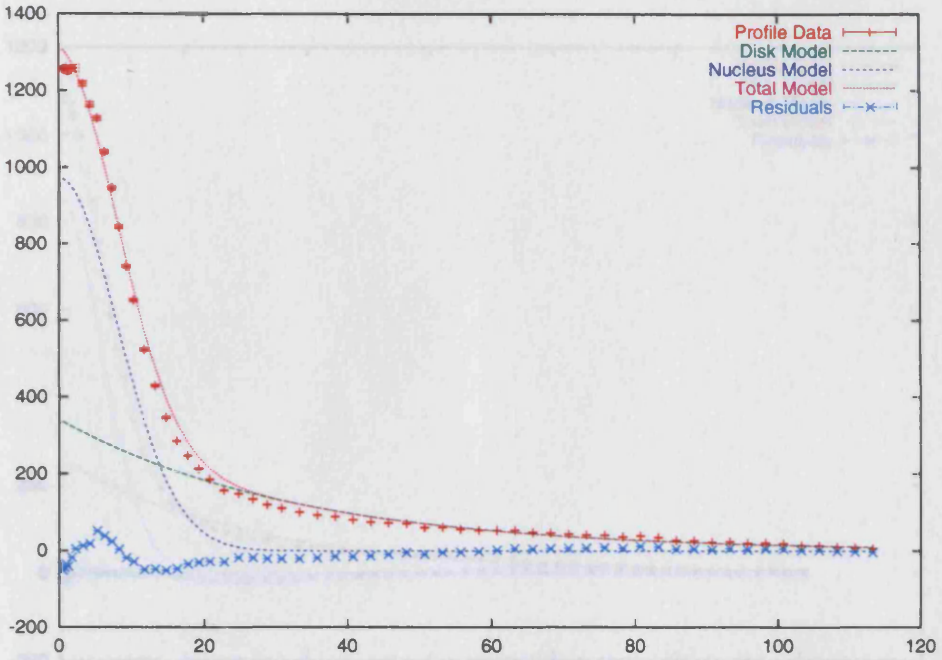

Figure 4.67: Mkn 291 J band profile decomposition

whilst remarkably Gaussian in profile, is *resolved.* It's width is approximately double that of the PSF.

The best explanation available at the moment is that the bulge and AGN profiles are co-incidentally such as to produce a Gaussian profile when summed.

Parameters from disk and nuclear fitting are given in table 4.1.

4.6.1.7 Mkn 42

Mkn 42 is one of the few cases where we can fit a sensible bulge component. However, it was found that fitting a de Vaucouleurs bulge profile, convolved with an estimated PSF worked far worse than fitting the bulge component with a Gaussian profile.

This is interesting in the light of figure 4.29 which shows a data from an HST Planetary camera image of the Mkn 42 nucleus, colour mapped so as to bring out the detail in the bulge. It reveals a complex, circular "mini-spiral" structure to the bulge, rather than the traditional elliptical bulge better fitted by an $r^{\frac{1}{4}}$ profile.

Parameters from disk, bulge and nuclear fitting are given in table 4.1.

The K band model fit in this object is influenced by the profile of the PSF being more peaked than a true Gausian. Combined with the difficulties seperating the unresolved nucleus and the barely resolved bulge component, the model in this case appears to underestimate the nucleus flux in favour of the bulge flux. Counteracting this requires

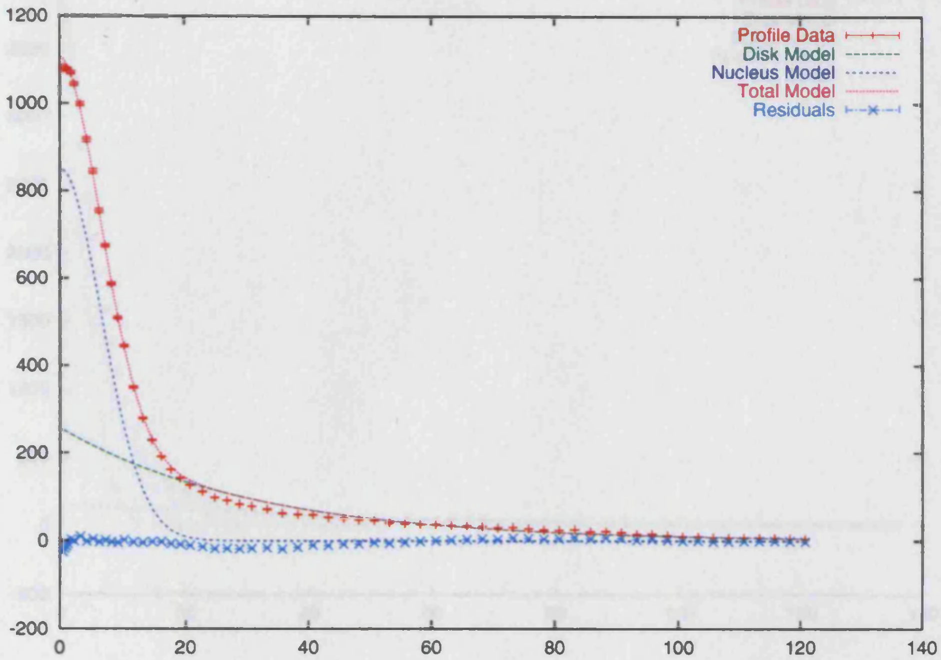

Figure 4.68: Mkn 291 H band profile decomposition

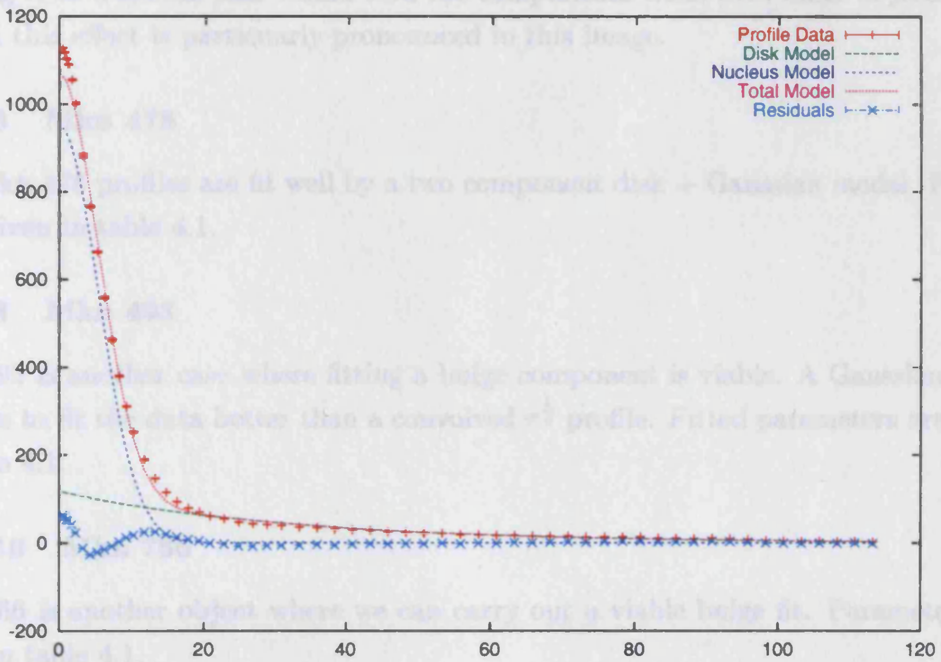

Figure 4.69: Mkn 291 K band profile decomposition

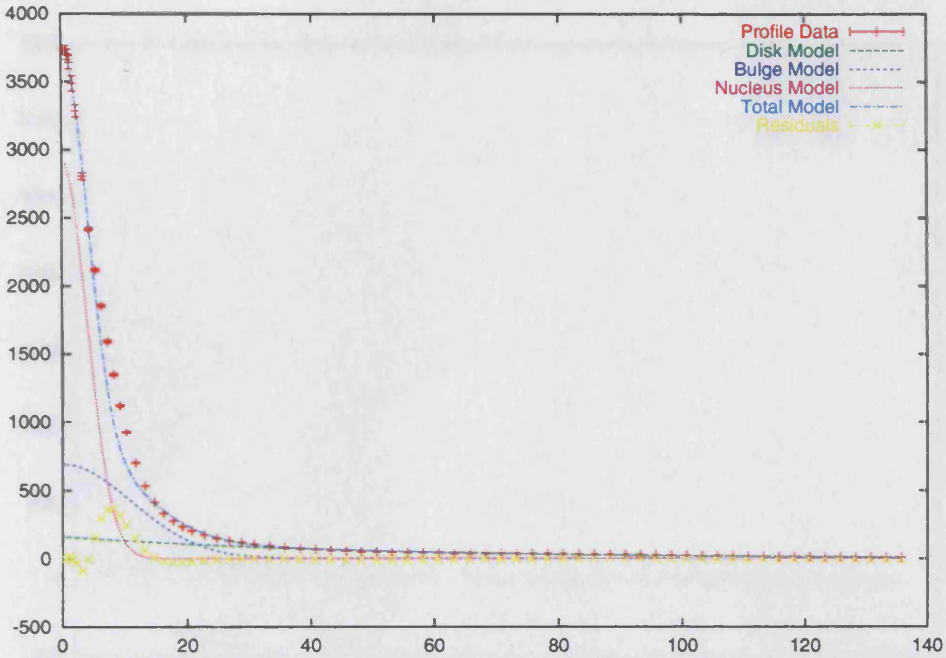

Figure 4.70: Mkn 42 J band profile decomposition

true PSF fitting which has not been implemented here, this case is not corrected as treating it as a special case would void the comparisons done with other objects, even though this effect is particuarly pronounced in this image.

4.6.1.8 Mkn 478

The Mkn 478 profiles are fit well by a two component disk + Gaussian model. Parameters given in table 4.1.

4.6.1.9 Mkn 493

Mkn 493 is another case where fitting a bulge component is viable. A Gaussian bulge appears to fit the data better than a convolved $r^{\frac{1}{4}}$ profile. Fitted parameters are given in table 4.1.

4.6.1.10 Mkn 766

Mkn 766 is another object where we can carry out a viable bulge fit. Parameters are given in table 4.1.

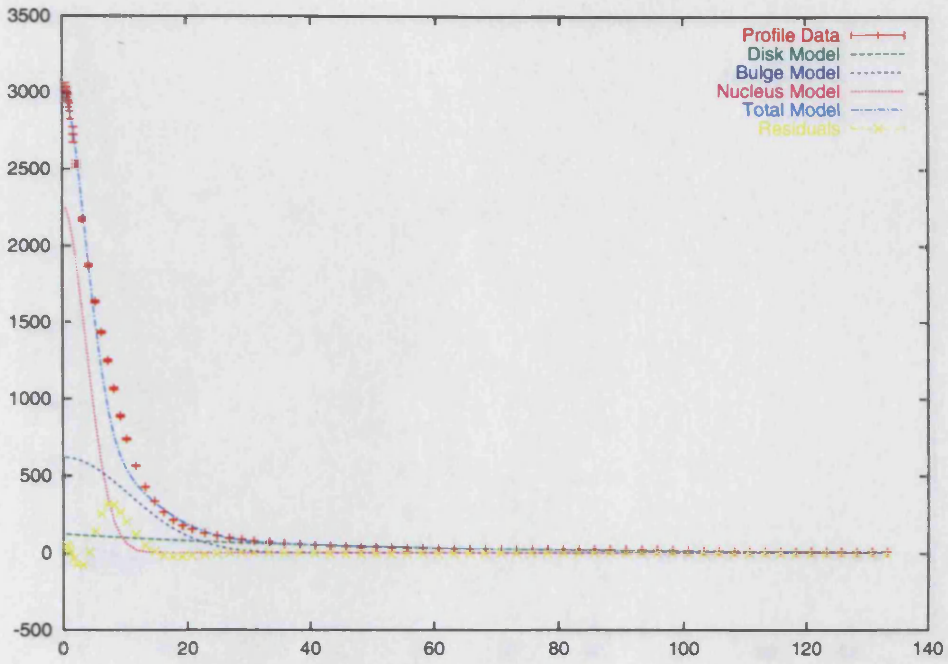

Figure 4.71: Mkn 42 H band profile decomposition

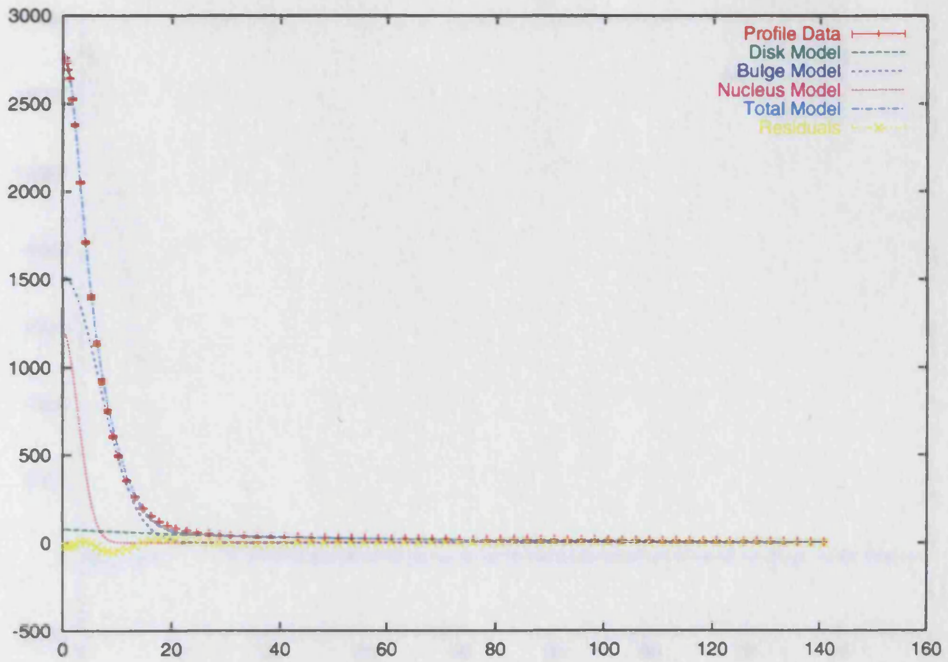

Figure 4.72: Mkn 42 K band profile decomposition

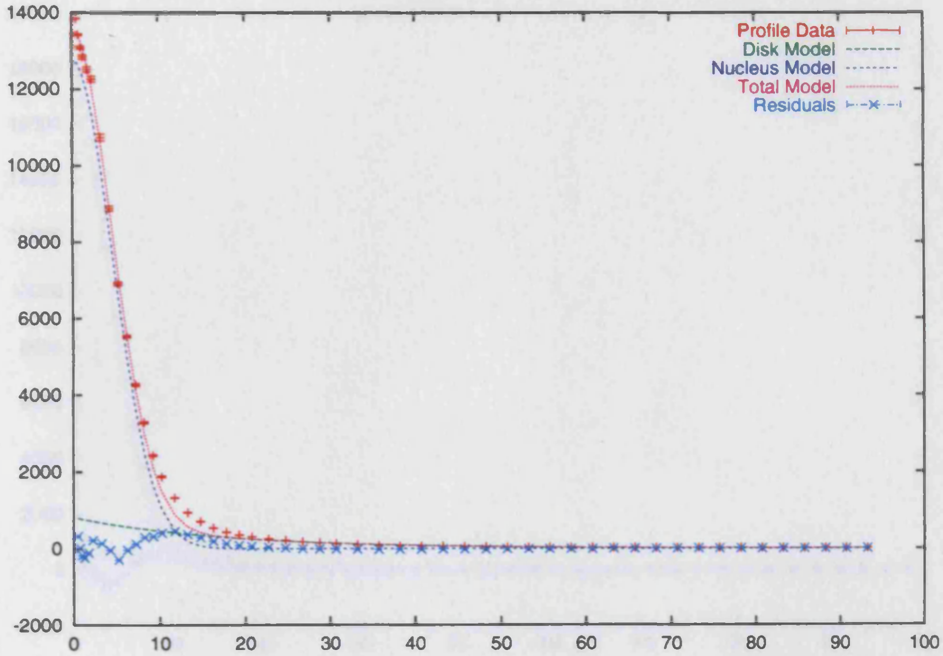

Figure 4.73: Mkn 478 J band profile decomposition

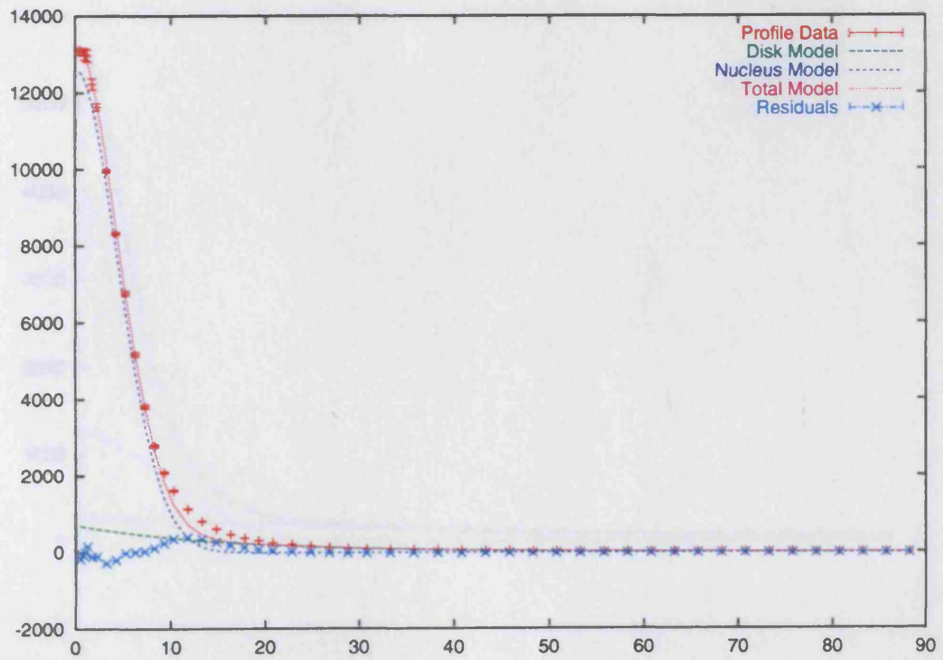

Figure 4.74: Mkn 478 H band profile decomposition

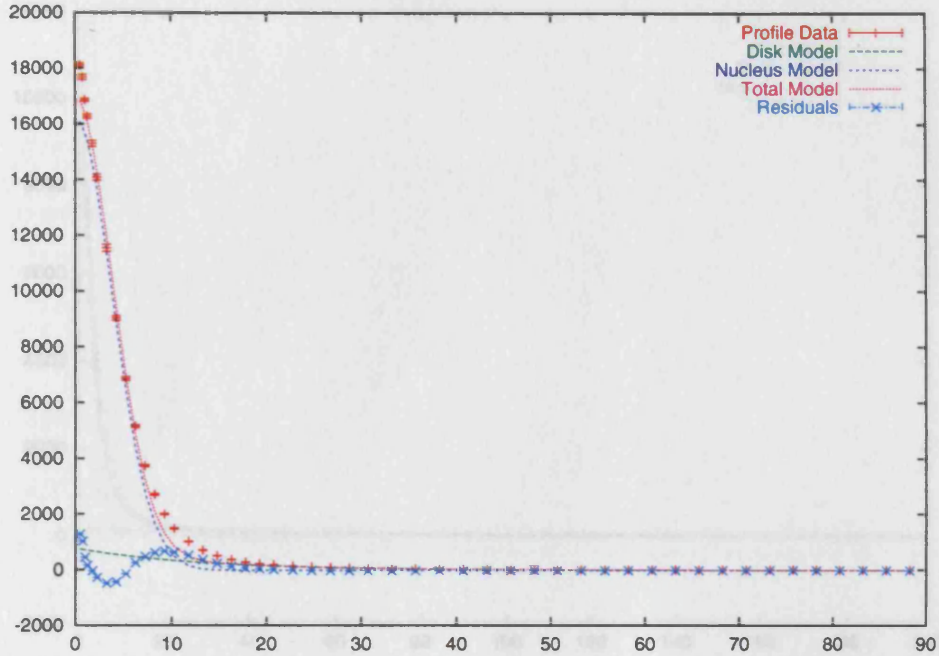

Figure 4.75: Mkn 478 K band profile decomposition

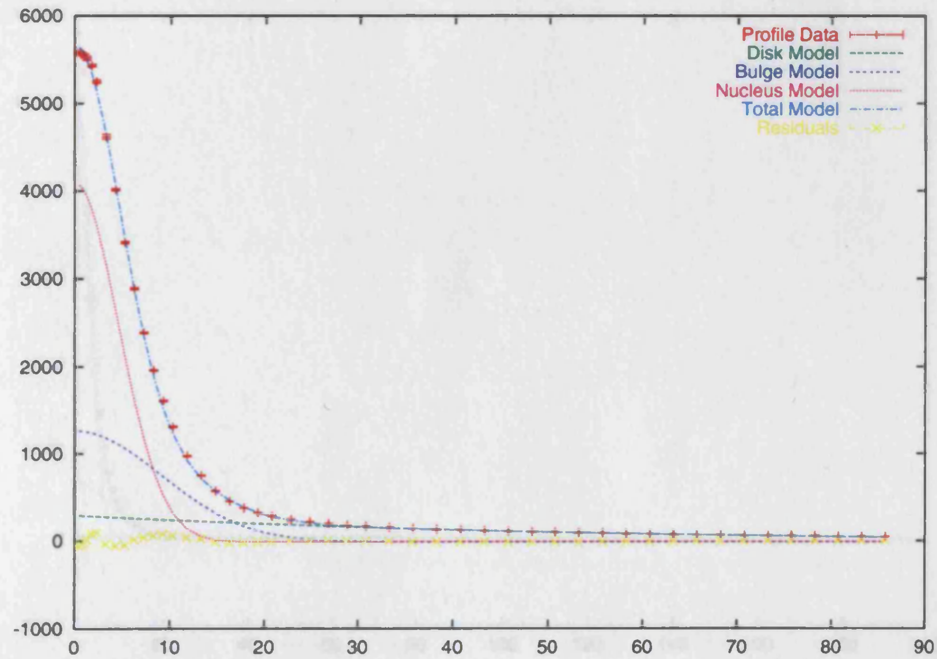

Figure 4.76: Mkn 493 J band profile decomposition

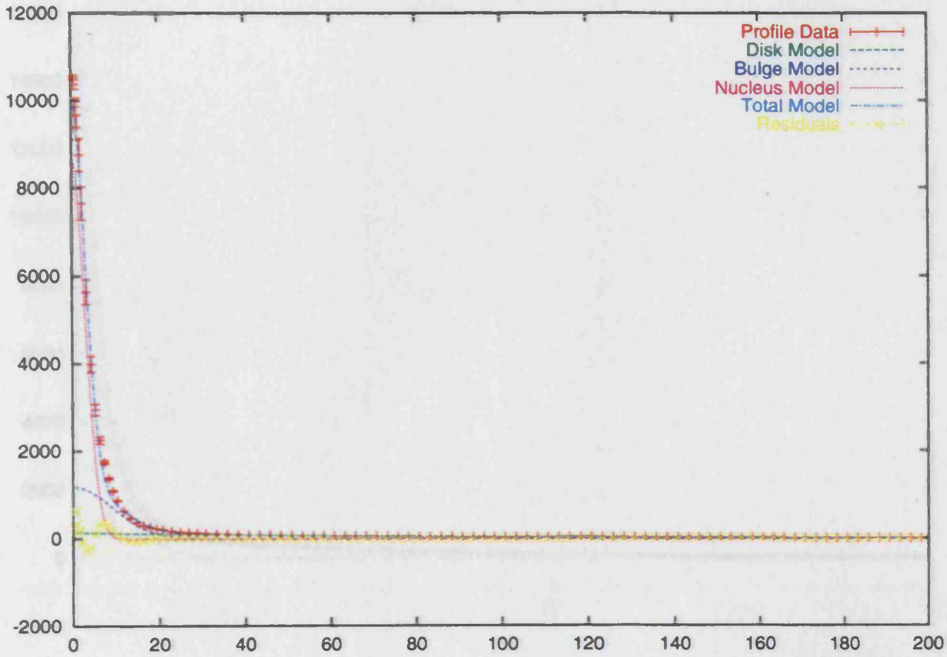

Figure 4.77: Mkn 493 H band profile decomposition

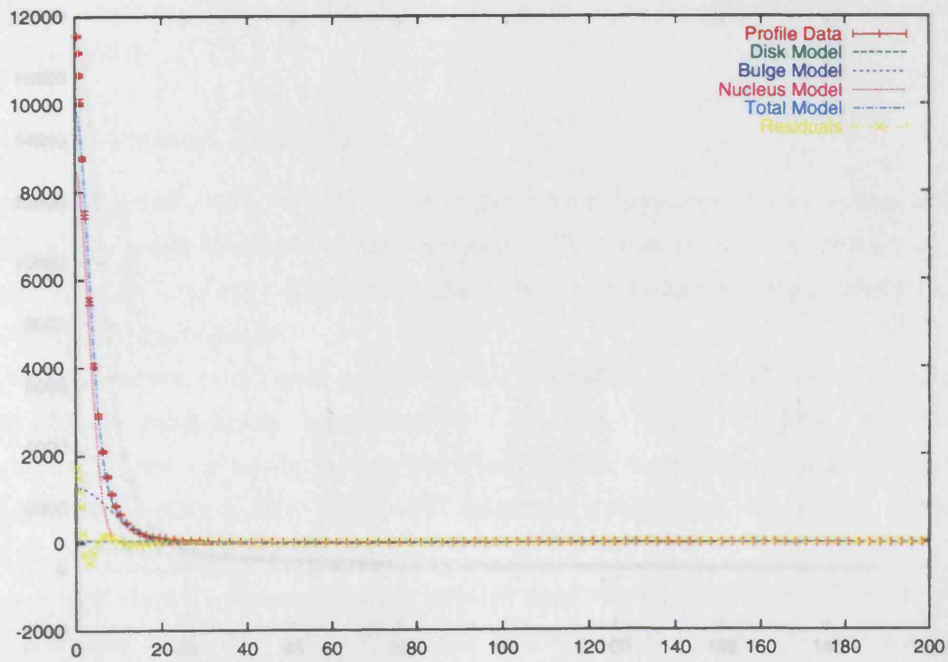

Figure 4.78: Mkn 493 K band profile decomposition

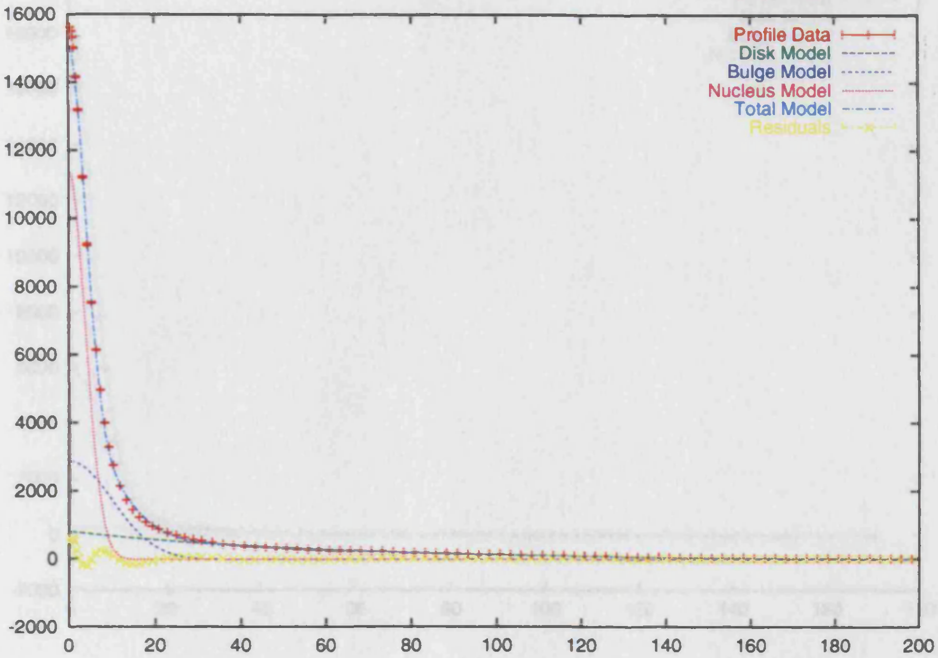

Figure 4.79: Mkn 766 J band profile decomposition

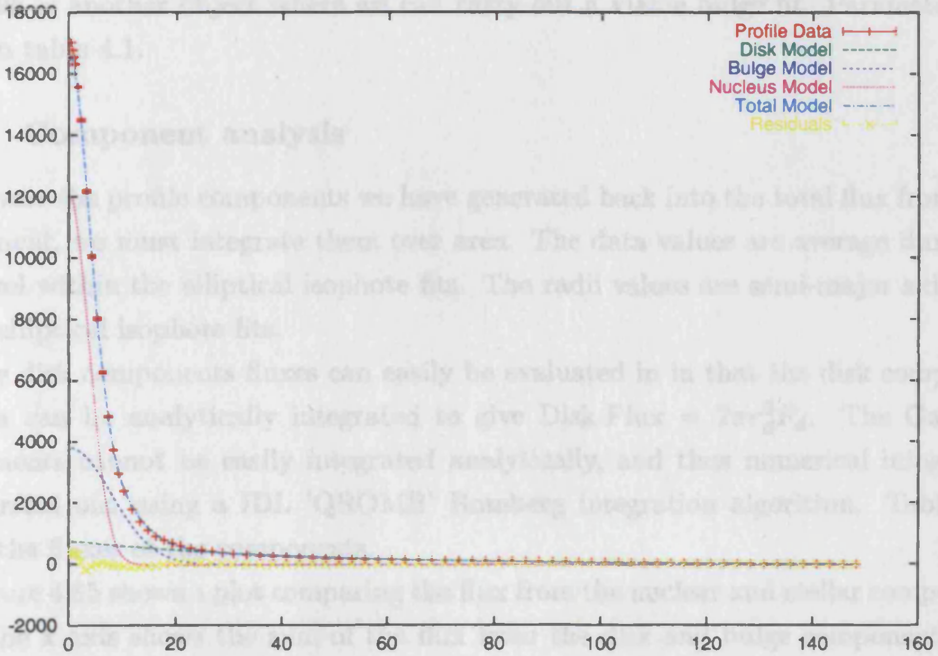

Figure 4.80: Mkn 766 H band profile decomposition

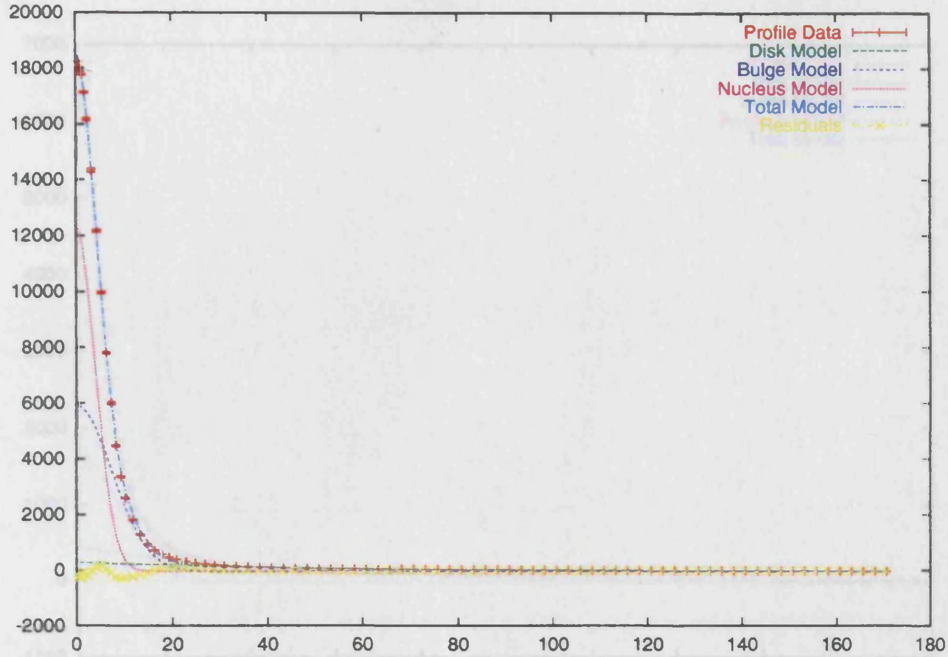

Figure 4.81: Mkn 766 K band profile decomposition

4.6.1.11 Mkn 896

Mkn 896 is another object where we can carry out a viable bulge fit. Parameters are given in table 4.1.

4.6.2 Component analysis

To convert the profile components we have generated back into the total flux from each component, we must integrate them over area. The data values are average flux units per pixel within the elliptical isophote fits. The radii values are semi-major axis radii of the elliptical isophote fits.

The disk components fluxes can easily be evaluated in in that the disk component formula can be analytically integrated to give Disk Flux $= 2\pi r_d^2 F_d$. The Gaussian components cannot be easily integrated analytically, and thus numerical integration was carried out using a IDL 'QROMB' Romberg integration algorithm. Table 4.2 shows the fluxes of the components.

Figure 4.85 shows a plot comparing the flux from the nuclear and stellar components - i.e. the x axis shows the sum of the flux from the disk and bulge components, and the y axis shows the flux from the nuclear component. The 3 colour bands are plotted with separate symbols. Figure 4.86 shows the near IR broad band spectra of the nuclear components, and figure 4.87 shows the J-H vs H-K colour scatter diagram for

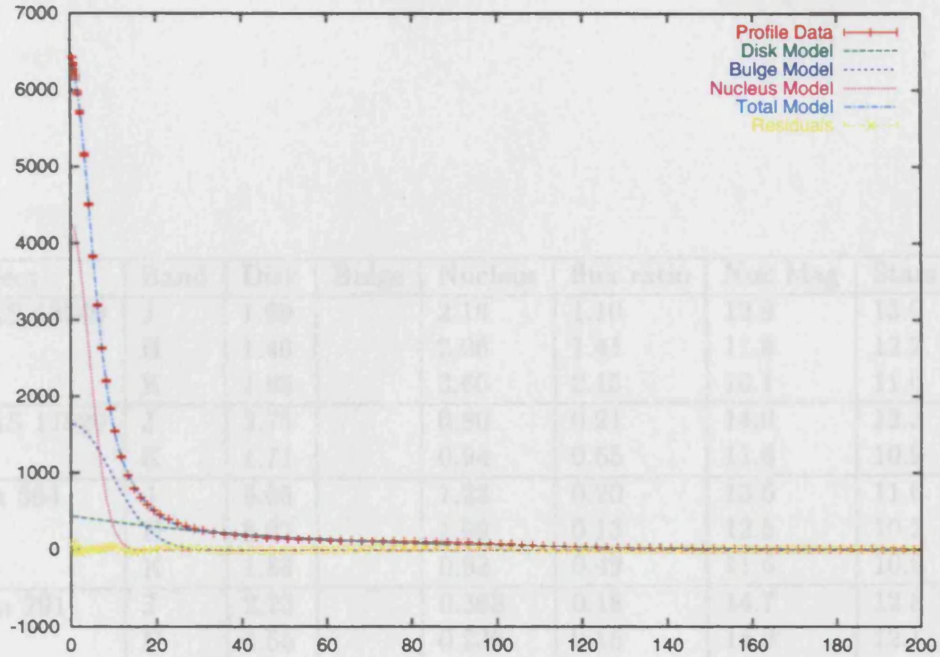

Figure 4.82: Mkn 896 J band profile decomposition

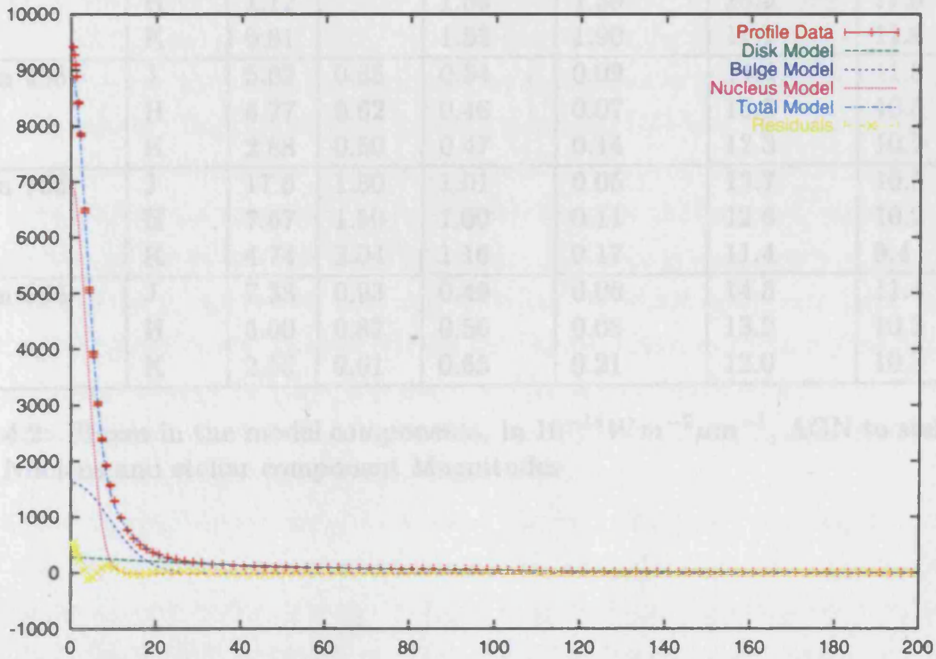

Figure 4.83: Mkn 896 H band profile decomposition

Object	Band	Disk	Bulge	Nucleus	flux ratio	Nuc Mag	Stars Mag
IRAS 13349	J	1.99		2.18	1.10	12.9	13.0
	H	1.46		2.06	1.41	11.8	12.2
	K	1.68		3.60	2.15	10.1	11.0
IRAS 17020	J	3.75		0.80	0.21	14.0	12.3
	K	1.71		0.94	0.55	11.6	10.9
Akn 564	J	6.05		1.23	0.20	13.5	11.6
	H	8.27		1.09	0.13	12.5	10.2
	K	1.88		0.92	0.49	11.6	10.8
Mkn 291	J	2.23		0.398	0.18	14.7	12.8
	H	1.55		0.236	0.15	14.2	12.1
	K	0.76		0.169	0.22	13.5	11.8
Mkn 42	J	2.30	0.53	0.28	0.10	15.1	12.6
	H	1.50	0.44	1.98	0.10	11.9	11.9
	K	1.06	0.43	0.06	0.04	14.6	11.1
Mkn 478	J	1.53		1.67	1.09	13.2	13.3
	H	1.12		1.56	1.39	13.5	12.5
	K	0.81		1.53	1.90	11.1	11.8
Mkn 493	J	5.02	0.65	0.54	0.09	14.4	11.9
	H	6.27	0.62	0.46	0.07	13.5	10.5
	K	2.88	0.50	0.47	0.14	12.3	10.2
Mkn 766	J	17.0	1.80	1.01	0.05	13.7	10.5
	H	7.67	1.50	1.00	0.11	12.6	10.2
	K	4.74	2.04	1.16	0.17	11.4	9.4
Mkn 896	J	7.38	0.93	0.49	0.06	14.5	11.4
	H	6.00	0.82	0.56	0.08	13.2	10.5
	K	2.53	0.61	0.65	0.21	12.0	10.3

Table 4.2: Fluxes in the model components, in $10^{-14} W m^{-2} \mu m^{-1}$, AGN to stellar flux ratio, Nucleus and stellar component Magnitudes

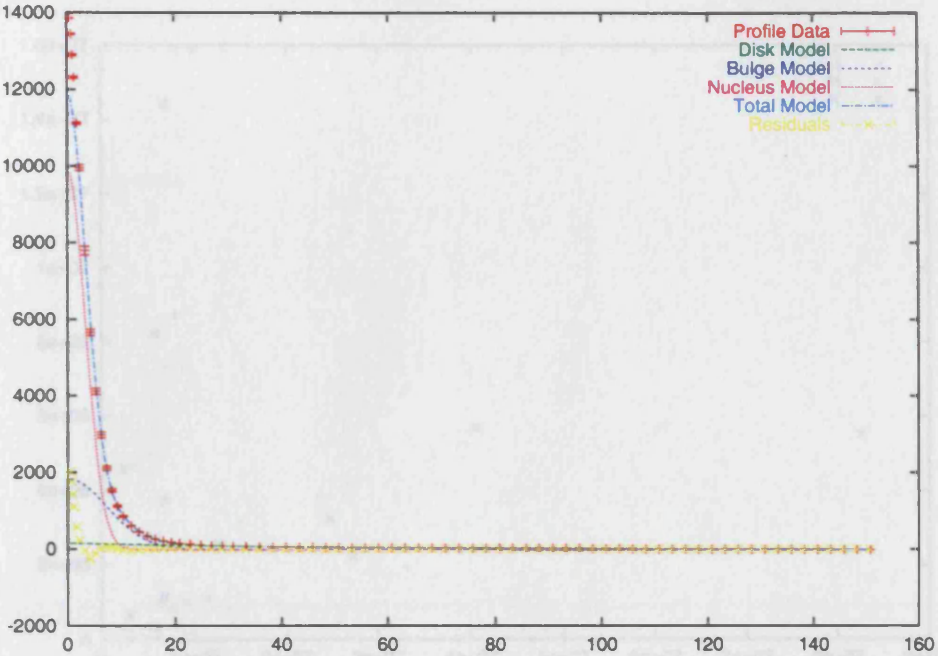

Figure 4.84: Mkn 896 K band profile decomposition

the NLS1 nuclear components. Our results here appear to be consistent with those obtained by simple aperture photometry of Seyfert galaxies by Alonso-Herrero et al. (1998) and Kotilainen et al. (1992), though our points do show a large scatter. Our outlying points can probably be attributed to anomalies in the model fitting process, as described above. Regions thought to be typical of AGN and stars are shown, taken from Kotilainen et al. (1992). Despite the large scatter, our nucleus components and stellar components do tend to cluster slightly towards the relevant regions. We do note that the Alonso-Herrero et al. (1998) values are from simple aperture photometry, with relatively large apertures, and will thus include a lot more star light than the nuclear components of our models. Given the values of the AGN to stellar flux ratios we measure and present in table 4.2, this could be a significant effect.

These results do show that our modeling has, at least partially, succeeded in separating the AGN from the stellar components in the images.

As noted previously, we should consider the fact that the "nuclear components" in this analysis are certainly contaminated with starlight from the galactic bulge to some degree. As the bulge in many of these objects is not spatially resolved in these images, it is impossible to overcome this. However, we do expect the active nucleus of the galaxy to be bright, and after subtracting out the disk and any resolved bulge components, this contamination is expected to be small.

In figure 4.88 we plot the K band nuclear component flux against the 0.1–2.5keV

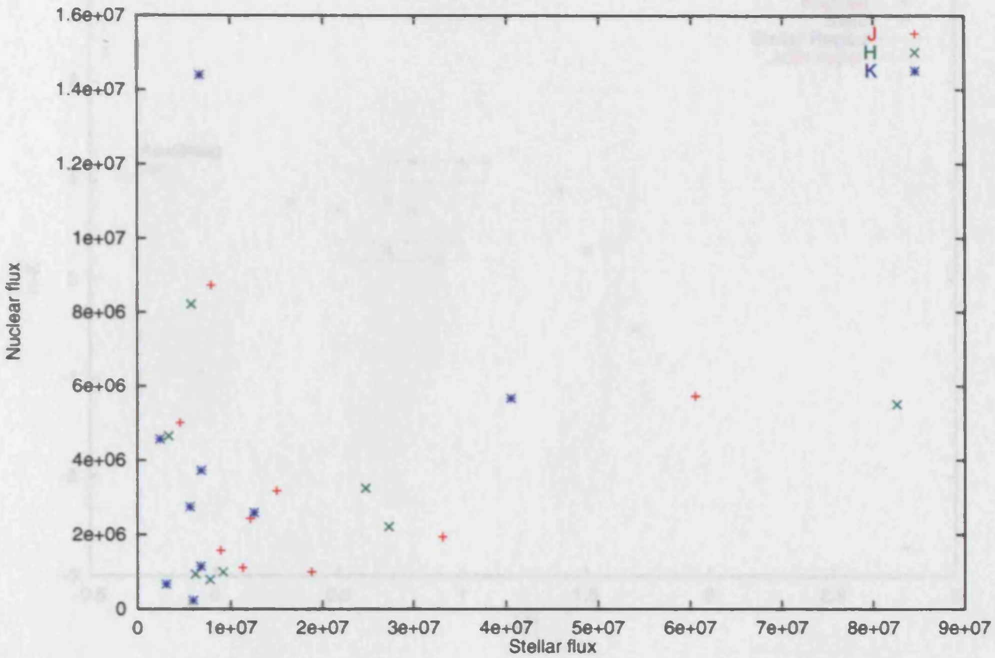

Figure 4.85: Nuclear vs Stellar component fluxes

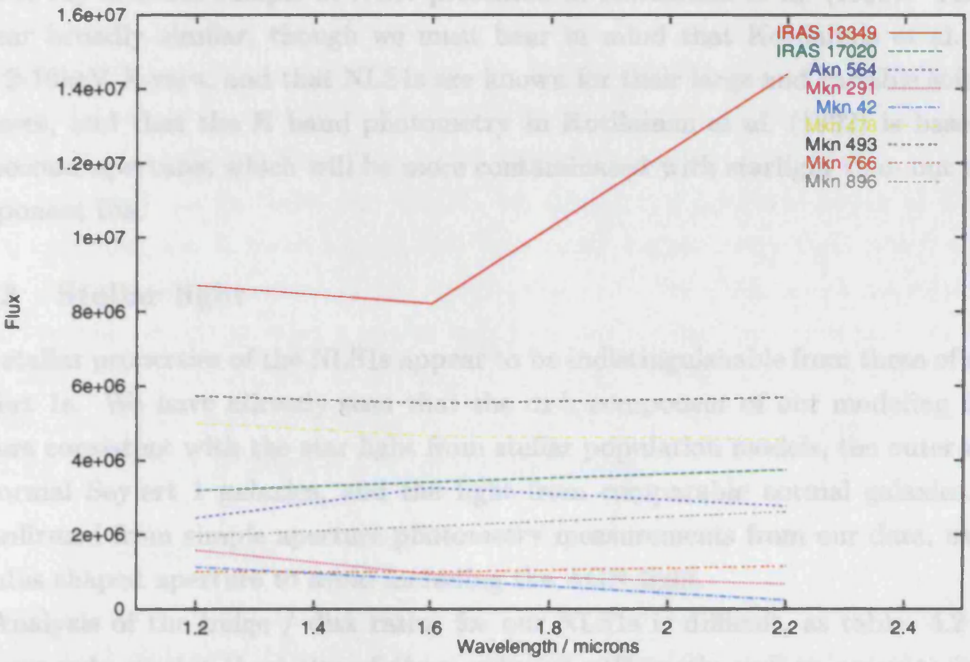

Figure 4.86: Near IR SEDs of the NLS1s. Wavelength in μm, flux in $10^{-20} W m^{-2} \mu m^{-1}$

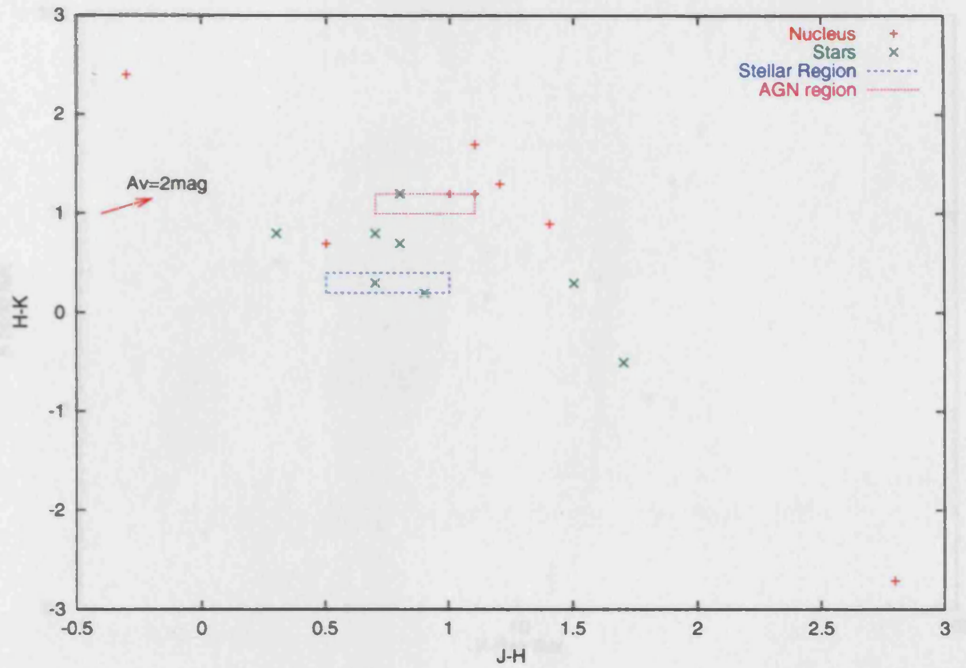

Figure 4.87: J-H vs H-K for the NLS1 nuclear components

X-ray flux from Brandt (1996). We can compare this to similar plots for a complete, hard X-ray selected sample of AGN presented in Kotilainen et al. (1992). The plots appear broadly similar, though we must bear in mind that Kotilainen et al. (1992) plot 2-10keV X-rays, and that NLS1s are known for their large and variable soft X-ray excesses, and that the K band photometry in Kotilainen et al. (1992) is based on 3 arc-second apertures which will be more contaminated with starlight than our nuclear component fits.

4.6.3 Stellar light

The stellar properties of the NLS1s appear to be indistinguishable from those of normal Seyfert 1s. We have allready seen that the disk component of our modeling fits has colours consistent with the star light from stellar population models, the outer regions of normal Seyfert 1 galaxies, and the light from comparable normal galaxies. This is confirmed from simple aperture photometry measurements from our data, using an annulus shaped aperture to avoid including the AGN light.

Analysis of the bulge / disk ratios for our NLS1s is difficult, as table 4.2 shows that we only resolve the bulge of these galaxies sufficiently well to separate it's flux from that of the AGN,using our modeling process, in half of our sample. However, for the objects where we are able to separate the bulge and AGN components, we obtain

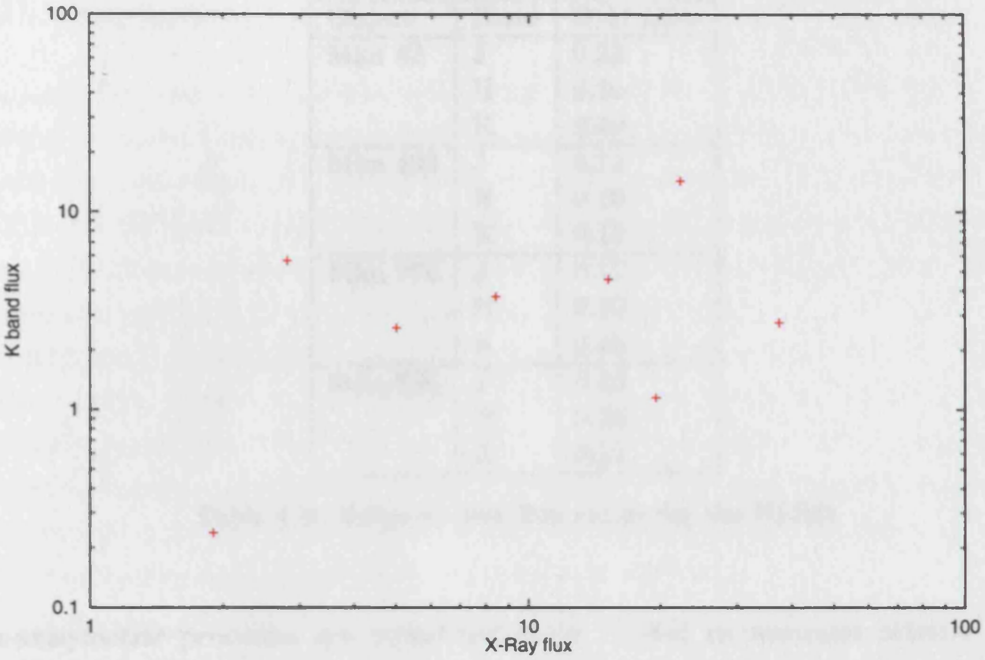

Figure 4.88: X-ray vs K band nuclear component flux for our NLS1s. X-ray data in units of $10^{-12}ergcm^{-2}s^{-1}$. K band in $10^{-14}Wm{-}2$.

the values in table 4.3. These values are consistent with those obtained for normal, inactive, spiral galaxies (e.g. Koeppen & Arimoto 1990, Giuricin et al. 1995), though the large spread of values published for this figure should be noted. We note the fact that our data tends to show an increasing bulge to disk ratio as we go from J to K band. We cannot be sure that this effect is not introduced by the observation or modeling techniques used; for example, the UKIRT tip-tilt system performs better at K than J band, and thus the K band images will be slightly higher resolution, which will lead to an apparent enhancement of the bulge relative to the disk as compared to the J band images, especially with a model based deconvolution algorithm such as the one used here. Whilst this effect is not large enough to account for the values presented, it prevents of from drawing quantative conclusions as to the stellar population or dust property differences between the bulge and disk areas.

4.6.4 Galactic Bars

Galactic Bars are an important part of AGN fueling; although fuel, in the form of stars, gas and dust, is plentiful in the disks of galaxies, it is not obvious how this material can be brought through the centrifugal barrier in to the nucleus of the host galaxy where it can join the accretion disk of the AGN. Galactic bars, and other large scale

Object	Band	B/D ratio
Mkn 42	J	0.23
	H	0.29
	K	0.40
Mkn 493	J	0.13
	H	0.10
	K	0.18
Mkn 766	J	0.11
	H	0.20
	K	0.43
Mkn 896	J	0.13
	H	0.14
	K	0.25

Table 4.3: Bulge to disk flux ratios for the NLS1s

non-axisymetric processes are considered to be related to starburst activity within the central few kilo-parsecs, which occurs preferentially in barred host galaxies (e.g. Heckman 1980). Bars and other non-axisymetric distortions in the host galaxy, such as disturbed morphologies from tidal interactions, have long been associated with the AGN fueling process (e.g. Dahari 1984), though features such as dust lanes can easily obscure bar features in optical data. Recent advances in this field have thus been made in the near IR, where dust obscuration is less able to confuse the assessment of the mass distribution in the imaged galaxies.

Knapen et al. (2000) derive bar statistics for a sample of Seyfert and normal galaxies from near IR imaging, by assuming that a bar exists whenever the radial profile of a galaxy image shows an increase in ellipticity over the same radius range as an approximately constant position angle. This is the case for 6 of our 9 objects (Mkn 766, Mkn 896, Mkn 493, Mkn 42, Mkn 291 and IRAS 17020). This bar fraction is consistent with that given for Seyferts in Knapen et al. (2000) (20 out of 29 objects), though our statistics are obviously limited by our small sample size.

If NLS1s gain their obscure properties by accreting close to their Eddington limit, we might expect to see an increased bar fraction in the NLS1s as a result of the need to transport more fuel to the nucleus. Our finding that the bar fractions in normal Seyferts and NLS1s are similar are consistent with a slightly higher bar fraction in the NLS1s, given the limitations created by the small sample size in our study.

4.7 Discussion

It appears that our initial aims to completely separate the nuclear AGN light from the starlight of the host galaxy by spatially resolving the nuclear bulge in the host were, in general, too optimistic. Even with the good spatial resolution obtained from UKIRT / UFTI ($\approx$ 0.3"), in many cases, the galactic bulge, if present, remained essentially unresolved, though we do claim that our models do perform better than simply reducing the size of a synthetic photometry aperture.

Additionally, we again come across the problem of the lack of a consistent comparison sample in the literature. There are a wide and diverse range of methods for attempting to separate AGN and starlight contributions to photometry data, and it is difficult to compare results from different methods, each of which usually applies best to a given type of data. This is linked to the fact that galaxy morphology is a complex subject in its own right, even without the AGN complication.

Further, we note that even in situations where our modeling seems successful, there are still some indications of complications; for example in Mkn 896, where we fit three model components, leaving minimal residuals, and have physically satisfactory model parameters (eg the nuclear Gaussian fit has a width consistent with the width of the point spread function of the imaging system). In this case, we might be satisfied that we have successfully separated the AGN and nuclear components, until we examine the HST data displayed in figure 4.9, which reveals spiral structure within the region we have classed as the nuclear AGN. Such spiral structure can only originate from starlight, thus demonstrating that we have not really modeled the stellar contribution well. On a more positive note, if we accept that our nuclear component is thus still contaminated with starlight, we can still use it as an upper limit to the true nuclear flux, in the knowledge that it will be closer to the true value that a simple aperture photometry value, even if a synthetic aperture is placed around the PSF of the nucleus in the image.

4.8 Conclusions

In summary, we can conclude the following main points from this work,

- The Near IR colours of the Active nucleus in NLS1s, as measured from the nuclear component of the model fits to our images, are consistent with those of other Seyfert 1s presented in the literature.

- The Near IR colours of the star light from the host galaxies of NLS1s, as measured from the non nuclear components of the model fits to our images, are consistent with those of normal stars and galaxies.

- The IR to X-ray flux ratio from the NLS1s is consistent with that from other Seyfert 1s.

We have no evidence to suggest that the NLS1s are in any way different from normal Seyferts in terms of the results of our near IR imaging studies.

In addition, these studies do not reveal convincing evidence that the NLS1s might be preferentially oriented face on to our line of sight. Future work involving more sophisticated, 2 dimensional, modeling of the images will allow us to asses whether "inner bar" structures within the image allow us to place any constraints on the orientation of the AGN in these images.

Chapter 5

SEDs of NLS1s

5.1 Introduction

NLS1s have been noted for their unusual optical spectra and more recently for their unusual X-ray properties. We wish to investigate whether NLS1s are unusual in other wavebands too, and as part of this investigation, have built up Spectral Energy Distributions (SEDs) over various parts of the spectrum for a sample of NLS1s.

Investigation of the mid to far IR regions has been made possible through the use of the ISOPHOT photometer on board ISO, the Infrared Space Observatory. We have extended the wavelength coverage of this data into the sub-mm region with observations using the Sub-mm Common User Bolometer Array (SCUBA) on the James Clerk Maxwell Telescope (JCMT) on Mauna Kea, Hawaii.

The ISO (Kessler et al. 1994) was a 60cm diameter aperture satellite telescope cooled with 2000 litres of super fluid helium, which operated from November 1995 until April 1998 when its cryogen became exhausted.

There are two key ISO programmes investigating AGN; a European Core Programme focussed at low redshift, and a US Key Project to examine quasars spanning a large range of redshifts and SEDs (eg X-ray and radio quiet / loud). This data should provide a useful comparison sample to many other projects. Despite significant problems with the ISO data calibration, particularly of faint objects such as quasars, the Key Project data should be published shortly.

Photometry data from the literature have also been accumulated to define the SEDs of NLS1s, though the fact that this data has been obtained with a broad and inhomogeneous range of instrumentation, techniques, aperture sizes and analysis methods makes it necessary to verify independently any interesting effects which appear in the data.

5.2 ISO and SCUBA photometry

A detailed report of this work is given by Law-Green, Hirst, Boisson, O'Brien & Ward (2000); a summary of the results is presented here.

We have observed 10 NLS1s with ISOPHOT at wavelengths between 4μm and 160μm. 8 NLS1s were also observed with SCUBA at 450μm and 850μm. Two were securely detected at 850μm. In common with previous ISO results, we find that the mid to far IR emission of the NLS1s is well described by a two component dust emission model, comprising two black body components, generally at temperatures of around 300K and 80K. In objects where we include near IR and optical photometry points, a third black body component at around 1500K fits the data well. An example is given in figure 5.1.

Initial results (figure 5.2, from Law-Green et al. (2000)) suggest possible correlations between the temperature parameters of the black body fits, and the radio and X-ray luminosities of the objects.

We note at this point that radio quiet AGN tend to radiate about 30% of their total luminosity in the far IR band. In extreme cases this can rise to almost 90% of the bolometric luminosity. Thermal dust is thought to be the only significant emission mechanism in the sub-mm through thermal IR regions (Robson 1996).

5.3 Full SEDs

Photometry data was mined from the NASA Extragalactic Database (NED[1]), to build up SEDs of NLS1s over as broad a frequency range as possible. Unfortunately, few objects in the database actually have such a broad range of data points, and it should be remembered that these data are highly inhomogeneous, being taken from observations using a broad range of techniques, instrumentation and parameters such as aperture size. However, they still serve as a useful guide to the SEDs of NLS1s. Figures 5.3–5.19 show the data thus obtained for objects where NED returned 5 or more detections. Figure 5.20 shows a composite SED of all the NED returned data points, normalised at 12μm. The X axis in these plots shows the frequency, ν in Hz, plotted on a log scale, the Y axis shows νF_ν in Wm^{-2}, on a log scale. The error bars shown are those returned as the uncertainty in the photometry value by NED. We plot νF_ν rather than simply F_ν as the former represents the total power radiated per unit frequency, rather than simply the flux density which has units of $Wm^{-2}Hz^{-1}$ and thus represents a different amount of energy at different frequencies.

[1]The NASA/IPAC Extragalactic Database (NED) is operated by the Jet Propulsion Laboratory, California Institute of Technology, under contract with the National Aeronautics and Space Administration.

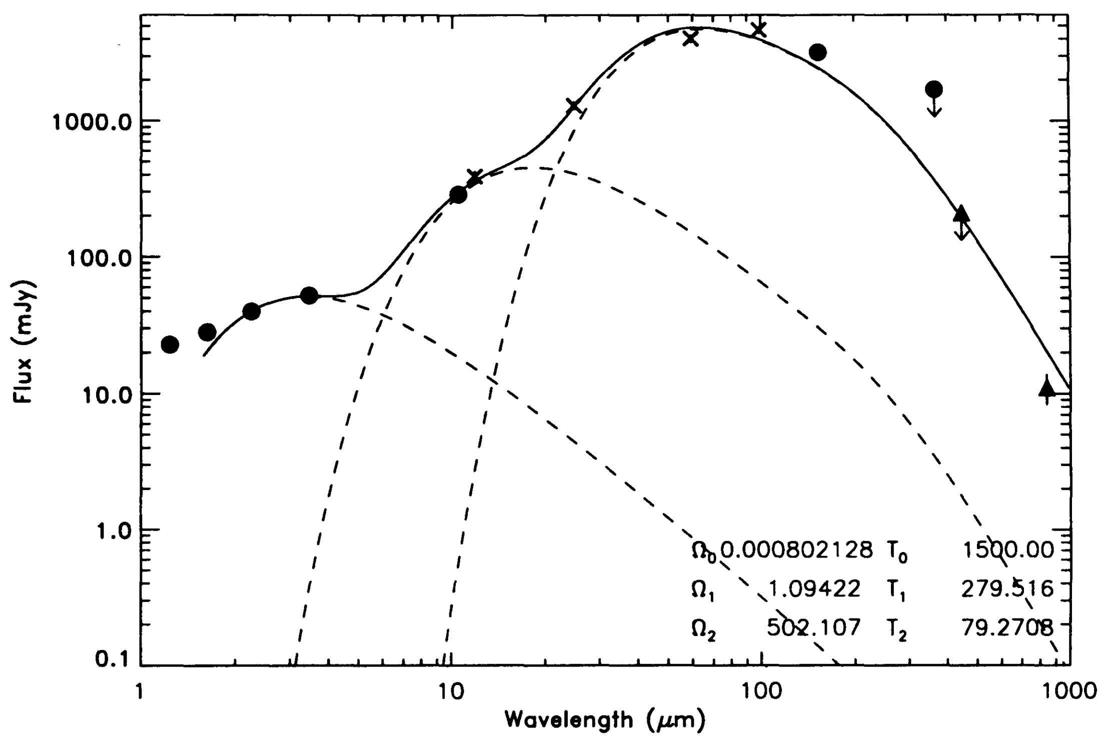

Figure 5.1: 3 component black body model fit to the SED of Mkn 766, from Law-Green et al. (2000)

These SEDs do not appear remarkable when compared to published SEDs of other types of AGN (e.g. Elvis et al. 1994). Obviously, NLS1s, are in general, radio quiet, which is obvious in comparison to radio loud quasar SEDs. Many of the notable SED features of the NLS1 class, for example the ultra soft X-ray spectrum, are not apparent in these diagrams, simply due to the manner in which the data are presented; X-ray astronomers often quote a single X-ray flux and a spectral index as a broad measure of the X-ray spectrum. Only the flux gets recorded by the NED photometry database, and thus the soft X-ray excess is not noted. Although NED records flux points from all the publications contained in its source list, and thus will imply variability if different papers provide obviously different photometry values, it tends to be poor at noting X-ray and short time scale variability. This is because many of these studies are done from monitoring the light curve during an (often fragmented) observation, resulting in a single publication detailing the light curves, rather than from different observers noting different flux values between separate observations spaced months to years apart. In addition, where photometry from different publications appear to be mutually inconsistent, it is often the case that the difference can be explained by the difference in aperture sizes, filters or observing techniques employed by the different authors,

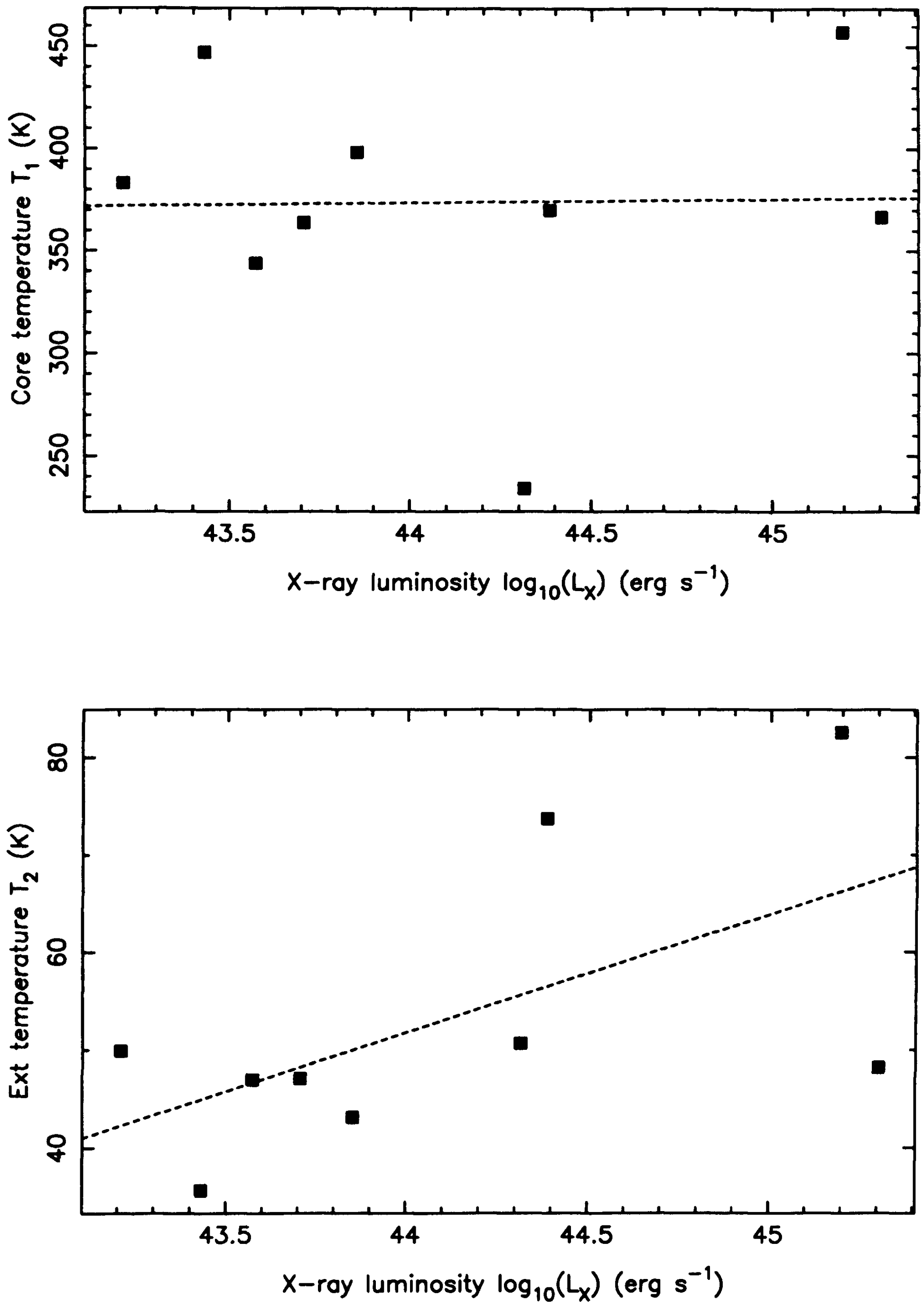

Figure 5.2: Black body fit temperatures vs X-ray luminosity, from Law-Green et al. (2000)

especially when combined with a realistic estimate of the errors on the photometry data.

Taking the composite plot at face value, a striking feature is the range of spectral slopes present in the data. From being normalised at $12\mu m$ the data spreads over a range of 10^3 in X-ray flux. Whether this represents variability, intrinsic diversity in the source population or results from the range of data reduction techniques, is unclear from this data alone. In reality, it would seem that all three factors play some role. In subjectively comparing this data with published SEDS (e.g. Elvis et al. 1994), no obvious differences are noted.

5.4 Conclusions

This initial study suggested that a more complete investigation of the SEDs of NLS1s, particularly in the Far IR – Sub mm region, would be interesting in terms of investigating dust density and temperature distributions in NLS1s. This project was carried out using data from the FIR photometer on board the ISO satellite and the SCUBA sub millimetre camera on the JCMT. Results of this study are presented in Law-Green et al. (2000).

This data supports thermal dust emission as the significant emission mechanism for the mid to far IR radiation from our NLS1 sample. Our data is consistent with two, or sometimes three, distinct dust regions at different temperatures, a cool extended component at 40–80K, a warm component at 250–450K and a hot component at $\approx$ 1500K. Black body models of these three dust distributions accurately model the 4–$1000\mu m$ emission from the NLS1s we have studied.

We also note that the temperature ratio of the warm to cool dust components appears to be anti correlated with the radio luminosity of the NLS1s (Law-Green et al. 2000). Assuming that the bright radio sources are beamed, and thus to some degree pole-on, the correlation is in the sense that pole-on sources have a warmer cool dust, or cooler warm dust. It is unclear whether this can be attributed to a geometric effect such as orientation or obscuration.

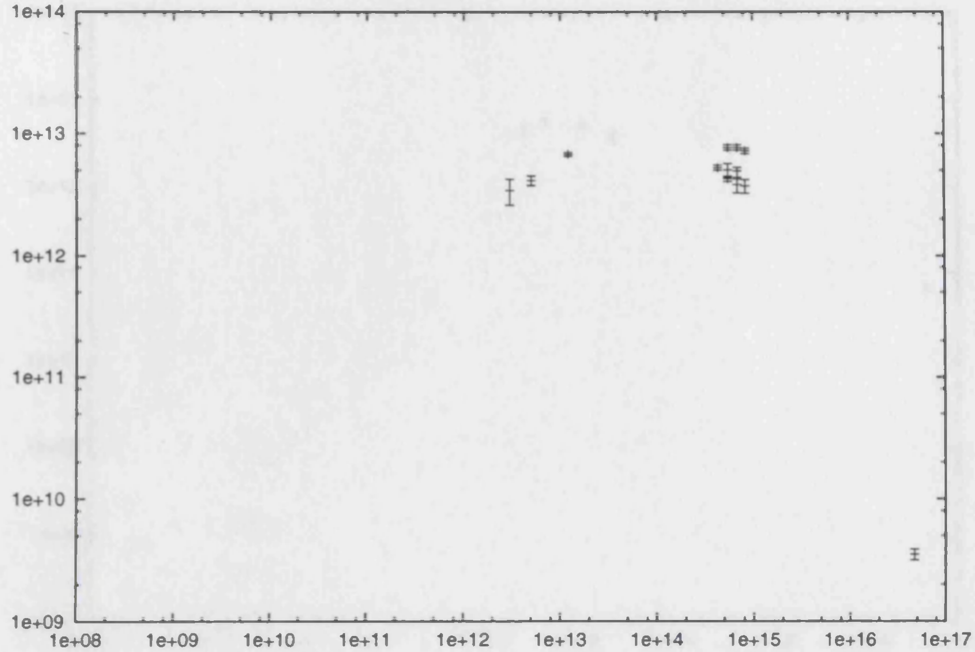

Figure 5.3: SED of 1E 1346+266

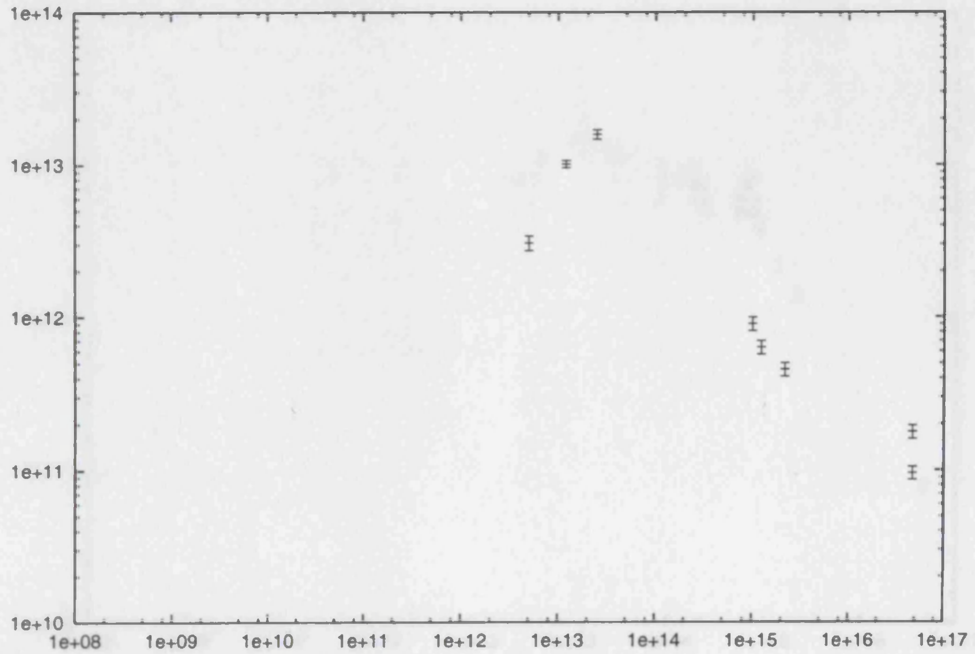

Figure 5.4: SED of IRAS 13349+2438

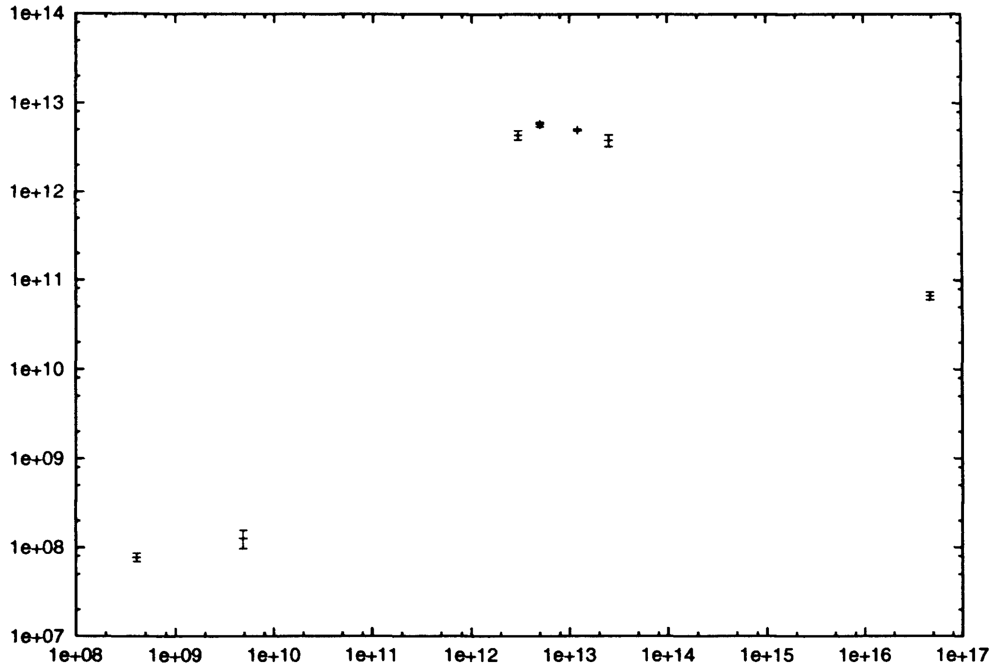

Figure 5.5: SED of IRAS 17020+4544

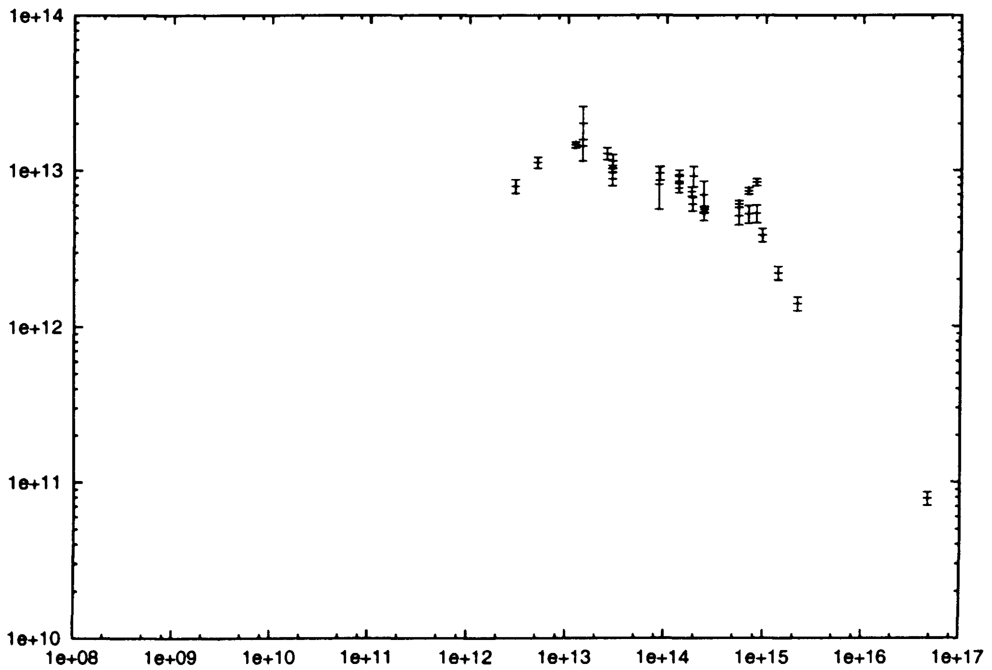

Figure 5.6: SED of I Zw 001

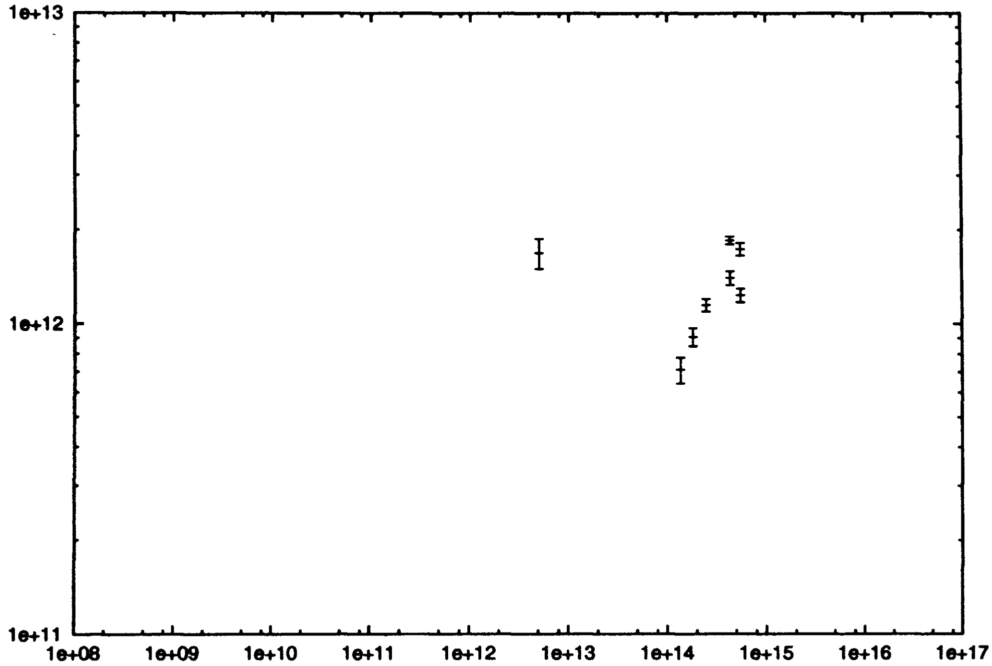

Figure 5.7: SED of MRK 291

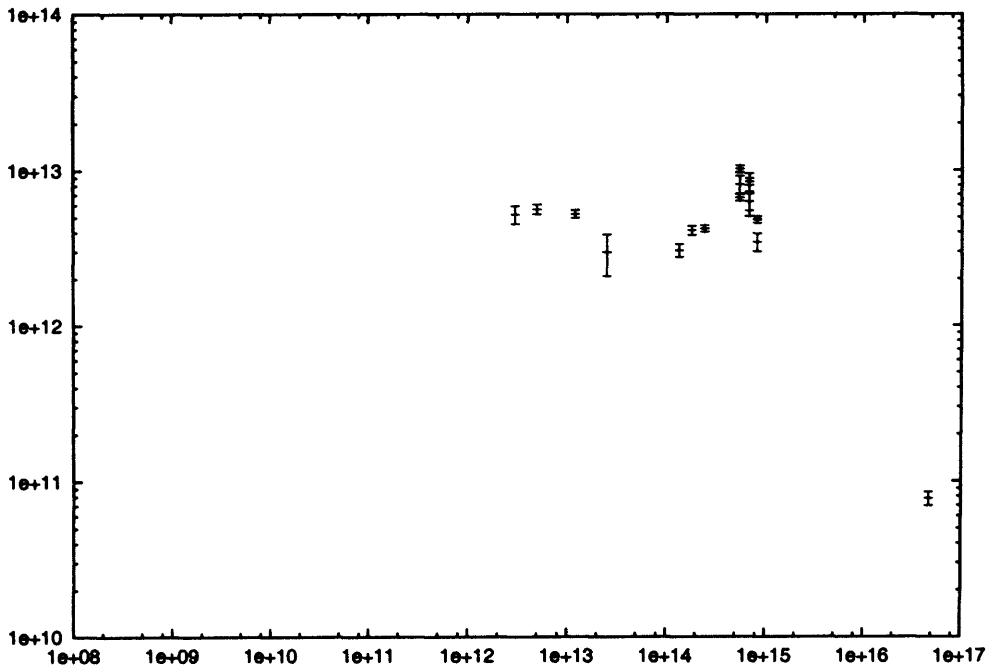

Figure 5.8: SED of MRK 359

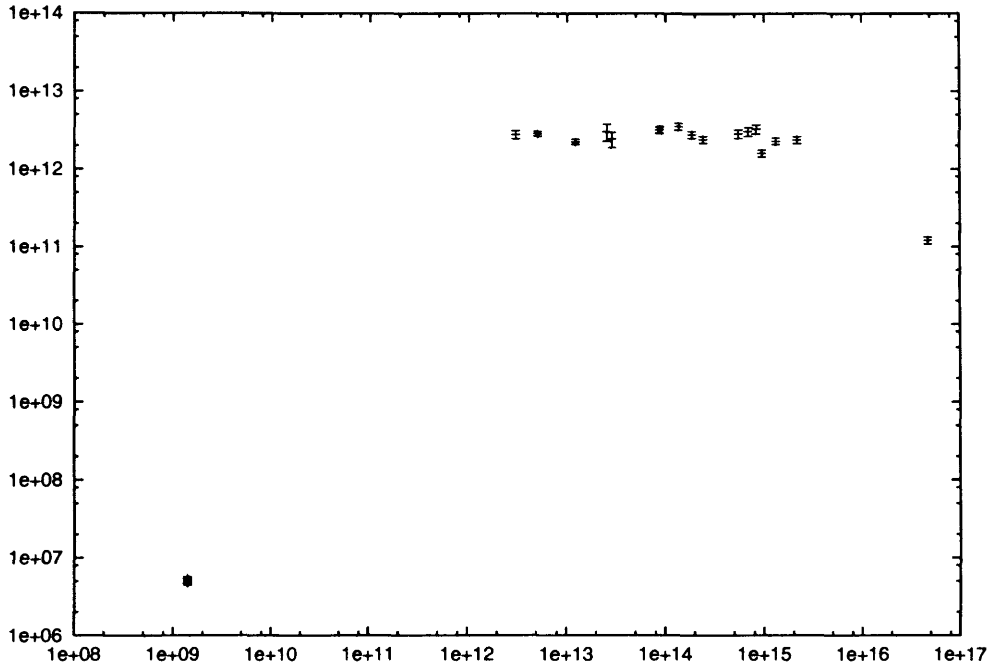

Figure 5.9: SED of MRK 478

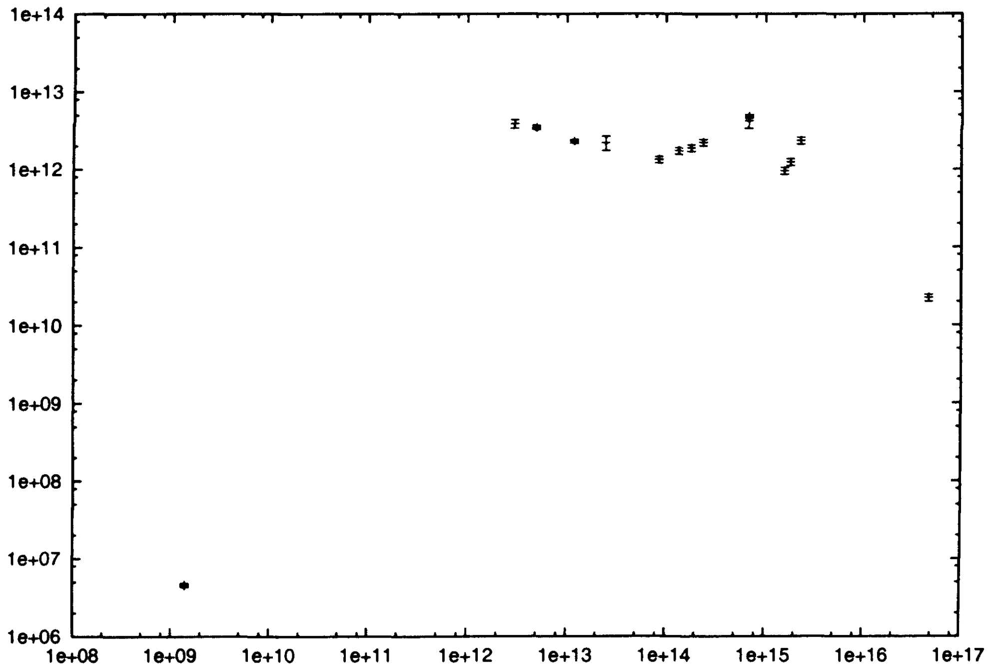

Figure 5.10: SED of MRK 493

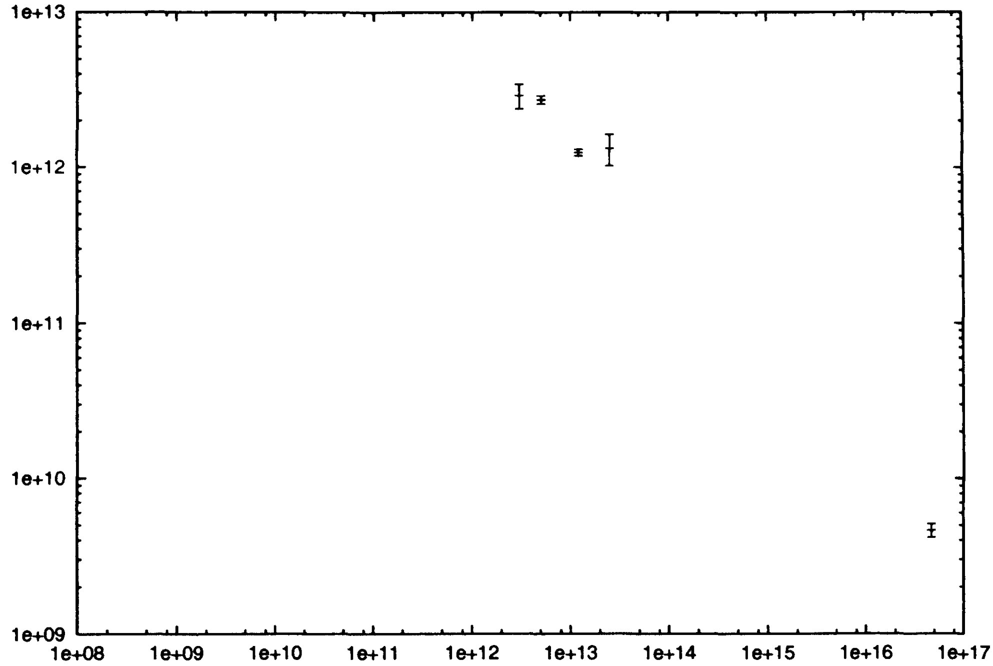

Figure 5.11: SED of MRK 507

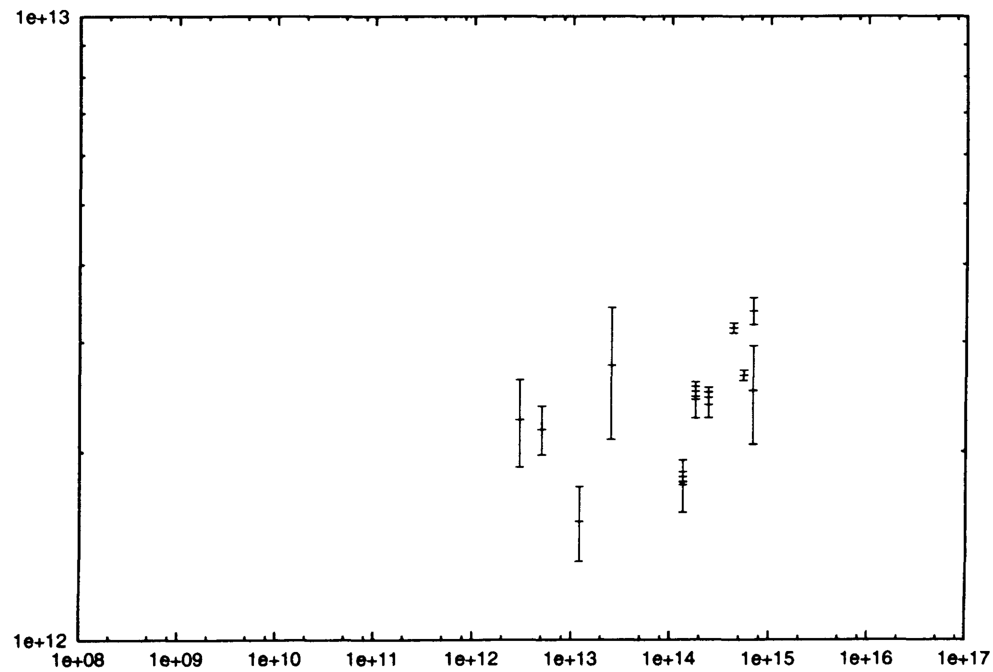

Figure 5.12: SED of MRK 684

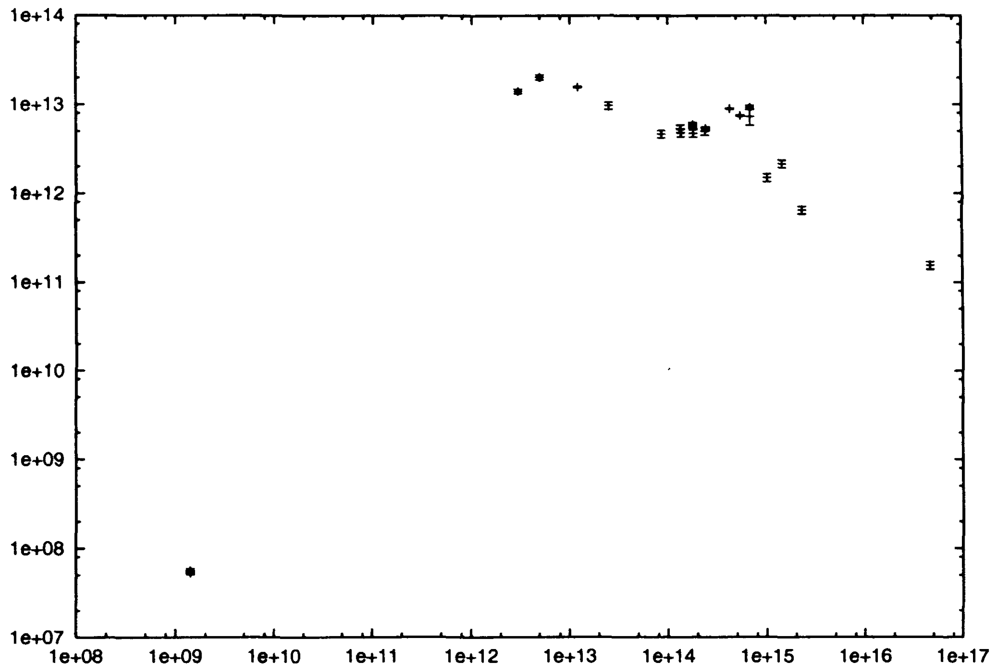

Figure 5.13: SED of MRK 766

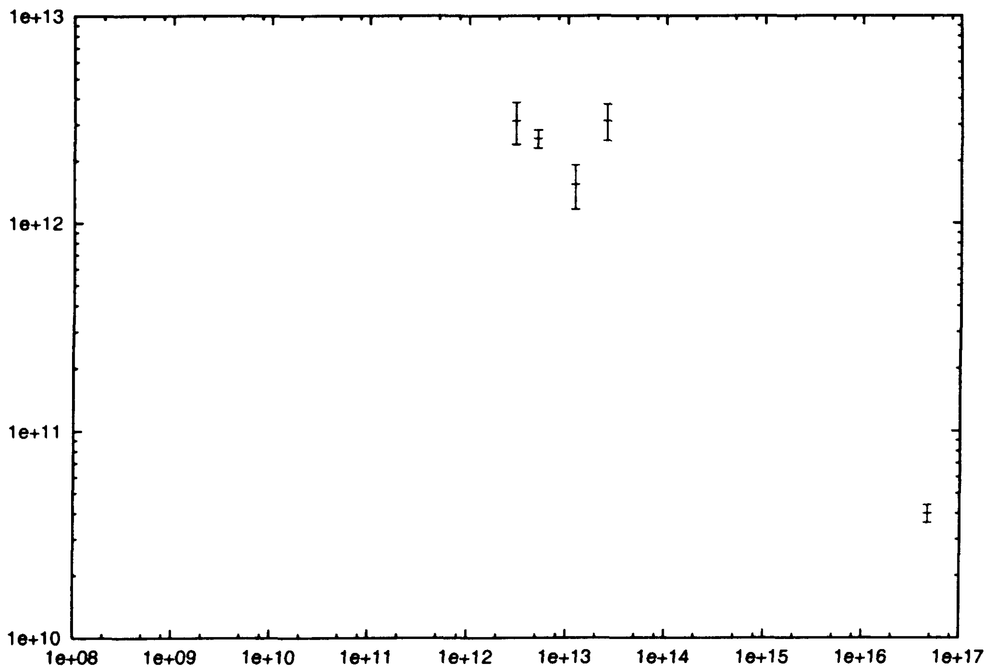

Figure 5.14: SED of MRK 896

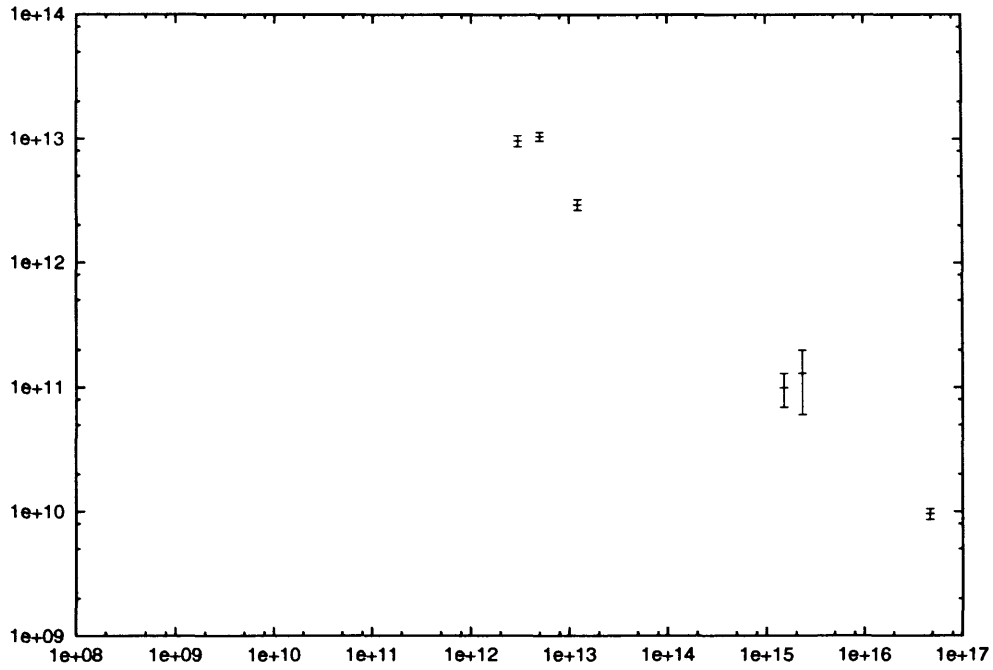

Figure 5.15: SED of MRK 957

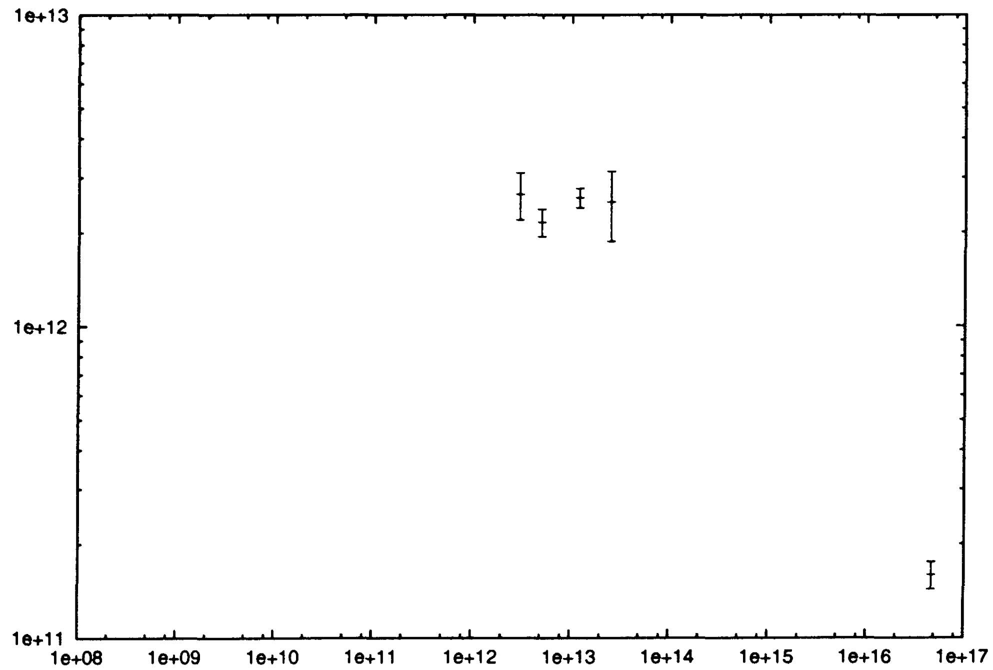

Figure 5.16: SED of MRK 1044

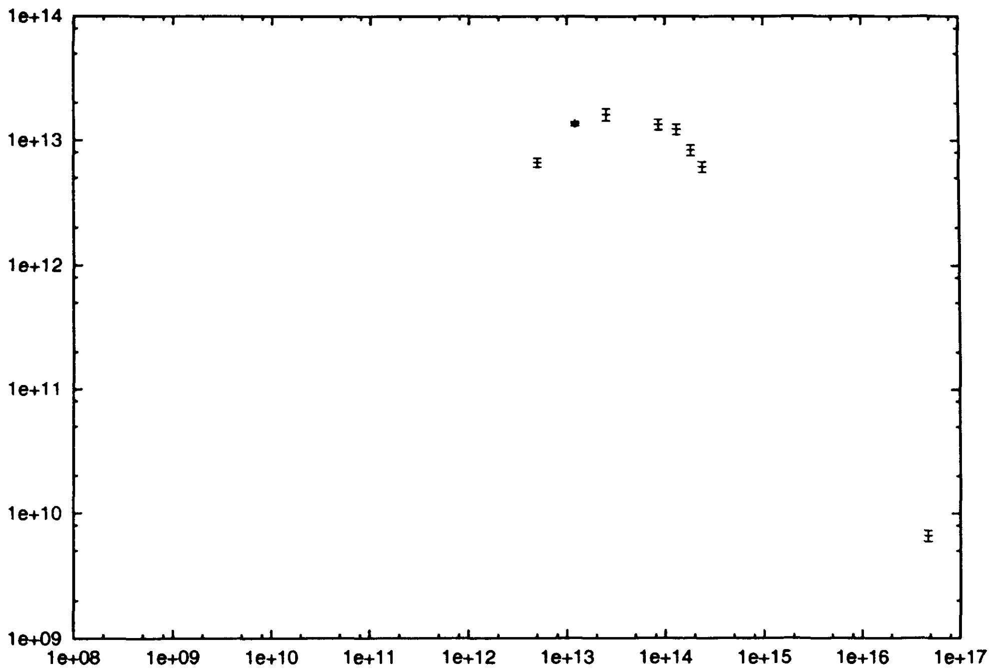

Figure 5.17: SED of MRK 1239

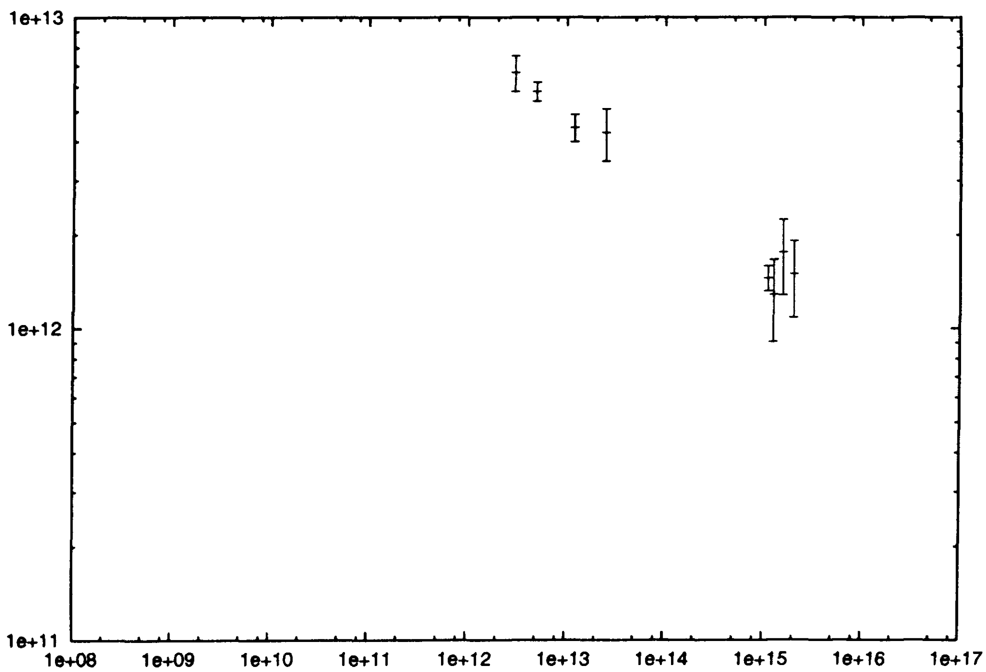

Figure 5.18: SED of NGC 4748

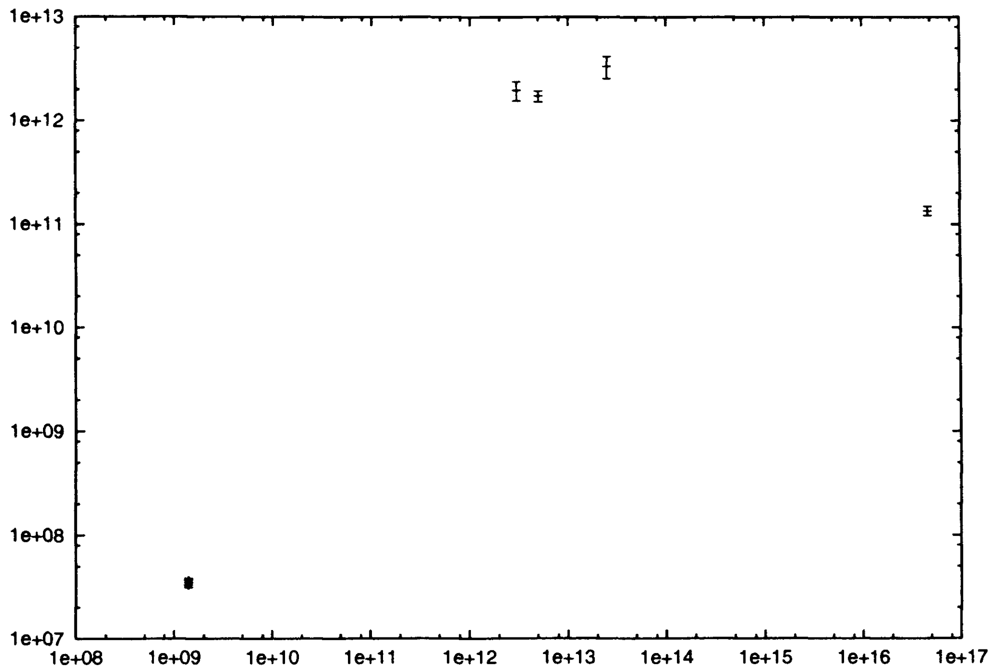

Figure 5.19: SED of RE J1034+393

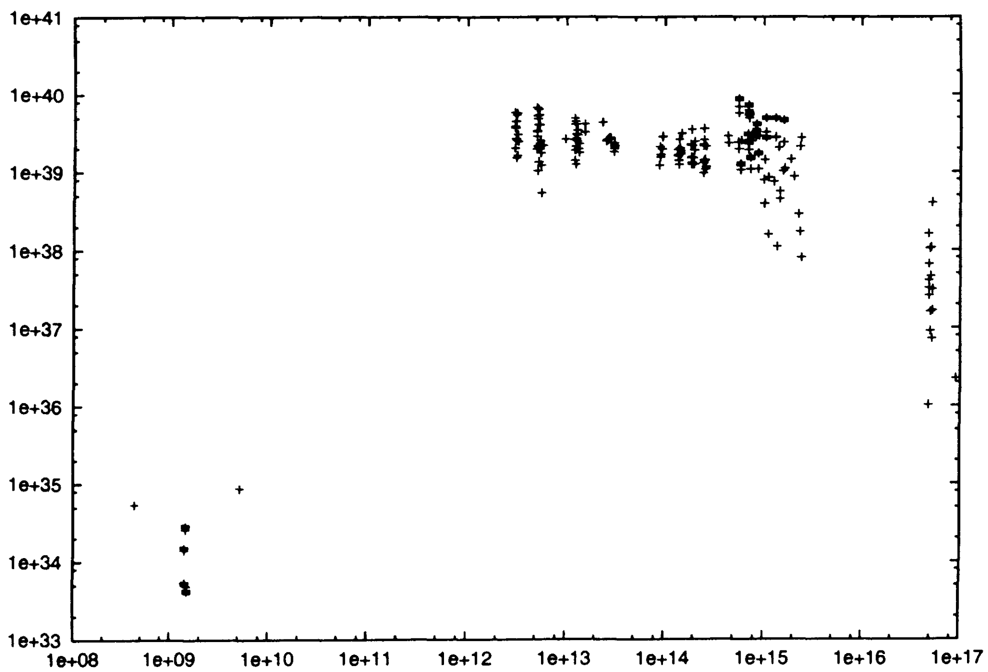

Figure 5.20: Composite SED

Chapter 6

Conclusions and Future Work

Originally, a class of NLS1s were identified based on their optical spectroscopic properties. Later it appeared that they showed unusual characteristics in the X-ray spectra. The work reported here aimed to investigate whether, as a class, NLS1s display significant differences to BLS1s in other ways, eg. their IR spectra and morphology, radio properties and spectral energy distributions.

The first order conclusion is that in the above respects their properties are not significantly different from BLS1s. Although a negative result, it is nevertheless important in placing NLS1s in the broader context of AGN unification schemes.

6.1 Overview

We have reviewed the literature on AGN and especially NLS1s, including the currently available models of the NLS1 phenomenon, and how they fit in with general models of AGN. NLS1s are problematic in that they do not have an obvious slot in the orientation based unified scheme. Various models have been proposed, both to fit NLS1s into the OBUS, and to unify them with BLS1s through non orientation based schemes. It has become clear that orientation effects may play a smaller role in unifying AGN generally than originally thought, and that at least in some objects or types of object, dust further out in the host galaxy might dominate over the hypothetical dust torus in providing the obscuration which appears to play a large role in AGN appearances.

We have carried out near IR spectroscopic observations of a sample of NLS1s, and find that none of the NLS1s show broad components to their near IR permitted lines, through to Pa α in the K band. This suggests that the broad components to the optical lines are not being reddened out by moderate amounts of dust. We analyse the Balmer decrements of the permitted hydrogen lines to search for evidence of reddening, and find that the data are consistent with un-reddened line ratios from case B recombination theory at 20,000K, concluding that dust does not significantly affect the Hydrogen line emission from NLS1s. Some of our NLS1s show near IR high ionisation lines, though this does not appear to be a universal feature of the class.

We have acquired radio image data, both from data archives and new observations we obtained using both the VLA and MERLIN. Our radio data suggests that the pole-on model is not generally valid for all NLS1s. However it might be consistent for the subset of NLS1s showing a correlation between radio luminosity and optical continuum polarisation and which appear to be those objects showing radio structures suggestive of pole-on orientation. This is a tenuous result at present, and we plan to test it more extensively shortly, based on additional observations.

Imaging studies of NLS1s in the near infrared, have been carried out using the UFTI camera on UKIRT, followed by modeling to separate the light contributions from the host galaxy and active nucleus. We note that it is difficult to make detailed quantative comparisons to the results reported in other papers in the literature due to the lack of a standard method of separating the AGN from the galactic disk and bulge light.

6.2 Extreme examples in the NLS1 population

Although the statistics are limited, our data do suggest that the NLS1 population may include examples that sample the extremes of parameter space. This suggestion is triggered by figure 3.22, which shows Mkn 1239 and Mkn 766 as "unusual" objects in a plot of optical continuum polarisation vs radio power, followed immediately by the fact that Mkn 766 shows strong signs of jet activity in our radio data from both the VLA and MERLIN. Mkn 766 is unique in our VLA data set as none of the other sources show resolved structure in the VLA images. The jet appears distorted, possibly through projection, indicating that the AGN in Mkn 766 could be oriented pole-on to our line of sight.

Co-incidentally, the only other object for which we have high resolution MERLIN data is Mkn 1239, another of the high polarisation objects. Mkn 1239 shows less direct evidence of jet activity in its radio source - we observe a double, or possibly triple, structure, but no direct evidence for a jet.

Finally we notice that in the near IR spectra, Mkn 766 shows a good signal to noise ratio, yet we see no signs of the high ionisation species present in most of the other bright targets. This could be taken as evidence to suggest that the high accretion rate model does not apply to Mkn 766.

6.3 Narrow and Broad line Seyfert 1s

We propose that two models in the literature for NLS1s can account for the properties of most NLS1s. Firstly, the majority of NLS1 like objects appear to be consistent with models suggesting that NLS1s are in similar orientations to BLS1 objects, and that they have an unusually low mass central black hole, which is accreting close to its Eddington rate. Secondly, we suggest that Seyfert 1 objects which are in "pole-on" orientations to our line of sight do take on some of the properties of NLS1s. We cite Mkn 766 as an example of this; it shows bent jet structure in its radio morphology, high radio power and optical continuum polarisation, yet does not show high ionisation lines in its near IR spectrum.

6.4 Future Work

This work has provided an interesting, yet difficult to interpret, dataset.

Firstly, extensive photo-ionisation modeling of the emission line properties of the NLS1s is now possible. Other workers have studied and published optical spectra of many of our targets, so a model grid utilising CLOUDY or a similar code, can now be constrained with emission line data covering an extended range of ionisation potentials. This will allow us to parameterise the "hidden" high energy UV / ultra soft X-ray continuum, which is unobservable directly due to galactic hydrogen absorption. In addition, the extra hydrogen line and continuum data provided by the infrared data will enable the modeling of the effects of dust on the emission spectra to be be constrained much more tightly.

Our work on the radio properties of the NLS1s is an on going project as telescope schedules complete outstanding observations. Also, these observations can be combined to give enhanced data, for example concatenating the UV datasets from quasi-simultaneous VLA and MERLIN observations leads to maps covering a broader range of spatial frequencies than is possible from either of the two datasets independently. In addition, as mentioned in Chapter 3, our pending VLA data sets will provide the positional accuracy to allow us to map our remaining MERLIN data, providing high resolution images of a reasonable sample of NLS1s.

In the longer term future, instruments such as the Atacama Large Millimeter Array (ALMA) will allow milliarcsecond resolution imaging at millimetre wavelengths, allowing comparison of the radio and millimetre wave source structures, and possibly resolution of the dust distribution within the source. Detailed analysis of the SEDs will allow us to investigate what fraction of the optical / UV continuum is absorbed by the torus and re-radiated in the IR, which allows us to place more constraints on orientation models.

Techniques for the quantatitive analysis of galaxy images seem to be immature at the moment; efforts concentrate on the historical methods of simply carrying out photometry through different synthetic aperture sizes. Elliptical isophote and other kinds of surface photometry analysis work well under certain situations, but are limited when applied to a complex morphology such as a spiral containing an AGN.

Our future work will involve the development of image analysis techniques suitable for the analysis of images of the kind we obtained with UFTI and present in chapter 4. Computation resources are now available to carry out 2 dimensional fitting of a model to image data, making the need for some kind of radial or azimuthal fitting un-necessary. As it is this fitting that cannot easily cope with complex structures in the image, we anticipate that 2 dimensional modeling will be much more successful in parameterising galaxy and AGN host galaxy images.

Bibliography

Alonso-Herrero, A., Simpson, C., Ward, M. J. & Wilson, A. S. (1998), 'A near-infrared imaging study of Seyfert galaxies with extended emission-line regions', *Ap.J.* **495**, 196+.

Antonucci, R. (1993), 'Unified models for active galactic nuclei and quasars', *Ann. Rev. Ast. Ast* pp. 473+.

Becker, R. H., White, R. L. & Helfand, D. J. (1995), 'The first survey: Faint images of the radio sky at twenty centimeters', *Ap.J.* **450**, 559+.

Beichman, C. A., Soifer, B. T., Helou, G., Chester, T. J., Neugebauer, G., Gillett, F. C. & Low, F. J. (1986), 'Discovery of an infrared-loud quasar', *Ap.J.Lett.* **308**, L1–L5.

Best, P. N., Longair, M. S. & Rottgering, H. J. A. (1996), 'Evolution of the aligned structures in z 1 radio galaxies', *MNRAS* **280**, L9–L12.

Bischoff, K. & Kollatschny, W. (1999), 'Strong optical line variability in MKN 110', *A. & A.* **345**, 49–58.

Bleakley, P. (2000), Optical Observations of NLS1s, PhD thesis, University of Leicester. In Prep.

Boller, T., Brandt, W. N. & Fink, H. (1996), 'Soft X-ray properties of narrow-line Seyfert 1 galaxies.', *A. & A.* **305**, 53+.

Boroson, T. A. & Green, R. F. (1992), 'The emission-line properties of low-redshift quasi-stellar objects', *Ap.J. Suppl. Ser.* **80**, 109–135.

Brandt, N. B. (1996), Aspects of soft X-ray activity in the centres of radio-quiet active galaxies, PhD thesis, University of Cambridge.

Bridle, A. & Greisen, E. (1998), *AIPS cookbook*, The National Radio Astronomy Observatory.

Brotherton, M. S. (1996), 'The profiles of H beta and [O III] 5007 in radio-loud quasars', *Ap.J. Suppl. Ser.* **102**, 1+.

Clarke, B. G. (1980), 'An efficient implementation of the algorithm clean', *A. & A.* **89**, 377–378.

Clavel, J., Nandra, K., Makino, F., Pounds, K. A., Reichert, G. A., Urry, C. M., Wamsteker, W., Peracaula-Bosch, M., Stewart, G. C. & Otani, C. (1992), 'Correlated hard X-ray and ultraviolet variability in NGC 5548', *Ap.J.* **393**, 113–125.

Clavel, J., Reichert, G. A., Alloin, D., Crenshaw, D. M., Kriss, G., Krolik, J. H., Malkan, M. A., Netzer, H., Peterson, B. M., Wamsteker, W., Altamore, A., Baribaud, T., Barr, P., Beck, S., Binette, L., Bromage, G. E., Brosch, N., Diaz, A. I., Filippenko, A. V., Fricke, K., Gaskell, C. M., Giommi, P., Glass, I. S., Gondhalekar, P., Hackney, R. L., Halpern, J. P., Hutter, D. J., Joersaeter, S., Kinney, A. L., Kollatschny, W., Koratkar, A., Korista, K. T., Laor, A., Lasota, J. P., Leibowitz, E., Maoz, D., Martin, P. G., Mazeh, T., Meurs, E. J. A., Nair, A. D., O'Brien, P., Pelat, D., Perez, E., Perola, G. C., Ptak, R. L., Rodriguez-Pascual, P., Rosenblatt, E. I., Sadun, A. C., Santos-Lleo, M., Shaw, R. A., Smith, P. S., Stirpe, G. M., Stoner, R., Sun, W. H., Ulrich, M. H., Van Groningen, E. & Zheng, W. (1991), 'Steps toward determination of the size and structure of the broad-line region in active galactic nuclei. i - an 8 month campaign of monitoring NGC 5548 with IUE', *Ap.J.* **366**, 64–81.

Condon, J. J., Cotton, W. D., Greisen, E. W., Yin, Q. F., Perley, R. A., Taylor, G. B. & Broderick, J. J. (1998), 'The NRAO VLA Sky Survey', *AJ* **115**, 1693–1716.

Conway, J. (1984), Images from the VLA. published on VLA website.

Dahari, O. (1984), 'Companions of seyfert galaxies - a statistical survey', *AJ* **89**, 966–974.

de Vaucouleurs, G. (1977), 'Contributions to the galaxy photometry. i - standard total magnitudes, luminosity curves, and photometric parameters of 115 bright galaxies in the b system from detailed surface photometry', *Ap.J. Suppl. Ser.* **33**, 211–218.

Done, C., Pounds, K. A., Nandra, K. & Fabian, A. C. (1995), 'The complex variable soft X-ray spectrum of NGC 5548', *MNRAS* **275**, 417–428.

Elvis, M., Wilkes, B. J., McDowell, J. C., Green, R. F., Bechtold, J., Willner, S. P., Oey, M. S., Polomski, E. & Cutri, R. (1994), 'Atlas of quasar energy distributions', *Ap.J. Suppl. Ser.* **95**, 1–68.

Fabian, A. C., Nandra, K., Reynolds, C. S., Brandt, W. N., Otani, C., Tanaka, Y., Inoue, H. & Iwasawa, K. (1995), 'On broad iron K-alpha lines in Seyfert 1 galaxies', *MNRAS* **277**, L11–L15.

Fanti, C., Fanti, R., Dallacasa, D., Schilizzi, R. T., Spencer, R. E. & Stanghellini, C. (1995), 'Are compact steep-spectrum sources young?', *A. & A.* **302**, 317+.

Ferguson, J. W., Korista, K. T., Baldwin, J. A. & Ferland, G. J. (1997), '"locally optimally emitting clouds and the narrow emission lines in seyfert galaxies"', *Ap.J.* **487**, 122+.

Ferguson, J. W., Korista, K. T. & Ferland, G. J. (1997), 'Physical conditions of the coronal line region in Seyfert galaxies', *Ap.J. Suppl. Ser.* **110**, 287+.

Ferland, G. J. (1996), 'HAZY, a brief introduction to CLOUDY'.

Fiore, F., Laor, A., Elvis, M., Nicastro, F. & Giallongo, E. (1998), 'The variability properties of X-Ray steep and X-Ray flat quasars', *Ap.J.* **503**, 607+.

George, I. M. & Fabian, A. C. (1991), 'X-ray reflection from cold matter in active galactic nuclei and X-ray binaries', *MNRAS* **249**, 352–367.

Giuricin, G., Tektunali, F. L., Monaco, P., Mardirossian, F. & Mezzetti, M. (1995), '"the local galaxy density and the bulge-to-disk ratio of disk galaxies"', *Ap.J.* **450**, 41+.

Goodrich, R. W. (1989), 'Spectropolarimetry of 'narrow-line' Seyfert 1 galaxies', *Ap.J.* **342**, 224–234.

Gregory, P. C. & Condon, J. J. (1991), 'The 87gb catalog of radio sources covering delta between o and + 75 deg at 4.85 ghz', *Ap.J. Suppl. Ser.* **75**, 1011–1291.

Griffiths, R. G., Warwick, R. S., Georgantopoulos, I., Done, C. & Smith, D. A. (1998), 'The broad-band X-ray spectrum of Mrk 3', *MNRAS* **298**, 1159–1168.

Grupe, D., Beuermann, K., Mannheim, K. & Thomas, H. C. (1999), 'New bright soft X-ray selected ROSAT AGN. II. Optical emission line properties', *A. & A.* **350**, 805–815.

Hawarden, T. (1999), 'in UKIRT newletter issue 5'.

Heckman, T. M. (1980), 'Star formation and activity in the nuclei of barred galaxies', *A. & A.* **88**, 365+.

Hes, R. (1995), Orientation effects in QSOs, quasars and radio galaxies, PhD thesis, Rijksuniversiteit Groningen.

Hirst, P. (1996), Infrared spectroscopy of high redshift compact steep spectrum radio sources, Master's thesis, University of Manchester.

Hirst, P., Law-Green, D. & Ward, M. (1998), Multiwavelength properties of narrow-line seyfert 1's: Studying one extreme of the agn primary eigenvector, *in* 'IAU 194: Activity in Galaxies and related phenomena'.

Högbom, J. (1974), 'Aperture synthesis with a non regular distribution of baselines', *A. & A. Suppl. Ser.* **15**, 417–426.

Hure, J. M., Collin, S. & Pineau Des Forets, G. (1994), Structure of outer regions of accretion disks in agn. non irradiated, vertically average accretion disks., *in* 'IAU Symp. 159: Multi-Wavelength Continuum Emission of AGN', Vol. 159, pp. 483+.

Jackson, N. & Browne, I. W. A. (1991), 'Optical properties of quasars - II. emission-line geometry and radio properties.', *MNRAS* **250**, 422–431.

Kent, S. M. (1985), 'CCD surface photometry of field galaxies. II - bulge/disk decompositions', *Ap.J. Suppl. Ser.* **59**, 115–159.

Kessler, M., Laureijs, R. & Trams, N. (1994), The infrared space observatory (ISO): Scientific capabilities, *in* 'American Astronomical Society Meeting', Vol. 184, pp. 3901+.

Knapen, J. H., Shlosman, I. & Peletier, R. F. (2000), 'A subarcsecond resolution near-infrared study of Seyfert and "normal" galaxies. II. Morphology', *Ap.J.* **529**, 93–100.

Kodaira, K., Watanabe, M. & Okamura, S. (1986), 'A statistical study of luminosity profiles of galaxies using spheroid-disk composite models', *Ap.J. Suppl. Ser.* **62**, 703–749.

Koeppen, J. & Arimoto, N. (1990), '"the Hubble sequence of disk galaxies - A sequence of bulge-to-disk ratios"', *A. & A.* **240**, 22–35.

Kotilainen, J. K., Ward, M. J., Boisson, C., Depoy, D. L. & Smith, M. G. (1992), 'Near-infrared imaging of hard X-ray selected active galaxies. II - The non-stellar continuum', *MNRAS* **256**, 149–165.

Kukula, M. J., Holloway, A. J., Pedlar, A., Meaburn, J., Lopez, J. A., Axon, D. J., Schilizzi, R. T. & Baum, S. A. (1996), 'Unusual radio and optical structures in the Seyfert galaxy Markarian 6', *MNRAS* **280**, 1283–1292.

Laor, A., Fiore, F., Elvis, M., Wilkes, B. J. & MCDowell, J. C. (1994), 'The soft X-ray properties of a complete sample of optically selected quasars. 1: First results', *Ap.J.* **435**, 611–630.

Laor, A., Jannuzi, B. T., Green, R. F. & Boroson, T. A. (1997), 'The ultraviolet properties of the narrow-line quasar I Zw 1', *Ap.J.* **489**, 656+.

Laurent-Muehleisen, S. A., Kollgaard, R. I., Ryan, P. J., Feigelson, E. D., Brinkmann, W. & Siebert, J. (1997), 'Radio-loud active galaxies in the northern ROSAT All-Sky Survey. I. Radio identifications', *AAPS* **122**, 235–247.

Law-Green, J. D. B., Hirst, P., Boisson, C., O'Brien, P. T. & Ward, M. (2000), 'ISO and SCUBA photometry of Narrow-Line Seyfert 1's', *MNRAS* . In preperation.

Leighly, K. M. (2000), 'A comprehensive spectral and variability study of narrow-line seyfert 1 galaxies observed by ASCA: I. observations and time series analysis', *Ap.J. Suppl. Ser.* .

Leighly, K. M., Mushotzky, R. F., Nandra, K. & Forster, K. (1997), 'Evidence for relativistic outflows in Narrow-Line Seyfert 1 Galaxies', *Ap.J.Lett.* **489**, L25–+.

Madau, P. (1988), 'Thick accretion disks around black holes and the UV/soft X-ray excess in quasars', *Ap.J.* **327**, 116–127.

Malkan, M. A., Gorjian, V. & Tam, R. (1998), 'A hubble space telescope imaging survey of nearby active galactic nuclei', *Ap.J. Suppl. Ser.* **117**, 25+.

Malkan, M. A. & Sargent, W. L. W. (1982), 'The ultraviolet excess of seyfert 1 galaxies and quasars', *Ap.J.* **254**, 22–37.

Markl, G. & Hauptmann, H. (1983), '.', *J.Organomet.Chem.* **248**, 269.

Matt, G., Perola, G. C. & Piro, L. (1991), 'The iron line and high energy bump as X-ray signatures of cold matter in Seyfert 1 galaxies', *A. & A.* **247**, 25–34.

Mushotzky, R. F., Fabian, A. C., Iwasawa, K., Kunieda, H., Matsuoka, M., Nandra, K. & Tanaka, Y. (1995), 'Detection of broad iron K lines in active galaxies', *MNRAS* **272**, L9–L12.

Netzer, H. & Laor, A. (1993), 'Dust in the narrow-line region of active galactic nuclei', *Ap.J.Lett.* **404**, L51–L54.

Nicastro, F., Fiore, F. & Matt, G. (1999), 'Resonant absorption in the active galactic nucleus spectra emerging from photoionized gas: Differences between steep and flat ionizing continua', *Ap.J.* **517**, 108–122.

Orr, M. J. L. & Browne, I. W. A. (1982), 'Relativistic beaming and quasar statistics', *MNRAS* **200**, 1067–1080.

Osterbrock, D. E. (1989), *Astrophysics of Gaseous Nebulae and Active Galactic Nuclei*, University Science Books.

Osterbrock, D. E. & Pogge, R. W. (1985), 'The spectra of narrow-line Seyfert 1 galaxies', *Ap.J.* **297**, 166–176.

Pedlar, A., Kukula, M. J., Longley, D. P. T., Muxlow, T. W. B., Axon, D. J., Baum, S., O'Dea, C. & Unger, S. W. (1993), 'The radio nucleus of NGC 4151 at 50 GHz and 8 GHz', *MNRAS* **263**, 471+.

Pounds, K. A., Done, C. & Osborne, J. P. (1995), 'RE 1034+39: a high-state Seyfert galaxy?', *MNRAS* **277**, L5–L10.

Pounds, K. A., Nandra, K., Stewart, G. C., George, I. M. & Fabian, A. C. (1990), 'X-ray reflection from cold matter in the nuclei of active galaxies', *Nature* **344**, 132+.

Press, W. H., Teukolsky, S. A., Vetterling, T. W. & Flannery, B. P. (1992), *Numerical Recipes in C*, 2nd edn, Cambridge University Press.

Puchnarewicz, E. M., Mason, K. O., Cordova, F. A., Kartje, J., Brabduardi, A. A., Puchnarewicz, E. M., Mason, K. O., Cordova, F. A., Kartje, J., Branduardi-Raymont, G., Mittaz, J. P. D., Murdin, P. G. & Allington-Smith, J. (1992), 'Optical properties of active galaxies with ultra-soft X-ray spectra', *MNRAS* **256**, 589–623.

Puchnarewicz, E. M., Mason, K. O., Romero-Colmenero, E., Carrera, F. J., Hasinger, G., McMahon, R., Mittaz, J. P. D., Page, M. J. & Carballo, R. (1996), 'Optical and X-ray properties of the RIXOS active galactic nuclei - I. the continua', *MNRAS* **281**, 1243–1266.

Robson, I. (1996), *Active Galactic Nuclei*, Wiley.

Rodriguez-Pascual, P. M., Mas-Hesse, J. M. & Santos-Lleo, M. (1997), 'The broad line region of narrow-line Seyfert 1 galaxies.', *A. & A.* **327**, 72–80.

Shields, G. A. (1978), 'Thermal continuum from acretion disks in quasars', *Nature* **272**, 706–708.

Shuder, J. M. & Osterbrock, D. E. (1981), 'Empirical results from a study of active galactic nuclei', *Ap.J.* **250**, 55–65.

Siebert, J., Leighly, K. M., Laurent-Muehleisen, S. A., Brinkmann, W., Boller, T. & Matsuoka, M. (1999), 'An ASCA observation of the radio-loud narrow-line Seyfert 1 galaxy RGB J0044+193', *A. & A.* **348**, 678–684.

Srianand, R. & Gopal-Krishna (1998), 'Do the central engines of quasars evolve by accretion?', *A. & A.* **334**, 39–44.

Tanaka, Y., Nandra, K., Fabian, A. C., Inoue, H., Otani, C., Dotani, T., Hayashida, K., Iwasawa, K., Kii, T., Kunieda, H., Makino, F. & Matsuoka, M. (1995), 'Gravitationally redshifted emission implying an accretion disk and massive black-hole in the active galaxy MCG:-6-30-15', *Nature* **375**, 659+.

Thean, A. H. C., Pedlar, A., J., K. M. & A., B. S. (1997), Radio observations of Seyferts from the extended 12-micron sample, *in* S. S. Holt & T. Kallman, eds, 'AIP Conference Proceedings AAA, Accretion Processes in Astrophysical Systems', p. 215.

Thean, A. H. C., Pedlar, A., Kukula, M. J., Baum, S. A. & O'Dea, C. P. (2000), 'High-resolution radio observations of Seyfert galaxies in the extended 12-micron sample - I. the observations', *MNRAS* . In preparation.

Tokunga, A. J. (1986), *IRTF Photometry Manual*, University of Hawaii.

Turner, T. J., George, I. M., Nandra, K. & Turcan, D. (1999), 'On X-Ray variability in Seyfert galaxies', *Ap.J.* **524**, 667–673.

Turner, T. J. & Pounds, K. A. (1989), 'The exosat spectral survey of AGN', *MNRAS* **240**, 833–880.

Ueno, S., Koyama, K., Nishida, M., Yamauchi, S. & Ward, M. J. (1994), 'X-ray observations of Cygnus A using the Ginga satellite', *Ap.J.Lett.* **431**, L1–L4.

Ulvestad, J. S., Antonucci, R. R. J. & Goodrich, R. W. (1995), 'Radio properties of narrow-lined Seyfert 1 galaxies', *AJ* **109**, 81–86.

Walter, R. & Fink, H. H. (1993), 'The ultraviolet to soft X-ray bump of Seyfert-1 type active galactic nuclei', *A. & A.* **274**, 105+.

Wandel, A. (1997), 'Spectral dependence of the broad emission line region in active galactic nuclei', *Ap.J.Lett.* **490**, L131–+.

Wills, B. J. & Brotherton, M. S. (1995), 'An improved measure of quasar orientation', *Ap.J.Lett.* **448**, L81–+.

Wills, B. J. & Browne, I. W. A. (1986), 'Relativistic beaming and quasar emission lines', *Ap.J.* **302**, 56–63.

Wilson, A. S. & Colbert, E. J. M. (1995), 'The difference between radio-loud and radio-quiet active galaxies', *Ap.J.* **438**, 62–71.